VORTEX FLOW AROUND THE BASES OF OBSTACLES

by

Christopher James Baker

A Dissertation submitted to the University of Cambridge

for the degree of

Doctor of Philosophy

St. Catharine's College,
Cambridge.

September 1978.

PREFACE

The work described in this thesis was carried out mainly in the Aerodynamics Laboratory of the Engineering Department between October 1975 and September 1978. The author was in receipt of a maintenance grant from the Science Research Council for this period.

The research was carried out under the supervision of Mr. E.P.Sutton whose advice and assistance are gratefully acknowledged. Thanks are also due to Mr. G.Vaid and Mr. K.Saunders who built most of the apparatus, and to the staff of the Geology Department for making the sediment transport flume available. The author would also like to acknowledge the valuable discussions he has held with his fellow research students and with staff members of the fluid mechanics group. Finally he would like to thank his wife, who helped prepare the final draft of the thesis, and Mrs D.Piggott who typed the final draft.

Except where otherwise stated, this thesis describes work undertaken solely by the author. No part of it has been submitted to any other university.

C. J. Baker

C.J.Baker

St. Catharines College
Cambridge

September 1978

CONTENTS

Figures

SUMMARY

This thesis presents the results of experimental and theoretical investigations of the horseshoe vortex systems caused by boundary layer separation upstream of obstacles mounted on a wall. Flow visualization enabled these vortex systems to be described in detail for both laminar and turbulent flow upstream of the obstacles, for flow velocities between 0.3 ms^{-1} and 25 ms^{-1}. Pressure distributions on the wall beneath such systems are presented and the variation of the vortex and separation positions upstream of various obstacles is described in detail. A complex unsteady behaviour of laminar horseshoe vortex systems is described, and the frequency spectra of turbulent vortex systems are presented. For laminar vortex systems a theoretical study of the equations of motion has been made and the distributions of vortex circumferential velocity and pressure within the vortex cores have been derived, plausible assumptions having been made for the vortex radial velocity distribution. Some measurements have been made of the flow velocity within laminar horseshoe vortex systems using smoke flow visualization techniques.

The scour around obstacles mounted in a bed of sand beneath a water flow, caused by such horseshoe vortex systems, is also studied. A dimensional analysis has been carried out to determine what dimensionless combinations of the flow variables might influence the scour depth. Small scale experiments were carried out to determine how the scour depth varied with these dimensionless groups. The results of these experiments are compared with the results of previous investigations and the way the scour depth varies with these dimensionless groups has been clearly shown. A theoretical analysis of one aspect of the phenomenon of scour around obstacles is also presented.

Principal notation

c $\dfrac{u_r}{v_r}$

C_f Skin friction coefficient $\left[= \mu\left(\dfrac{du}{dy}\right)_{y=0} \Big/ \tfrac{1}{2}\rho\, u^2 \right]$

C_D Drag coefficient

C_L Lift coefficient

C_P Pressure coefficient based on undisturbed velocity and pressure
       at model position

$C_P{}'$ Pressure coefficient based on velocity and pressure far upstream
       of model

d Scour depth

d_e Equilibrium scour depth

d_s Diameter of sediment particle

D Model diameter

E $\dfrac{u_r r_r}{\nu}$

f Oscillation frequency

g Acceleration due to gravity

G $\left\{\left(\dfrac{\rho_s}{\rho}\right) - 1\right\} g\, d_s^3 \Big/ \nu^2$

H $\dfrac{\delta^*}{\theta}$

h Water depth

h_1, h_2 Metric coefficients

i Unit vector in x direction

j Unit vector in y direction

k Unit vector in z direction

k_1, k_2, k_3, k_4 Coefficients in scour depth equations

l Model height

M Mach number

n Co-ordinate and distance perpendicular to a streamline

N $\overline{U} \Big/ \left[\left\{\left(\dfrac{\rho_s}{\rho}\right) - 1\right\} g\, d_s\right]^{\frac{1}{2}}$

p Static pressure

$\bar{P}$ Dimensionless power spectral density

r Co-ordinate and distance in a radial vortex direction

R Cylinder radius

Re $\dfrac{v_r r_r}{\nu}$

s Co-ordinate and distance along a streamline

St $\dfrac{fD}{u}$

t Time

T $\left\{\left(\dfrac{\rho_s}{\rho}\right)-1\right\}g t\big/\bar{u}$

u Velocity in x, r and ξ directions

u^* $\left(\dfrac{\tau}{\rho}\right)^{\frac{1}{2}}$

U Velocity outside boundary layer in x and ξ directions

$\bar{u}$ Mean streamwise channel velocity

v Velocity in y, ϕ and η directions.

ω Velocity in z and ζ directions

x Co-ordinate and distance in a streamwise direction, zero at model centre, increasing downstream.

X $\dfrac{x}{D}$

y Co-ordinate and distance perpendicular to the wall or plate, zero on plate, increasing away from the wall or plate.

z Co-ordinate and distance perpendicular to the plane of symmetry of the flow, zero on the plane of symmetry, increasing in direction consistent with the directions of x, y and the 'right hand' rule.

α $\dfrac{r_r}{z_r}$

Γ $2\pi r v$ - a circulation

δ^* Displacement thickness $\displaystyle\int_0^\infty \left[1-\left(\dfrac{u}{U}\right)\right]dy$

ζ Co-ordinate perpendicular to the plate (streamline co-ordinate system), zero on plate, increasing away from plate.

η Co-ordinate perpendicular to a streamline (streamline co-ordinate system)

θ Momentum thickness $\int_{0}^{\infty} \left(\frac{u}{U}\right)\left[1 - \left(\frac{u}{U}\right)\right] dy$

μ Dynamic viscosity

ν Kinematic viscosity

ξ Co-ordinate along a streamline (streamline co-ordinate system)

ρ Fluid density

ρ_s Sediment density

σ Scaling parameter in ξ direction (section 2.6)

τ Shear stress

ϕ Angular co-ordinate

ω Vorticity

Common Subscripts etc.

c   Conditions at start of scour with continuous sediment motion

o   Conditions at start of clear water scour

   or   Value at model position

   or   Value at plate leading edge

r   Reference value

s   Value at the separation position

   or   Value on a streamline

v   Value at vortex position

∞ Value far upstream from model

—   (overbar) Non dimensional or mean value

_   (underbar) Vector

'   Fluctuating component

Any notation that is not listed above is defined where it occurs in the text, as are any deviations from the above notation.

CHAPTER 1

Introduction

The two dimensional flow field around cylindrical bodies has been extensively studied in the past, as has the subject of two dimensional boundary layer flow on a flat plate. However when a cylinder is mounted on a flat plate in a fluid flow the resulting flow field is complex and three dimensional. The boundary layer upstream of the cylinder undergoes a three dimensional separation, due to the adverse pressure gradient caused by the presence of the cylinder. The separated shear layer then rolls up to form a vortex around the base of the cylinder. The ends of this vortex are swept downstream and when viewed from above this vortex has a characteristic horseshoe like shape, which has led to its name - the horseshoe vortex. Such a vortex flow upstream of a 7.6 cm diameter cylinder, 3.8 cm in height, made visible by smoke filaments injected into the flow, is shown in the photograph of figure 1.1. This photograph was taken by E.P.Sutton and is printed in Thwaites (1960). The flow is from left to right and the boundary layer upstream of the cylinder is laminar. It can be seen that several vortices are visible in the plane of symmetry upstream of the cylinder, rotating in both clockwise and anti-clockwise directions. The reflection of these vortices in the plate on which the cylinder is mounted can also be seen. The fluid that flows into these vortices drains away along the axes of these vortices - that is, the vortices act as sinks for the upstream boundary layer fluid. Although the upstream boundary layer in this case is laminar, similar, though in general less complex, vortex systems form when the upstream boundary layer is turbulent.

Such horseshoe vortex flows may be found in several practical situations. For instance horseshoe vortex systems are found at the junction of

aeroplane wings and fuselages, and at the junction of plate and support in plate heat exchangers. Horseshoe vortex systems also exist around the base of bridge supports on a river bed. In this case the high shear stresses beneath such vortex systems may cause extensive sediment motion around the base of the bridge supports, and a scour hole may form around the supports. Similar scour holes can also be observed in snow drifts around telegraph poles, and recently scour holes of this type have been observed around craters on the surface of Mars (Greeley et al. (1974)).

In chapter 2 of this thesis experimental results are presented which describe horseshoe vortex systems formed by a separating laminar boundary layer upstream of models of various shapes.

Also in chapter 2 a theoretical analysis of laminar horseshoe vortex systems is presented, based on a solution of the equations of fluid motion. Similar experimental results are presented in chapter 3 for horseshoe vortex systems formed by separating turbulent boundary layers. Chapter 4 deals with the problem of scour around bridge supports, and both experimental and theoretical results are presented. Finally in chapter 5 conclusions are drawn from the results of chapters 2, 3 and 4.

Some notes on the presentation of material in this thesis will be made here. Firstly it should be borne in mind that much that is included in chapter 2, for laminar horseshoe vortices, applies equally well to turbulent horseshoe vortices. This applies in particular to section 2.2 (Dimensional analysis) and section 2.11 (Vorticity distributions).

Secondly on many figures an indication of the magnitude of errors in the experimental results has been included. It is possible that for the experimental results presented in some figures the magnitude of the errors may not be constant over the range of the experimental results presented. Thus the error values given should be regarded as only approximate indications of the errors that may occur, and should not be regarded as strict error limits.

Finally the main co-ordinate system used in this thesis will be de-fined. A cartesian system is used with co-ordinates x , y and z and flow velocities u, v and ω in the x, y and z directions re-spectively. The origin of this system is taken to be at the point where the model axes meet the wall on which they are mounted. The streamwise co-ordinate x increases in a downstream direction, y increases away from the wall and z increases away from the plane of symmetry of the flow in a direction consistent with the directions of x and y and the 'right hand rule'.

CHAPTER 2

The horseshoe vortex formed by a separating laminar boundary layer

2.1 Literature review

2.1.1 Experimental investigations

The experimental work of E.P.Sutton over a period of years from 1958 onwards (reported by Küchemann (1965)) has already been mentioned. This work was carried out in the small smoke tunnel at Cambridge University Engineering Department, used in the experiments described in later sections, and many excellent photographs were produced which showed much detail of the horseshoe vortex system. However the first significant published work on a horseshoe vortex system caused by a separating laminar boundary layer was that of Schwind (1962). For this investigation a specially built low speed wind tunnel was used, and horseshoe vortices were observed in front of a 60° wedge which divided the wind tunnel into two. Very detailed observations were made of the flow using smoke introduced into the flow upstream of the wedge, for speeds between 0.16 ms^{-1} and 1.33 ms^{-1}. Schwind observed five types of vortex regimes (figure 2.1.1). At the lowest speeds used he observed flow of the "regime 1" type, which he described as "a steady separation with no vortices visible". This description seems a little misleading. If the flow does separate upstream of the wedge, then downstream of the separation line, there will be a flow in the upstream direction, which implies some form of vortex behaviour. Perhaps it would be more correct to say that in "regime 1" type flow only a very weak, slowly rotating vortex is formed, that is observable only on the plane of symmetry. As the flow velocity was increased, flow of the "regime 2" type was observed, with a single steady clockwise rotating vortex and a small triangular shaped counter-rotating vortex visible. The need for velocity gradients to be continuous implies that a second vortex rotating in the same direction as the main vortex must be

present upstream of the small counter-rotating vortex, although this was
not observed by Schwind for flows of the regime 2 type. When such a
vortex was observed Schwind defined this as "regime 3" type flow, which
appeared as the velocity increased. A second small counter-rotating
vortex was also observed in this type of flow. As the velocity was
further increased the two clockwise rotating vortices were seen to start
to oscillate, the amplitude increasing with the velocity. In flows of
"regime 4" and "regime 5" types, which occurred at yet higher velocities,
regular oscillatory motion was observed with the main vortex apparently
becoming isolated from the rest of the vortex system and moving towards
the wedge, then moving back upstream. For "regime 4" type flow the
vortex was seen to combine with the second vortex, while for "regime 5"
type flow it was seen to pass beneath the second vortex. Since this
vortex could not pass out of the separated region it presumably combined
with an unobserved third clockwise rotating vortex.

Schwind pointed out that although the flow passed from regime 1 to
regime 5 types as the velocity increased, the velocity at which the flow
changed from one regime to another was by no means well defined and dif-
ferent flow regimes could exist at one velocity. From pulsed smoke ob-
servations, Schwind obtained some not very accurate measurements of the
velocity within the horseshoe vortex system, for steady vortex systems.
From cine film analysis he obtained much information on how the vortex
position changed with time for unsteady systems, both on and off the
plane of symmetry. He also attempted to find how the vortex position
varied with the various flow parameters, and how the oscillation frequency
varied for unsteady systems. However he met with little success.

Peake and Galway (1965a) studied the development of a laminar
boundary layer ahead of a 7 cm diameter cylinder mounted on a plate in a
water channel, at a velocity of 0.25 ms^{-1}. They also carried out a
similar investigation for flow around Rankine ovals (Peake and Galway

(1965b)). Although they were mainly concerned with the experimental and theoretical development of the boundary layer upstream of the separation line, they did make some dye flow observations of the horseshoe vortex systems ahead of the Rankine ovals. They observed up to three vortices rotating in the same direction, upstream of the ovals, and at least one counter-rotating vortex (figure 2.1.2). These works will be discussed further in section 2.1.2.

Several investigations have been carried out to study transition in a laminar boundary layer caused by obstacles immersed within the boundary layer. Gregory and Walker (1951), in experiments around small cones and cylinders observed "three or more" horseshoe vortices upstream of the obstacles. Mochizuki (1961a, 1961b) in studying the flow around hemi-spheres using smoke flow visualization techniques, obtained very detailed photographs of the wake formation, and also observed the horseshoe vortex system both upstream and downstream of the hemispheres.

A more extensive investigation of this type was carried out by Norman (1972). He studied the flow around cylinders and rectangular boundary layer trips at speeds from 0.3 ms^{-1} to 16 ms^{-1} using smoke flow visualizat-ion. He examined the configuration of the horseshoe vortices upstream of the trip and proposed two detailed models of the steady flow patterns observed (figure 2.1.3). These models, called by Norman the "Jet-Maze" and "Stairstep" models, differ in the order in which the different vortices within the vortex system are fed from the upstream boundary layer. Norman concluded that for his flow conditions the flow was of the "Jet-Maze" type. The system used by Norman for numbering the different vortices will be used in a modified form throughout this dissertation.

Norman also studied the flow around the side of the boundary layer trips using smoke flow visualization and hot wire anemometry. The whole horseshoe vortex system was seen to be further away from the wind tunnel wall on which the trip was placed than on the plane of symmetry, and the

core of the main vortex (1) appeared to be almost stagnant.

He also observed a type of oscillatory behaviour within the horse-shoe vortex system. However it was not possible to say to what flow regime of Schwind (1962) this behaviour corresponded. He also attempted to find how the separation position upstream of the trip varied with the flow parameters. There is considerable scatter in his results, but it does seem that the horseshoe vortex oscillations begin at a fairly constant value of Reynolds number based on trip size.

The Weapons Research Establishment (1967) has made a cine film of the flow upstream and downstream of spheres on a wall, immersed in a laminar boundary layer, for sphere diameters between 3 mm and 37 mm and wind speeds between 1.3 ms^{-1} and 4.8 ms^{-1}. Sublimation and smoke flow visualization techniques were used. At the lower wind speeds steady horseshoe vortices were seen upstream of the cylinder and these extended many sphere diameters downstream, forming a laminar wake. As the wind speed increased these vortices appeared to "burst" and become turbulent downstream of the sphere, the position of this burst moving upstream and closer to the sphere as the speed increased. When these bursts had moved to within a few diameters of the sphere the upstream horseshoe vortex systems began to oscillate regularly, and these oscillations seemed to pass downstream, producing regular oscillations in both the laminar and turbulent parts of the vortex wake. To which of the oscillatory regimes of Schwind (1962) these oscillations belonged could not be distinguished. As the speed increased further, the turbulence passed into the vortex systems upstream of the spheres.

Sedney (1973) reviewed the subject of transition caused by boundary layer trips for both subsonic and supersonic speeds. He also reviewed some papers which are of relevance to the work described in Chapter 3, where the horseshoe vortex caused by a separating turbulent boundary layer is discussed.

Finally mention should be made of the work of Bossel and Honnold
(1976). They studied the flow ahead of plate fin heat exchangers using
dye flow visualization in a low speed water tunnel. They observed flow
patterns similar to those described by Norman (1972), differing slightly
in the order of feeder layers observed (figure 2.1.4). At the lowest
water velocities used they observed a flow very similar to Schwind's
"regime 1" type flow, where only a weakly rotating vortex could be seen.

2.1.2 Theoretical aspects

The development of a laminar boundary layer upstream of an obstacle
on a flat plate, when the pressure distribution on the plate due to the
obstacle is assumed to be known, can be calculated using two different
types of method. Firstly a differential method can be used in which the
boundary layer equations and the continuity equation are solved by using
finite difference methods. The position of the separation line ahead of
the obstacle can then be determined by finding the envelope of the limit-
ing streamlines. An example of this type of calculation is that of
Dwyer (1968), who calculated the boundary layer development ahead of a
circular cylinder on a plate at a speed of 30.5 ms^{-1}. Secondly an
integral method can be used in which the boundary layer momentum integral
equations are solved, together with an assumed family of velocity pro-
files. A general calculation method of this type was developed by
Timman (1955). Peake and Galway (1965a), (1965b) used a modification of
this method suggested by Cooke (1959) to calculate the boundary layer
development ahead of a cylinder on a plate, and ahead of a Rankine oval
on a plate. They utilised the small cross flow assumption of Zaat (1956)
with this method of Timman and Cooke, which enabled the streamwise and
crossflow momentum equations to be solved independently. This method
will be discussed more fully in section 2.6.

The methods that have been used for the solution of the Navier-
Stokes equations for vortex cores have been well reviewed by Hall (1966).

In section 2.9 one of these methods (that of Rott (1958)) will be applied to the solution of the Navier-Stokes equations for a horseshoe vortex core.

Schwind (1962) and Roper (1967) both applied vorticity considerations to their studies of horseshoe vortex systems. (The work of Roper concerns a horseshoe vortex system caused by the separation of a turbulent boundary layer, but the following analysis applies equally well to a horseshoe vortex system formed by a laminar boundary layer undergoing separation. The work of Roper will be considered further in Chapter 3).

Both Schwind and Roper start with the vector form of the Navier-Stokes equations

$$\frac{\partial \underline{u}}{\partial t} - \underline{u} \times \underline{\omega} = -\nabla \left(\frac{p^*}{\rho} + \frac{u^2}{2} \right) + \nu \nabla^2 \underline{u} \tag{2.1.1}$$

where $\underline{u}$ is the vector velocity, p^* is the piezometric pressure; ρ is the fluid density, ν the fluid kinematic viscosity and $\underline{\omega} \left(= \nabla \times \underline{u} \right)$ the vorticity vector. After some manipulation Schwind derives

$$\frac{D\underline{\omega}}{Dt} = \left(\underline{\omega} \cdot \nabla \right) \underline{u} + \nu \nabla^2 \underline{\omega} \tag{2.1.2}$$

where D/Dt is the substansive derivative. Following Schwind we non-dimensionalize using

$$\overline{\nabla} = x_r \nabla \quad , \quad \overline{u} = \frac{u}{u_r} \quad , \quad \overline{\omega} = \frac{\omega x_r}{u_r} \quad , \quad \overline{t} = \frac{u_r t}{x_r} \tag{2.1.3}$$

where u_r and x_r are reference velocities and lengths respectively. This leads to

$$\frac{D\overline{\omega}}{D\overline{t}} = \frac{\nu}{u_r x_r} \nabla^2 \overline{\omega} + \left(\overline{\omega} \cdot \overline{\nabla} \right) \overline{u} \tag{2.1.4}$$

where $u_r x_r / \nu$ is a Reynolds number. Equation (2.1.4) implies that as the Reynolds number changes the time average dimensionless vorticity (and hence velocity) distributions must change. Schwind suggests that this

explains the existence of different vortex regimes, the vorticity equation

(2.1.4) being satisfied by different flow geometries at different

Reynolds numbers.

Roper (1967) applied equation (2.1.1) to the control volume shown in

figure 2.1.5. After some manipulation he obtained the integral equation

$$\int_A^B (\underline{u} \times \underline{\omega}) \cdot \underline{ds} = \nu \oint_{ABCDA} (\nabla \times \underline{\omega}) \cdot \underline{ds} \tag{2.1.5}$$

Roper then applied the following boundary conditions to equation

(2.1.5)

(a) the no slip condition on CD and DA

(b) the condition that the velocity perpendicular to ABCD is zero.

He then obtained the following equations

$$\left[\frac{p^*}{\rho}\right]_D = \left[\frac{p^*}{\rho}\right]_C - \nu \int_D^C \frac{\partial^2 v}{\partial x^2} \cdot dy \tag{2.1.6}$$

$$\left(\frac{u^2}{2}\right)_\infty = \nu \int_D^C \frac{\partial^2 v}{\partial x^2} \cdot dy - \nu \int_D^A \frac{\partial^2 u}{\partial y^2} \cdot dx \tag{2.1.7}$$

where u and v are the velocity components in the x and y direct-

ions and the subscript ∞ indicates a value away from the plate far up-

stream. Because of the occurrence of the second derivatives of velocity

in equations (2.1.6) and (2.1.7) these equations seem to have no easy

solution, and do not really help in understanding the flow within a horse-

shoe vortex system.

Finally the inviscid flow analysis of Hawthorne (1954) and later

works of the same type will be described. Hawthorne (1954) studied the

secondary flow about struts and aerofoils. He assumed that the flow

about these bodies could be described by the potential flow appropriate

to the body shape, together with a small perturbation of the velocity in

the oncoming flow. Thus effectively the flow around struts and aerofoils

in a shear flow was studied. It was found that blunt nosed aerofoils amplified the initial flow perturbations so that in the vicinity of the body large concentrations of vorticity appeared, and the theory became invalid. Cusped struts were found to amplify the perturbations to a lesser degree, and the inviscid flow theory remained valid.

Hawthorne and Martin (1955) studied the flow around a hemisphere in a shear flow using a similar inviscid flow analysis. The analysis showed two concentrations of vorticity downstream of the hemisphere (figure 2.1.6) and experiments confirmed this. These vorticity concentrations correspond in sign and position to the two branches of the horseshoe vortex system trailing downstream of the hemisphere. Thus paradoxically the horseshoe vortex, which is essentially caused by separation of a viscous boundary layer can be modelled to some extent by an inviscid flow analysis.

Finally the work of Rowe (1966) should be mentioned. He used similar techniques to those described above, and calculated the secondary flow distribution around various shapes of model in a shear flow and found the position of the vorticity concentrations upstream of these models.

2.2 Dimensional analysis

If, in a horseshoe vortex system around an obstacle formed by the separation of an incompressible laminar boundary layer, x_v is the distance from the obstacle centre to the centre of the vortex core on the plane of symmetry, then one may write

$$x_v = fn\left(D, l, U, \delta^*, H, u_y', \mu, \rho\right) \tag{2.2.1}$$

where D is the obstacle diameter and l the obstacle height. U is the free stream fluid velocity, and δ^* and H are, respectively, the boundary layer displacement thickness and form parameter at the obstacle position when the obstacle is not in position. u_y' is the distribution of turbulence within the oncoming boundary layer, and μ and ρ are the

fluid viscosity and density respectively.

Non-dimensionalizing equation (2.2.1) becomes

$$\frac{x_v}{D} = fn\left(\frac{UD}{\nu}, \frac{D}{L}, \frac{D}{\delta^*}, H, \frac{u_y'}{U}\right) \tag{2.2.2}$$

where $\nu \left[=\frac{\mu}{\rho}\right]$ is the kinematic viscosity.

Similarly if x_s is the distance from the obstacle centre to the separation line upstream of the obstacle on the plane of symmetry

$$\frac{x_s}{D} = fn\left(\frac{UD}{\nu}, \frac{D}{L}, \frac{D}{\delta^*}, H, \frac{u_y'}{U}\right) \tag{2.2.3}$$

It will be shown in section 2.4 that for some values of the flow parameters, horseshoe vortex systems exhibit regular oscillatory behaviour. If f is the frequency of such oscillations then one may write

$$\frac{fD}{U} = fn\left(\frac{UD}{\nu}, \frac{D}{L}, \frac{D}{\delta^*}, H, \frac{u_y'}{U}\right) \tag{2.2.4}$$

In the following sections the variation of the dependent dimensionless variables ($\frac{x_v}{D}$, $\frac{x_s}{D}$ and $\frac{fD}{U}$) will be considered for several different obstacle shapes. For all the obstacles used $\frac{D}{L}$ is small (= 0.21 in most cases) and it will be assumed that the values of the dependent dimensionless variables do not depend on this dimensionless group. Also it will be seen that the form parameter H does not vary greatly (section 2.3) and it will be assumed that such small variations do not affect the dependent dimensionless variables. Further the variations of the turbulence distribution throughout the boundary layer will not be considered. (It will be shown that the only significant variations in the turbulence distribution occur at the higher velocities used).

Thus for a horseshoe vortex system caused by a separating laminar boundary layer we are left with

$$\frac{x_v}{D}, \frac{x_s}{D}, \frac{fD}{U} = fns\left(\frac{UD}{\nu}, \frac{D}{\delta^*}\right) \tag{2.2.5}$$

In the following sections the dependent dimensionless variables will be plotted in the $\frac{UD}{\nu}$ against $\frac{D}{\delta^*}$ plane.

2.3 Experimental apparatus and procedure

2.3.1 Wind tunnels

Two wind tunnels were used for this part of the investigation; a smoke tunnel was used to make visual observations of horseshoe vortex systems and to measure the flow velocities within such systems, while Number 1B Low Speed Wind Tunnel was used to make detailed measurements of the pressure distributions beneath horseshoe vortex systems and of the oscillation frequencies of such systems.

The smoke tunnel is shown schematically in figure 2.3.1. The models used were mounted on a plate parallel to the flow, along the tunnel centre line. Smoke was introduced into the flow through a rake of small tubes mounted on a streamlined strut upstream of the plate. The smoke was produced by a smoke generator of the Preston and Sweety type, and consisted of a fog of fine droplets of paraffin. The tunnel speed could be varied between about 0.3 ms^{-1} and 4 ms^{-1} with the smoke streamlines remaining steady. The working section could be brightly illuminated for the purposes of photography through perspex slits in the side of the tunnel.

Number 1B Low Speed Wind Tunnel, which will from now on be referred to as the 51 cm x 71 cm tunnel, is shown schematically in figure 2.3.2. Since this tunnel was used at speeds very much lower than was usual (at between 0.5 ms^{-1} and 4 ms^{-1}), several modifications were carried out. Firstly extra screens were inserted in the tunnel upstream of the working section, so that the tunnel could be run at higher fan speeds than would otherwise have been the case (and hence steadier flows were obtained). Secondly vortex generators were inserted at the upstream end of the diffuser, to ensure that diffuser separation did not occur. To generate the laminar boundary layers needed for this investigation, the tunnel

wall boundary layer was removed by using a suction slot (powered by a Keith Blackman 8HE Pump) that could be inserted at various positions on the wind tunnel wall. Thus a new laminar boundary layer grew on the wind tunnel wall downstream of the suction slot. Four positions of the suction slot were used, and for each position great care was taken to ensure that the wind tunnel wall downstream of the suction slot was perfectly smooth, by filling any cracks between the suction slot and the downstream wind tunnel wall with a filler, and then sanding and painting over the filler until no discontinuity could be detected. As the tunnel speed was varied the suction power was also varied so that all the boundary layer on the upstream wind tunnel wall was sucked away at all tunnel speeds. The suction power was measured by measuring the pressure drop across an orifice plate within the suction pipe, and was varied by opening and closing a valve within this pipe. Thus it was possible to reproduce the suction power required to suck away the tunnel wall boundary layer once a calibration had been carried out.

2.3.2 Wind tunnel flow characteristics

Because some measurements of a quantitative nature were made in the smoke tunnel (the measurements of velocity within horseshoe vortex systems), measurements were made of the velocity distributions in the empty working section. These distributions were measured by traversing a Pitot tube across the working section. The static pressure was measured at a hole in the wind tunnel wall within the working section. These velocity distributions are shown in figure 2.3.3. It can be seen that there is approximately a 10% change in velocity across the section in the x direction, and approximately a 20% change in velocity across the section in the y direction (outside the tunnel wall boundary layer). This effect is particularly noticable at the lower speed used. For this reason all measurements of velocity within horseshoe vortex systems were

made at ⌣ and above the higher speed used here.

Because of this non-uniformity of the flow it was decided not to measure accurately the boundary layer characteristics on the plate on which the models were mounted, but simply to use the Blasius formulae for flat plate boundary layers in zero pressure gradient to calculate their nominal values.

However in the more controlled flow conditions of the 51 cm x 71 cm tunnel the mean velocity and turbulence profiles of the boundary layers on the wind tunnel wall downstream of the suction slot were measured, by traversing a hot wire 'u' probe throughout the boundary layer. (see section 2.3.6).

Some of these profiles, measured at the model position, for all four suction slot positions used, are shown in figure 2.3.4. It can be seen that there is a rather high level of turbulence in the tunnel free stream. This is possibly due to the extra screens placed upstream of the working section. At the higher speeds used this turbulence is amplified within the boundary layer, an indication that transition to turbulence is beginning to occur at these speeds. The boundary layer displacement thickness and form parameter were calculated from these and other profiles and their variation with tunnel speed is shown in figure 2.3.5. If one assumes that there was an error in measuring the velocities in figure 2.3.4 of 15%, say (which is in fact as accurately as the velocities could be determined at the low speeds used) then the displacement thickness δ^*

$(= \int_0^\infty \left[1 - \left(\frac{u}{U} \right) \right] dy$) may be in error by up to 3%, the momentum

thickness θ (= $\int_0^\infty \left(\frac{u}{U} \right) \left[1 - \left(\frac{u}{U} \right) \right] dy$) by up to 6% and the

form parameter H (= δ^*/θ) by up to 9%. This explains the seemingly large variation in the values of H indicated in figure 2.3.5. However all values of H are within 9% of 2.59, the value for boundary layer growth on a flat plate in zero pressure gradient.

Experiments with hot wire probes held close to the surface indicate

that a laminar flow region adequate for the present experiments exists on the wind tunnel wall behind the suction slot (figure 2.3.6). The dotted lines in this figure indicate the approximate boundary of the region where the turbulence level in the boundary layer is one and a half times that measured on the wall centre line at a height of 1 mm above the wall. Thus even when the suction slot is 0.45 m away from the model position a region 0.36 m wide of adequate laminar flow exists on the wind tunnel wall.

2.3.3 Models

For the flow visualization experiments carried out in the smoke tunnel several cylinders of different diameters and heights were used. These were made from brass tube, painted matt black and screwed to the plate in the smoke tunnel. A 7.62 cm diameter, 3.81 cm high cylinder was most commonly used for flow visualization, and was also used when horseshoe vortex velocity measurements were made.

For the more quantitative measurements made in the 51 cm x 71 cm tunnel three models were used; a circular cylinder, a circular cylinder with a splitter plate, and a streamlined model consisting of a hemicylindrical nose section followed by a faired tail section. The dimensions are given in figure 2.3.7. It was hoped to use a streamlined model of the same height on the other models, but when built this proved to be too heavy to traverse along the wind tunnel wall (in order to make pressure measurements), so a shorter model was used. (These three different types of models were used to study the effect of the different flow patterns within the wake of the models on the oscillatory behaviour of horseshoe vortex systems).

The blockage correction of Maskell (1966) was applied to calculate the effective flow velocities within the wind tunnel, for all the tests carried out in the 51 cm x 71 cm tunnel. This correction states that the effective velocity is given by $U(1 + \varepsilon)$ where U is the wind tunnel

velocity without the model in the working section and ε is given by

$$\varepsilon = \left[1 + \left(\frac{C_D}{-C_{pb}} \right)\left(\frac{S}{C} \right) \right]^{\frac{1}{2}} - 1 \qquad\qquad (2.3.1)$$

where C is the wind tunnel cross sectional area, S is the area of the model normal to the flow, and C_D and C_{pb} are, respectively, assumed drag coefficients and base pressure coefficients for the model. The blockage corrections ε , calculated from equation (2.3.1) were small and were found to be 0.005 for the streamlined model, and 0.025 for the cylinder and cylinder with splitter plate models.

Because of the non-uniform nature of the flow no blockage corrections were applied to any of the results obtained in the smoke tunnel.

2.3.4 Flow visualization photography

Photographs were taken in the smoke tunnel using a Nikon F135 mm camera. Cine films were taken using a Beaulieu R16 cine camera.

2.3.5 Pressure measurements

Measurements were made of the pressure variation on the plane of symmetry upstream of the models using the apparatus shown in figure 2.3.8, which was built into the wind tunnel wall downstream of the suction slot in the 51 cm x 71 cm tunnel. The models were traversed through a small distance (2 cm) and the pressure was measured successively at each of six pressure tappings 2 cm apart, using a Furness micromanometer FM332, with a full scale deflection of 1 mm of water. Thus a continuous pressure distribution was obtained. The model traverse gear was connected to a potentiometer powered by a D.C. supply, so that the cylinder movement could be recorded on either a D.C voltmeter, or on the x axis of a chart recorder. The Furness micromanometer produced an electrical output which could also be recorded on a D.C. voltmeter or on the y axis of the chart recorder. If a chart recorder was used a trace of the pressure distribution could be obtained directly. Two Solartron D.C. Voltmeters and a Moseley Autograf 3S chart recorder were used.

An apparatus very similar to that described above was also used to

make pressure measurements in the smoke tunnel. Details of this apparatus are given by Shellim (1976).

2.3.6 Hot wire anemometry

To measure the frequency of oscillation of horseshoe vortex systems hot wire probes were inserted through the wall of the wind tunnel so that the tip of the probe was only a short distance away from the wind tunnel wall (figure 2.3.9a). Flow visualization carried out in the smoke tunnel showed that the presence of the probe did not affect the vortex system when it was placed in this position, but if the tip of the probe entered the core of the main vortex, then the whole vortex system began to oscillate irregularly.

DISA 'u' probes were used almost exclusively as the sensing element at an overheat ratio of 1.8, and a block diagram of the system used is shown in figure 2.3.10. The output from the 55D01 bridge was linearized by a 55D10 linearizer and the linearized output was measured on a 55D30 D.C. voltmeter and on a 55D36 RMS meter. Signals were filtered to remove the D.C. component using a Krohn-Hite 3550 filter, and were recorded on a Racal T3000 tape recorder. The signal was also displayed on a Telequipment DM53A storage oscilloscope for visual examination. Some photographs were taken of the oscilloscope display using a Polaroid camera.

Similar probes were used to make measurements in the model wakes. The method of mounting these probes is shown in figure 2.3.9b. Also they were used to measure the velocity and turbulence profiles in the boundary layer on the wind tunnel wall. The traverse gear used for this is shown in figure 2.3.9c.

The signals were linearized because many of the signals that were to be analyzed had large values of turbulence intensity (over 50%). These signals would have been distorted by the non-linear output characteristics of the bridge if no linearizer had been used.

Spectral analyses were carried out on the recorded signals using the CUED CED509 $\propto$ minicomputer. The spectral analysis programme was developed by S.Norman and details of the programme may be found in Norman (1977). Using a fast Fourrier transform this programme analyzes a fluctuating signal and produces (in either graphical or digital form) an output which shows how the power spectral density varies with frequency. The area under the power spectral density curve is a measure of the power of the fluctuating input signal. Thus any peaks in this curve indicate frequencies at which a large proportion of the power of the fluctuating signal is present. For instance a sine wave with only one discrete frequency will produce a sharp peak at this frequency on the power spectral density-frequency curve.

All of the values of power spectral density that are shown in figures later in this dissertation are non-dimensionalized by dividing by the mean square of the fluctuating signal.

2.3.7 Velocity measurements

If the velocity within horseshoe vortex systems were to be measured by any of the conventional means (such as Pitot tubes or hot wire probes) it would be very difficult to interpret the results since the extent to which these probes affect the flow would not be known. It was thus decided at the beginning of this investigation to make a simple laser anemometer to make velocity measurements within the horseshoe vortex system. This instrument can measure flow velocity at a point in a flow where two laser beams are crossed and thus no probe is inserted into the flow. Accordingly the experiments were designed to make laser anemometry possible in the 51 cm x 71 cm tunnel. It was decided to measure the flow around models downstream of a suction slot in the wind tunnel wall rather than to measure the flow around models mounted on a plate in a wind tunnel, because this made it possible to use an already existing optical

system. Unfortunately there were several unforseen problems with the laser anemometer and it proved to be impossible to make the required measurements with this instrument.

It was then decided to make measurements of the flow velocity by making cine films, at a nominal speed of 64 frames/second, of smoke filaments entering the vortex system, and then making measurements from these films to determine how far the ends of the smoke filaments had travelled between successive frames. The exact speed at which the cine camera filmed was determined by filming the output of a D.C. voltmeter to which an oscillating signal of exactly 1.25 Hz was applied, and counting the number of frames between maxima of the voltmeter output. The camera was found to be filming at 58.8 frames/second.

So in this way a set of velocity measurements could be made on the plane of symmetry upstream of the models used. Such an experiment was easily set up in the smoke tunnel and proved to be successful. So a similar experiment was set up in the 51 cm x 71 cm tunnel. The apparatus used is shown in figure 2.3.11. The smoke was injected into the flow from a probe just downstream of the suction slot. The horseshoe vortex was illuminated through a window set into the wind tunnel wall, by two Wattastar lamps, and cine films were taken through a perspex sheet set into the wind tunnel floor. The smoke probe was designed so that smoke filaments were introduced into the flow 1 cm below the centre line of the wind tunnel wall. This was because preliminary tests revealed that the flow on the wind tunnel wall had a small upwards component close to the centre line and the flow direction was at about 2° to the horizontal. This small deviation of the flow from the horizontal is of no consequence to the pressure and hot wire measurements described in the following sections, but for the horseshoe vortex to be adequately visualised the smoke filaments had to be introduced into the flow a small distance below the wall centre line.

2.4 Flow visualization results

2.4.1 General description of horseshoe vortex flows

Figure 1.1, taken from Thwaites (1960), shows a photograph taken by E.P.Sutton in the smoke tunnel used for flow visualization experiments in this investigation. It shows the flow pattern on the plane of symmetry upstream of a short cylinder on a plate, formed by the separation of a laminar boundary layer. The reflection of this flow pattern in the plate can also be seen.

Figure 1.1 is typical of the flow patterns seen in the smoke tunnel at the lower speeds used. There are at least three vortices rotating in the clockwise direction and two smaller vortices rotating in the opposite direction. The exact number of vortices was seen to depend upon the flow speed and cylinder size, more vortices appearing as the speed increased. With a 7.62 cm diameter cylinder in the tunnel, above a certain flow speed (approximately 0.65 ms^{-1}) the entire horseshoe vortex system began to oscillate in a regular manner with the two largest clockwise rotating vortices moving towards one another and apart again. At higher speeds (above approximately 0.8 ms^{-1}) the largest clockwise rotating vortex ceased to be fed by smoke during part of the oscillation period and seemed to become detached from the rest of the vortex system. At still higher speeds (above approximately 1.4 ms^{-1}) the flow appeared to be very un-steady and turbulent and showed no traces of periodicity. These steady and oscillating horseshoe vortex systems will be discussed in more detail in the following sections.

2.4.2 Detailed description of steady horseshoe vortices

Consider the horseshoe vortex system that is shown in the photo-graphs of figure 2.4.1. The filament of smoke that feeds into the vortex system is being moved closer to the plate on which the cylinder is mounted as we proceed from figure 2.4.1a to figure 2.4.1g. When the filament just begins to flow into the vortex system, it flows into a small anticlock-

wise rotating vortex formed by separation of the flow from the face of the cylinder. The smoke filament passes around the base of the cylinder (figure 2.4.1a). We will call this vortex, vortex 0 .

As the smoke filament moves closer to the plate, it flows down the face of the cylinder, then along the plate away from the cylinder and into a small triangular vortex. This vortex assumes a horseshoe shape around the side of the cylinder. We will call this vortex (for reasons that will become apparent later) vortex 1' (figure 2.4.1b).

As the smoke filament moves still closer to the plate, it flows away from the cylinder, over vortex 1' and into a small flattened vortex rotating in the same direction as vortex 1'. We will call this vortex vortex 2' (figure 2.4.1c).

As the movement of the smoke filament continues, the smoke flows into a large vortex, rotating in a clockwise direction and situated between vortex 1' and the cylinder. This vortex will be referred to as vortex 1 , or the primary vortex (figures 2.4.1d and 2.4.1e).

With the smoke filament still closer to the plate, the smoke flows into two further vortices rotating in the same direction as vortex 1. The one closer to the cylinder will be referred to as 'vortex 2', the one further away as 'vortex 3' (figure 2.4.1f and g).

The order of 'feeder layers' for vortices 2 and 3 is not very clear from the photographs but it appears from these figures that as the smoke filament moves towards the plate vortex 3 is fed first, then vortex 2 and when the smoke filament is right next to the surface of the plate vortex 3 is fed once more. The streamline pattern that can be inferred from these photographs is shown in figure 2.4.2a.

This type of vortex system is an example of a six vortex system which was the most complex system observed in the smoke tunnel. Four and two vortex systems were also observed under different flow conditions and the streamline patterns observed are shown in figure 2.4.2b and 2.4.2c. Also

in this figure the various separation lines (S , S_0, S_1, S_2), attachment lines (A_o, A_1, A_2) and free stagnation points ($SP1, SP2$) are shown.

Figure 2.4.3 shows how the number of vortices varies with the flow parameters, determined from observations around cylinders of various sizes. (The value of δ^* was calculated from the Blasius formula). It can be seen that the number of vortices that were observable increases as $\frac{UD}{\nu}$ and $\frac{D}{\delta^*}$ increase.

2.4.3 Detailed description of oscillating horseshoe vortex systems

In this section the photographs of an oscillating horseshoe vortex system shown in figure 2.4.4 will be considered. In these photographs, taken from a positive cine film, smoke appears black against a white background. The primary vortex (1) initially moves towards the cylinder (frames 1-9) and the smoke filament to it is cut so it appears to become isolated. Then it moves back upstream and entrains smoke from the outer layers of the secondary vortex (2) (frames 10-14) until the initial flow pattern is reestablished. It is not possible to determine whether vortex 1 does cease to be fed by any fluid as it moves towards the cylinder, or whether the smoke filament is cut and vortex 1 simply seems to become isolated.

The paths taken by vortices 1, 2 and 3 during one oscillation are shown in figure 2.4.5. It is instructive to consider the vortex system to consist of potential vortices and their images (in a manner similar to Schwind (1962)) and to analyse the movements of figure 2.4.5 in this light (figure 2.4.6a). As vortex 1 is convected downstream (frames 1 to 9) it becomes influenced to a greater extent by its image in the cylinder and thus moves down towards the plate. As it moves closer to the plate it becomes influenced more and more by its image in the plate and thus moves back upstream where it entrains the outer layers of vortex 2 (frames 10 to 14).

As vortex 1 moves towards the cylinder vortex 1' must move with it,

since it is caused by separation under vortex 1. Since the effect of vortex 1' on vortex 2 is to pull it down onto the plate (figure 2.4.6b) when vortex 1' moves away from vortex 2, vortex 2 rises from the plate (frames 3-10). In a similar manner when vortex 1 (and hence vortex 1') moves back towards vortex 2, vortex 1' influences vortex 2 to a greater extent and vortex 2 moves back towards the plate (frames 11-14).

The oscillating flow described above is very similar to the "regime 4" flow of Schwind (section 2.1.1). However it was not possible to observe Schwind's "regime 5" flow. As the tunnel speed was increased above approximately 1.4 ms^{-1} (with a 7.62 cm diameter cylinder) the horseshoe vortex system appeared to become turbulent and no regular oscillatory motion could be seen.

2.4.4   The horseshoe vortex away from the plane of symmetry

Figure 2.4.7 shows a horseshoe vortex system viewed at an angle of 30° to the plane of symmetry. This was made visible by illuminating the flow through a perspex slit in the side of a cylinder. The smoke feeder filament on the plane of symmetry moves closer to the plate from figure 2.4.7a to figure 2.4.7c.

Vortices 1, 2 and 3 can be clearly seen in these photographs. It should be noted that all the smoke making them visible has come from the plane of symmetry. This does not mean that the vortices are not being fed by fluid in this plane. A smoke feeder filament can be dimly seen entering vortex 1 in figure 2.4.7a and vortex 1' can also just be seen in this photograph.

Visual observations at angles of greater than 30° to the plane of symmetry suggest that all the vortices move to greater distances from the plate than on the plane of symmetry. Also the number of vortices seems to increase further around the cylinder. For example where only two vortices were seen on the plane of symmetry, four might be seen at an angle of 45° to the plane of symmetry. However it proved impossible to

take photographs at angles very much greater than 30° to the plane of symmetry.

2.4.5 Comparison of flow visualization and pressure distributions

Pressure distributions were measured using the apparatus of Shellim (1976), described in section 2.3.5 and two typical results are shown in figure 2.4.8. The qualitative nature of these results should be borne in mind. The pressure coefficient C_p' used in this section is based upon the velocity and pressure close to the leading edge of the plate on which the cylinder is mounted. The curves of figure 2.4.8 are tracings of chart recorder outputs.

First consider the curve marked A, which is a pressure distribution at flow conditions for which a steady horseshoe vortex system existed.

The position of the pressure minimum was seen to correspond closely to the position of the primary vortex when smoke flow visualization was carried out. Thus the position of the primary vortex can be determined from pressure distributions, and this method was used to find the position of the primary vortex in the more controlled flow conditions of the 51 cm x 71 cm tunnel.

Now consider curve B. Flow visualization showed that at these flow conditions an unsteady horseshoe vortex system existed. Thus a pressure distribution similar to curve B is indicative of an unsteady horseshoe vortex system.

Curve A also shows a slight levelling out at $\frac{x}{D} = -0.92$. Flow visualization showed this to be the position of vortex 1′. A slight dip in the curve can also be seen at $\frac{x}{D} = -1.06$, and flow visualization showed this to be the position of vortex 2.

2.4.6 Effect of hot wire probes on horseshoe vortex systems

Since it was intended to study the periodic behaviour of horseshoe vortex systems using hot wire probes, flow visualization experiments were

carried out to study the effect of such probes on the flow. It was found that if the probe entered the primary vortex, this vortex began to oscillate irregularly at speeds where the flow would otherwise be steady. However, as can be seen from figure 2.4.9, if the probe is inserted only a small distance into the flow (of the order of 1 mm) then the probe appears to have no effect on the flow.

2.5 Plane of symmetry pressure measurements

In this section pressure distributions on the plane of symmetry upstream of the models will be presented. The pressure coefficient C_p used in this section is based upon the velocity and pressure at the model position without the model being in position. The pressure distributions on the plane of symmetry upstream of the cylinder model are shown in figure 2.5.1. These curves are tracings of chart recorder outputs. It can be seen that there are two types of distribution. For $\frac{UD}{\nu} < 5,000$ the curves have minima, which the smoke tunnel results suggest are at the position of the primary vortex. For $\frac{UD}{\nu} > 5,000$ no minima can be seen and flow visualization results suggest that oscillating vortex systems exist. As $\frac{UD}{\nu}$ increases, the vortex position moves upstream away from the cylinder. The variation of the vortex position with the flow parameters will be considered further in sections 2.6 and 2.7.

In section 2.4.5 a levelling out of the pressure distributions at the position of vortex $1'$, and a slight dip at the position of vortex 2 were described. No such effects can be seen in the pressure distributions of figure 2.5.1, but it is possible that they are obscured by the rather large errors indicated.

At the model leading edge ($\frac{x}{D} = -0.5$), C_p is below 1.0. It can be seen that as $\frac{UD}{\nu}$ and $\frac{D}{\delta^*}$ increase, C_p at $\frac{x}{D} = -0.5$ also increases. This can be explained in the following manner. As the flow variables change, the vertical dimensions of the vortex system do not change sig-

nificantly. (For example, for $\frac{D}{l} = 2.0$, the free stagnation point SP1 was found to have a value of $\frac{y}{D}$ of 0.072 ± 0.005 at all flow velocities, and one of the streamlines that approached it was found to have an upstream value of $\frac{y}{D}$ of 0.115 ± 0.005). Thus as $\frac{UD}{\nu}$ or $\frac{D}{\delta^*}$ increases and the boundary layer becomes thinner, then the fluid that passes close to the upstream edge of the cylinder will come from a region of higher non-dimensional velocity. Now C_p at $\frac{x}{D} = -0.5$ is given by

$$C_{P\left[\frac{x}{D} = -0.5\right]} = \frac{\left(P\left[\frac{x}{D} = -0.5\right] - P_0\right)}{\frac{1}{2} \cdot \rho \cdot U_o^2} \qquad (2.5.1)$$

where the subscript $_o$ refers to conditions at the model position without the model being in position. Now $P\left[\frac{x}{D} = -0.5\right]$ is approximately equal to the stagnation pressure on the streamline passing down the face of the cylinder:

$$P\left[\frac{x}{D} = -0.5\right] = P_\infty + \frac{1}{2}\rho u_\infty^2 \qquad (2.5.2)$$

where P_∞ is the pressure far upstream and u_∞ is the velocity on that particular streamline far upstream. If one assumes that $P_o \simeq P_\infty$ and $U_o \simeq U_\infty$ then we have

$$C_{P\left[\frac{x}{D} = -0.5\right]} \simeq \left(\frac{u_\infty}{U_\infty}\right)^2 \qquad (2.5.3)$$

So as the dimensionless velocity on the streamline passing down the face of the cylinder increases (i.e. as $\frac{UD}{\nu}$ and $\frac{D}{\delta^*}$ increase) then $C_{P\left[\frac{x}{D} = -0.5\right]}$ will also increase.

Also shown in figure 2.5.1 are the pressure distributions measured without the model in position. It can be seen that the models are in a region of slightly favourable pressure gradient.

Figure 2.5.2 shows pressure distributions ahead of the cylinder, obtained with the suction slot in positions 1, 2 and 3. These show the variation in the pressure distribution as $\frac{D}{\delta^*}$ varies. The distributions for an oscillatory type of flow show little variation, but where the

vortex position can be distinguished, it can be seen that the vortex moves away from the model as $\dfrac{D}{\delta^*}$ decreases.

Figure 2.5.3 compares the pressure distributions upstream of all the models used. There is little difference between the distributions for the cylinder and the cylinder with splitter plate. However, other things being equal, upstream of the vortex position the pressure coefficient at any point ahead of the streamline model is less than at the equivalent point ahead of the cylinder. This is due to the streamlined model, being shorter than the others, disturbing the flow to a lesser extent and thus any deviations in pressure from the upstream value occur closer to the model. Thus upstream of the vortex position ahead of the streamlined model at any value of $\dfrac{x}{D}$, one would expect C_p to be lower than at the same value of $\dfrac{x}{D}$ ahead of the other models.

2.6 Prediction of the separation position upstream of a cylinder on a plate

2.6.1 Introduction

In the previous section it was shown how the position of the horse-shoe vortex on the plane of symmetry upstream of a cylinder could be determined from pressure distributions. It seems possible that this vortex position might be fixed by the position of the separation line upstream of the cylinder. Therefore in this section two integral methods will be used to determine how this separation position varies with the flow parameters. These methods are:-

1) The method of Timman (1955) using the small crossflow assumption of Zaat (1956).

2) A modification to method (1) suggested by Cooke (1959) (as used by Peake and Galway (1965a) (1965b)).

2.6.2 Co-ordinate system and integral equations

It is assumed in what follows that the boundary layer upstream of the cylinder is laminar up to the separation line on the plane of symm-

etry. We will use an orthogonal coordinate system (ξ, η, ζ). In studies of three dimensional boundary layers it is usual to define a streamline coordinate system and we will do so here. We write ξ as the velocity potential, η as the stream function and ζ as the coordinate perpendicular to the wall on which the boundary layer is growing. We also write

$$ds = h_1 \, d\xi$$
$$dn = h_2 \, d\eta$$

where s and n are distances in the ξ and η directions and h_1 and h_2 are metric coefficients. The momentum integral equations may be written, in streamline coordinates,

$$\frac{1}{U^2 h_1}\frac{d}{d\xi}\left(\theta_{11} U^2\right) + \frac{1}{U^2 h_2}\frac{\partial}{\partial\eta}\left(\theta_{12} U^2\right) + \frac{\delta_1^*}{U h_1}\frac{\partial U}{\partial\xi} + \frac{\delta_2^*}{U h_2}\frac{\partial U}{\partial\eta}$$

$$+ \frac{1}{R_2}\left(\theta_{11} - \theta_{22}\right) + \frac{1}{R_1}\left(\theta_{12} + \theta_{21}\right) = \frac{\nu}{U^2}\left(\frac{\partial u}{\partial\zeta}\right)_{\zeta=0} \tag{2.6.1}$$

$$\frac{1}{U^2 h_1}\frac{\partial}{\partial\xi}\left(\theta_{21} U^2\right) + \frac{1}{U^2 h_2}\frac{\partial}{\partial\eta}\left(\theta_{22} U^2\right) + \frac{1}{R_1}\left(\theta_{22} - \theta_{11} - \delta_1^*\right)$$

$$+ \frac{1}{R_2}\left(\theta_{21} + \theta_{12} + \delta_2^*\right) = \frac{\nu}{U^2}\left(\frac{\partial v}{\partial\zeta}\right)_{\zeta=0} \tag{2.6.2}$$

where u, v are the velocities in the ξ, η directions; U is the velocity along a streamline outside the boundary layer; R_1, R_2 are the radii of curvature of the $\eta = $ constant and $\xi = $ constant lines respectively and

$$\delta_1^* = \int_0^\infty \left(1 - \frac{u}{U}\right) d\zeta \qquad\qquad \delta_2^* = -\int_0^\infty \left(\frac{v}{U}\right) d\zeta$$

$$\theta_{11} = \int_0^\infty \frac{u}{U}\left(1 - \frac{u}{U}\right) d\zeta \qquad \theta_{22} = -\int_0^\infty \left(\frac{v}{U}\right)^2 d\zeta$$

$$\theta_{21} = -\int_0^\infty \left(\frac{uv}{U^2}\right) d\zeta \qquad \theta_{12} = \int_0^\infty \frac{v}{U}\left(1 - \frac{u}{U}\right) d\zeta$$

Also if the flow external to the boundary layer can be assumed to be potential flow it can be shown that

$$h_1 = h_2 = \frac{1}{U} . \qquad\qquad (2.6.3)$$

2.6.3 Potential flow upstream of a circular cylinder

In the following sections it will be assumed that the pressure field upstream of the separation line can be approximated by the potential flow pressure distribution. Thus some results for the potential flow upstream of a cylinder are given here.

If U is the velocity a distance x upstream of a cylinder of radius R, on the plane of symmetry, then it is easily shown that

$$U = U_\infty \left(1 - \frac{R^2}{x^2}\right) \qquad\qquad (2.6.4)$$

$$\frac{dU}{dx} = 2 U_\infty \frac{R^2}{x^3} \qquad\qquad (2.6.5)$$

where U_∞ is the velocity far upstream. (See, for example, Duncan et al. (1970)).

2.6.4 Integral method based on the methods of Timman and Zaat

Timman (1955) formulated an integral method to solve equations (2.6.1) and (2.6.2) by assuming the following velocity profiles.

$$\frac{u}{U} = f_1(z') - T_1 f_2(z') - T_2 f_3(z') \tag{2.6.6}$$

$$\frac{v}{U} = -T_3^2 \cdot T_4 \cdot f_2\left(\frac{z'}{T_3}\right) \tag{2.6.7}$$

where $\quad 1 - f_1(z') = 2 f_2(z') + e^{-z'^2}$

$$= 2 f_3(z') + (1 + z'^2) e^{-z'^2}$$

$$= \frac{2}{3\sqrt{\pi}} z' e^{-z'^2} + \frac{2}{\sqrt{\pi}} \int_{z'}^{\infty} e^{-t^2} dt$$

$$T_1 = \sigma U\left(\frac{\partial u}{\partial \xi}\right)$$

$$T_2 = 0 \quad \text{if } T_1 > 0$$

$$T_2 = T_1 \quad \text{if } T_1 < 0$$

$$\zeta = (\sigma \nu)^{\frac{1}{2}} z'$$

As we are only concerned with flow on a plane of symmetry we will not consider further the crossflow velocity profiles (equation 2.6.7) or the definitions of T_3 and T_4.

At the point of separation on the plane of symmetry the shear stress in the streamwise direction must fall to zero:

$$\left(\frac{\partial u}{\partial \zeta}\right)_{\zeta=0} = \left(\frac{\partial u}{\partial z'}\right)_{z'=0} = 0$$

From equation (2.6.6)

$$\left[f_1'(z') - T_1 f_2'(z') - T_1 f_3'(z')\right]_{z'=0} = 0 \tag{2.6.8}$$

since in this case $T_2 = T_1$ as $T_1 < 0$ (adverse pressure gradient).

Also

$$\left[\frac{\partial f_1(z')}{\partial z'}\right]_{z'=0} = \frac{4}{3\sqrt{\pi}}$$

$$\left[\frac{\partial f_2(z')}{\partial z'}\right]_{z'=0.} = -\frac{2}{3\sqrt{\pi}}$$

$$\left[\frac{\partial f_3(z')}{\partial z'}\right]_{z'=0} = -\frac{2}{3\sqrt{\pi}}$$

So from equation (2.6.8), at the separation point

$$\frac{4}{3\sqrt{\pi}} + \frac{4}{3\sqrt{\pi}} T_1 = 0$$

$$T_1 = -1 \tag{2.6.9}$$

From the definition of T_1, and remembering that $dx = h_1 d\xi$ $(= \frac{d\xi}{u}$ from equation 2.6.3) it is easily shown that

$$T_1 = \frac{\sigma \partial u}{\partial x}$$

So if $\sigma = \sigma_s$ and $x = x_s$ at the separation point equation (2.6.9) gives

$$\sigma_s \left(\frac{\partial u}{\partial x}\right)_{x=x_s} = -1 \tag{2.6.10}$$

Now Zaat, making the assumption of small crossflow (i.e. that v is small, which it is close to the plane of symmetry) derives from equations (2.6.1) and (2.6.2) the equation

$$\frac{\partial}{\partial \xi}\left(\frac{u^4 \sigma}{\bar{\rho}}\right) = 5.08 \frac{u^2}{\bar{\rho}} \tag{2.6.11}$$

where $\bar{\rho}$ $\left[= \frac{1}{h_2^2 u^2}\right] = 1$, in this case. Now on the plane of symmetry $d\xi = u\,dx$ and this equation becomes

$$\frac{\partial}{\partial x}(u^4 \sigma) = 5.08 u^3 \tag{2.6.12}$$

From equations (2.6.4) and (2.6.12)

$$\frac{d}{dx} u_\infty^4 \left(1 - \frac{R^2}{x^2}\right)^4 \sigma = 5.08\left(1 - \frac{R^2}{x^2}\right)^3 \tag{2.6.13}$$

Now integrating between $x = x_o$ and $x = x_s$

$$U_\infty^4 \left(1 - \frac{R^2}{x_s^2}\right)^4 \sigma_s - U_\infty^4 \left(1 - \frac{R^2}{x_o^2}\right)^4 \sigma_o$$

$$= 5 \cdot 08 \,(x_s - x_o) + 15 \cdot 24 \left(\frac{1}{x_s} - \frac{1}{x_o}\right) R^2 - 5 \cdot 08 \left(\frac{1}{x_s^3} - \frac{1}{x_o^3}\right) R^4$$

$$+ 1 \cdot 02 \left(\frac{1}{x_s^5} - \frac{1}{x_o^5}\right) R^6 \tag{2.6.14}$$

From equations (2.6.5) and (2.6.10)

$$\sigma_s = - \frac{x_s^3}{2 U_\infty R^2} \tag{2.6.15}$$

Now if when $x = x_o$, $\sigma = \sigma_o$ it may be shown that (Peake and Galway (1965b))

$$\theta_o = 0 \cdot 293 \,(\sigma_o \nu)^{\frac{1}{2}}$$

where θ_o is the momentum thickness at $x = x_o$. Thus

$$\sigma_o = 11 \cdot 6 \, \frac{\theta_o^2}{\nu} \tag{2.6.16}$$

Finally let $X_s = \frac{x_s}{2R}$ and $X_o = \frac{x_o}{2R}$. From equations (2.6.14) to (2.6.16)

$$4 \left(1 - \frac{X_s^{-2}}{4}\right)^4 X_s^3 + 10 \cdot 16 \, X_s + 7 \cdot 12 \, X_s^{-1} - 0 \cdot 64 \, X_s^{-3} + 0 \cdot 03 \, X_s^{-5}$$

$$= 11 \cdot 6 \left(\frac{U_\infty \theta_o}{\nu}\right)\left(\frac{\theta_o}{R}\right)\left(1 - \frac{X_o^{-2}}{4}\right)^4 + 10 \cdot 16 \, X_o + 7 \cdot 12 X_o^{-1} - 0 \cdot 64 \, X_o^{-3}$$

$$+ 0 \cdot 03 \, X_o^{-5}.$$

Now assume that at $x = x_o$, $\theta = \theta_o = 0$; i.e. assume boundary layer growth from the leading edge of a flat plate. The last equation becomes

$$4 \left(1 - \frac{X_s^{-2}}{4}\right)^4 X_s^3 + 10 \cdot 16 \, X_s + 7 \cdot 12 \, X_s^{-1} - 0 \cdot 64 \, X_s^{-3} + 0 \cdot 03 \, X_s^{-5}$$

$$= 10 \cdot 16 \, X_o + 7 \cdot 12 \, X_o^{-1} - 0 \cdot 64 \, X_o^{-3} + 0 \cdot 03 \, X_o^{-5} \tag{2.6.17}$$

2.6.5 <u>Integral method based on the methods of Timman, Cooke and Zaat</u>

Cooke (1959) wrote the velocity profile given by Timman (equation 2.6.6) as

$$\frac{u}{U} = f_1(z') - T_1 f_2(z')$$

(2.6.18)

to obtain better agreement with a known exact solution. Now using this equation, an equation similar to equation (2.6.8) can be derived

$$\left[f_1'(z') - T_1 f_2(z') \right]_{z'=0} = 0$$

(2.6.19)

Using equation (2.6.19) an equation similar to equation 2.6.10 can be derived

$$\sigma_s \left[\frac{\partial u}{\partial x} \right]_{x=x_6} = -2$$

Thus the $X_o - X_s$ relation becomes (if $\theta = 0$ at $x = x_o$)

$$8 \cdot \left(1 - \frac{X_s^{-2}}{4} \right)^4 X_s^3 + 10 \cdot 16 \, X_s + 7 \cdot 12 \, X_s^{-1} - 0 \cdot 64 \, X_s^{-3} + 0 \cdot 03 \, X_s^{-5}$$

$$= 10 \cdot 16 \, X_o + 7 \cdot 12 \, X_o^{-1} - 0 \cdot 64 \, X_o^{-3} + 0 \cdot 03 \, X_o^{-5}$$

(2.6.20)

2.6.6 <u>Experimental results and discussion</u>

The solutions of equations (2.6.17) and (2.6.20) are plotted in figure 2.6.1. It can be seen that they both have the same form although equation (2.6.20) predicts rather smaller values of X_s than equation (2.6.17), at the same value of X_o. However for both curves X_s increases as X_o increases. Also it appears that X_s depends upon X_o and not upon any other flow parameters such as $\frac{UD}{\nu}$ and $\frac{D}{\delta^*}$ (It is of course possible to express $X_o \left[= \frac{x_o}{D} \right]$ in terms of the other flow parameters since for a laminar boundary layer on a flat plate in zero pressure gradient

$$\frac{\delta^*}{|x_o|} = 1 \cdot 73 \left(\frac{U|x_o|}{\nu} \right)^{-\frac{1}{2}}$$

which gives

$$\frac{|x_o|}{D} \simeq 0.33 \left(\frac{UD}{\nu}\right)\left(\frac{\delta^*}{D}\right)^2 \qquad (2.6.21)$$

Experiments were carried out to determine whether or not the flow studied in this investigation (the flow around a cylinder mounted on a wind tunnel wall downstream of a suction slot) could be considered equivalent to a cylinder mounted on a flat plate. With the suction slot in position 1, the position of the separation point on the plane of symmetry upstream of the cylinder model was measured. This position was made visible by letting smoke into the flow from a small hole at the base of the cylinder, and measuring how far upstream the smoke was carried. These results are shown in figure 2.6.1 (x_o is in this case defined as the distance from the leading edge of the suction slot to the cylinder centre). It can be seen that there is little variation of the separation position with Reynolds number, which is what the analysis of the previous sections shows to be the case for a cylinder on a flat plate. Thus it would seem that the flow studied here can be taken to be equivalent to the flow upstream of a cylinder on a flat plate, in this respect at least.

It can also be seen from figure 2.6.1 that the analysis predicts a separation position upstream of the measured position. This is because the potential flow velocity distribution upstream of the cylinder can only be regarded as an approximation. The potential flow pressure distribution on the plane of symmetry upstream of an infinite two dimensional cylinder (which is clearly closely related to the potential flow velocity distribution) is given by (Belik (1973))

$$C_p = \frac{1}{2X^2} - \frac{1}{16\,X^4} \qquad (2.6.22)$$

Equation (2.6.22) is plotted in figure 2.6.2 together with some measured pressure distributions. It can be seen that at a given point

upstream of the vortex system the potential flow pressure gradient is steeper than the measured pressure gradient. Thus one would expect the analysis to predict a separation position upstream of the measured position.

2.7 Variation of the horseshoe vortex position

Figures 2.7.1, 2.7.2 and 2.7.3 show how $\frac{x_v}{D}$, the dimensionless vortex position, varies for the cylinder, cylinder with splitter plate, and streamlined models respectively. Contours of $\frac{x_v}{D}$ are plotted in the $\frac{UD}{\nu}$ - $\frac{D}{\delta^*}$ plane as suggested by the dimensional analysis of section 2.2. The values of x_v were obtained from pressure distributions with the suction slot in all four positions. The dotted lines in the figures join experimental points corresponding to one suction slot posit-ion. The positions of the experimental points in figures 2.7.1 to 2.7.3 are at the position of the "decimal points" of the values of $\left|\frac{x_v}{D}\right|$. The possible error in $\left|\frac{x_v}{D}\right|$ indicated on figures 2.7.1 to 2.7.3 is con-siderable since it was not possible to determine accurately the position of the minima in the pressure distributions. Bearing this in mind there can be seen to be little difference between figures 2.7.1, 2.7.2 and 2.7.3. This fact is also apparent from figure 2.7.4 which is a plot of the variation of $\frac{x_v}{D}$ for the three models as $\frac{D}{\delta^*}$ varies, for $\frac{UD}{\nu}$ = 3000. For all models as $\frac{UD}{\nu}$ increases, $\left|\frac{x_v}{D}\right|$ increases, and as $\frac{D}{\delta^*}$ increases, $\left|\frac{x_v}{D}\right|$ decreases. No pressure minima were observed for values of $\frac{UD}{\nu}$ above approximately 5,000, and the flow visualizat-ion (section 2.4) suggests that when $\frac{UD}{\nu}$ is above this value oscillat-ing vortex systems exist.

It was shown in section 2.6 that the position of the separation line ahead of a cylinder on a plate depends upon $\frac{x_c}{D}$ where x_c is the distance from the cylinder centre to the leading edge of the plate. If the separation position fixes the vortex position then the analysis and

experimental results of the previous section lead one to expect that the vortex position would remain constant for each suction slot position i.e. along the dotted lines in figure 2.7.1 to 2.7.3. This can be seen not to be the case. Thus one must conclude that the vortex position is not solely determined by the separation position, but some other effect plays a part. What this effect may be has not been determined.

Finally it can be seen from figures 2.7.1 to 2.7.4 that as $\frac{D}{\delta^*}$ increases, at fixed $\frac{UD}{\nu}$, $\left|\frac{x_v}{D}\right|$ decreases. Equation (2.6.21) for the case of a cylinder on a flat plate is

$$\left|\frac{x_o}{D}\right| = 0.33 \left(\frac{UD}{\nu}\right)\left(\frac{\delta^*}{D}\right)^2$$

So at constant $\frac{UD}{\nu}$ a reduction in $\frac{D}{\delta^*}$ is equivalent to an increase in $\left|\frac{x_o}{D}\right|$, and, from figure 2.6.1, an increase in $\left|\frac{x_o}{D}\right|$ leads to an increase in $\left|\frac{x_s}{D}\right|$. Thus as $\frac{D}{\delta^*}$ decreases, $\left|\frac{x_s}{D}\right|$ will increase. If one assumes that the horseshoe vortex position is largely determined by the separation position, then it is to be expected that $\left|\frac{x_v}{D}\right|$ will also increase, as is seen to be the case.

2.8 The oscillatory behaviour of horseshoe vortex systems

To study the oscillatory behaviour of horseshoe vortex systems, a hot wire probe was placed in the flow so that its wire was 1 mm from the wind tunnel wall, with the suction slot in position 1. Flow visualization suggests that with the probe in this position the flow was not affected (section 2.4.6). The hot wire output was recorded at several velocities and spectral analyses were carried out. The spectra obtained were not repeatable, the number and magnitude of peaks in the spectra at any one velocity varying from run to run. The hot wire output was then displayed on a storage oscilloscope and the situation was clarified. At any one speed four different waveforms could be seen at different times:-

(a) a steady trace with no oscillations,

(b) a low frequency oscillation, ($St = \dfrac{fD}{U} \simeq 0.26$)

(c) a high frequency oscillation, ($St \simeq 0.40$, increasing to

about 0.60 at higher $\dfrac{UD}{\nu}$)

(d) an irregular turbulent trace.

Photographs of waveforms (b), (c) and (d) are shown in figure 2.8.1. Each of the above four states might exist for any length of time between 1 second and 5 minutes and the flow switched from one state to another in a completely random manner. At the lowest speeds used, state (a) was observed more often than the other states, but as the velocity increased state (b) became the most often observed state. As the velocity was increased further state (c) was observed more often and at the highest speeds only a turbulent trace (state (d)) could be seen.

After many attempts tape recordings were made of signals of just one of the above states, of sufficient length to enable a spectral analysis to be carried out. The spectra obtained are shown in figures 2.8.2a and 2.8.2b. Note that the flow parameters are almost identical in both cases, but the peaks occur at completely different frequencies. In figure 2.8.2a, for the dominant peak, $St = 0.26$, and in figure 2.8.2b, for the dominant peak, $St = 0.36$. The smaller peaks in both spectra are harmonics of the main peaks. They appear simply because of the shape of the waveform of the hot wire output, which is in turn dependent upon the exact position of the hot wire probe in the flow. A spectral analysis carried out when both frequencies were present in the signal is shown in figure 2.8.3. Two peaks and their harmonics can be seen.

The spectrum of turbulence obtained at the highest speeds used is shown in figure 2.8.4. It can be seen that there is no dominant peak in the spectrum.

Further tests were carried out with the suction slot at positions 2, 3 and 4. With the suction slot at position 2, the unsteady behaviour was similar to that described above, but with the suction slot at position 3

the lower frequency oscillations were seen only very occasionally. With the suction slot at position 4 no regular oscillatory motion was observed. With the slot at this position the periods of steady flow were observed at much higher velocities than for suction slot positions 1 to 3. These periods of steady flow were interrupted by bursts of irregular turbulent flow. These bursts of turbulent flow were probably caused by bursts of turbulence in the upstream boundary layer passing into the vortex system.

The variation of Strouhal number with the flow parameters for both types of oscillation is shown in figure 2.8.5. The frequencies were measured by displaying the hot wire output on a storage oscilloscope and measuring the distance between adjacent peaks in the waveform, from many different output traces, and taking the average distance between peaks to be a measure of the oscillation period. It can be seen from figure 2.8.5 that for the high frequency oscillation (the 'primary' oscillation) St increases as $\frac{UD}{\nu}$ increases, while for the low frequency oscillation (the 'secondary' oscillation) St remains fairly constant. (There was a considerable variation in the oscillation frequency at any one set of flow conditions as can be judged from the width of the dominant peaks in the spectra of figure 2.8.2.).

Schwind (1962), as stated in section 2.1.1, observed two types of oscillation (figure 2.1.1). At a speed of 0.45 ms^{-1} he measured a frequency of oscillation of 0.8 Hz for flows of the regime 4 type and a frequency of 1.4 Hz for flows of the regime 5 type. Thus it would seem likely that the high frequency or primary oscillation noted here can be identified with Schwind's regime 5 and the low frequency or secondary oscillation with Schwind's regime 4. Schwind observed that in general regime 5 oscillations occur at higher speeds than regime 4 oscillations (although they could both occur at the same speed). This agrees well with the results presented here where the primary oscillations persist to much higher values of $\frac{UD}{\nu}$ than do the secondary oscillations.

The above describes the oscillatory behaviour of the horseshoe vortex systems. However it does not explain what causes these oscillations. One can however eliminate some possible causes. To test whether the wake vortex shedding of the cylinder had any effect on the oscillations, tests were carried out with a cylinder with splitter plate and with a streamlined model, for both of which the wake spectrum was found to be significantly different from that of the cylinder (see figure 2.8.6). Results almost identical to those described above were obtained. Also it can be seen from figure 2.8.7 that the Strouhal number for the wake vortex shedding of the cylinder is approximately 0.16 at all tunnel speeds, which bears no relationship to the observed frequencies of oscillation of the horseshoe vortex system. Thus it appears that one can eliminate wake vortex shedding as a possible cause of the oscillations.

Figure 2.8.8 shows the speed of rotation of the wind tunnel fan non-dimensionalized using the cylinder diameter and the wind tunnel free stream velocity, plotted against a Reynolds number based on cylinder diameter. Again the Strouhal number bears no relationship to the Strouhal number of the vortex oscillations. In fact this Strouhal number decreases with Reynolds number while the Strouhal number of the vortex oscillations increases with Reynolds number. So it would appear that these oscillations are not affected by any disturbances caused by the fan.

Now consider the spectrum shown in figure 2.8.9. This shows the spectrum recorded in the boundary layer on the wind tunnel wall downstream of the suction slot, at the same flow conditions as for figure 2.8.2, but with the cylinder not in position. The spectrum shows a large D.C. peak together with several other peaks. However these peaks do not correspond to either of the horseshoe vortex oscillation frequencies at this speed. In fact two of the dominant peaks on this spectrum, the ones at 9.4 Hz and 18.8 Hz do not change their position as the tunnel speed varies. This would suggest that they are related to an oscillation fre-

quency of the wind tunnel structure. So it would appear that any disturbances present in the boundary layer upstream of the model do not affect the horseshoe vortex oscillations.

Thus having eliminated all the above possibilities for the cause of vortex oscillations the author can see only one explanation for these oscillations; that is, at certain values of $\frac{UD}{\nu}$ and $\frac{D}{\delta^*}$ the horseshoe vortex itself becomes unstable for some reason, and begins to oscillate in one of two "natural" modes, the higher frequency mode becoming more dominant as the Reynolds number increases.

Thus one question remains to be answered. That is what is the mechanism that initiates this instability? It seems possible that the oscillations are initiated by bursts of turbulence passing into the vortex systems from the upstream boundary layer. To test this hypothesis two hot wire signals were recorded simultaneously, one hot wire being in the boundary layer upstream of the horseshoe vortex ($\frac{x}{D} = -2.08$), and one being beneath the vortex system as usual ($\frac{x}{D} = -0.81$). A photograph of the oscilloscope output is shown in figure 2.8.10, over a period of time during which the vortex oscillations began. The upper trace in the photograph shows the output from the hot wire probe in the upstream boundary layer and the lower trace shows the output from the hot wire probe beneath the vortex. The period of time covered by this photograph is sufficiently large to record any bursts of turbulence detected by the upstream probe that might be convected into the vortex system at the time when oscillations begin. It can be seen that there are no such bursts of turbulence shown on the photograph, so it would seem the vortex oscillations are not initiated by bursts of turbulence. (It should be noted that the slight high frequency "ripple" on the oscilloscope trace is at the mains frequency of 50 Hz and originates within the electronic system and not within the flow).

So if the disturbances that initiate the oscillations do not come

quency of the wind tunnel structure. So it would appear that any disturbances present in the boundary layer upstream of the model do not affect the horseshoe vortex oscillations.

Thus having eliminated all the above possibilities for the cause of vortex oscillations the author can see only one explanation for these oscillations; that is, at certain values of $\frac{UD}{\nu}$ and $\frac{D}{\delta^*}$ the horseshoe vortex itself becomes unstable for some reason, and begins to oscillate in one of two "natural" modes, the higher frequency mode becoming more dominant as the Reynolds number increases.

Thus one question remains to be answered. That is what is the mechanism that initiates this instability? It seems possible that the oscillations are initiated by bursts of turbulence passing into the vortex systems from the upstream boundary layer. To test this hypothesis two hot wire signals were recorded simultaneously, one hot wire being in the boundary layer upstream of the horseshoe vortex ($\frac{x}{D} = -2.08$), and one being beneath the vortex system as usual ($\frac{x}{D} = -0.81$). A photograph of the oscilloscope output is shown in figure 2.8.10, over a period of time during which the vortex oscillations began. The upper trace in the photograph shows the output from the hot wire probe in the upstream boundary layer and the lower trace shows the output from the hot wire probe beneath the vortex. The period of time covered by this photograph is sufficiently large to record any bursts of turbulence detected by the upstream probe that might be convected into the vortex system at the time when oscillations begin. It can be seen that there are no such bursts of turbulence shown on the photograph, so it would seem the vortex oscillations are not initiated by bursts of turbulence. (It should be noted that the slight high frequency "ripple" on the oscilloscope trace is at the mains frequency of 50 Hz and originates within the electronic system and not within the flow).

So if the disturbances that initiate the oscillations do not come

from upstream of the models, then it seems likely that they originate downstream of the models. Evidence for this comes from the film made by the Weapons Research Establishment (1967), described in section 2.1.1. This shows that vortex oscillations appear to be initiated by disturbances caused by "bursting" of the horseshoe vortices trailing downstream of the model. The film showed that as the flow velocity increased these vortex bursts moved upstream of the cylinder until the horseshoe vortex system becomes entirely turbulent, and the same sort of behaviour was observed in this investigation, with the vortices upstream of the models becoming turbulent as the velocity increased.

Thus in conclusion it would seem that horseshoe vortex oscillations are initiated by disturbances in the vortex system downstream of the model, but the frequency of oscillation is determined solely by the values of $\dfrac{UD}{\nu}$ and $\dfrac{D}{\delta^*}$, and not by the frequency of wake vortex shedding, or of any other small disturbances in the flow in the wind tunnel.

2.9 Solution of the Navier-Stokes equations for a laminar horseshoe vortex

2.9.1 Introduction

In this section the application of the equations of fluid motion to a horseshoe vortex system is considered. It is assumed in what follows that the horseshoe vortex system being considered has been formed by the separation of a laminar boundary layer upstream of a cylindrical obstacle, although this analysis could equally well apply to separation upstream of a non-cylindrical obstacle.

A cylindrical polar system of co-ordinates will be used, as shown in figure 2.9.1; r is the radial co-ordinate, z is the axial co-ordinate along the vortex axis and ϕ is the angular co-ordinate. The velocities in the r, z, ϕ directions are u, w, v respectively. Clearly, since the horseshoe vortex system is curved, for this system of co-ordinates to be unambiguous the radius of curvature of the centre line of the vortex

must be large compared to the vortex radius. This is assumed to be the case in the region of the horseshoe vortex system on and close to the plane of symmetry. In this "plane of symmetry" region a simple analytical solution to the equations of motion can be derived.

2.9.2 Equations of motion

In this section the equations of motion that can be expected to apply for the core region of a laminar horseshoe vortex are presented in a dimensionless form. Hall (1966) shows that many vortex systems can be regarded as being quasi-cylindrical, i.e. using the co-ordinate system of figure 2.9.1.

$$\frac{\partial}{\partial z} \ll \frac{\partial}{\partial r} \qquad (2.9.1)$$

which implies that the vortex core radius is much less than the length of the vortex core. This is the case in horseshoe vortex systems. Hall makes the further assumption that the flow in such systems is axially symmetric, i.e.

$$\frac{\partial}{\partial \phi} = 0 \qquad (2.9.2)$$

This assumption can be expected to be valid in the central region of the horseshoe vortex where the streamlines can be expected to possess such axial symmetry. Having made these assumptions Hall derives, for a laminar quasi-cylindrical vortex

(a) the continuity equation

$$\frac{\partial \rho}{\partial t} + \frac{1}{r} \frac{\partial}{\partial r} (\rho u r) + \frac{\partial}{\partial z} (\rho \omega) = 0 \qquad (2.9.3)$$

(b) the momentum equations

$$\frac{\rho v^2}{r} = \frac{\partial p}{\partial r} \qquad (2.9.4)$$

$$\rho \left(\frac{\partial v}{\partial t} + u \frac{\partial v}{\partial r} + \omega \frac{\partial v}{\partial z} + \frac{u v}{r} \right) = \frac{1}{r^2} \frac{\partial}{\partial r} \left[\mu r^2 \left(\frac{\partial v}{\partial r} - \frac{v}{r} \right) \right] \qquad (2.9.5)$$

$$\rho\left(\frac{\partial \omega}{\partial t} + u\frac{\partial \omega}{\partial r} + \omega\frac{\partial \omega}{\partial z}\right) = -\frac{\partial p}{\partial z} + \frac{1}{r}\frac{\partial}{\partial r}\left(\mu r\frac{\partial \omega}{\partial r}\right) \qquad (2.9.6)$$

From here we make the further assumptions that

(a) the motion is steady so $\dfrac{\partial}{\partial t} = 0$

(b) ρ and μ are constants.

At this point we introduce the dimensionless variables $\bar{r}, \bar{z}, \bar{u}, \bar{v}, \bar{\omega}, \bar{p}$,

where

$$\bar{r} = \frac{r}{r_r} \qquad\qquad \bar{z} = \frac{z}{z_r}$$

$$\bar{u} = \frac{u}{v_r} \qquad\qquad \bar{\omega} = \frac{\omega}{v_r} \qquad\qquad (2.9.7)$$

$$\bar{v} = \frac{v}{v_r} \qquad\qquad \bar{p} = \frac{p}{\rho v_r^2}$$

In general z_r, r_r and v_r can be any reference length in the axial direction, any reference length in the radial direction, and any reference velocity respectively. For our purposes however z_r can be taken simply as being the diameter of the cylinder, r_r as an arbitary core radius on the plane of symmetry, and v_r as the value of v at $r = r_r$ on the plane of symmetry.

Now substituting (2.9.7) in equations (2.9.3) to (2.9.6)

$$\frac{1}{\bar{r}}\frac{\partial}{\partial \bar{r}}\left(\bar{r}\,\bar{u}\right) + \alpha \frac{\partial \bar{\omega}}{\partial \bar{z}} = 0 \qquad (2.9.8)$$

$$\frac{\bar{v}^2}{\bar{r}} = \frac{\partial \bar{p}}{\partial \bar{r}} \qquad (2.9.9)$$

$$\bar{u}\frac{\partial \bar{v}}{\partial \bar{r}} + \alpha\,\bar{\omega}\frac{\partial \bar{v}}{\partial \bar{z}} + \frac{\bar{u}\bar{v}}{\bar{r}} = \frac{1}{R_e}\frac{1}{\bar{r}^2}\frac{\partial}{\partial \bar{r}}\left[\bar{r}^2\left(\frac{\partial \bar{v}}{\partial \bar{r}} - \frac{\bar{v}}{\bar{r}}\right)\right] \qquad (2.9.10)$$

$$\bar{u}\frac{\partial \bar{\omega}}{\partial \bar{r}} + \alpha\,\bar{\omega}\frac{\partial \bar{\omega}}{\partial \bar{z}} = -\alpha\frac{\partial \bar{p}}{\partial \bar{z}} + \frac{1}{R_e}\left[\frac{1}{\bar{r}}\frac{\partial}{\partial \bar{r}}\left(\bar{r}\frac{\partial \bar{\omega}}{\partial \bar{r}}\right)\right] \qquad (2.9.11)$$

So we can see that the flow is determined by two dimensionless groups

(1) $\alpha = \dfrac{r_r}{z_r}$; a ratio of the vortex core radius on the plane of symmetry to a reference length in the axial direction.

(2) $R_e = \dfrac{v_r r_r}{\nu}$; a Reynolds number based on the velocity at the edge of the vortex core on the plane of symmetry, and the radius of the vortex core on the plane of symmetry.

2.9.3 The plane of symmetry region

Now we make the assumption that on, and close to, the plane of symmetry of a horseshoe vortex system

$$\bar{u} = -c\bar{r} \qquad (2.9.12)$$

(This assumption was also made by Rott (1958) and the first part of what follows is similar, in outline, to the analysis presented in that paper. However Rott did not present the analysis in a dimensionless form, and he did not use it to describe the flow on a plane of symmetry of a horseshoe vortex system, but applied the analysis to "bath tub" vortices). With this assumption equation (2.9.8) gives

$$\frac{\partial \bar{\omega}}{\partial \bar{z}} = \frac{2c}{\alpha}$$

i.e. $$\bar{\omega} = \frac{2c}{\alpha} \bar{z} \qquad (2.9.13)$$

since $\bar{\omega} = 0$ on $\bar{z} = 0$ (i.e. on the plane of symmetry itself).

Equation (2.9.13) suggests that $\bar{\omega}$ is not a function of $\bar{z}$ on and close to the plane of symmetry, if equation 2.9.12 is valid.

The second momentum equation (2.9.10) becomes

$$-c\bar{r}\frac{\partial \bar{v}}{\partial \bar{r}} + 2c\bar{z}\frac{\partial \bar{v}}{\partial \bar{z}} - c\bar{v} = \frac{1}{R_e}\frac{1}{\bar{r}^2}\left[\bar{r}^2\frac{\partial^2 \bar{v}}{\partial \bar{r}^2} + \bar{r}\frac{\partial \bar{v}}{\partial \bar{r}} - \bar{v}\right] \qquad (2.9.14)$$

If we let

$$E = c R_e = \frac{u_r r_r}{\nu} \qquad (2.9.15)$$

(since from equation (2.9.12) $c = \dfrac{u_r}{v_r}$ where $u = -u_r$ at $r = r_r$)

we obtain

$$\bar{r}^2 \frac{d^2\bar{v}}{d\bar{r}^2} + \left(\bar{r} + E\bar{r}^3\right)\frac{d\bar{v}}{d\bar{r}} - \left(1 - E\bar{r}^2\right)\bar{v} = 2E\bar{z}\frac{d\bar{v}}{d\bar{z}}\bar{r}^2 \qquad (2.9.16)$$

To solve equation (2.9.16) we use the method of separating the variables

$$\bar{v} = f(\bar{r})\, g(\bar{z}) \qquad (2.9.17)$$

where $f(\bar{r})$ is a function of $\bar{r}$ only and $g(\bar{z})$ is a function of $\bar{z}$ only. Equation (2.9.16) becomes

$$\frac{\left[\bar{r}^2 \frac{d^2 f}{d\bar{r}^2} + \left(\bar{r} + E\bar{r}^3\right)\frac{df}{d\bar{r}} - \left(1 - E\bar{r}^2\right)f\right]}{f\bar{r}^2} = \frac{\left[2E\bar{z}\frac{dg}{d\bar{z}}\right]}{g} = A,$$

where a is a constant.

So we have

$$\frac{2E\bar{z}}{g}\frac{dg}{d\bar{z}} = A$$

This integrates to give

$$\frac{g(\bar{z})}{g_1(\bar{z})} = (\bar{z})^{\frac{A}{2E}} \qquad (2.9.18)$$

where $g_1(\bar{z}) = g(\bar{z})$ at $\bar{z} = 1$. This equation suggests that if $a \neq 0$, $g(\bar{z}) = 0$ when $\bar{z} = 0$. So if $a \neq 0$, $\bar{v} = 0$ on the plane of symmetry (from equation (2.9.17)); i.e. there is no circumferential velocity component on the plane of symmetry. This is obviously untrue, so a must be equal to zero and

$$g(\bar{z}) = g_1(\bar{z}). \qquad (2.9.19)$$

So the circumferential velocity is obtained from

$$\bar{r}^2 \frac{d^2 f}{d\bar{r}^2} + \left(\bar{r} + E\bar{r}^3\right)\frac{df}{d\bar{r}} - \left(1 - E\bar{r}^2\right)f = 0 \qquad (2.9.20)$$

Since $\bar{v} = g_1(\bar{z})f(\bar{r})$ this becomes

$$\bar{r}^2 \frac{d^2\bar{v}}{d\bar{r}^2} + \left(\bar{r} + E\bar{r}^3\right)\frac{d\bar{v}}{d\bar{r}} - \left(1 - E\bar{r}^2\right)\bar{v} = 0 \qquad (2.9.21)$$

Equation (2.9.21) can be directly integrated twice by making the substitution $\bar{\Gamma} = 2\pi\bar{r}\bar{v}$ where $\bar{\Gamma}$ is a dimensionless circulation. The equation reduces to

$$\bar{r}\,\frac{d^2\bar{\Gamma}}{d\bar{r}^2} + (E\bar{r}^2 - 1)\frac{d\bar{\Gamma}}{d\bar{r}} = 0 \tag{2.9.22}$$

which has the solution

$$\bar{\Gamma} = 2\pi\bar{r}\bar{v} = A_2 + A_1\,e^{-E\bar{r}^2/2}$$

Let us consider the boundary conditions. At the vortex centre the circumferential velocity must fall to zero; i.e. $\bar{v} = 0$ at $\bar{r} = 0$. Thus

$$A_1 = -A_2$$

Also at the edge of the vortex core $\bar{v} = 1$ at $\bar{r} = 1$. Thus

$$A_1 = 2\pi\left(1 - e^{-E/2}\right)^{-1} \tag{2.9.23}$$

So the solution for $\bar{v}$ is

$$\bar{v} = \frac{1}{\bar{r}}\left(\frac{1 - e^{-E\bar{r}^2/2}}{1 - e^{-E/2}}\right) \tag{2.9.24}$$

The form of equation (2.9.24) is shown in figure 2.9.2 where $\bar{v}$ is plotted against $\bar{r}$ for various values of E (The curve for $E = 1.8$ will be referred to in section 2.10). These curves all show a maximum value of $\bar{v}$ at some value of $\bar{r}$ ($= \bar{r}_m$) (except for the $E = 0$ curve). The position of this maximum can readily be located by letting $\frac{d\bar{v}}{d\bar{r}} = 0$ This gives

$$\bar{r}_m = \left(\frac{2.51}{E}\right)^{\frac{1}{2}} \tag{2.9.25}$$

The radial position at which the circumferential velocity is maximum is given by equation (2.9.25). The velocity $\bar{v}$ at this radius is given by

$$\bar{v}_m = \left(\frac{E}{2.51}\right)^{\frac{1}{2}}\left(\frac{1 - e^{-1.25}}{1 - e^{-E/2}}\right) \tag{2.9.26}$$

Equation (2.9.21) can be directly integrated twice by making the substitution $\overline{\Gamma} = 2\pi \overline{r}\,\overline{v}$ where $\overline{\Gamma}$ is a dimensionless circulation. The equation reduces to

$$\overline{r}\,\frac{d^2\overline{\Gamma}}{d\overline{r}^2} + \left(E\overline{r}^2 - 1\right)\frac{d\overline{\Gamma}}{d\overline{r}} = 0 \tag{2.9.22}$$

which has the solution

$$\overline{\Gamma} = 2\pi\overline{r}\,\overline{v} = A_2 + A_1\,e^{-\frac{E\overline{r}^2}{2}}$$

Let us consider the boundary conditions. At the vortex centre the circumferential velocity must fall to zero; i.e. $\overline{v} = 0$ at $\overline{r} = 0$. Thus

$$A_1 = -A_2$$

Also at the edge of the vortex core $\overline{v} = 1$ at $\overline{r} = 1$. Thus

$$A_1 = 2\pi\left(1 - e^{-E/2}\right)^{-1} \tag{2.9.23}$$

So the solution for $\overline{v}$ is

$$\overline{v} = \frac{1}{\overline{r}}\left(\frac{1 - e^{-\frac{E\overline{r}^2}{2}}}{1 - e^{-E/2}}\right) \tag{2.9.24}$$

The form of equation (2.9.24) is shown in figure 2.9.2 where $\overline{v}$ is plotted against $\overline{r}$ for various values of E (The curve for $E = 1.8$ will be referred to in section 2.10). These curves all show a maximum value of $\overline{v}$ at some value of $\overline{r}$ $(= \overline{r}_m)$ (except for the $E = 0$ curve). The position of this maximum can readily be located by letting $\frac{d\overline{v}}{d\overline{r}} = 0$ This gives

$$\overline{r}_m = \left(\frac{2.51}{E}\right)^{\frac{1}{2}} \tag{2.9.25}$$

The radial position at which the circumferential velocity is maximum is given by equation (2.9.25). The velocity $\overline{v}$ at this radius is given by

$$\overline{v}_m = \left(\frac{E}{2.51}\right)^{\frac{1}{2}}\left(\frac{1 - e^{-1.25}}{1 - e^{-E/2}}\right) \tag{2.9.26}$$

Equations (2.9.25) and (2.9.26) are shown in graphical form in figures 2.9.3a and b.

Let us consider the pressure within the core of the horseshoe vortex system in the plane of symmetry region. From equations (2.9.11) and (2.9.13)

$$4c^2 \frac{\bar{z}}{\alpha} = -\alpha \frac{d\bar{p}}{d\bar{z}}$$

(2.9.27)

since from equation (2.9.13) $\quad \dfrac{\partial \bar{\omega}}{\partial \bar{r}} = 0$

Equations (2.9.27) and (2.9.9) suggest that

$$\bar{P} - \bar{P}_{o,o} = p_{\scriptscriptstyle 1}(\bar{z}) + p_{\scriptscriptstyle 2}(\bar{r})$$

(2.9.28)

where $\bar{P}_{o,o}$ is the value of $\bar{p}$ at $\bar{r} = 0$ and $\bar{z} = 0$, $p_{\scriptscriptstyle 1}$ is a function of $\bar{z}$ only, and is given by equation (2.9.27), and $p_{\scriptscriptstyle 2}$ is a function of $\bar{r}$ only and is obtained from equation (2.9.9).

From equation (2.9.27)

$$p_{\scriptscriptstyle 1}(\bar{z}) = -2\left(\frac{c}{\alpha}\right)^2 \bar{z}^2$$

(2.9.29)

and from equations (2.9.9) and (2.9.24)

$$p_{\scriptscriptstyle 2}(\bar{r}) = \int_0^{\bar{r}} \frac{1}{\bar{r}^3} \left(\frac{1 - e^{-E\bar{r}^2/2}}{1 - e^{-E/2}}\right)^2 \cdot d\bar{r}$$

(2.9.30)

Equation (2.9.30) leads to exponential integrals that have to be evaluated numerically. $p_{\scriptscriptstyle 2}(\bar{r})$ and $p_{\scriptscriptstyle 1}(\bar{z})$ are plotted in figures 2.9.4a and b for various values of E and $\frac{c}{\alpha}$.

From equation (2.9.27) it can be seen that at $\bar{z} = 0$

$$\frac{d\bar{p}}{d\bar{z}} = 0 \quad , \quad \frac{d^2\bar{p}}{d\bar{z}^2} < 0$$

So at $\bar{z} = 0$ the variation of $\bar{p}$ with respect to $\bar{z}$ shows a maximum. This agrees with the experimental results of Vasanta Ram (1963), shown in figure 2.9.5. Although the results of Vasanta Ram were for a horseshoe vortex system caused by a turbulent boundary layer separation, it

can be seen that the variation of $\bar{p}$ with respect to $\bar{z}$ does show a maximum value on the plane of symmetry.

As previously noted equations (2.9.8) to (2.9.11) suggest that the flow is controlled by two dimensionless groups R_e and α. However for the plane of symmetry region an inspection of the final results (equations (2.9.24) to (2.9.26), (2.9.28) to (2.9.30) shows that the relevant groups are:-

1) $E = c R_e = \dfrac{u_r r_r}{\nu}$ — a Reynolds number based on the radial velocity at the edge of the vortex core.

2) $\dfrac{c}{\alpha} = u_r z_r / v_r r_r$

Now if we define Q as a volume flow rate into the vortex core

$$Q = (2\pi r_r u_r) z_r \tag{2.9.31}$$

then

$$\frac{c}{\alpha} = \frac{Q}{(2\pi r_r v_r) r_r} = \frac{Q}{\Gamma_r r_r} \tag{2.9.32}$$

where $\Gamma_r = 2\pi r_r v_r$. This is a Rossby number based on a volume flow rate, a circulation at the edge of the vortex core, and the vortex core radius on the plane of symmetry.

In the preceding analysis r_r, the reference radius, has been defined somewhat arbitrarily. If we now identify r_r with r_m, the radius at which the velocity $\bar{v}$ on the plane of symmetry is a maximum (i.e. the radius of the "eye" of the vortex), we have from equation (2.9.25)

$$\bar{r}_m = 1 = \left(\frac{2 \cdot 51}{E}\right)^{\frac{1}{2}}$$

$$E = \frac{r_r u_r}{\nu} = 2 \cdot 51 \tag{2.9.33}$$

Substituting in equation (2.9.24)

$$\bar{v} = \frac{1}{\bar{r}} \left(\frac{1 - e^{-1 \cdot 25 \bar{r}^2}}{1 - e^{-1 \cdot 25}} \right) \tag{2.9.34}$$

The pressure distribution in the radial direction follows from equation (2.9.9)

$$p_2(\bar{r}) = \int_0^{\bar{r}} \frac{1}{\bar{r}^3} \left(\frac{1 - e^{-1.25\bar{r}^2}}{1 - e^{-1.25}} \right)^2 d\bar{r}$$

(2.9.35)

Equations (2.9.34) and (2.9.35) are plotted in figure 2.9.6. It can be seen that if r_r is defined as the point at which the velocity is maximum, the velocity and pressure distributions are independent of Reynolds number.

The two descriptions of the velocity field given in equations (2.9.24) and (2.9.34) are complementary. If r_r is defined as the radius of the vortex core (which may be taken as the region in which the assumption of axial symmetry holds) then the radius $\bar{r}_m$ of the 'eye' of the vortex is dependent upon Reynolds number, as given by equation (2.9.25). However equation (2.9.34) suggests that if the radius is non-dimensionalized on the radius of the eye of the vortex, then the velocity and pressure distributions are independent of Reynolds number.

2.9.4 Continuity considerations

In this section an attempt will be made to show how the vortex Reynolds number E varies with the large scale flow parameters ($\frac{UD}{\nu}$ and $\frac{D}{\delta^*}$). We define r_r as the radius of the core of the primary vortex of a laminar horseshoe vortex system (i.e. the region in which the assumption of axial symmetry holds). Assume that the flow rate into this vortex core is proportional to the flow rate in the upstream boundary layer. By continuity we have

$$2\pi r_r u_r \propto U(\delta - \delta^*)$$

(2.9.36)

where δ is the upstream boundary layer thickness and δ^* is the displacement thickness. Now for a flat plate boundary layer in zero pressure gradient

$$\delta = 3\delta^*$$

(2.9.37)

Thus from equations (2.9.36) and (2.9.37)

$$r_r u_r \; \alpha \; U \delta^* \tag{2.9.38}$$

or

$$\frac{r_r u_r}{\nu} = E \; \alpha \; \frac{U \delta^*}{\nu} = \left(\frac{U D}{\nu}\right)\left(\frac{\delta^*}{D}\right) \tag{2.9.39}$$

So one would expect E to be proportional to $\dfrac{U D}{\nu}$ and inversely proportional to $\dfrac{D}{\delta^*}$. The constant of proportionality depends upon the constant in equation (2.9.36) and must be determined experimentally.

2.10 Velocity distributions within horseshoe vortex systems

2.10.1 Comparison of vortex flows in the two wind tunnels

As was stated in section 2.3 it was intended to use a laser anemometer to make measurements of flow velocities within horseshoe vortex systems. However with the experimental configuration used this proved to be impossible. It was decided to measure flow velocities by filming smoke filaments entering the vortex systems and measuring the difference in position of the ends of the smoke filaments between successive frames. It was found possible to make measurements in the smoke tunnel so that the velocities at most points within the horseshoe vortex system on the plane of symmetry upstream of a cylinder could be determined. However when the experiments were set up in the 51 cm x 71 cm wind tunnel a difference in the vortex flow structure in this tunnel and in the smoke tunnel became apparent. In the 51 cm x 71 cm tunnel there seemed to be a great deal more "divergence" upstream of and within the horseshoe vortex systems. That is to say the streamlines close to the plane of symmetry upstream of the horseshoe vortex system in this tunnel were swept away from the plane of symmetry within the horseshoe vortex systems very much more quickly than in those systems formed in the smoke tunnel. Thus smoke rarely penetrated into the lower velocity regions of the vortex systems formed in the 51 cm x 71 cm tunnel, and it was not possible to measure the velocities

within these systems.

Thus in the more confined flow of the smoke tunnel the flow is more vigorous on the plane of symmetry upstream of the cylinder than for the flow in the 51 cm x 71 cm tunnel. This may be due to either or both of two effects. Firstly the flow upstream of the cylinder in the 51 cm x 71 cm tunnel is not influenced by the "images" of the cylinder in the wind tunnel walls (figure 2.10.1a), these images being too far away. However in the smoke tunnel the "images" of the cylinder in the sides of the tunnel are effectively much closer to the cylinder. One would therefore expect them to influence the flow upstream of the cylinder. These "images" tend to force the flow towards the plane of symmetry (figure 2.10.1a) and this may explain the more vigorous flow observed on the plane of symmetry upstream of the cylinder in the smoke tunnel.

Secondly the cylinder used in the smoke tunnel is very much shorter than that used in the 51 cm x 71 cm tunnel (3.8 cm instead of 30.5 cm). Thus flow on the plane of symmetry can pass over the cylinder rather than having to diverge from the plane of symmetry to pass around the cylinder. This again would lead to a more vigorous flow on the plane of symmetry.

To test which of these two effects predominate the flow upstream of a 7.6 cm diameter cylinder, 12.7 cm in height was observed in the smoke tunnel. In figure 2.10.1b a photograph of the flow upstream of this cylinder is shown together with a similar photograph of the flow upstream of the shorter cylinder usually used in the smoke tunnel. It can be seen that there is a significant difference between these flows. The vortex system upstream of the taller cylinder is flatter and somewhat less well defined than that upstream of the shorter cylinder. Also much of the flow was observed to diverge away from the plane of symmetry upstream of the vortex system. This is similar to the flow that was observed upstream of the 30.5 cm high cylinder in the 51 cm x 71 cm tunnel, but in that tunnel the flow diverged from the plane of symmetry to a much greater

extent and was therefore more difficult to photograph.

So it would seem that this divergence of the flow becomes more prom-
inent as the height of the cylinder is increased, and as the ratio of
the cylinder diameter to the wind tunnel width decreases. That is, both
of the two effects described above play a part.

Because of the well defined nature of the flow upstream of the
7.6 cm diameter by 3.8 cm high cylinder mounted in the smoke tunnel it
was decided to make measurements of velocity upstream of this cylinder
only. However when considering these results the preceding discussion
should be kept in mind.

2.10.2 Velocity measurements in the smoke tunnel

Velocity measurements on the plane of symmetry upstream of a
cylinder in the smoke tunnel are shown in figure 2.10.2, for $\frac{UD}{\nu}$ =
2,610, $\frac{D}{\delta^*}$ = 14.8. The sections for which velocity profiles are pre-
sented are shown in figure 2.10.2a. The velocity profile in a direction
parallel to the plate for a section perpendicular to the plate, upstream
of the vortex system is shown in figure 2.10.2b. Velocity profiles in
directions parallel and perpendicular to the plate at a section perpen-
dicular to the plate just downstream of the separation point are shown in
figures 2.10.2c and d respectively; similar profiles through vortex 2 are
shown in figures 2.10.2e and f; through vortex 1' in figures 2.10.2g and
h; and through vortex 1 in figures 2.10.2i and j. The velocity profiles
in directions parallel and perpendicular to the plate for a section
through the centre of vortex 1 parallel to the plate are shown in figures
2.10.2k and l. The reversed flow within the vortex systems can be plainly
seen in these figures. The expected double crossover in the velocity pro-
file can also be seen in figure 2.10.2g. Here the flow in vortex 1' is
in the   stream direction close to the plate, in the upstream   direction
away from the wall, and in the   stream direction out of the vortex
system.

Within the vortex system a significant vortex radial flow component could only be measured within vortices 1 and 2 (figures 2.10.2e,f,i, and j). In these figures the velocity components parallel to and perpendicular to the plate correspond to the vortex circumferential and radial components respectively. The radial component of velocity can be seen to be an order of magnitude smaller than the circumferential component.

Within the cores of the vortices the radial flow component was measured in two ways; by resolving the flow velocity at the measurement sections in a radial direction, and by measuring the variation of the distance of a streamline from the vortex centre between two successive crossings by the streamline of the measurement section. The latter method effectively gives a mean radial velocity for half a streamline spiral around the vortex. However these methods gave more or less identical results close to the centre of the vortices.

In the analysis of section 2.9 the assumption was made that the vortex radial velocity was linearly proportional to the distance from the centre of the vortex. From figure 2.10.2j (for vortex 1) it can be seen that this is the case only within the very centre of the vortex core (region XY). This region lies within the velocity peaks of the circumferential velocity profile.

The Reynolds number based on the radius of region XY and the radial velocity at its edge (E) can be calculated to be 1.8 ± 0.3 for the flow conditions of figure 2.10.2. The theoretical velocity distribution for this Reynolds number, given by equation 2.9.24, is shown in figure 2.9.2. Although this curve is of the same form as the measured velocity distribution within the region XY, there are not enough experimental points in this region to enable a detailed comparison to be made between experimental and theoretical results.

The form of the profile of radial velocity within the horseshoe vortex core (figure 2.10.2j) suggests that a better theoretical descript-

ion of the vortex circumferential velocity profile might be obtained by
assuming a parabolic distribution of the radial velocity within the
vortex core, in the analysis of section 2.9. Although this presents no
great mathematical difficulty, this extension to the analysis is not
presented for the following reason. A comparison of figures 2.10.2i and
j (for a section perpendicular to the plate through vortex 1) with
figures 2.10.2k and l (for a section parallel to the plate through
vortex 1) shows that the assumption of axial symmetry within vortex 1 is
only true close to the centre of the vortex where the radial velocity
profile can be taken as linear. Away from the centre of the vortex al-
though the radial velocity distribution can be seen to be roughly para-
bolic in planes both parallel and perpendicular to the plate, it can be
seen that the basic assumption of axial symmetry is violated.

Figure 2.10.3 shows the velocity variation along streamlines within
the horseshoe vortex systems for the same conditions as figure 2.10.2.
In this figure s is the distance along the streamlines measured from
$\frac{x}{D}$ = -1.75, and u_s is the velocity along the streamlines. Figure
2.10.3a is a scale drawing of the vortex system showing the position of
the streamlines considered. This figure presents essentially the same in-
formation as figure 2.10.2 but shows some interesting features. Firstly
it can be seen that whenever one of the streamlines passes beneath
vortices 1 or 2 (sections C and B in the figure) then the velocity rises
to a maximum. Secondly from figures 2.10.3d and f it can be seen that
when a streamline approaches a stagnation point nearly all the loss of
streamline velocity occurs in the vicinity of the stagnation point.

Figure 2.10.4 shows velocity profiles in directions perpendicular
and parallel to the plate, for a section perpendicular to the plate,
through the centre of vortex 1 at four different speeds. Equation
2.9.24 suggests that the velocity profiles within the region of the vortex
core where the radial velocity distribution is linear, should change as

the Reynolds number changes. However figure 2.10.4 shows that the non-dimensional velocity profiles do not vary greatly in and beneath the vortex core. Any variation may however be obscured by the rather large errors indicated. Above the vortex core however the streamwise velocity profiles do vary with the flow parameters. This is because as $\dfrac{UD}{\nu}$ increases vortex 1 moves away from the cylinder to a position where the dimensionless velocity outside the vortex system is higher.

2.10.3 Associated measurements

It is of interest at this point to compare the nominal values of the flow parameters, predicted by a calibration of the empty smoke tunnel and by flat plate boundary layer theory, with the measured values. At a point upstream of the separation line, for the conditions of figure 2.10.2, at $\dfrac{x}{D}$ = -2.25, the measured flow velocity was 0.56 ms^{-1} as compared to the value of 0.5 ms^{-1} given by the tunnel calibration. The displacement thickness at this point was 0.33 cm ($\pm$ 0.02), while the value given by flat plate boundary layer theory is 0.38 cm. So it can be concluded that the nominal values of the flow parameters in the smoke tunnel are reasonably accurate.

Also marked in figure 2.10.2b are the regions of the boundary layer which pass into the different vortices of the vortex system. It can be seen that the fluid from the outer edge of the boundary layer does not enter the vortex system, but passes around the side or over the top of the cylinder. It is possible to calculate the total volume flow into each vortex as a percentage of the total volume flow into the vortex system (i.e. the flow into vortices 1, 1$'$, 2, 2$'$ and 3; the flow into vortex 0 is small and difficult to distinguish from the flow that does not enter the vortex system). These results are shown in table 1. (The assumption is made that the lower regions of the boundary layer all flow into vortex 2, which may or may not be correct; see section 2.4.2).

Table 1 ($\dfrac{UD}{\nu} = 2{,}610$, $\dfrac{D}{\delta^*} = 14.8$)

Vortex	1	2	3	1$'$	2$'$
% Volume flow	43.3	19.7	8.4	18.1	10.5

So it can be seen that nearly half the volume flow into the vortex system is into vortex 1. Also the flows into vortices 1$'$ and 2$'$ are comparable with the flows into vortices 2 and 3 respectively.

Finally in figure 2.10.5 the distribution of skin friction beneath the horseshoe vortex system is shown. The data presented in this figure was taken from the velocity profiles of figure 2.10.2 and other velocity profiles. The dotted lines in the figure indicate a region where the skin friction could not be measured, such as near a separation or attachment point, but where its variation could be deduced, i.e. C_f must fall to zero at such a point. The most striking feature of this figure is the high value of $|C_f|$ beneath vortex 1, approximately five times the free stream value upstream of the vortex system. Beneath vortex 2, the value of $|C_f|$ is somewhat less than the upstream value, and beneath vortex 3 it is much less. Thus although over much of the vortex system on the plane of symmetry there is a reduction in $|C_f|$ from its free stream value, there is a considerable increase in $|C_f|$ beneath vortex 1.

2.11 Vorticity Distributions

In this section the distribution of vorticity within horseshoe vortex systems will be considered. However it is first necessary to set out some basic concepts relating to vorticity. The vorticity of a fluid flow with velocity components u, v and ω in the x, y and z directions is given by

$$\underline{\omega} = \left(\frac{\partial \omega}{\partial y} - \frac{\partial v}{\partial z}\right)\underline{i} + \left(\frac{\partial u}{\partial z} - \frac{\partial \omega}{\partial x}\right)\underline{j} + \left(\frac{\partial v}{\partial x} - \frac{\partial u}{\partial y}\right)\underline{k} \tag{2.11.1}$$

Vortex lines can be constructed which are everywhere parallel to the vorticity vector. All the vortex lines passing through a closed curve

form a vortex tube. It is easily shown that for such a vortex tube of
area S

$$\int \underline{\omega} \cdot \underline{dS} = \text{constant} \tag{2.11.2}$$

As a consequence of this result it can be shown that vortex lines cannot
start or end within a fluid.

For a control volume within the fluid the net outflow of vorticity
must be zero. Now vorticity can be transported in two ways; by convect-
ion or by diffusion. Vortex lines, which are usually fluid lines, are
convected through the flow and can be distorted and stretched as the flow
passes around obstacles. Vorticity diffusion occurs when there is a
vorticity gradient and its magnitude is proportional to the magnitude of
this vorticity gradient. Thus the net convection of vorticity out of any
control volume within the fluid must be equal to the net vorticity dif-
fusion into the contral volume.

Now consider the flow configuration shown in figure 2.11.1 where a
cylinder is mounted on a plate on which a boundary layer is growing. On
the plane of symmetry upstream of the cylinder the vorticity is given by

$$\underline{\omega} = \left(\frac{\partial v}{\partial x} - \frac{\partial u}{\partial y}\right) \underline{k} = \omega_2 \underline{k} \tag{2.11.3}$$

since $\omega = \frac{\partial u}{\partial z} = \frac{\partial v}{\partial z} = 0$. Thus in the two dimensional
boundary layer upstream of the cylinder the vorticity vector and the
vortex lines are parallel to the plate and perpendicular to the plane of
symmetry. Now consider vortex tubes consisting of such vortex lines as
they are carried by the flow towards the cylinder. The boundary layer
upstream of the cylinder undergoes a three dimensional separation, and
the vortex tubes comprising it are concentrated into the vortices of any
horseshoe vortex system that might form. These vortex tubes are swept
and stretched around the side of the cylinder. Since these vortex tubes
are always composed of the same fluid, the area of these tubes must de-
crease as they are stretched to conserve their volume. Thus from equation

2.11.2 their vorticity must increase. Thus as vortex lines are convected into the horseshoe vortex system this tendency for the vorticity to increase must be matched by vortex diffusion to the plate or cylinder. Or alternatively vorticity of the opposite sign must diffuse from the plate or the cylinder.

Now consider the streamwise momentum equation for fluid flow.

$$\frac{\partial u}{\partial t} + u \frac{\partial u}{\partial x} + v \frac{\partial u}{\partial y} + w \frac{\partial u}{\partial z} = -\frac{1}{\rho} \frac{\partial p}{\partial x} + \nu \left(\frac{\partial^2 u}{\partial x^2} + \frac{\partial^2 u}{\partial y^2} + \frac{\partial^2 u}{\partial z^2} \right)$$

(2.11.4)

This equation will be applied to the flow on the plane of symmetry of figure 2.11.1. Now at $y = 0$, $u = v = w = \frac{\partial u}{\partial x} = \frac{\partial u}{\partial z} = \frac{\partial^2 u}{\partial x^2} = \frac{\partial^2 u}{\partial z^2} = 0$. So if the flow is steady (i.e. $\frac{\partial u}{\partial t} = 0$) equation (2.11.4) becomes

$$\frac{1}{\rho} \left(\frac{\partial p}{\partial x} \right)_{y=0} = \nu \left(\frac{\partial^2 u}{\partial y^2} \right)_{y=0}$$

(2.11.5)

From equations (2.11.3) and (2.11.5)

$$\frac{1}{\rho} \left(\frac{\partial p}{\partial x} \right)_{y=0} = -\nu \left(\frac{\partial \omega_z}{\partial y} \right)_{y=0}$$

(2.11.6)

since $\frac{\partial v}{\partial x} = 0$ on $y = 0$. Thus the vorticity gradient at $y = 0$, which is proportional to the magnitude of vorticity diffusion, is proportional to the streamwise pressure gradient.

Thus if

$$\left(\frac{\partial p}{\partial x} \right)_{y=0} > 0$$

(2.11.7)

then

$$\left(\frac{\partial \omega_z}{\partial y} \right)_{y=0} < 0$$

(2.11.8)

and the vorticity distribution for small values of y is as sketched in figure 2.11.2(a). Here there is diffusion of +ve vorticity away from the wall (or alternatively diffusion of -ve vorticity to the wall).

If $\left(\dfrac{\partial p}{\partial x}\right)_{y=0} < 0$ (2.11.9)

then $\left(\dfrac{\partial \omega_z}{\partial y}\right)_{y=0} > 0$ (2.11.10)

and the vorticity distribution for small values of y is as sketched in figure 2.11.2b. Here there is diffusion of +ve vorticity to the wall (or alternatively diffusion of -ve vorticity from the wall).

Now the variation of pressure beneath horseshoe vortex systems has been described in section 2.6. A typical pressure distribution on the plane of symmetry is sketched in figure 2.11.2(c). Figure 2.11.2(d) shows the direction of the diffusion of +ve vorticity that can be inferred from figure 2.11.2(c) and equation (2.11.6). One would expect that the largest vorticity gradients near the wall would occur in the region of the greatest pressure gradient, and that most vorticity diffusion would take place in this region.

The vorticity distribution within a horseshoe vortex system is shown in figure 2.11.3. These curves were calculated from the velocity profiles of figure 2.10.2. Figure 2.11.3(a) shows the vorticity distribution in the unseparated boundary layer. It can be seen that vorticity of negative sign is being convected by the flow. In this region equation (2.11.3) reduces to

$$\underline{\omega} = -\left(\dfrac{\partial u}{\partial y}\right)\underline{k}$$ (2.11.11)

Since $\dfrac{\partial u}{\partial y}$ is +ve , $\underline{\omega}$ is -ve. The slope of the vorticity profile at the wall in this case is small, as one would expect from equation (2.11.6) as the pressure gradient is small. Figures 2.11.3b, c and d show the vorticity profiles just downstream of separation, through the centre of vortex 2 and through the centre of vortex 1 respectively. The slopes of the vorticity distributions at y = 0 in figures 2.11.3(b) and 2.11.3(c) are slightly negative which is as one would expect from equation (2.11.6) since at these points $\left(\dfrac{\partial p}{\partial x}\right)_{y=0} > 0$ From figure

2.11.3(d) the vorticity gradient at $y = 0$, is approximately zero, which again is as one would expect since $\left(\frac{\partial p}{\partial x}\right)_{y=0} \simeq 0$ at this point. However the large negative values of the vorticity gradient for $y > 0$ do give some indication of the magnitude of the vorticity diffusion in the region of large pressure gradient between vortex 1 and the cylinder.

It can be seen from the preceding discussion that vortex diffusion from the plate beneath the horseshoe vortex system plays an important role in determining the flow pattern. It was thus of interest to see what form the flow pattern would take if this source of vorticity diffusion were absent. So flow visualization experiments were carried out in the smoke tunnel using the apparatus shown in figure 2.11.4a. Here the region of the plate on which the cylinder is mounted, downstream of the observed separation line has been removed, so that there is no vorticity diffusion from the plate in this region. Photographs of one of the resulting flow patterns on the plane of symmetry upstream of two cylinders, one mounted on either side of the plate, are shown in figures 2.11.4b to 2.11.4g. The streamlines feeding the vortex systems move downwards in the photographs from figure 2.11.4b to 2.11.4g. The flow can be seen to be complex with fluid from one side of the plate passing through the hole in the plate to the part of the vortex system on the other side of the plate. The streamlines that can be deduced from these photos are sketched in figure 2.11.5. It can be seen that the vortex system formed by, say, the separated fluid from the bottom of the plate in the photograph forms the counter-rotating vortices that are required to keep the vortices formed by the separating fluid from the top half of the plate in equilibrium, and vice versa.

So it can be concluded that vorticity diffusion from the plate beneath the vortex does play an important role in determining the flow pattern within the vortex system, since when there is no such diffusion the flow patterns are changed significantly.

CHAPTER 3

The horseshoe vortex formed by a separating turbulent boundary layer

3.1 Literature review

3.1.1 Experimental investigations of horseshoe vortices

The first investigation of a horseshoe vortex system formed by a separating turbulent boundary layer seems to have been made by Vasanta Ram (1963). He studied the horseshoe vortex ahead of a 15 cm diameter cylinder on a plate in a wind tunnel at a Reynolds number ($\frac{UD}{\nu}$) of 4.1×10^5, for the following two different sets of upstream boundary layer conditions:-

(1) $\frac{D}{\delta^*}$ = 33.3, H = 1.56, $\frac{D}{l}$ = 0.32

(2) $\frac{D}{\delta^*}$ = 7.6, H = 1.35, $\frac{D}{l}$ = 0.32

He measured the pressure distribution on the cylinder and on the plate around the cylinder. Some of these experimental results were used in section 2.9 (figure 2.9.5). One of the measured pressure distributions on the plane of symmetry upstream of the cylinder is shown in figure 3.1.1. The position of the primary vortex, indicated by the minimum in the pressure distribution can be clearly seen. Vasanta Ram also performed some oil flow visualization on the plate and made measurements of the flow direction around the side of the cylinder using a three hole yawmeter.

The work of Roper (1967) has already been mentioned in section 2.1.2 where his control volume vorticity analysis was discussed. He carried out flow visualization experiments around a 5.04 cm diameter cylinder mounted on a ground plane in a water flume, using the hydrogen bubble technique. The flow conditions for his experiments were as follows:-

$\frac{UD}{\nu}$ = 2740-3180, $\frac{D}{\delta^*}$ = 8.7, H = 1.7, $\frac{D}{l}$ = 0.61

(The values of $\frac{D}{\delta^*}$ and H were not given by Roper, but were calculated

from the velocity profiles that were given. The equivalent cylinder

height (L) was taken as being the water depth at the model position).

He observed the whole flow field around the cylinder including the wake

flow. He observed a form of oscillatory behaviour within the horseshoe

vortex system (figure 3.1.2). However he seems to confuse the observed

motion of the hydrogen bubbles used for flow visualization with the motion

of the horseshoe vortices themselves. When the streak of hydrogen bubbles

passes from one vortex to another during the oscillation Roper describes

this as the formation of a new vortex, whereas it is simply that the

hydrogen bubbles make a different vortex visible. However it would appear

that the oscillatory behaviour he observed can be described as follows

(figure 3.1.2). The primary vortex (1) broke away from the rest of the

vortex system, moved downstream towards the cylinder, and then back up-

stream where it appeared to combine with vortex 2 producing a burst of

turbulence. Roper considered this oscillation to take place at the freq-

uency of wake vortex shedding, even though the Strouhal number of the

vortex oscillation was approximately equal to 0.1, about half the usual

value of the Strouhal number of wake vortex shedding. However Roper did

not measure the frequency of wake vortex shedding, so his conclusions

could not be verified.

Belik (1973) investigated the horseshoe vortex systems ahead of

cylinders of different sizes mounted on plates in a wind tunnel. Using

vorticity arguments, he derived a functional expression similar to equat-

ion (2.2.5) which was arrived at in this investigation by simple dimen-

sional analysis. Using oil flow visualization he measured the variation

in the position of the primary separation line as the flow parameters

varied between the limits

$$0.35 \times 10^5 < \frac{U D}{\nu} < 2.2 \times 10^5 \qquad\qquad 5.4 < \frac{D}{\delta^*} < 86.0$$

$$H \doteq 1.5 \qquad\qquad 0.2 < \frac{D}{L} < 0.6$$

(The values of H and δ^* were calculated from the information given by Belik).

He concluded that the dimensionless position of the separation line, $\frac{x_s}{D}$, depended upon the dimensionless group $\frac{u\delta^*}{\nu}$ only. (This group is related to the dimensionless groups derived in section 2.2 since

$$\frac{u\delta^*}{\nu} = \left(\frac{uD}{\nu}\right)\left(\frac{D}{\delta^*}\right)^{-1} \tag{3.1.1}$$

Belik also measured the pressure distribution upstream of the cylinder for some tests. One of his results is shown in figure 3.1.1, with the result of Vasanta Ram. Again the position of the horseshoe vortex core can be clearly seen.

Westkaemper (1968) correlated the results of previous investigations into the variation of the separation position upstream of wall mounted obstacles in a supersonic flow. He produced the correlation

$$\frac{x_s}{D} = -2\cdot15 \qquad \left[\frac{D}{l} < 0\cdot89\right]$$

$$\frac{x_s}{D} = -2\cdot42\left(\frac{D}{l}\right)^{-0\cdot7} + 0\cdot5 \qquad \left[\frac{D}{l} > 0\cdot89\right]$$

$1.9 < M < 11.8; \ 0.24 \times 10^6 < \frac{uD}{\nu} < 17.4 \times 10^6; \ 7 < \frac{D}{\delta^*} < 42;$

$0.1 < \frac{D}{l} < 5.0;$ No data for H was given.

(x_s is the distance from the obstacle centre to the separation position on the plane of symmetry and M is the Mach number).

Sedney and Kitchens (1975) studied the flow ahead of models of different shapes and sizes placed on the wall of a supersonic wind tunnel for the following flow conditions

$1.5 < M < 4.5, \ 2.9 \times 10^6 < \frac{uD}{\nu} < 1.8 \times 10^8, \ 3.8 < \frac{D}{\delta^*} < 30.5,$

$0.19 < \frac{D}{l} < 1.88;$ (No data for H was given).

Using various flow visualization techniques they were able to measure the position of the separation and attachment lines ahead of the cylinders and other models used. They concluded that the correlation of Westkaemper

(1968) described above did not predict the primary separation position well, for these flow conditions, giving values of $\left|\dfrac{x_s}{D}\right|$ that were too large. They were also able to observe up to three separation and attachment lines ahead of the models in the boundary layer and using the flow models of Norman (1972) they were able to deduce four different types of flow pattern on the plane of symmetry (figure 3.1.3). The type of flow pattern observed changed as the flow parameters varied, the number of vortices in general decreasing as the Reynolds number increased. Sedney and Kitchens could offer no explanation for this interesting fact which is contrary to the observed behaviour of horseshoe vortices formed by the separation of a low speed laminar boundary layer. The author is of the opinion that this effect is in some way due to the complicated interaction between the horseshoe vortex and the bow shock ahead of the models, but the nature of this interaction is unknown.

Finally mention should be made of the experimental work of Shabaka (1975). In a continuing investigation he has measured the axial velocity profiles in a turbulent horseshoe vortex core downstream of a wing body junction, using a pitot tube. These profiles allow the position of the vortex core to be determined downstream of the junction. Shabaka however did not measure the flow upstream of the wing body junction.

3.1.2 Boundary layer measurements and calculations

Two comprehensive sets of measurements of the flow in the boundary layer upstream of the separation line ahead of an obstacle have been made; by Hornung and Joubert (1963), and East and Hoxey (1969a and b).

Hornung and Joubert (1963) measured velocity profiles upstream of a streamlined body with a circular cylindrical nose section 0.56 m in diameter. The flow conditions for these experiments were

$\dfrac{UD}{\nu} = 0.65 \times 10^6$; $\dfrac{D}{\delta^*} = 44.0$; No data for H or $\dfrac{D}{l}$ was given.

(The value of $\dfrac{D}{\delta^*}$ given here was calculated from the flow parameters 0.38 m

upstream of the cylinder leading edge, i.e. at $\frac{x}{D} = -1.18$). They also measured the direction of the flow using a yaw meter and observed the turbulent horseshoe vortex system downstream of the separation line using smoke flow visualization.

East and Hoxey (1969a and b) measured the flow ahead of a similar model, 0.61 cm diameter, at the following flow conditions

$$\frac{UD}{\nu} = 3.72 \times 10^6, \quad \frac{D}{\delta^*} = 30.2, \quad H = 1.40, \quad \frac{D}{l} = 0.58$$

(The values of $\frac{D}{\delta^*}$ and H given here were calculated from the flow parameters 0.46 m upstream of the cylinder leading edge, i.e. at $\frac{x}{D}$ = -1.25). They measured velocity profiles, pressure distributions, skin friction, and the direction of the flow, at a number of points ahead of and around the side of the model. They did not make any detailed observations downstream of the separation line.

As noted in section 2.1.2 there are two types of methods that have been used for boundary layer calculations. Firstly there are differential methods, where the boundary layer equations are solved numerically. Using a method of this type, Nash (1969) calculated the boundary layer development ahead of a cylindrical obstacle and found the results compared well with the results of Hornung and Joubert (1963). Secondly there are integral methods where the three dimensional momentum integral equations are solved using an assumed family of velocity profiles. Johnston (1960a) developed a method of this type, and used it to predict the separation position ahead of a wall with a jet impinging upon it. This method will be discussed in detail in section 3.5.

3.1.3 Topology of surface streamline patterns

In section 3.3.2 the results of oil flow visualization around the base of cylinders on a wall will be presented. Oil flow visualization shows the direction of the "limiting streamlines", i.e. the limiting direction of the flow as the wall is approached. Maskell (1955) first

studied the concept of limiting streamlines. He found that at all points on a surface the limiting streamlines can have only one direction, except at certain points, referred to as singular points. These singular points are associated with separation of the flow from the surface and with the reattachment of the flow. (This is not to say that all points along a three dimensional separation line are singular points). In figure 3.1.4 several types of limiting streamline patterns are shown in the vicinity of singular points (after Hunt et al. (1978)). Figures 3.1.4a and 3.1.4b show nodal points of attachment and separation respectively; figures 3.1.4c and 3.1.4d show saddle points of separation and attachment respectively; figures 3.1.4e, 3.1.4f and 3.1.4g show the limiting streamline patterns called foci which can also be referred to as nodes. The regions of existence of these singular points are also indicated in terms of the values of J, λ and Δ where

$$J = \frac{\partial e_u}{\partial x} \cdot \frac{\partial e_v}{\partial y} - \frac{\partial e_u}{\partial y} \cdot \frac{\partial e_v}{\partial x} \qquad (3.1.2)$$

$$\Delta = \frac{\partial e_u}{\partial x} + \frac{\partial e_v}{\partial y} \qquad (3.1.3)$$

$$\lambda = \frac{\Delta}{2} \pm \sqrt{\left(\frac{\Delta^2}{4} - J\right)} \qquad (3.1.4)$$

and e_u and e_v are the surface shear stress vectors in the x and y directions respectively. The derivation of equations (3.1.2) to (3.1.4) is given by Hunt et al. (1978).

By extending the work of Perry and Fairlie (1974), Hunt et al. (1978) also derive a formula relating the number of nodal points and saddle points on and around a finite body mounted on an infinite plane.

$$\left(\Sigma_N - \Sigma_S\right)_{PLANE\ AND\ BODY} = 0 \qquad (3.1.5)$$

where Σ_N is the number of nodal points and Σ_S is the number of saddle points.

Now consider figures 3.1.5(a) and (b) which show the surface stream-
lines of the flow around a cuboid on a plane. By considering the number
of nodal and saddle points it can be seen that equation (3.1.5) is
verified in this case.

Hunt et al. also derived a similar formula relating the number of
nodal and saddle points in a flow plane. Consider figure 3.1.5(c), where
the streamlines in the plane of symmetry of the cuboid are sketched. For
such a plane Hunt derives

$$\left(\Sigma_N - \Sigma_S\right) + \frac{1}{2}\left(\Sigma_{N'} - \Sigma_{S'}\right) = 0 \qquad\qquad (3.1.6)$$

where $\Sigma_{N'}$ and $\Sigma_{S'}$ are the number of "half" nodal and saddle points on
the surface of the plane and cuboid. By counting the number of nodal and
saddle points, and the number of half nodal and saddle points, it can be
seen that equation (3.1.6) is verified in this case.

3.2 Experimental apparatus and procedure

3.2.1 Wind tunnels

The experiments to investigate the horseshoe vortex formed by a
separating turbulent boundary layer were carried out with the models
mounted on

(a) the floor of No. 1B wind tunnel (the 51 cm x 71 cm tunnel),

(b) on a false floor mounted within the working section of the wind tunnel
(figure 3.2.1).

Two series of tests were carried out on the wind tunnel floor, with
two extensions of different length (1.2 m and 3.3 m) inserted upstream of
the model position, thus extending the length of the working section. In
each case the boundary layer was tripped at the downstream end of the con-
traction by a rod of square cross section, 4 mm in height, spanning the
tunnel. Thus in each series of tests boundary layers of different thick-
nesses were obtained. With the short extension in position the model
position was 1.6 m downstream of the trip and with the long extension in

position the model position was 3.7 m downstream of the trip.

Velocity and turbulence profiles were measured at the model position using a hot wire probe (see section 3.2.5). Some of these profiles are shown in figures 3.2.2a and 3.2.2b for the long extension upstream of the working section and in figures 3.2.2c and 3.2.2d for the short extension upstream of the working section. Velocity profiles at the model position on the false floor are shown in figure 3.2.2e. (These profiles were measured with a rake of 13 flattened Pitot tubes placed at the model position). The mean velocity profiles of figures 3.2.2a, 3.2.2c and 3.2.2e are plotted in the form of "Clauser" diagrams in figure 3.2.3a (with the long extension to the working section), figure 3.2.b (with the short extension to the working section) and figure 3.2.3c (with the false floor in position). It can be seen from figures 3.2.2 and 3.2.3 that these profiles are typical of turbulent boundary layers (see, for example, Klebanoff (1955)), and they plot as straight lines in the Clauser diagram as expected (except close to the floor in the laminar sub layer and in the outer region of the boundary layer).

Figure 3.2.4 shows how the boundary layer parameters H and δ^* vary with wind speed. It can be seen that at the lower speeds, with the short extension in position, H has values outside the range 1.3 - 1.7 that one would expect for normal turbulent boundary layers. For experiments with both the short and the long extension in position H decreases as the wind speed increases.

Many experimenters use the parameter $\frac{u\theta}{\nu}$ to describe the state of turbulent boundary layers. Although this parameter is not used in this investigation values of $\frac{u\theta}{\nu}$ are given here for completeness. For tests with the long extension in position, $\frac{u\theta}{\nu}$ at the model position varies between approximately 450 and 10,000; with the short extension in position between approximately 250 and 7,000; and for tests on the false floor $\frac{u\theta}{\nu}$ at the model position varies between approximately 900 and

1800.

3.2.2 Models

The same 6.35 cm diameter cylinder and cylinder with splitter plate models used in the study of laminar horseshoe vortices were used for this part of the study (see figure 2.3.7). A model of the same section as the streamlined model shown in figure 2.3.7 was also used but its height was the same as the other models (30.5 cm). In addition to these models seven 30.5 cm high circular cylinders were used for oil flow visualization studies. They had diameters of 10.2 cm, 8.9 cm, 7.6 cm, 6.4 cm, 5.1 cm, 3.8 cm and 2.5 cm. The 10.2 cm diameter cylinder was constructed in sections so that its height could be varied.

The dimensional analysis of section 2.2 applies to horseshoe vortices formed by separating turbulent boundary layers as well as to vortices formed by separating laminar boundary layers. Thus any measurements of vortex or separation position can be plotted in the $\frac{UD}{\nu}$ versus $\frac{D}{\delta^*}$ plane. The positions of such measurements in this plane are shown in figure 3.2.5 for the 6.35 cm diameter models on the tunnel floor with the long and short extensions to the working section in position, and on the false floor placed in the working section. In this figure the positions of the experiments of Roper (1967) and Vasanta Ram (1963) are also shown.

3.2.3 Flow visualization experiments

Surface oil flow visualization around the models was carried out on the wind tunnel floor and false floor, and on the models themselves, using a suspension of titanium dioxide in paraffin with small quantities of oleic acid added to prevent flocculation of the suspension. This mixture was spread in a thin film on the surface over which the oil flow visualization was carried out. When the wind tunnel was run the shear stresses on the surface moved the suspension in the direction of the surface streamlines, and the pattern of these streamlines was made visible.

Smoke flow visualization was carried out on the plane of symmetry up-

stream of the 10.2 cm diameter cylinder. Smoke was injected into the
boundary layer upstream of the model through holes in the floor of the
long extension, just downstream of the boundary layer trip. The smoke,
a fine suspension of kerosene oil droplets, was produced by a Taylor 3020
smoke generator. Photographs were taken of the flow upstream of the cyl-
inder using a Nikon 35 mm camera. The smoke was illuminated by a
"Wattastar" lamp, the light from which was focussed on to the region of
the horseshoe vortex system by a system of cylindrical lenses and slits
(figure 3.2.6). The light plane in the region of the vortex system was
about 5 mm thick.

3.2.4 Pressure measurement

Measurements of the pressure distribution on the plane of symmetry
were carried out on the wind tunnel floor using an apparatus very similar
to that described in section 2.3.5, mounted beneath the floor of the wind
tunnel. Readings were taken using the Furness micromonometer, and an
ordinary inclined tube alcohol manometer at low and high speeds respect-
ively. Pressure measurements were carried out with models mounted on the
wind tunnel false floor by fixing the model in one position and measuring
the pressure upstream of the model at twenty pressure tappings, spaced at
4 mm intervals, using a multitube, inclined tube manometer (figure 3.2.1).

3.2.5 Hot wire anemometry

The unsteady behaviour of the vortex systems was investigated in a
manner similar to that described in section 2.3.6 using a hot wire probe
mounted such that the tip of the probe was only a small distance from the
wind tunnel floor. The unsteady wake flow downstream of the models was
investigated by mounting the hot wire probe at various positions down-
stream of the models, again in a manner similar to that described in
section 2.3.6. The hot wire apparatus was identical to that described in
that section and spectral analyses were also carried out as described in
that section.

3.3 Flow visualization

3.3.1 Oil flow visualization

The method of oil flow visualization, using a suspension of titanium dioxide in paraffin, was used to determine the surface streamline pattern on the models, and on the wind tunnel floor adjacent to them. Figure 3.3.1a shows a photograph of the flow pattern on the wind tunnel floor around a 10.2 cm diameter cylinder. The surface streamlines are sketched in figure 3.3.1b. The saddle point of primary separation (S) can be seen upstream of the cylinder, but its position is indistinct since much of the titanium dioxide suspension has been brought into this region by the flow. The saddle point of secondary separation (S_1) can also be seen. Between S and S_1 there must be a nodal point of attachment but this cannot be distinguished on the photograph. The primary and secondary separation lines, which are composed of ordinary separation points, are also shown in figures 3.3.1a and b. Around the side of the cylinder the primary separation line becomes indistinguishable from the other surface streamlines. The position of the attachment line A_o very close to the cylinder, can also be distinguished from the photograph. The large deposit of titanium dioxide in the wake of the cylinder and the symmetric surface streamline pattern in the wake are the products of the unsteady wake flow and as such can only give some time average indication of the position of the surface streamlines in the wake.

The flow pattern upstream of the cylinder that can be inferred from these results is shown in figure 3.3.2. It consists of four vortices (0, 1, 1' and 2). However there may be other vortices present that are not strong enough to cause a recognizable surface streamline pattern to form.

One interesting surface streamline pattern that was seen to occur occasionally (in an unpredictable fashion) is sketched in figure 3.3.3. Here the secondary separation line appears to be split in two, becoming

very indistinct near the plane of symmetry, with surface streamlines

apparently crossing it. There are two possible explanations for this

type of flow pattern:-

(1) the 'split' separation line is a genuine effect and there is a

secondary separation off, but not on, the plane of symmetry;

(2) the 'split' separation line and the surface streamlines

apparently crossing it are no more than time average patterns

caused by an unsteady flow.

It is not possible to say which of the two explanations is the correct

one.

The flow patterns on the models themselves were also visualized using

this method and these are sketched in figure 3.3.4. The flow on the front

of all the models was qualitatively the same (figure 3.3.4a). A separat-

ion line (S_o) can be seen close to the wind tunnel floor (where the

boundary layer on the upstream face of the cylinder separates due to the

adverse pressure gradient caused by the horseshoe vortex system). A

nodal point of attachment can also be seen about 0.8 model heights from

the wind tunnel floor. Thus the flow on the front of the models above

the horseshoe vortex region is far from being two dimensional. The

separation line showing laminar boundary layer separation from the side

of the cylinder is shown in figure 3.3.4b. This separation line is at

about 80° of arc from the leading edge of the cylinder, but near the wind

tunnel floor separation occurred further around the cylinder, at about

110° degrees of arc, probably due to the boundary layer on the cylinder

at this point being turbulent and better able to withstand adverse press-

ure gradients. Further around in the wake of the cylinder another separat-

ion line could be seen. Stewart (1977) is of the opinion that this type

of line is due to a secondary separation beneath the cylinder wake

vortices. Figure 3.3.4c shows the surface streamlines on the side of the

cylinder with splitter plate model. Laminar boundary layer separation can

again be distinguished at about 80° of arc from the leading edge of the cylinder and an attachment line can be seen on the splitter plate. The surface streamline on the side of the streamlined model (figure 3.3.4d) reveal a complex three dimensional separation bubble on the side of the model, presumably caused by laminar boundary layer separation, transition of the separated shear layer, and reattachment of the turbulent shear layer. Downstream of the attachment line the flow remained attached to the surface till close to the trailing edge.

Much information was recorded on how the primary and secondary separation lines varied with the flow parameters. This information will be presented in section 3.6.

3.3.2 Smoke flow visualization

Photographs were taken of the horseshoe vortex flow upstream of a 4" diameter cylinder mounted on the floor of the 51 cm x 71 cm diameter tunnel, using the lighting arrangement described in section 3.2.3, with the long extension upstream of the working section. Two different types of photograph were taken. Firstly with long exposures (1/15s to 1/60s) photographs of the type shown in figure 3.3.5a were taken. These photographs show a time mean position of the horseshoe vortices on the plane of symmetry upstream of the cylinder. In figure 3.3.5a vortex 1 can be seen. Secondly with short exposures (1/500s to 1/1000s) photographs of the type shown in figure 3.3.5b were taken. This photograph does not show the horseshoe vortices, which can only be seen in the longer exposure photographs which show the mean flow pattern. However it does show the large scale turbulent structures in the upstream boundary layer. These structures are distorted as they are convected into the vortex system and the nature of this distortion can be described. It can be seen from figure 3.3.5b that upstream of the vortex system the large scale eddies within the boundary layer have their downstream sides at an angle of about 40° to the wind tunnel floor (arrow A in the photograph). Similar obser-

vations have been made by Bandyopadhay (1977) in his extensive flow visualization studies of turbulent boundary layers. However just upstream of the cylinder above the horseshoe vortex system these large scale structures are at a much greater angle to the wind tunnel flow (up to 90°). (Arrow B in the photograph). Similar distortion of the large scale structures was observed in a large number of photographs. This distortion may be explained in the following manner. Head and Bandyopadhay (1978) have considered turbulent boundary layers to be made up of hairpin vortices; i.e. vortices with a hairpin like shape with the "ends" of the hairpin emerging from the laminar sub-layer. These hairpin vortices appear to have a preferred inclination of 40° to the wind tunnel floor on which the boundary layer is growing. This corresponds to the angle of the front of the large scale turbulent structures of figure 3.3.5b and these structures can be considered to consist of many such hairpin vortices. The angle of these hairpin vortices to the floor is determined by the balance between two forces. Firstly the self induced forces on these vortices tend to increase their angle of inclination to the floor. Secondly the mean shear stresses within the boundary layer tend to decrease the angles of inclination of these vortices. As the boundary layer approaches separation these mean shear stresses fall, and as a result the angle of the vortices to the floor must increase, as has been seen to be the case.

3.4 Plane of symmetry pressure measurements

Figure 3.4.1 shows the pressure distributions measured ahead of the 6.35 cm diameter cylinder with the long extension ahead of the working section. It can be seen that there is very little variation in these pressure distributions over the range of Reynolds number covered.

All the pressure distributions show a levelling out at $\frac{x}{D} \simeq -0.8$, and following the argument of section 2.4.5 it seems reasonable to infer that this is the position of the centre of the primary horseshoe vortex. This position does not seem to vary with Reynolds number.

Figure 3.4.2 shows similar pressure distributions ahead of the cylinder with the short extension in position. The curves are similar to those of figure 3.4.1 in that they do not vary appreciably with Reynolds number. The curves all show a levelling out, or a slight dip, at $\frac{x}{D} \simeq -0.8$, so the vortex position seems to be the same as for the tests with the long extension in position (i.e. at lower $\frac{D}{\delta^*}$).

The dotted line in figure 3.4.2 is an approximation to the pressure distributions upstream of the separation position and can be represented by

$$C_p = 0.51 + 0.18\left(\frac{x}{D}\right) \qquad (3.4.1)$$

This pressure distribution will be used in section 3.5 to calculate a theoretical value of the separation position using the integral method of Johnston (1960a).

Figure 3.4.3 shows a similar set of curves obtained when the model was placed on the false floor in the wind tunnel. Again there can be seen to be little variation with Reynolds number over the range covered. The distributions all show a slight dip at $\frac{x}{D} \simeq -0.75 \rightarrow -0.80$, so it would seem that the vortex position is closer to the cylinder than for the tests with the long and short extension in position, i.e. $\left|\frac{x_v}{D}\right|$ decreases as $\frac{D}{\delta^*}$ increases.

Now let us compare figures 3.4.1 to 3.4.3. The major difference between these figures is the difference in the value of C_p at $\frac{x}{D} = -0.5$. As $\frac{D}{\delta^*}$ increases (from figure 3.4.1 to figure 3.4.3), $C_p\left[\frac{x}{D} = -0.5\right]$ also increases. Similar variations were also observed for pressure distributions beneath laminar horseshoe vortices described in section 2.5. In that section it was shown that such behaviour was consistent with the observed fact that the dimensions of the vortex system do not change with the flow parameters. The pressure coefficient C_p at $\frac{x}{D} = -0.5$ was shown to be approximately equal to $(\frac{u}{U})^2$ where u is

the velocity on the streamline that passes down the face of the cylinder. Thus as $\frac{D}{\delta^*}$ increases (the boundary layer becoming thinner), since the vortex dimensions remain constant, $(\frac{u}{U})$ on the streamline passing down the face of the cylinder also increases, and thus C_p at $\frac{x}{D} = -0.5$ increases.

Since similar behaviour can be seen in the results of figures 3.4.1 to 3.4.3 it can be concluded that for turbulent horseshoe vortices also, the dimensions of the vortex system do not change as $\frac{D}{\delta^*}$ changes.

Figure 3.4.4 shows the pressure distributions obtained ahead of differently shaped models. It can be seen that for the cylinder, cylinder with splitter plate, and streamlined models there is little difference in the pressure distributions. So it would appear that the flows in the model wakes do not significantly affect these upstream pressure distributions.

The pressure distributions described in this section are similar in form to those obtained by Vasanta Ram (1963) and Belik (1973), shown in figure 3.1.1. The position of the minimum (and hence of the primary vortex) on the pressure distribution of Vasanta Ram (1963) is much more distinct than on the distributions described here. This may be due to the very much higher Reynolds number used in the experiments of Vasanta Ram (1963).

3.5 The prediction of the separation position using the integral method

of Johnston

Johnston (1960a) developed an integral method to find the point of boundary layer separation ahead of a wall being impinged upon by a confined jet (figure 3.5.1). In this section this method will be used to calculate the separation position upstream of a cylinder mounted on a wall, since it is possible that this separation position fixes the position of the horseshoe vortex.

Johnston (1960a) wrote the momentum integral equation on a plane of

symmetry in a three dimensional flow as

$$\frac{\partial \theta_{11}}{\partial x} = \frac{C_{fx}}{2} - \frac{(2\theta_{11} + \delta_1{}^*)}{u} \frac{\partial u}{\partial x} - \theta_{11} \frac{\partial \alpha'}{\partial n} - \frac{\partial \theta_{12}}{\partial n} \qquad (3.5.1)$$

where the symbols have the same meaning as in section 2.6. In addition

(i) C_{fx} is the skin friction in the streamwise direction,

(ii) α' is the angle of the free stream streamlines to the plane

of symmetry.

He then assumes that the pressure distribution on the plane of symmetry
can be given by the potential flow pressure distribution outside the
boundary layer. This leads to

$$\frac{\partial \alpha'}{\partial n} = - \frac{1}{u} \frac{\partial u}{\partial x} \qquad (3.5.2)$$

In another publication Johnston (1960b) had found that many turbulent
boundary layers have a velocity distribution which takes a triangular
shape when plotted in a polar form, as shown in figure 3.5.2. In the
inner region of such a distribution

$$\omega = M_1 u \qquad (3.5.3)$$

where M_1 is a constant, and in the outer region

$$\omega = M_2 (u - u) \qquad (3.5.4)$$

where M_2 is also a constant. Now for $\dfrac{u \theta_{11}}{\nu}$ greater than 10^4 Johnston
used the flow model to show

$$-\theta_{12} = M_2 \left(\theta_{11} - \delta_1{}^* \right) \qquad (3.5.5)$$

which leads to

$$- \frac{\partial \theta_{12}}{\partial n} = \frac{\partial M_2}{\partial n} \left(\theta_{11} - \delta_1{}^* \right) \qquad (3.5.6)$$

on the plane of symmetry. Then he showed that for a region where the
free stream streamlines are circular arcs

$$\frac{\partial M_2}{\partial n} = 2 \frac{\partial \alpha'}{\partial n} \tag{3.5.7}$$

To obtain better agreement with the experimental situation that he was studying, Johnston changed the constant 2.0 in equation (3.5.7) to 1.0. This is a vital step in the analysis. If this constant were not 1.0 the equations could not take their final simple form.

He then obtains from equations (3.5.6) and (3.5.7)

$$\frac{\partial \theta_{12}}{\partial n} = - \frac{\partial \alpha'}{\partial n} \left(\theta_{11} - \delta_1^* \right) \tag{3.5.8}$$

Equations (3.5.1), (3.5.2) and (3.5.8) result in the integral equation

$$\theta_{11} U^2 = \left[\theta_{11} U^2 \right]_{x=x_o} + \int_{x_o}^{x} \frac{C_{fx}}{2} U^2 dx \tag{3.5.9}$$

Johnston then solved this equation in a stepwise manner with the help of the Ludwieg and Tillmann (1949) skin friction relation for two dimensional turbulent boundary layers

$$C_{fx} = 0.246 \, e^{-1.561 H} \left(\frac{U \theta_{11}}{\nu} \right)^{-0.268} \tag{3.5.10}$$

He also used the von Doenhoff and Tetervin (1943) equation

$$\frac{\partial H}{\partial x} = e^{4.68(H-2.975)} \left[- \frac{2}{U} \left(5.89 \, \log_{10} \left(4.075 \, \frac{U \theta_{11}}{\nu} \right) \right)^2 \frac{dU}{dx} - 2.035 \, \frac{(H-1.286)}{\theta_{11}} \right]$$

$$\tag{3.5.11}$$

It should be emphasised that equations (3.5.10) and (3.5.11) were derived for two dimensional flows and there is no evidence that they apply to three dimensional flows. Using equations (3.5.9) to (3.5.11) Johnston found the variation in H, θ_{11} and C_{fx} upstream of the separation line

ahead of the wall. He identified the separation position as the position where C_{fx} fell to zero. Good agreement was found between this theory and experimental results, for the flow configuration of figure 3.5.1.

This method has been used to find the variation with the flow parameters of the separation position ahead of cylinders on a wall. Equations (3.5.9) to (3.5.11) were used even though there was no evidence to show that they were applicable to this case. A computer programme was written which calculated the variation of H and C_{fx} ahead of the cylinder. It was assumed that the pressure distribution upstream of the cylinder was given by equation (3.4.1), the measured pressure distribution upstream of the separation position ahead of cylinders, with the short extension to the working section in position. The free stream velocity distribution upstream of the cylinders (required to solve equation (3.5.9)) could then be calculated since

$$C_p = \frac{p - p_0}{\frac{1}{2} \rho U_0^2} \simeq \frac{p - p_\infty}{\frac{1}{2} \rho U_\infty^2} \tag{3.5.12}$$

where the subscript $_0$ refers to conditions at the model position without the model being in position, and $p_0 \simeq p_\infty$, $U_0 \simeq U_\infty$, where the subscript $_\infty$ refers to conditions far upstream. Also, outside the boundary layer

$$p + \frac{1}{2} \rho U^2 = p_\infty + \frac{1}{2} \rho U_\infty^2 \tag{3.5.13}$$

From equations (3.5.12) and (3.5.13) an equation can be derived for the velocity distribution outside the boundary layer

$$\left(\frac{U}{U_\infty} \right)^2 = 1 - C_p \tag{3.5.14}$$

The input required by the computer programme were the flow parameters H, $\frac{U \delta^*}{\nu}$ and $\frac{D}{\delta^*}$ at a value of $\frac{x}{D} = -2.5$. (The reason for using the parameter $\frac{U \delta^*}{\nu}$ instead of $\frac{UD}{\nu}$ will be explained in the next section). The separation position was taken as being the point at

ahead of the wall. He identified the separation position as the position where C_{fx} fell to zero. Good agreement was found between this theory and experimental results, for the flow configuration of figure 3.5.1.

This method has been used to find the variation with the flow parameters of the separation position ahead of cylinders on a wall. Equations (3.5.9) to (3.5.11) were used even though there was no evidence to show that they were applicable to this case. A computer programme was written which calculated the variation of H and C_{fx} ahead of the cylinder. It was assumed that the pressure distribution upstream of the cylinder was given by equation (3.4.1), the measured pressure distribution upstream of the separation position ahead of cylinders, with the short extension to the working section in position. The free stream velocity distribution upstream of the cylinders (required to solve equation (3.5.9)) could then be calculated since

$$C_p = \frac{p - p_0}{\frac{1}{2}\rho U_0^2} \simeq \frac{p - p_\infty}{\frac{1}{2}\rho U_\infty^2} \tag{3.5.12}$$

where the subscript $_0$ refers to conditions at the model position without the model being in position, and $p_0 \simeq p_\infty$, $U_0 \simeq U_\infty$, where the subscript $_\infty$ refers to conditions far upstream. Also, outside the boundary layer

$$p + \frac{1}{2}\rho u^2 = p_\infty + \frac{1}{2}\rho U_\infty^2 \tag{3.5.13}$$

From equations (3.5.12) and (3.5.13) an equation can be derived for the velocity distribution outside the boundary layer

$$\left(\frac{u}{U_\infty}\right)^2 = 1 - C_p \tag{3.5.14}$$

The input required by the computer programme were the flow parameters H, $\frac{u\delta^*}{\nu}$ and $\frac{D}{\delta^*}$ at a value of $\frac{x}{D} = -2.5$. (The reason for using the parameter $\frac{u\delta^*}{\nu}$ instead of $\frac{uD}{\nu}$ will be explained in the next section). The separation position was taken as being the point at

which C_{fx} fell to zero. A typical result is shown in figure 3.5.3. By varying the input data the variation of $\frac{x_s}{D}$ with the flow parameters could be determined. It was found that, to an accuracy of 2%, the predicted variation of $\frac{x_s}{D}$ is given by

$$\frac{x_s}{D} =$$

$$- \left[\frac{1}{15}\frac{D}{\delta^*}\right]^{-0.02} \cdot \left[\frac{U\delta^*}{\nu} \times 10^{-4}\right]^{0.3H^{-5.0}} \cdot \left[-1.54H^2 + 4.7H - \frac{3.09}{H}\right]$$

$$(3.5.15)$$

for $5 < \frac{D}{\delta^*} < 25$; $5,000 < \frac{U\delta^*}{\nu} < 25,000$; $1.3 < H < 1.7$. Figure 3.5.4a shows $\frac{x_s}{D}$ plotted against $\frac{D}{\delta^*}$ with H as parameter (for $\frac{U\delta^*}{\nu} = 10,000$) and figure 3.5.4b shows $\frac{x_s}{D}$ plotted against $\frac{U\delta^*}{\nu}$ with H as parameter (for $\frac{D}{\delta^*} = 10.0$). It can be seen that $\left|\frac{x_s}{D}\right|$ does not vary significantly as $\frac{D}{\delta^*}$ varies, but increases as $\frac{U\delta^*}{\nu}$ increases and as H increases. These results and their implications will be discussed in the next section.

3.6 Variation of the dimensions of the horseshoe vortex system with the flow parameters

The experimental results presented in this section were obtained in two different ways. Firstly the data on the variation of the vortex position with the flow parameters was taken from the pressure distributions described in section 3.4, while the data on the variation of the saddle points of primary and secondary separation were obtained from oil flow visualization studies.

Figure 3.6.1 shows how the dip in the pressure distributions identified as the vortex position varies with $\frac{UD}{\nu}$ and $\frac{D}{\delta^*}$. Because the pressure distributions from which this data was taken did not show well defined minima at the vortex position, the values of $\frac{x_v}{D}$ shown in this

figure are not very accurate. However it does seem that as $\frac{D}{\delta^*}$ increases the horseshoe vortex moves closer to the cylinder.

Figure 3.6.2 shows how the non-dimensional primary separation position $\frac{x_s}{D}$ varies with the flow parameters. The results are plotted in the $\frac{U\delta^*}{\nu}$ versus $\frac{D}{\delta^*}$ plane rather than the $\frac{UD}{\nu}$ versus $\frac{D}{\delta^*}$ plane. This is simply because the experimental points are better distributed in this plane, and the variations in $\frac{x_s}{D}$ that occur are more easily discernable. (The choice of $\frac{U\delta^*}{\nu}$ rather than $\frac{UD}{\nu}$ in no way invalidates the dimensional analysis of section 2.2 since

$$\frac{U\delta^*}{\nu} = \left(\frac{UD}{\nu}\right)\left(\frac{D}{\delta^*}\right)^{-1} \qquad)$$

Figure 3.6.2a shows how $\frac{x_s}{D}$ varies with the long extension to the working section in position; figure 3.6.2b shows how $\frac{x_s}{D}$ varies with the short extension in position; and figure 3.6.2c shows how $\frac{x_s}{D}$ varies with the cylinders on the false floor. The values of $\frac{x_s}{D}$ are given as numbers in the $\frac{U\delta^*}{\nu} - \frac{D}{\delta^*}$ plane. The position of the experiments in this plane correspond to the position of the "decimal points" in the values of $\frac{x_s}{D}$. The approximate variation in the form parameter H is also shown in these figures, as are lines of constant $\frac{UD}{\nu}$.

Although there were considerable errors involved in the measurement of $\frac{x_s}{D}$, certain trends in its variation can be discerned in figure 3.6.2. $\left|\frac{x_s}{D}\right|$ appears to decrease as $\frac{D}{\delta^*}$ increases and as $\frac{U\delta^*}{\nu}$ increases. The first of these trends can also be seen in figure 3.6.3 which shows a cross plot of figures 3.6.2(a) and (b) where $\frac{x_s}{D}$ is plotted against $\frac{D}{\delta^*}$ for $\frac{U\delta^*}{\nu}$ = 10,000, for tests with both extensions to the working section in position. Figure 3.6.3 also shows a similar plot for $\frac{U\delta^*}{\nu}$ = 2,500, for tests on the false floor. It can be seen that there is some variation between the results of the three series of tests and it seems likely that this variation is due to the difference in the parameters $\frac{U\delta^*}{\nu}$ and H. This will be discussed further later in

this section.

Belik (1973) suggests that $\frac{x_s}{D}$ depends on $\frac{U\delta^*}{\nu}$ only. The results of figure 3.6.3 show this not to be the case, since $\frac{x_s}{D}$ can be seen to vary with $\frac{D}{\delta^*}$.

Figures 3.6.4a, b and c show the variation in the non-dimensionalized distance from the cylinder centre to the secondary saddle point of separation ($\frac{x_{s_1}}{D}$) for tests with the long extension upstream of the working section, the short extension in position, and for tests on the false floor respectively. It should be pointed out that it was possible to determine the position of the secondary separation point more accurately than the position of the primary separation point since the oil flow pattern was more distinct in the region of the secondary separation point.

Certain trends in the variation of $\frac{x_{s_1}}{D}$ with the flow parameters can be discerned from these figures. As $\frac{U\delta^*}{\nu}$ increases, $\left|\frac{x_{s_1}}{D}\right|$ increases somewhat. Taken with what was said above this means that the primary and secondary separation lines move together as $\frac{U\delta^*}{\nu}$ increases. Also it would seem from comparing figures 3.6.4a, b and c that $\left|\frac{x_{s_1}}{D}\right|$ decreases as $\frac{D}{\delta^*}$ increases.

It is of interest to compare this trend with the trend shown in the variation of the vortex position with the flow parameters, shown in figure 3.6.1, where $\left|\frac{x_v}{D}\right|$ also decreases as $\frac{D}{\delta^*}$ increases. Since the secondary separation is caused by adverse pressure gradients beneath the main horseshoe vortex, one would expect the variations in $\frac{x_v}{D}$ and $\frac{x_{s_1}}{D}$ to be similar, as they are. However it was not possible to detect any variation in $\frac{x_v}{D}$ as $\frac{UD}{\nu}$ (or $\frac{U\delta^*}{\nu}$) increases, but this may be due simply to the difficulty in measuring the vortex position precisely from the pressure distribution.

Now the results of figure 3.6.2b, for the variation of $\frac{x_s}{D}$ upstream of the cylinders with the short extension upstream of the working section, will be compared with the results given by the integral method of

Johnston (equation 3.5.15 and figure 3.5.4). For $\frac{D}{\delta^*} = 14.6, \frac{U\delta^*}{\nu} = 6090$, $H = 1.4$, the measured value of $\left|\frac{x_s}{D}\right|$ was 1.12 (figure 3.6.2b). The value predicted by the integral method is $\left|\frac{x_s}{D}\right| = 1.30$. So the integral method overestimates the numerical value of $\frac{x_s}{D}$. This is found to be the case generally.

However equation (3.5.15) does predict that as $\frac{D}{\delta^*}$ increases $\left|\frac{x_s}{D}\right|$ decreases somewhat, and such a trend can be observed in the experimental results. (It can be seen from figures 3.5.4 and 3.6.2b that the predicted variation is however much smaller than the measured variation). Equation (3.5.15) also predicts that $\left|\frac{x_s}{D}\right|$ increases as $\frac{U\delta^*}{\nu}$ increases. However the opposite trend can be observed in the experimental results. But as $\frac{U\delta^*}{\nu}$ increases in the experiment, H decreases at the model position, as indicated in figure 3.6.2b. Equation (3.5.15) shows that $\left|\frac{x_s}{D}\right|$ is more dependent upon H than upon $\frac{D}{\delta^*}$ or $\frac{U\delta^*}{\nu}$, and that it decreases as H decreases. So in the experiments the effect of an increase in $\frac{U\delta^*}{\nu}$ in increasing $\left|\frac{x_s}{D}\right|$ may be masked by the effect of a decrease in H in decreasing $\left|\frac{x_s}{D}\right|$, and this may explain the observed trend in the experimental results. $*$

At this point it is worth discussing some of the limitations of Johnston's integral method and of its application to the experimental results. Perhaps the most sweeping approximation made by Johnston in the derivation of his method was the use of the two dimensional skin friction and form parameter equations (equations (3.5.10) and (3.5.11)). The flow on the plane of symmetry upstream of cylinders is however not two dimensional, the flow diverging away from the plane of symmetry. The vortex tubes in the boundary layer upstream of the cylinder are stretched as they approach the cylinder, their area thus decreasing and their vorticity increasing (section 2.11). Head (1976) showed that the effect of such stretching of the vortex tubes is to increase the transfer of streamwise momentum through the boundary layer. Thus the skin friction at the wall

$*$ See footnote on next page

will be increased by vortex stretching. So the effect of vortex stretching will be to cause C_f to fall to zero closer to the cylinder than would have been the case without vortex stretching, i.e. separation will occur closer to the cylinder. Thus one would expect that the use of the two dimensional skin friction and form parameter equations, which do not take into account vortex stretching, would predict separation upstream of the measured position, which was seen to be the case.

The input parameters for the computer programme of Johnston's method ($\frac{U\delta^*}{\nu}$, $\frac{D}{\delta^*}$ and H) had to be specified at $\frac{x}{D}$ = -2.5. Thus it is not strictly valid to compare the results of this method directly with the experimental results where $\frac{U\delta^*}{\nu}$ $\frac{D}{\delta^*}$ and H are specified at the model position, $\frac{x}{D}$ = 0·0. However it seems unlikely that any variations of $\frac{U\delta^*}{\nu}$, $\frac{D}{\delta^*}$ and H at $\frac{x}{D}$ = -2.5, with the model in position, from their values at $\frac{x}{D}$ = 0.0, without the model in position, will be very large. One would therefore expect the conclusions reached above to still apply.

Finally oil flow visualization tests were carried out around the base of a 10.16 cm diameter cylinder, as the cylinder height was varied. The variation of $\frac{x_s}{D}$ and $\frac{x_{s_1}}{D}$ with the height:diameter ratio ($\frac{L}{D}$) is shown in figure 3.6.5. It can be seen that if $\frac{L}{D}$ > 1.5 then changes in this ratio hardly affect $\frac{x_s}{D}$ and $\frac{x_{s_1}}{D}$. Since for all the other tests reported in this chapter $\frac{L}{D}$ > 3.0, then it is justifiable to neglect $\frac{L}{D}$ when considering the variation of $\frac{x_s}{D}$ and $\frac{x_{s_1}}{D}$ with the flow parameters. The curves of figure 3.6.5 also suggest that for constant $\frac{U\delta^*}{\nu}$ $\frac{D}{\delta^*}$ and H :

$$|x_s| - \frac{D}{2} \propto D \qquad\qquad (\tfrac{L}{D} > 1.5)$$

$$|x_s| - \frac{D}{2} \propto L \qquad\qquad (\tfrac{L}{D} < 0.3)$$

So the length of the separated region scales on the cylinder diameter

when the cylinder is tall, and on the cylinder height when the cylinder
is short.

3.7 The frequency spectra of horseshoe vortices formed by separating turbulent boundary layers

Figure 3.7.1 shows the power spectrum of the velocity fluctuations
of a horseshoe vortex system upstream of a circular cylinder mounted on
the floor of the 51 cm x 71 cm tunnel with the short extension in position.
The power spectral density is non dimensionalised using the mean square of
the fluctuating velocity. It can be seen from the figure that the power
spectrum can be represented by a smooth curve to within experimental
error. Most of the spectra presented in this section are drawn in the form
of smooth curves for the sake of clarity. However it should be remembered
that the measured spectra are of the type shown in figure 3.7.1.

Figure 3.7.2a shows the horseshoe vortex spectra upstream of the 6.35
diameter circular cylinder at two different speeds with the long extension
to the working section in position. Also on this figure are shown the
boundary layer spectra at the model position with the model absent, meas-
ured at the same height above the wind tunnel floor and at the same flow
velocities as the horseshoe vortex spectra.

Figure 3.7.2b shows similar vortex and boundary layer spectra at two
different flow velocities with the short extension to the working section
in position. Figure 3.7.2c shows similar spectra with the cylinder mounted
on the false floor, at one flow velocity.

It can be seen from this figure that at any one set of flow conditions
the horseshoe vortex spectra and boundary layer spectra without the model
in position are very similar. Thus one can conclude that the distribution
of turbulent energy with frequency within horseshoe vortex systems is
determined by the energy distribution in the upstream boundary. However
it should be noted that within horseshoe vortex systems the actual turb-
ulence intensity ($\frac{\sqrt{\overline{u'^2}}}{u}$) was found to be in the region of 0.40, while

within the undisturbed boundary layer, at the same value of $\frac{y}{D}$, $\frac{\sqrt{\overline{u'^2}}}{u}$ was found to be in the region of 0.10-0.15. (Here u is the local streamwise velocity, not the free stream velocity).

The effect of a change in the flow conditions can also be seen in figures 3.7.2a and b. As the flow velocity increases (i.e. as $\frac{UD}{\nu}$ and $\frac{D}{\delta^*}$ increase) it can be seen that at the low frequency end of these spectra the power spectral density decreases, while at the high frequency end, the power spectral density increases. This one would expect since as the flow speed increases the frequencies associated with the large energy carrying turbulence structures within the upstream boundary layer must also increase, and hence energy must be transferred from the low frequency range of these spectra to the high frequency range.

The effect of a change in $\frac{D}{\delta^*}$ on the vortex spectra can be seen in figure 3.7.3 where the three high velocity vortex spectra of figure 3.7.2 are compared. It can be seen that the horseshoe vortex spectrum with the model mounted on the false floor (at $\frac{D}{\delta^*}$ = 30.5) contains less energy at low frequencies and more at high frequencies than the other two spectra (at $\frac{D}{\delta^*}$ = 9.6 and 6.6). As δ^* decreases (and $\frac{D}{\delta^*}$ increases) the large energy carrying eddies within the boundary layer upstream of the vortex system become smaller and hence the frequencies associated with them become larger. Thus one would expect this transfer of energy to the high frequencies within the upstream boundary layer, and therefore also within the vortex systems.

Figure 3.7.4 shows the spectra of the horseshoe vortices upstream of three different models; the 6.35 cm diameter cylinder, the cylinder with splitter plate, and the streamlined model. It can be seen that there is little difference between the spectra. The wake spectra of these three models are shown in figure 3.7.5. They can be seen to differ significantly, the spectrum of the cylinder wake showing a well defined peak at the vortex shedding frequency, while the other spectra do not show such well defined

peaks. Thus it can be concluded that the wake flow of the models does not affect the spectra of velocity fluctuations within the horseshoe vortex system.

No regular horseshoe vortex oscillations have been observed for the turbulent vortex systems considered here. However oscillations have been observed by Roper (1967) (section 3.1.1) at flow conditions similar to those of the present experiments (figure 3.2.5). The cause of this discrepancy is unknown but it may be that the boundary layer upstream of the cylinder used by Roper was not fully turbulent and the oscillations he observed were in fact laminar horseshoe vortex oscillations.

CHAPTER 4

Scour around obstacles in an erodible bed

4.1 Introduction

Two flow mechanisms are responsible for the formation of scour holes around the bases of obstacles, such as bridge piers, set in an erodible river bed.

(a) The contraction of the flow channel formed by adjacent piers causes an increase in the flow velocity between the piers.

(b) The adverse pressure gradient ahead of a pier causes separation of the oncoming shear flow from the bed, and causes part of it to roll up and form a horseshoe vortex, wrapped around the front of the pier and trailing downstream on both sides. When the bed is erodible the high shear stresses under such a vortex cause a scour hole to be formed at the base of the pier.

Two types of scour can be identified:-

(a) clear water scour, where movement of sediment only takes place in the vicinity of the bridge piers. An equilibrium depth of scour is reached when the shear stresses on the boundary of the scour hole fall below the value needed for movement of sediment;

(b) scour with continuous sediment motion, where the whole river bed is in motion. In this case the equilibrium depth of scour is reached when the inflow of sediment into the scour hole is equal to the outflow of sediment from the scour hole.

In this chapter the scour holes formed around isolated cylinders on a flat bed of sand will be considered. That is to say the horseshoe vortex system will be considered to be the only mechanism of scour.

4.2 Dimensional analysis

For a fully developed channel flow one may write the functional

relationship

$$\bar{u} = fn\left(\tau, d_s, h, \rho, \nu\right)$$

where $\bar{u}$ is the mean channel velocity, τ is the bed shear stress, d_s is the roughness size (which is assumed to be equal to the median grain diameter), h is the water depth, ρ is the water density and ν is the kinematic viscosity of the water. Thus non-dimensionalizing

$$\frac{\bar{u}}{u_*} = fn\left(\frac{u_* d_s}{\nu}, \frac{h}{d_s}\right) \tag{4.2.1}$$

where $u_* \left(= \left(\frac{\tau}{\rho}\right)^{\frac{1}{2}}\right)$ is the friction velocity.

In what follows it will be assumed that the flow is a fully developed channel flow with a velocity distribution (outside the laminar sub-layer) given by

$$\frac{u}{u_*} = 2 \cdot 5 \ln\left(\frac{y}{d_s}\right) + B \tag{4.2.2}$$

where u is the mean velocity at a distance y above the bed and B is given by

$$B = fn\left(\frac{u_* d_s}{\nu}\right)$$

For scour around a cylinder in an erodible bed consisting of a non-cohesive bed material, due to a fully developed channel flow, one may write the functional relationship

$$d = fn\left(\bar{u}, h, \nu, \rho_s, \rho, (\rho_s - \rho)g, d_s, D, t\right) \tag{4.2.3}$$

where d is the maximum scour depth in the scour hole at time t, ρ_s is the sediment density and D is the cylinder diameter. (The inclusion of g only in the combination $(\rho_s - \rho)g$ implicitly assumes that the flow is deep enough for free surface effects to be insignificant.)

Now it follows from equation (4.2.1) that u_* is determined if $\bar{u}$, h, d_s, and ν are specified. Therefore if one assumes a logarithmic velocity distribution it follows from equation (4.2.2) that the velocity profile in the channel is determined if $\bar{u}, h, d_s$ and ν (and therefore u_*) are specified. Therefore no other velocity profile parameters are

included in equation (4.2.3). Also no parameters which describe the turbulence characteristics of the flow are included, it being assumed that any variations in the turbulence that might occur will not significantly affect the scour depth. This will not be the case when a large amount of sediment is carried into the scour hole in suspension. Then one would expect that the upstream turbulence distribution must affect the overall sediment distribution within the flow and hence must affect the scouring process. So the following dimensional analysis will not apply when the upstream flow carries a large amount of suspended sediment.

Non-dimensionalizing equation (4.2.3)

$$\frac{d}{D} = fn\left(N, \frac{h}{d_s}, \frac{\bar{U}d_s}{\nu}, \frac{D}{h}, T, \frac{\rho_s}{\rho}\right) \qquad (4.2.4)$$

where $N = \dfrac{\bar{U}}{\left[\left\{\left(\frac{\rho_s}{\rho}\right)-1\right\}g\,d_s\right]^{1/2}}$

$$T = \frac{\left\{\left(\frac{\rho_s}{\rho}\right)-1\right\}g\,t}{\bar{U}}$$

Now consider the dimensionless group $\dfrac{\bar{U}d_s}{\nu}$, the Reynolds number based on mean flow velocity and sediment size. This may be replaced by the group $\dfrac{u_* d_s}{\nu}$ since from equation (4.2.1) it follows that

$$\frac{u_* d_s}{\nu} = fn\left(\frac{\bar{U}}{u_*}, \frac{h}{d_s}\right)$$

$$= fn\left[\frac{\left(\frac{\bar{U}d_s}{\nu}\right)}{\left(\frac{u_* d_s}{\nu}\right)}, \frac{h}{d_s}\right]$$

which gives

$$\frac{u_* d_s}{\nu} = fn\left[\frac{\bar{U}d_s}{\nu}, \frac{h}{d_s}\right]$$

Now consider steady state conditions when $d = d_e$ the equilibrium scour depth. The dimensionless group that characterizes the time development of scour can be neglected i.e. the group T. Now most natural river beds are composed of sand and gravel for which $\dfrac{\rho_s}{\rho}$ is constant

and equal to 2.65. Thus this group can be neglected as long as any experiments that are carried out use sand as a bed material.

So equation (4.2.4) becomes

$$\frac{d_e}{D} = fn\left(N, \frac{h}{d_s}, \frac{u_* d_s}{\nu}, \frac{D}{h}\right) \tag{4.2.5}$$

Now the flow upstream of the obstacle may be one of three types

(a) $\qquad \frac{u_* d_s}{\nu} < 5$: hydraulically smooth

(b) $\qquad 5 < \frac{u_* d_s}{\nu} < 70$: transitional

(c) $\qquad 70 < \frac{u_* d_s}{\nu}$ $\qquad$: fully rough.

If the flow is of type (c) then viscosity (and hence $\frac{u_* d_s}{\nu}$) will cease to be important. (The velocity profile upstream of the cylinder will in this case be determined by N and $\frac{h}{d_s}$, and B in equation (4.2.2) becomes a constant. Since the form of this velocity profile determines the nature of the horseshoe vortex system, viscosity (and hence $\frac{u_* d_s}{\nu}$) will cease to influence the nature of the horseshoe vortex system.) Thus for flows of type (c) $\frac{u_* d_s}{\nu}$ ceases to be an important variable and

$$\frac{d_e}{D} = fn\left(N, \frac{h}{d_s}, \frac{D}{h}\right) \tag{4.2.6}$$

(In neglecting $\frac{u_* d_s}{\nu}$ the group $\frac{\bar{U} D}{\nu}$ which is still included implicitly in equation (4.2.5) has also been neglected. Thus equation (4.2.6) can only apply when a change in $\frac{\bar{U} D}{\nu}$ does not cause a fundamental change in the flow pattern around the cylinder. Thus, for example, if a change in $\frac{\bar{U} D}{\nu}$ causes the boundary layer on the cylinder surface away from the bed to change from laminar to turbulent at its point of separation (with a consequent change in the extent of the wake and the flow pattern around the cylinder) then it is not justifiable to neglect $\frac{\bar{U} D}{\nu}$ or $\frac{u_* d_s}{\nu}$).

Now the significance of the group N will be considered. This group determines the type of scour that will occur. For $N < N_o$(say), the

and equal to 2.65. Thus this group can be neglected as long as any experiments that are carried out use sand as a bed material.

So equation (4.2.4) becomes

$$\frac{d_e}{D} = fn\left(N, \frac{h}{d_s}, \frac{u_* d_s}{\nu} \cdot \frac{D}{h}\right)$$

(4.2.5)

Now the flow upstream of the obstacle may be one of three types

(a) $\quad\quad \frac{u_* d_s}{\nu} < 5$: hydraulically smooth

(b) $\quad 5 < \frac{u_* d_s}{\nu} < 70$: transitional

(c) $\quad 70 < \frac{u_* d_s}{\nu} \quad\quad$: fully rough.

If the flow is of type (c) then viscosity (and hence $\frac{u_* d_s}{\nu}$) will cease to be important. (The velocity profile upstream of the cylinder will in this case be determined by N and $\frac{h}{d_s}$, and B in equation (4.2.2) becomes a constant. Since the form of this velocity profile determines the nature of the horseshoe vortex system, viscosity (and hence $\frac{u_* d_s}{\nu}$) will cease to influence the nature of the horseshoe vortex system.) Thus for flows of type (c) $\frac{u_* d_s}{\nu}$ ceases to be an important variable and

$$\frac{d_e}{D} = fn\left(N, \frac{h}{d_s}, \frac{D}{h}\right)$$

(4.2.6)

(In neglecting $\frac{u_* d_s}{\nu}$ the group $\frac{\bar{U} D}{\nu}$ which is still included implicitly in equation (4.2.5) has also been neglected. Thus equation (4.2.6) can only apply when a change in $\frac{\bar{U} D}{\nu}$ does not cause a fundamental change in the flow pattern around the cylinder. Thus, for example, if a change in $\frac{\bar{U} D}{\nu}$ causes the boundary layer on the cylinder surface away from the bed to change from laminar to turbulent at its point of separation (with a consequent change in the extent of the wake and the flow pattern around the cylinder) then it is not justifiable to neglect $\frac{\bar{U} D}{\nu}$ or $\frac{u_* d_s}{\nu}$).

Now the significance of the group N will be considered. This group determines the type of scour that will occur. For $N < N_o$(say), the

shear stresses underneath the horseshoe vortex system are not large enough to cause sediment to be moved and no scour occurs. If $N_o < N < N_c$, where N_c is the value of N for which general sediment motion begins on the bed upstream of the cylinder, then clear water scour will occur. If $N_c < N$ then scour with continuous sediment motion will occur.

The relative importance of the group N in clear water scour and scour with continuous sediment motion can be deduced in the following way. Suppose a scour hole in equilibrium exists and the conditions are such that clear water scour occurs. If the flow velocity $\bar{U}$ is increased slightly (by $\Delta \bar{U}$, say) the horseshoe vortex system within the scour hole becomes more able to transport sediment (since faster moving fluid feeds into the vortex system) and hence the scour hole becomes deeper (by $\left(\Delta d_e \right)$, say). Now suppose a scour hole in equilibrium exists and the conditions are such that scour with continuous sediment motion occurs. If the flow velocity is again increased by $\Delta \bar{U}$, the horseshoe vortex system within the scour hole will again be able to transport more sediment out of the scour hole, but now more sediment will be moving into the scour hole due to the increased capacity of the upstream flow to transport sediment. So if the scour depth changes by $\left(\Delta d_e \right)'$, then it seems likely that

$$\left(\Delta d_e \right)' < \left(\Delta d_e \right)$$

So it would seem the variations in $\bar{U}$ (and hence in N) cause larger variations in d_e (and hence in $\dfrac{d_e}{D}$) in clear water scour than in scour with continuous sediment motion.

Now the significance of the dimensionless group $\dfrac{D}{h}$ will be considered. As $\dfrac{D}{h}$ becomes 'large' one would expect that the shear stress beneath the horseshoe vortex would tend to decrease since the flow becomes similar to the flow in a confined jet impinging upon a wall mounted perpendicular to the jet axis. In such a case a closed separation bubble is formed at the base of the wall. The flow within such a closed separation bubble is very much less vigorous than within the "open" separated flow of

a horseshoe vortex system, into which fluid is continually flowing. Hence one would expect that the bed shear stresses beneath a closed separation bubble will be very much lower than beneath an "open" horseshoe vortex system. Thus one would expect the scour depth beneath the horseshoe vortex system to decrease as $\frac{D}{h}$ becomes large. Indeed the results of Carstens and Sharma (1975) show this to be the case, since for $\frac{D}{h} = 2.94$, they found that the deepest scour occurred behind the cylinder due to scouring by vortices in the cylinder wake, and there was little scour in front of the cylinder. Also if $\frac{D}{h}$ is "small", and hence h is relatively large, one would expect that variations in h would cease to influence the flow near the bed. Hence variations in $\frac{D}{h}$ would cease to be important. Thus one would expect that $\frac{D}{h}$ would only be an important variable if it were neither "large" or "small" but what values of $\frac{D}{h}$ correspond to "large" and "small" is not known.

The scour depth at any time t is given by equation (4.2.4) while the equilibrium scour depth is given by equation (4.2.5). From these two functional relationships

$$\frac{d}{d_e} = fn\left(N, \frac{h}{d_s}, \frac{u_* d_s}{\nu}, \frac{D}{h}, T\right) \qquad (4.2.7)$$

where the dimensionless ratio $\frac{\rho_s}{\rho}$ has been assumed constant and has therefore been neglected. Equation (4.2.7) applies when the flow upstream of the cylinder is either hydraulically smooth or transitional. If the upstream flow is fully rough then $\frac{u_* d_s}{\nu}$ ceases to be important (provided changes in $\frac{\bar{u} D}{\nu}$ do not change the flow pattern fundamentally). So equation (4.2.7) becomes

$$\frac{d}{d_e} = fn\left(N, \frac{h}{d_s}, \frac{D}{h}, T\right) \qquad (4.2.8)$$

At this point it should be pointed out that for experimental work it is often convenient to replace $\frac{u_* d_s}{\nu}$ by the group G, where

$$G = \left\{\left(\frac{\rho_s}{\rho}\right) - 1\right\} g\, d_s^3 \Big/ \nu^2$$

Now
$$G = \left\{ \left(\frac{u_* d_s}{\nu} \right)^2 \Big/ N^2 \right\} \cdot \left(\frac{\bar{U}}{u_*} \right)^2$$

$$G = fn \left(N, \frac{u_* d_s}{\nu}, \frac{h}{d_s} \right) \tag{4.2.9}$$

So it is justifiable to consider this group instead of $\frac{u_* d_s}{\nu}$ in any of the functional expressions derived above. This group reflects the influence of viscosity in very much the same way as $\frac{u_* d_s}{\nu}$. For small values of this group (<1500, approximately) the flow is hydraulically smooth. For $G > 4 \times 10^4$, the flow is hydraulically rough. Thus when $G > 4 \times 10^4$ one would expect it to become unimportant in a similar manner to $\frac{u_* d_s}{\nu}$.

4.3 Literature review

4.3.1 Experimental investigations

Many experimental investigations of the subject of scour around bridge piers have been carried out and reviews have been presented by Breusers et al. (1977) and Melville (1975). Here some of the previous investigations will be considered in the light of the dimensional analysis of section 4.2.

Shen et al. (1969) attempt to correlate maximum depth of scour with $\frac{\bar{U} D}{\nu}$ and produce the formula

$$d_e = 0.00073 \left(\frac{\bar{U} D}{\nu} \right)^{0.619} feet \tag{4.3.1}$$

If this formula is compared with equations (4.2.5) and (4.2.6) it can be seen that it is at least inadequate and for some types of flow completely invalid. The dimensional nature of the left-hand side of equation (4.3.1) is also very unsatisfactory.

Nicollet and Ramette (1971) conducted experiments on the basis of the functional expression

$$\frac{d_e}{D} = fn \left(\frac{\bar{U} d_s}{\nu}, \frac{D}{d_s} \right) \tag{4.3.2}$$

which the dimensional analysis of the previous section shows to be inadequate.

Leclerc (1971) used the functional expression

$$\frac{d_e}{D} = fn\left(\frac{u_* d_s}{\nu}\right) \qquad (4.3.3)$$

and found that the water depth h was not an important variable. However this was because at the test position in the flume that was used, the flow was not fully developed and any change in h did not change the boundary layer thickness at the test position (and hence the horseshoe vortex system was unaffected). Several previous experimenters have made this error.

Hancu (1971) used the expression

$$d_e = fn\left(\bar{u}, \bar{u}_c, D, g\right) \qquad (4.3.4)$$

which although inadequate is of interest since it appears to be the first time that the variable $\bar{u}_c$ (the value of $\bar{u}$ at which scour with continuous sediment transport starts) was introduced. Bonosoundas (1973) also used this variable. Firstly he wrote

$$d_e = fn\left(\rho, \nu, d_s, \rho_s, (\rho_s - \rho)g, \bar{u}, h, D, g, t\right)$$

Non-dimensionalizing he obtained

$$\frac{d_e}{D} = fn\left(\frac{\bar{u}^2}{\left[\left(\frac{\rho_s}{\rho}\right)-1\right]g d_s}, \frac{d_s}{h}, \frac{\bar{u} d_s}{\nu}, \frac{gD}{\bar{u}^2}, \frac{D}{d_s}, \frac{\bar{u}t}{D}\right)$$

Bonosoundas' dimensional analysis is interesting but several criticisms can be made. Firstly one of the variables $\rho_s, \rho, g, (\rho_s - \rho)g$ is redundant since the fourth is a function of the first three. Secondly in non-dimensionalizing, ten independent variables result in six dimensionless groups, instead of the seven predicted by the theory of dimensional analysis.

From a formula by Velikanow, Bonosoundas then wrote

$$\frac{\bar{u}}{\bar{u}_c} = fn\left(\frac{\bar{u}^2}{\left[\left(\frac{\rho_s}{\rho}\right)-1\right]g d_s}, \frac{h}{d_s}\right)$$

He then made the mistake of replacing both $\dfrac{\bar{u}^2}{\left[\left(\frac{\rho_s}{\rho}\right)-1\right]g d_s}$

and $\frac{h}{d_s}$ by $\frac{\bar{u}}{\bar{u}_c}$ in the functional expression, whereas it is only justifiable to replace one of the groups by $\frac{\bar{u}}{\bar{u}_c}$.

Bonsoundas then neglected $\frac{\bar{u}t}{D}$, thereby limiting the analysis to the derivation of an expression for ultimate depth of scour only. He also neglected $\frac{\bar{u}d_s}{\nu}$ without stating when this assumption applies. He also neglected the group $\frac{\bar{u}^2}{gD}$ which is justifiable since

$$\frac{\bar{u}^2}{gd_s} = fn\left(\bar{u}^2 \middle/ \left[\left(\frac{\rho_s}{\rho}\right) - 1\right] gd_s , \frac{D}{d_s} , \frac{\rho_s}{\rho}\right)$$

But he did not make this clear. Finally replacing $\frac{D}{d_s}$ by $\frac{D}{h}$ (which is not justifiable unless $\frac{h}{d_s}$ is included in the functional expression since

$$\frac{D}{d_s} = fn\left(\frac{D}{h} , \frac{h}{d_s}\right)$$

he obtained

$$\frac{d_e}{D} = fn\left(\frac{\bar{u}_c}{\bar{u}} , \frac{D}{h}\right) \tag{4.3.5}$$

So although equation (4.3.5) appears to be more simple than equations (4.2.5) and (4.2.6), and the dimensional analysis seems complete, there are several vital flaws in the argument.

Many formulae have been produced by Indian researchers which claim to relate the ultimate scour depth to the various dimensionless groups. These are reviewed by Henderson (1966). Among them are the formulae

$$\frac{h}{D} + \frac{d_e}{D} = 1\cdot8\left(\frac{h}{D}\right)^{0.75} \tag{4.3.6}$$

$$\frac{h}{D} + \frac{d_e}{D} = 4\cdot2\left(\frac{h}{D}\right)^{0.78} \cdot \frac{\bar{u}}{\sqrt{gh}} \tag{4.3.7}$$

which can be seen to be inadequate.

Perhaps the only previous experimental results that are systematic enough to enable them to be plotted in the form suggested by the dimensional analysis are those of Chabert and Engeldinger (1956). This is done in section 4.6.

Finally mention must be made of several other interesting investigations of particular aspects of this subject. Laursen (1960), (1963), al-

though not stating so explicitly assumes that the contraction mechanism of scour described in section 4.1 is the dominant one and does not discuss the role of horseshoe vortex systems. He presented theoretical analyses and experimental results for both clear water scour and scour with continuous sediment motion. For the latter he gave the formula

$$\frac{d_e}{D} = 1.5 \left(\frac{D}{h}\right)^{-0.3} \tag{4.3.8}$$

White (1975) carried out experiments at Froude numbers between 0.8 and 1.2 for several different obstacle shapes and compared the results with several of the above formulae.

Carstens and Sharma (1975) carried out experiments in a flow with a large value of $\frac{D}{h}$ and the scour upstream of the cylinder was found to be less than the scour downstream of the cylinder caused by wake vortices.

Nicollet (1975) carried out a limited series of experiments to study scour around cylinders in a bed of cohesive material. The observed scour holes were of approximately the same size as those in a bed of non-cohesive material but were more "ragged" in appearance.

Finally mention must be made of the extensive experiments of Melville (1975). He did not attempt to find how the scour depth varied with the flow parameters but studied the flow in preformed concrete scour holes in an attempt to gain an understanding of the flow. These scour holes were models of the holes that Melville had observed around cylinders in a bed of sand. A photograph of a scour hole typical of those he observed is reproduced in figure 4.3.1, together with a sketch of a longitudinal section through the scour hole. He observed that the upstream slope of the scour hole was at an angle to the horizontal equal to the angle of repose of the sediment, except in a region close to the base of the cylinder (figure 4.3.1b). Scouring took place in this region. A heap of deposited sediment was observed in the wake of the cylinder.

In the preformed scour holes he measured mean velocities, turbulence

intensities and spectra, and surface shear stresses. However to make these measurements he used hot film anemometers and preston tubes. The effect of these probes on the complex three dimensional separated flow within the scour holes is unknown, and these results can at best only be regarded as qualitative. However the turbulence spectra measured by Melville within a vortex system upstream of a cylinder on a flat bed are very similar to those described in section 3.7. Melville also made detailed observations of the formation of scour holes and carried out flow visualization of the horseshoe vortex system using both dye and hydrogen bubble visualization techniques.

4.3.2 Theoretical investigations

Because of the complex nature of the scouring problem theoretical investigations have proved to be difficult to conduct. However two interesting attempts have been made.

Carstens (1966) applied the sediment pickup function of Le Feuvre (1966) to this problem. This must be a somewhat dubious assumption in view of the fact that the flow geometry studied by Le Feuvre (water flowing over a preformed isolated scour hole) is very different from the flow around the base of bridge piers. He then applied this function to some results of Chabert and Engeldinger (1956) and obtained the formula

$$\frac{d_e}{D} = 0.546 \left(\frac{N^2 - 1.64}{N^2 - 5.02} \right)^{5/6} \tag{4.3.9}$$

Grodowozyk et al. (1968) analyse scour around a cylindrical obstacle by using the shallow water hypothesis and solving numerically the linearized shallow water equations using the method of characteristics. The results compare reasonably well with experimental results although the authors admit that this analysis does not take into account the horseshoe vortex system, but assumes that scour is caused by a perturbation in the velocity field.

4.4 Experimental apparatus and procedure

The experimental results described in this chapter were obtained in the sediment transport flume at Cambridge University Geology Department. The flume has a working section 5 m long by 0.3 m wide and tests were carried out at a point 4.5 m from the start of the working section (figure 4.4.1).

The surface flow velocity in the flume, U, was measured by timing a small piece of plastic as it floated down a 2 m length of the flume. The mean velocity profiles at the working point in the flume were measured using a pitot tube and an inclined tube manometer. Although this proved to be rather inaccurate at the lower velocities there was no other method readily available. Some typical velocity profiles are shown in figure 4.4.2 in the form of a "Clauser plot". It can be seen that away from the bed $\frac{u}{U}$ increases linearly with $\frac{Uy}{\nu}$, showing that the logarithmic velocity distribution is valid. The "Clauser plot" enables the ratio $\frac{U}{u_*}$ to be calculated since

$$\frac{U}{u_*} = \left(\frac{2}{C_f}\right)^{\frac{1}{2}}$$

where C_f , the skin friction, is taken from the Clauser plot. This ratio was required to calculate values of $\frac{u_* d_s}{\nu}$. These calculated values showed that in nearly all the tests carried out in the flume, the flow was hydraulically smooth.

Once U and u_* were known the mean channel velocity $\bar{U}$ could be calculated from the equation

$$\frac{\bar{U}}{u_*} = \frac{U}{u_*} - 2.5$$

(Yalin (1972)), which is obtained by an integration of the logarithmic velocity distribution (equation 4.2.2).

The four cylinders around which the scour depth was measured had diameters of 1.27 cm, 2.54 cm, 3.81 cm and 5.08 cm. The Reynolds numbers based on the cylinder diameters ($\frac{UD}{\nu}$) were between 10^3 and 2.5×10^4.

As $\dfrac{\bar{U}D}{\nu}$ rises above approximately 2×10^5 the boundary layer on the cylinder surface changes from being laminar to turbulent at its point of separation. Thus for these experiments the boundary layer on the cylinder is laminar at separation.

Tests were carried out using sand of median diameter 0.45 mm (giving a nominal value of G of 1.47×10^3) and at nominal water depths of 5.5 cm and 11.0 cm (giving values of $\dfrac{h}{d_s}$ of 120 and 240 and values of $\dfrac{D}{h}$ between 0.12 and 0.92). The form of the scour hole was similar to that observed by previous investigators, and the maximum scour depth (d) was seen to occur on the upstream stagnation line of the cylinder. (For the tests where there was general sediment motion, the equilibrium scour depth was arbitrarily defined as the maximum scour depth observed. This is because the scour depth varies by up to 10% as bed forms more through the scour hole.

In practice the flow in rivers can be either hydraulically smooth, transitional or fully rough. Thus the value of G given above (which corresponds to a flow that is hydraulically smooth) does correspond to a practical case. Values of G which correspond to transitional and fully turbulent flows occurred in the experiments of Chabert and Engeldinger (1956) which are discussed in section 4.6. The range of $\dfrac{D}{h}$ for these experiments also corresponds to the range that one would expect to meet in practice. However the values of $\dfrac{h}{d_s}$ (120 and 240) are somewhat lower than one would expect to meet in a practical situation. However for the experiments of Chabert and Engeldinger (1956), $\dfrac{h}{d_s}$ has higher and more realistic values (up to 1400).

4.5 Experimental results and discussion

4.5.1 Description of the scouring process

All the scour holes that were observed were similar to those observed by Melville (1975) (figure 4.3.1). The deepest scour was seen to occur on the front stagnation line of the cylinder, and this depth will

from now on be referred to as the scour depth, and its maximum value as the equilibrium scour depth. Measurements showed that the upstream slope of the scour hole was at an angle close to the angle of repose of the sand (30°) except for a small region close to the cylinder. This region is where the horseshoe vortex system lies and scouring takes place in this region. During the scouring process sand is picked up by the horseshoe vortex system in this region and is carried around the cylinder and deposited in the wake. Thus a pile of sand forms there. More sand then slips down the upstream surface of the scour hole into the horseshoe vortex system and the scour hole continues to grow until, for clear water scour, the shear stress beneath the horseshoe vortex system falls to such a value that it cannot remove any sediment, or, for scour with continuous sediment motion, the inflow of sediment into the scour hole equals the outflow of sediment.

It appears that the extent of the scour hole upstream of the cylinder is not directly related to the original length of the separated region upstream of the cylinder. This is because once scour has begun the extent of the scour hole is determined by the slope of the upstream face, which is in turn dependent upon the angle of repose of the sediment, and not upon the original length of the separated region.

4.5.2 Equilibrium depth of scour

Figures 4.5.1(a) and (b) show $\frac{d_e}{D}$ plotted against N with $\frac{D}{h}$ as parameter, for the two values of $\frac{h}{d_s}$. It can be seen that there are three distinct ranges of N

(a) $N < N_o$ (from figure 4.5.1(a), $N_o \doteq 1.9$; from figure 4.5.1(b),

$N_o \doteq 1.9$). No sediment motion was observed in the flume.

(b) $N_o < N < N_c$ (from figure 4.5.1(a), $N_c \doteq 3.1$, from figure 4.5.1(b),

$N_c \doteq 3.0$). The experimental results lie on a straight line for

all values of $\frac{D}{h}$. Upstream of the cylinders scour was only ob-

served close to the cylinders, so this region corresponds to clear

water scour.

(c) $N > N_c$. The experimental results cease to show any variation with N , but do vary with $\dfrac{D}{h}$. As $\dfrac{D}{h}$ increases, $\dfrac{d_e}{D}$ decreases. Sediment motion was observed over the entire bed, so this region corresponds to scour with continuous sediment motion.

First of all the clear water scour region will be considered. From figure 4.5.1(a) for $\dfrac{h}{d_s} = 240$

$$\frac{d_e}{D} = 1.2\,N - 2.2 \tag{4.5.1}$$

From figure 4.5.1(b) for $\dfrac{h}{d_s} = 120$

$$\frac{d_e}{D} = N - 1.9 \tag{4.5.2}$$

The small difference between these equations is some measure of the effect of the group $\dfrac{h}{d_s}$ on $\dfrac{d_e}{D}$. This effect can be seen to be slight.

As $\dfrac{D}{h}$ increases one would expect the shear stress beneath the horseshoe vortex system to decrease and hence the equilibrium scour depth should decrease. This appears to be the case in the region of scour with continuous sediment motion, but not in the region of clear water scour. The arguments of section 4.2 also lead one to expect that for scour with continuous sediment motion the scour depth should depend upon N less than in clear water scour. This can be seen to be true from figures 4.5.1(a) and 4.5.1(b) where $\dfrac{d_e}{D}$ shows little variation with N in the region of scour with continuous sediment motion.

In figure 4.5.1(c) $\dfrac{d_e}{D}$ is plotted against $\dfrac{D}{h}$ in the region of scour with continuous sediment motion for $\dfrac{h}{d_s} = 240$. The experimental points lie about the line

$$\frac{d_e}{D} = 1.0 \left(\frac{D}{h} \right)^{-0.18} \tag{4.5.3}$$

It was not possible to draw a similar graph for $\dfrac{h}{d_s} = 120$, since there are few experimental results in the region of scour with continuous

sediment motion, for this value of $\dfrac{h}{d_s}$ (figure 4.5.1b).

4.5.3 Time development of scour

Figures 4.5.2a to c show the development of the scour depth with time. It can be seen from these figures that clear water scour develops more slowly than scour with continuous sediment motion. As N increases it appears that the rate of development of clear water scour slows down, but the rate of development of scour with continuous sediment motion increases. Thus the type of scour that takes longest to develop occurs when N has a value just below N_c i.e. when general sediment motion is almost taking place.

No great difference can be seen between figures 4.5.2(a) to (c) so it would seem that $\dfrac{D}{h}$ does not significantly affect the rate of development of scour   (at least for $0.24 < \dfrac{D}{h} < 0.48$).

4.5.4 Dye flow visualization

The horseshoe vortex upstream of a 5.08 cm diameter cylinder was observed by introducing dye into the flow upstream of the cylinder and the flow patterns that were seen are sketched in figure 4.5.3. No difference in flow patterns was observed with or without general sediment motion. Two vortices rotating in the same direction were observed both at the start and end of the scouring process. This implies that a counterrotating vortex must exist between them, but this was not observed.

It is interesting to note that water from all levels of the upstream flow feeds these vortex systems, so that it was possible to see a filament of dye, that was introduced into the flow near the surface, pass down the upstream face of the cylinder into the vortex system. Also when the scour hole was fully developed the vortex systems were still fed from all levels of the upstream flow.

4.6 Comparison with the results of Chabert and Engeldinger (1956)

When a search of the literature was being made, it became apparent

that most previous experimental investigations were carried out in such a way that it is impossible to plot the results in a way similar to figures 4.5.1(a) and (b) because two or more dimensionless groups were varied simultaneously. However the results of Chabert and Engeldinger (1956) for scour around circular cylindrical piers in a bed of sand are ideally suited to be plotted in such a way.

For these tests $\frac{UD}{\nu}$ varied between approximately 6×10^4 and 2×10^5. Thus for most tests one would expect the boundary layer on the cylinder surface to be laminar at its separation point, but for the higher Reynolds numbers the boundary layer at this point may be turbulent, and the flow pattern around the cylinder may be changed substantially. (Since the boundary layer on full scale bridge piers is invariably turbulent at the separation point, future experimenters using small scale models should artificially 'trip' the boundary layer on the cylinder surface to obtain flow patterns similar to those around full scale bridge piers.

Figures 4.6.1a and b show $\frac{d_e}{D}$ plotted against N at constant $\frac{D}{h}$, for two different values of $\frac{h}{d_s}$ with G kept constant throughout. It can be seen that these figures have the same form as figures 4.5.1(a) and (b). For clear water scour figure 4.6.1a gives

$$\frac{d_e}{D} = 0.97N - 1.3 \tag{4.6.1}$$

when $\frac{h}{D} = 66.7$, and figure 4.6.1b gives

$$\frac{d_e}{D} = 1.03N - 1.3 \tag{4.6.2}$$

when $\frac{h}{D} = 33.3$. It can be seen that N_o is significantly less than in the author's own experiments, presumably because of the large difference in G. Again it can be seen that $\frac{d_e}{D}$ does not depend upon $\frac{D}{h}$ for clear water scour, for $0.25 < \frac{D}{h} < 1.5$.

Figure 4.6.1c shows the variation of $\frac{d_e}{D}$ with $\frac{D}{h}$ for scour with continuous sediment motion. For $\frac{h}{d_s} = 66.7$ the points lie about

that most previous experimental investigations were carried out in such

a way that it is impossible to plot the results in a way similar to

figures 4.5.1(a) and (b) because two or more dimensionless groups were

varied simultaneously. However the results of Chabert and Engeldinger

(1956) for scour around circular cylindrical piers in a bed of sand are

ideally suited to be plotted in such a way.

For these tests $\frac{UD}{\nu}$ varied between approximately 6×10^4 and

2×10^5. Thus for most tests one would expect the boundary layer on the

cylinder surface to be laminar at its separation point, but for the

higher Reynolds numbers the boundary layer at this point may be turbulent,

and the flow pattern around the cylinder may be changed substantially.

(Since the boundary layer on full scale bridge piers is invariably turb-

ulent at the separation point, future experimenters using small scale

models should artificially 'trip' the boundary layer on the cylinder sur-

face to obtain flow patterns similar to those around full scale bridge

piers.

Figures 4.6.1a and b show $\frac{d_e}{D}$ plotted against N at constant

$\frac{D}{h}$, for two different values of $\frac{h}{d_s}$ with G kept constant through-

out. It can be seen that these figures have the same form as figures

4.5.1(a) and (b). For clear water scour figure 4.6.1a gives

$$\frac{d_e}{D} = 0.97N - 1.3 \qquad (4.6.1)$$

when $\frac{h}{D} = 66.7$, and figure 4.6.1b gives

$$\frac{d_e}{D} = 1.03N - 1.3 \qquad (4.6.2)$$

when $\frac{h}{D} = 33.3$. It can be seen that N_o is significantly less

than in the author's own experiments, presumably because of the large dif-

ference in G. Again it can be seen that $\frac{d_e}{D}$ does not depend upon

$\frac{D}{h}$ for clear water scour, for $0.25 < \frac{D}{h} < 1.5$.

Figure 4.6.1c shows the variation of $\frac{d_e}{D}$ with $\frac{D}{h}$ for scour

with continuous sediment motion. For $\frac{h}{d_s} = 66.7$ the points lie about

the line

$$\frac{de}{D} = 1.0 \left(\frac{D}{h}\right)^{-0.25} \tag{4.6.3}$$

and for $\frac{h}{D_s} = 33.3$.

$$\frac{de}{D} = 1.35 \left(\frac{D}{h}\right)^{-0.36} \tag{4.6.4}$$

It can be seen that equations (4.6.3) and (4.6.4) have the same form as equation (4.5.3) but the numerical constants differ significantly. This is perhaps not surprising when one considers the large differences in $\frac{h}{d_s}$ and G.

So it would seem that in the region of clear water scour, the equilibrium scour depth is given by

$$\frac{de}{D} = K_1 N - K_2 \tag{4.6.5}$$

where K_1 and K_2 do not depend significantly upon $\frac{D}{h}$ in the range $0.12 < \frac{D}{h} < 1.5$, but do vary as $\frac{h}{d_s}$ and G vary. In the region of scour with continuous sediment motion

$$\frac{de}{D} = K_3 \left(\frac{D}{h}\right)^{-K_4} \tag{4.6.6}$$

where K_3 and K_4 do not depend upon N (at least for $N < 6.0$) but do vary as $\frac{h}{d_s}$ and G vary.

The question now arises as to how the constants K_1, K_2, K_3 and K_4 vary with $\frac{h}{d_s}$ and G. Chabert and Engeldinger (1956) do not give very much more data for clear water scour than that shown in figure 4.6.1, so any conclusions must be made on the somewhat limited basis of equations (4.5.1), (4.5.2), (4.6.1) and (4.6.2). These equations suggest that K_1 remains approximately constant as $\frac{h}{d_s}$ and G vary, while K_2 does not vary greatly as $\frac{h}{d_s}$ varies, but appears to be dependent upon G. Obviously there is a need here for further experiments to be carried out to describe the variations of K_1 and K_2 more fully.

Chabert and Engeldinger (1956) however do give a great deal of in-

formation for scour with continuous sediment motion, over a large range of $\frac{h}{d_s}$ and G. It was possible to draw further graphs similar to figure 4.6.1(c). They were all of the same form, and the scour depth varied only slightly with N. The variations of K_3 and K_4 with $\frac{h}{d_s}$ and G are shown in figures 4.6.2(a) and (b). From figure 4.6.2(a) it can be seen that K_3 decreases as $\frac{h}{d_s}$ increases and G decreases. From figure 4.6.2(b) it can be seen that K_4 seems to be almost in-dependent of $\frac{h}{d_s}$ but increases as G decreases. Also shown in figures 4.6.2(a) and (b) are the values of K_3 and K_4 taken from equation 4.5.3. It can be seen that the value of K_3 fits well into the results of Chabert and Engeldinger, but the value of K_4 does not, being very much lower than one would expect. No explanation has been found for this. There is a need here for further experiments both to explain this discrepancy and to find values of K_3 and K_4 at values of $\frac{h}{d_s}$ and G which lie outside the range of variables covered by Chabert and Engeldinger.

It is surprising that K_4 varies with G, even when G is above 4×10^4 and the flow is hydraulically rough. One would expect any variation in G would have little effect on the scour depth when it is above this value. This is possibly a spurious effect caused by the changes in flow pattern that occur when $\frac{\bar{U}D}{\nu}$ rises above 10^5, but this is only conjecture.

Finally it should be pointed out that there are, to the author's knowledge, no published results which can be compared with the results of figure 4.5.3 for the time development of scour. There is a need for further experiments to be carried out to describe fully how the time development of scour varies with the flow parameters.

4.7 Analytical formula for scour around bridge piers

In this section an analytical formula will be derived which relates the equilibrium scour depth around a circular cylinder to the flow variables, for clear water scour.

Consider the simplest possible type of vortex system, consisting of just one vortex around a cylindrical obstacle, on a rigid bed (figure 4.7.1). Now by assuming that the flow velocity along AD can be described by potential theory and by applying the no slip condition on BC and CD it is easily shown that Γ_o, the circulation around the ABCD (proceeding in a clockwise direction), is given by

$$\Gamma_o = + U \left(x_B + \frac{D}{2}\right)^2 \Big/ x_B \qquad (4.7.1)$$

(where U is the upstream free stream flow velocity and the flow across AB is assumed to have no component of velocity perpendicular to the bed). It is shown in section 3.6 that for a turbulent horseshoe vortex system

$$\frac{x_s}{D} \simeq + 1.1 \qquad (4.7.2)$$

If we assume that x_B can be equated with x_s without any of the above assumptions being violated then Γ_o should approximate to the circulation around the horseshoe vortex on the plane of symmetry.

i.e. $$\Gamma_o = + UD \frac{0.36}{1.1} \simeq + \frac{UD}{3} \qquad (4.7.3)$$

As a scour hole forms underneath the vortex system, the system sinks into the scour hole. As the depth of scour increases, then the shear stress beneath the vortex system decreases, until at a depth d_e the shear stress is not large enough to move any sediment, for clear water scour. This is defined as the equilibrium scour depth.

The shape of the scour hole is shown schematically in figure 4.7.2. The sides of the scour hole are at an angle ϕ (the angle of repose of the sediment) to the horizontal. except for the portion of the scour

hole underneath the horseshoe vortex system (AB). Sediment is being removed from this section by the horseshoe vortex system, and is replaced by further sediment sliding down the sides of the scour hole.

Now assume that the vortex system within the scour hole may be represented by a circular forced vortex motion of radius r and maximum circulation Γ .

Then

$$\Gamma = 2\pi r v \qquad (4.7.4)$$

where v is the tangential velocity on the edge of the vortex. Assume that the radius of this vortex is given by

$$r = r_0 \left(1 + \frac{k_1 d}{D}\right) \qquad (4.7.5)$$

where r_0 is the vortex radius on a flat bed and k_1 is a constant during the scouring process. Also assume that

$$\Gamma = \Gamma_0 \qquad (4.7.6)$$

Dye flow visualisation (section 4.5.4) shows that the same portion of the upstream fluid flows into the vortex system within the scour hole, as on a flat bed. Thus the input of vorticity to the vortex system remains constant. If one assumes, as seems reasonable, that the vortex radius increases as the scour depth increases, then one would expect Γ to increase, since for a vortex tube

$$\Gamma \propto \omega r^2 \qquad (4.7.7)$$

where ω is the total vorticity of the vortex core which may be expected to remain constant as the scour depth varies. However as the scour depth increases one would expect the amount of vorticity diffusion out of the vortex system to the cylinder surface to increase since more of the cylinder surface becomes exposed. This effect will tend to decrease ω . Thus since r increases and ω decreases it seems reasonable to assume that Γ remains approximately constant, and equal to Γ_0 the circulat-

ion around the vortex on a flat bed.

From equations (4.7.3) to (4.7.6)

$$v = -\frac{uD}{6\pi r_o}\left(1 + \frac{k_1 d}{D}\right)^{-1}$$
(4.7.8)

Figure 4.7.3 shows the forces on an idealised sediment particle at the equilibrium scour depth when the particle is beneath the vortex system and just about to be moved by the flow. The flow within the vortex system applies two forces to the particle.

(a) a drag force parallel to the slope of the scour hole (F)

(b) a lift force perpendicular to the slope of the scour hole (L).

If moments are now taken about the point X when the particle is just on the point of moving up the slope then

$$W x_1 = F x_3 + L x_2$$
(4.7.9)

By trigonometry

$$x_1 = \left(\frac{d_s}{2}\right) \cos\left(60° - \alpha\right)$$

$$x_2 = \left(\frac{d_s}{2}\right) \cos 60°$$
(4.7.10)

$$x_3 = \left(\frac{d_s}{2}\right) \sin 60°$$

Thus from equations (4.7.9) and (4.7.10)

$$W \cos\left(60° - \alpha\right) = F\frac{\sqrt{3}}{2} + \frac{L}{2}$$
(4.7.11)

Now $W = \frac{\pi d_s^3}{6}(\rho_s - \rho) g$
(4.7.12)

Assume that F and L are given by the following expressions

$$F = C_D . \frac{1}{2} \rho v_e^2 . \left(\frac{\pi d_s^2}{4}\right)$$
(4.7.13)

$$L = C_L . \frac{1}{2} \rho v_e^2 . \left(\frac{\pi d_s^2}{4}\right)$$
(4.7.14)

where C_D is a drag coefficient and C_L is a lift coefficient,

V_e is the tangential vortex velocity at the equilibrium scour depth and its use here as the "characteristic" velocity for the forces on a sediment particle can only be a gross approximation. From equations (4.7.11) to (4.7.14)

$$V_e^2 = \frac{8}{3} \frac{\cos(60°-\alpha)}{(C_D\sqrt{3}+C_L)} \left(\frac{\rho_s}{\rho}-1\right) g \, d_s \tag{4.7.15}$$

Now in the part of the scour hole from which sediment is being removed, flow visualization suggests

$$30° < \alpha < 40°$$

So $\quad 0.87 < \cos(60°-\alpha) < 0.94$

Thus from now on $\cos(60°-\alpha)$ will be assumed to be approximately constant. The coefficients C_D and C_L for a particle on a slope are known to depend upon Reynolds number. In this case the appropriate Reynolds number is $\frac{V_e \, d_s}{\nu}$. If $V_e \left(\simeq \bar{u}\right) = 0.5 \text{ ms}^{-1}$, $d_s = 5 \times 10^{-4}$ and $\nu = 10^{-6}$ (which are typical values for rivers) then $\frac{V_e \, d_s}{\nu} = 250$. For this Reynolds number Coleman (1972) shows that C_D for a particle on a slope is approximately equal to 3.0 and does not vary as the Reynolds number varies between 70 and 1000. If the same can be said for C_L then one may write

$$V_e^2 = K_2\left(\frac{\rho_s}{\rho}-1\right) g \, d_s \tag{4.7.16}$$

where K_2 is a constant given by

$$K_2 = \frac{8}{3} \frac{\cos(60°-\alpha)}{C_D\sqrt{3}+C_L} \tag{4.7.17}$$

Thus if we equate the value of V_e given by (4.7.16) with that given by (4.7.8) (letting $v=V_e$ and $d=d_e$ in the latter) then we have

$$K_2\left(\frac{\rho_s}{\rho}-1\right)g \, d_s = \left\{+ \frac{U.D}{6\pi r_o} \left(1 + \frac{K_1 d_e}{D}\right)^{-1}\right\}^2 \tag{4.7.18}$$

If we let $c = \dfrac{\bar{u}}{u}$ equation (4.7.16) becomes, after some rearrangement

$$\frac{d_e}{D} = K_1 N - K_2 \qquad\qquad (4.7.19)$$

where $\qquad K_1 = \left(\dfrac{1}{6\pi k_1 k_2^{\frac{1}{2}} c}\right)\left(\dfrac{D}{r_o}\right) \qquad\qquad (4.7.20)$

and $\qquad K_2 = \dfrac{1}{k_1} \qquad\qquad\qquad\qquad (4.7.21)$

Equation (4.7.19) describes the variation of $\dfrac{d_e}{D}$ with N for clear water scour. The linear form of this equation is similar to that of equation 4.6.5, which describes the experimental results of the author and of Chabert and Engeldinger (1956).

Now consider K_1 and K_2 and their component variables $\dfrac{r_o}{D}$ k_1, k_2 and c. Strictly these quantities should be considered to be functions of all the independent variables of equation (4.2.3). So a dimensional analysis gives the result (for equilibrium scour depth around a bridge pier in a sand bed).

$$K_1, K_2 = fns\left(N, \frac{h}{d_s}, \frac{D}{h}, G\right) \qquad\qquad (4.7.22)$$

So strictly K_1 and K_2 are functions of four dimensionless groups. However now consider each of the component variables in turn.

(i) $\dfrac{r_o}{D}$ (the non-dimensional vortex radius on a flat bed) can be expected to remain constant for all flow conditions, since the dimensions of turbulent horseshoe vortex systems do not change greatly as the flow conditions change (chapter 3).

(ii) k_1 relates the vortex radius to the scour depth. At a fixed value of the scour depth d, the dimensions of the scour hole are largely controlled by the value of the angle of repose of the sediment, and not by the flow conditions. This angle of repose of the sediment in fact varies only with the sediment's size and shape (Henderson (1966)). Since the vortex radius is determined by the scour hole dimensions, for any one sediment

k_1 will be constant.

(iii) k_2 has already been shown to be approximately constant.

(iv) $c \left[= \dfrac{\bar{u}}{u} \right]$ does not change greatly as the flow conditions

vary, usually being in the range 0.85 to 0.90.

Thus for any one sediment $\dfrac{r_0}{D}$, k_1, k_2 and c can be considered to be constant and thus K_1 and K_2 can be considered constant for any one sediment. So it would appear that K_1 and K_2 are only dependent upon the sediment size and shape and thus are only dependent upon the dimensionless groups in equation (4.7.22) that contain the variable d_s (it being assumed that this variable specifies the sediment completely) i.e.

$$K_1, K_2 = fns \left(\dfrac{h}{d_s}, G \right) \tag{4.7.23}$$

which is the relationship found experimentally (section 4.5).

k_1 will be constant.

(iii) k_2 has already been shown to be approximately constant.

(iv) $c \left[= \dfrac{\bar{u}}{u} \right]$ does not change greatly as the flow conditions vary, usually being in the range 0.85 to 0.90.

Thus for any one sediment $\dfrac{r_0}{D}$, k_1 , k_2 and c can be considered to be constant and thus K_1 and K_2 can be considered constant for any one sediment. So it would appear that K_1 and K_2 are only dependent upon the sediment size and shape and thus are only dependent upon the dimensionless groups in equation (4.7.22) that contain the variable d_s (it being assumed that this variable specifies the sediment completely) i.e.

$$K_1, K_2 = fns \left(\frac{h}{d_s}, G \right) \tag{4.7.23}$$

which is the relationship found experimentally (section 4.5).

CHAPTER 5

Conclusions

5.1 <u>The horseshoe vortex formed by a separating laminar boundary layer</u>

(a) The horseshoe vortex upstream of a cylinder in a laminar boundary layer has been visualized using smoke flow visualization. Three different types of vortex system have been observed which are, with increasing $\frac{UD}{\nu}$:-

(i) steady horseshoe vortex systems with 2, 4 or 6 vortices, the number of vortices increasing as $\frac{UD}{\nu}$ increases;

(ii) horseshoe vortex systems which exhibit a regular oscillatory motion;

(iii) horseshoe vortex systems which exhibit an irregular unsteady behaviour.

(b) Pressure distributions were measured on the plane of symmetry upstream of models of various types over a wide range of flow conditions $(2000 < \frac{UD}{\nu} < 16{,}000,\ 20 < \frac{D}{\delta^*} < 70)$. Two types of pressure distribution were measured:-

(i) pressure distributions which showed minima. Flow visualization shows that such minima are at the position of the horseshoe vortex. Thus the vortex position can be determined from such pressure distributions;

(ii) pressure distributions which show no minima. Flow visualization shows that this type of pressure distribution occurs when the horseshoe vortex systems are unsteady.

(c) The variation of the position of the primary horseshoe vortex in steady vortex systems, as $\frac{UD}{\nu}$ and $\frac{D}{\delta^*}$ vary, has been presented in a graphical form. $\left|\frac{x_v}{D}\right|$ increases as $\frac{UD}{\nu}$ increases and as $\frac{D}{\delta^*}$ decreases. A theoretical analysis which predicts the position of the

separation line upstream of a circular cylinder on a plate, suggests that the horseshoe vortex position is not solely determined by this separation position but some other effect plays a part.

(d) The oscillatory behaviour of horseshoe vortex systems was found to be complex. As the Reynolds number $\left[\dfrac{UD}{\nu}\right]$ increased steady horseshoe vortex systems began to oscillate intermittently and randomly at two different frequencies. As $\dfrac{UD}{\nu}$ increased further the periods of oscillation became longer, the high frequency oscillation becoming more common. At yet higher $\dfrac{UD}{\nu}$ the oscillations became irregular and the horseshoe vortex system became turbulent. These oscillations are not caused by vortex shedding in the wake of the models or by any small disturbances within the wind tunnel. It is concluded that these oscillations are initiated by 'bursting' of the horseshoe vortices downstream of the models. The frequency of these oscillations is solely determined by the values of $\dfrac{UD}{\nu}$ and $\dfrac{D}{\delta^*}$.

(e) A theoretical solution of the equations of motion for laminar horseshoe vortex systems has been presented. Solutions are presented for the plane of symmetry region of the vortex system. In this region the solution shows that the two relevant dimensionless groups are a Reynolds number based on the vortex core radius and radial velocity at the edge of this core, and a Rossby number. If the radius of the vortex core is taken to be the radius within which the assumption of axial symmetry holds then the velocity and pressure distributions within the vortex core are shown to be Reynolds number dependent. If the radius of the vortex core is taken to be the point at which the velocity is maximum then these velocity and pressure distributions are shown to be independent of Reynolds number.

(f) The velocity distributions within steady laminar horseshoe vortex systems have been measured using smoke flow visualization. A radial flow component can be measured only in vortices 1 and 2, and appears to in-

crease linearly with the distance from the centre of the vortex, in the central region of the vortex. The experimental data was not sufficient to enable a detailed comparison to be made with the previously mentioned theoretical analysis. There was found to be little variation in the dimensionless velocity profiles, within the vortex system, as the flow speed varied, although any variation may well have been obscured by the rather large measurement errors.

(g) The skin friction coefficient beneath vortex 1 was found to have a numerical value of five times its value far upstream of the cylinder, for $\frac{UD}{\nu}$ = 2,610, $\frac{D}{\delta^*}$ = 14.8.

5.2 The horseshoe vortex formed by a separating turbulent boundary layer

(a) Oil flow visualization suggests that for the flow conditions of these experiments only four vortex systems exist (i.e. for $4000 < \frac{UD}{\nu} < 90,000$, $4 < \frac{D}{\delta^*} < 30$).

(b) Long exposure photographs of smoke flow visualization show the time mean horseshoe vortex flow pattern. Short exposure photographs show large scale turbulent structures in the boundary layer upstream of the cylinder, with their upstream edges at 40° to the flow direction. Closer to the cylinder, above the vortex system, these large scale structures are distorted and take on larger angles to the flow direction (up to 90°).

(c) Pressure distributions were measured upstream of various models and all the measured pressure distributions showed minima at what was taken to be the position of the primary horseshoe vortex. Little variation of these distributions with Reynolds number could be detected, although they do vary as $\frac{D}{\delta^*}$ varies.

(d) The variation in the position of the primary horseshoe vortex with the flow parameters has been presented graphically, as has the variation in the positions of both primary and secondary separation lines. $\left|\frac{x_v}{D}\right|$ decreases as $\frac{D}{\delta^*}$ increases. $\left|\frac{x_s}{D}\right|$ decreases as $\frac{U\delta^*}{\nu}$ increases

and $\frac{D}{\delta^*}$ increases. $\left|\frac{x_{s_1}}{D}\right|$ decreases as $\frac{u_s^*}{\nu}$ decreases and $\frac{D}{\delta^*}$ increases.

The position of the primary separation line has also been calculated using the integral method of Johnston (1960a). This method is shown not to predict well the separation position, although it does shed some light on how the observed separation positions vary with the flow parameters. In particular it shows that the primary separation position is very sensitive to changes in the upstream value of the form parameter H .

(e) The frequency spectrum of velocity fluctuations at a given height within a turbulent horseshoe vortex system appears to be very much the same as the frequency spectrum at the same height within the upstream boundary layer. The nature of the flow within the model wakes does not appear to affect these spectra.

5.3 Scour around obstacles in an erodible bed

(a) The functional expression for the ultimate scour depth caused by a horseshoe vortex system around an isolated cylinder in a sand bed is given by

$$\frac{d_e}{D} = fn\left(N, \frac{u_* d_s}{\nu}, \frac{D}{h}, \frac{h}{d_s}\right)$$

for a hydraulically smooth or transitional upstream flow. For a fully turbulent upstream flow $\frac{u_* d_s}{\nu}$ may become unimportant if changes in $\frac{\overline{u} D}{\nu}$ do not alter the flow pattern substantially.

(b) The functional expression for the rate of development of scour around such cylinders can be written as

$$\frac{d_e}{D} = fn\left(N, \frac{u_* d_s}{\nu}, \frac{D}{h}, \frac{h}{d_s}, T\right)$$

for a hydraulically smooth or transitional upstream flow, while for a fully turbulent upstream flow $\frac{u_* d_s}{\nu}$ may become unimportant.

(c) In the region of clear water scour

$$\frac{d_e}{D} = K_1 N - K_2$$

where K_1 appears to be constant and K_2 depends upon $\dfrac{h}{d_s}$ and G but not upon $\dfrac{D}{h}$.

(d) In the region of scour with continuous sediment motion

$$\frac{d_e}{D} = K_3 \left(\frac{D}{h}\right)^{-K_4}$$

where K_3 and K_4 depend upon $\dfrac{h}{d_s}$ and G but not upon N .

(e) The time development of clear water scour is less rapid than the time development of scour with continuous sediment motion.

(f) The type of scour that takes longest to develop occurs when N is just below the value needed for general sediment motion.

(h) The horseshoe vortex system is fed from all layers of the flow at all times during the scouring process.

(i) A simple theoretical analysis has been presented which accurately describes the variation of the scour depth with the flow parameters, for clear water scour.

5.4 Unresolved problems and suggestions for future work

As can be seen from the previous chapters several problems remain unresolved and further work is required.

Firstly the problem of the variation of vortex and separation positions has not been adequately resolved, for either laminar or turbulent horseshoe vortices. For laminar systems the separation and vortex positions should be measured simultaneously. The difference in the way that these two positions vary could then be examined closely and this may lead to a better understanding of the mechanisms that cause these variations. For turbulent horseshoe vortices further experiments need to be carried out to confirm the trends in the variation of the separation positions described in section 3.6.

Secondly the boundary layer calculation methods of sections 2.6 and 3.5 could be investigated more closely. The various assumptions made in these methods (form of velocity profiles, skin friction and form parameter equations etc.) could be checked by direct experiment. Also other forms of calculation methods could be applied to the problem, such as the integral

method of Thwaites and the differential method of Dwyer (1968).

Thirdly the oscillations of horseshoe vortices could be investigated in further detail. In particular it would be useful to simultaneously visualize laminar horseshoe vortex oscillations upstream of a cylinder and the vortex bursts downstream of the same cylinder to demonstrate whether or not these vortex bursts initiate horseshoe vortex oscillations. Also turbulent horseshoe vortices could be investigated at flow conditions similar to those of Roper (1967), to see if the oscillations he observed could be reproduced.

In the previous chapters the effects of variations of the height/diameter ratio of the cylinders has been almost ignored. As can be seen from sections 2.10.1 and 3.6 these effects are significant and could be investigated more closely.

The variations of the constants K_1, K_2, K_3 and K_4 of the scour depth equations (4.6.5) and (4.6.6) need to be investigated more fully by further experiments, as does the variation of scour depth with time. Also it is possible that an analysis similar to that of section 4.7 (for clear water scour) could be developed for scour with continuous sediment motion.

Initially it was hoped that the work of chapters 2 and 3 would be helpful in gaining an understanding of the scour process described in chapter 4. Although the flow patterns at the start and end of the scouring process were similar in that the number of vortices were the same it has to be admitted that it was difficult to relate the work on vortices on a flat bed to the work on scour. However, it is possible that the work of chapters 2 and 3 might be useful for developing methods of scour protection by placing "rip-rap" (large stone particles) in the regions of high shear stresses upstream of bridge piers. With such scour protection the bed around the bridge pier should remain plane and one would expect the experimental results of chapters 2 and 3 to be applicable. Further experiments to describe the flow around cylinders on a rough rigid bed would also be of interest in this respect.

REFERENCES

Bandyopadhyay, P. (1977). Combined smoke flow visualization and hot wire anemometry in turbulent boundary layers: Turbulence Symposium, Tech. Univ. Berlin.

Belik, L. (1973). The secondary flow about circular cylinders mounted normal to a flat plate: Aero. Quart. 24, 47-54.

Bonosoundas, M. (1973). Flow regimes and scour at round bridge piers: Oskar V. Miller Inst. Report 28.

Bossel, U., Honnold, F. (1976). On the formation of horseshoe vortices in plate fin heat exchangers: Archives of Mechanics (Warsaw), 28, 773-780.

Breusers, H., Nicollet, G., Shen, H. (1977). Local scour around cylindrical piers: Journ. Hyd. Res. 15, 3, 211-252.

Carstens, M. (1966). Similarity laws for localized scour: ASCE Journ. Hyd. Div. 92, HY3, 13-36.

Carstens, T., Sharma, H. (1975). Local scour around large obstructions: IAHR Conf. Proc. San Paulo, 2, 251-262.

Chabert, J., Engeldinger, P. (1956). Etude des affouillements autour des piles des ponts: Laboratoire National d'Hydrolique, Chatou, France.

Coleman, N. (1972). The drag coefficient of a stationary sphere on a boundary of similar spheres: Houille Blanche 27, 17-21.

Cooke, J. (1959). Approximate calculation of three dimensional laminar boundary layers: A.R.C. R. and M. 3201.

Duncan, W., Thom, A., Young, A. (1970). Mechanics of fluids: Arnold.

Dwyer, H. (1968). Solution of a three dimensional boundary layer flow with separation: AIAA Journ. 6, 7, 1336-1342.

East, L., Hoxey, R. (1969a and b). Low speed three dimensional turbulent boundary layers. Part 1: RAE Tech. Rep. 69041.

Part 2: RAE Tech. Rep. 69137.

Greeley, R., Iverson, J., Pollack, J., Udovich, N., White, B. (1974). Wind tunnel studies of Martian aeolian processes. Proc. Roy. Soc. Lond. A, $\underline{341}$, 331-360.

Gregory, N., Walker, W. (1951). The effect of transition on isolated surface excrescences in the boundary layer: A.R.C. R and M. 2779.

Grodowozyk, M., Maggiolo, O., Folguera, H. (1968). Localized scour in erodible bed channels: Journ. Hyd. Res. $\underline{6}$, 4, 289-326.

Hall, M. (1966). The structure of concentrated vortex cores: Progress in Aero. Science $\underline{7}$, Chapter 4: Pergamon Press.

Hancu, S. (1971). Sur le calcul des affouillement locaux dans la zone des piles du pont: IAHR Conf. Proc. Paris $\underline{3}$, 209-306.

Hawthorne, W. (1954). The secondary flow about struts and aerofoils: Journ. Aero. Sci. $\underline{21}$, 9, 588-606.

Hawthorne, W., Martin, M. (1955). The effect of density gradient and shear on the flow over a hemisphere: Proc. Roy. Soc. Lond. A. $\underline{232}$, 184-195.

Head, M. (1976). Eddy viscosity in turbulent boundary layers: Aero. Quart. $\underline{27}$, 270-275.

Head, M., Bandyopadhyay, P. (1978). Combined flow visualization and hot wire measurements in turbulent boundary layers: AFOSR - Le High Workshop on coherent structures in turbulent boundary layers: May 1st-3rd.

Henderson, F. (1966). Open channel flow: Macmillan.

Hornung, H., Joubert, P. (1963). Mean velocity profiles in turbulent boundary layers: Journ. Fluid Mech. $\underline{15}$, 368-384.

Hunt, J., Abell, C., Peterka, J., Woo, H. (1978). Kinematical studies of the flows around free or surface mounted obstacles; applying topology to flow visualization: Journ. Fluid Mech. $\underline{86}$, 1, 179-201.

Johnston, J. (1960a). The turbulent boundary layer at a plane of symmetry in a three dimensional flow: Trans. ASME D $\underline{82}$, 622-628.

Johnston, J. (1960b). On the three dimensional boundary layer generated
by secondary flow: Trans. ASME D 82, 233-248.

Klebanoff, P. (1955). Characteristics of turbulence in a boundary layer
with zero pressure gradient: NACA Report 1247.

Küchemann, D. (1965). Report on IUTAM symposium on concentrated vortex
motions in fluids: Journ. Fluid Mech. 21, 1, 1-20.

Leclerc, J. (1971). Recherche des lois regussant les phenomenes
d'affouillements au pied des piles de pont: IAHR Conf. Proc.
Paris 3, 323-330.

Le Feuvre (1966). Sediment transport functions with special emphasis
on localised scour: Georgia Inst. of Tech. Ph.D. Thesis.

Laursen, E. (1960). Scour at bridge crossings: ASCE Journ. Hyd. Div.
86, HY2 39-54.

Laursen, E. (1963). An analysis of relief bridge scour: ASCE Journ.
Hyd. Div. 89, HY3, 93-118.

Ludwieg, H., Tillmann, W. (1949). Ing. Archiv. 17, 4.

Maskell, E. (1955). Flow separation in three dimensions: RAE Report
2565;

Maskell, E. (1966). A theory of the blockage effects on bluff bodies
and stalled wings in a closed wind tunnel: ARC R. and M. 3400.

Melville, B. (1975). Local scour at bridge sites: Ph.D. Thesis, Univ.
of Auckland.

Mochizuki, M. (1961a). Smoke observation on boundary layer transition
caused by a spherical element: Journ. Phys. Soc. Japan 16, 5,
995-1008.

Mochizuki, M. (1961b). Hot wire investigations of smoke patterns caused
by spherical roughness element: Nat. Sci. Rep. Ochanomizu Univ.,
Tokyou 12, 2.

Nash, J. (1969). The calculation of three dimensional turbulent boundary
layers in incompressible flow: Journ. Fluid Mech. 37, 4, 625-642.

Nicollet, G. (1975). Affouillements au pied des piles de pont en milieu cohesif: IAHR Conf. Proc. San Paulo, 2, 478-484.

Nicollet, G., Ramette, M. (1971). Affouillement au voisinage de piles de pont cylindriques circulaires: IAHR Conf. Proc. Paris 3, 315-322.

Norman, R. (1972). On obstacle generated secondary flows in laminar boundary layers and transition to turbulence: Ph.D. Thesis, Illinois Inst. of Technology.

Norman, S. (1977). Forces on cylinders under waves: Ph.D. Thesis, Cambridge University.

Peake, D., Galway, R. (1965a). The three dimensional separation of a plane incompressible laminar boundary layer produced by a circular cylinder mounted normal to a flat plate: N.R.C. report. LR 428.

Peake, D., Galway, R. (1965b). The three dimensional separation of a plane incompressible laminar boundary layer produced by a Rankine oval mounted normal to a flat plate: N.R.C. report. LR 446.

Perry, A., Fairlie, B. (1974). Critical points in flow patterns: Advances in Geophysics: Pergamon Press.

Roper, A. (1967). A cylinder in a turbulent shear layer: Ph.D. Thesis, Colorado State University.

Rott, N. (1958). On the viscous core of line vortices: ZAMP 9, 543-553.

Rowe, M. (1966). Some secondary flow problems in fluid mechanics: Ph.D. Thesis, Cambridge Univ.

Schwind, R. (1962). The three dimensional boundary layer near a strut: Gas Turbine Lab. Report, M.I.T.

Sedney, R. (1973). A survey of the effects of small protuberances on boundary layer flows: AIAA Journ. 11, 6, 782-792.

Sedney, R., Kitchens, C. (1975). The structure of three dimensional separated flows in obstacle, boundary layer interactions. AGARD Conf. Proc. No. 168.

Shabaka, I. (1975). A preliminary investigation of turbulent flow on a simplified wing body junction: I.C. Aero. Rep. 75-05.

Shellim, M. (1976). Pressure distribution along a plate upstream of a cylindrical projection: Cambridge Univ. Eng. Dept. Undergraduate project.

Shen, H., Schneider, V., Karaki, S. (1969). Local scour around bridge piers: ASCE Journ. Hyd. Div. 95, HY6, 1919-1940.

Stewart, A. (1977). Flow around slender bodies at yaw: Ph.D. Thesis, Cambridge Univ.

Timman, R. (1955). The theory of three dimensional boundary layers: Symposium on boundary layer effects in aerodynamics; N.P.L.

Thwaites, B. (1960). Incompressible aerodynamics: Oxford Univ. Press.

Vasanta Ram, V. (1963). Untersuchungen über die Eckengrenz schicht an einem Kreizylinder mit Seitenwand: Inst. Fluid Mech. Braunschweig, Report 63/46.

von Doenhoff, A., Tetervin, N. (1943). Determination of general relations for the behaviour of turbulent boundary layers: NACA Rep. 772.

Weapons Research Establishment, South Australia (1967). Mechanics of boundary layer transition: Film.

Westkaemper, J. (1968). Turbulent boundary layer separation ahead of cylinders: AIAA Journ. 6, 7, 1352-1355.

White, W. (1975). Scour around bridge piers in steep streams: IAHR Conf. Proc. San Paulo, 2, 279-285.

Yalin, M.S. (1972). The mechanics of sediment transport: Pergamon Press.

Zaat, J. (1956). A simplified method for the calculation of three dimensional laminar boundary layers: N.L.L. Report F. 184.
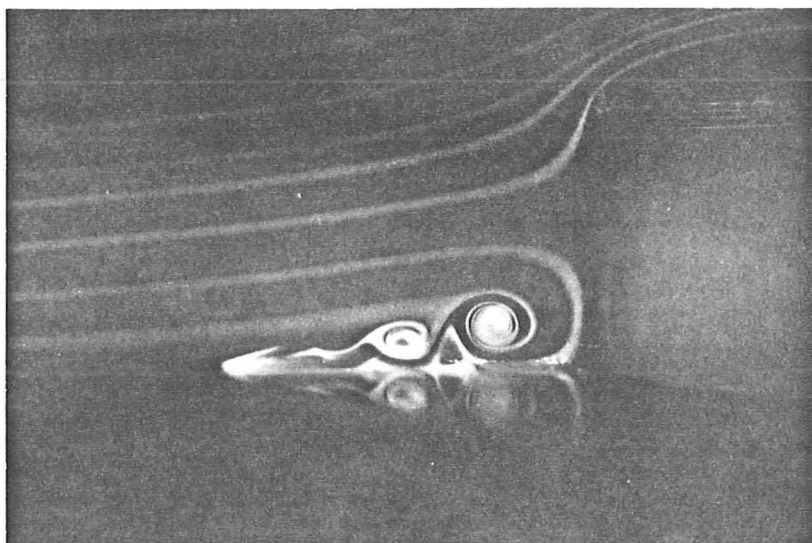
FIGURE 1.1 Sutton's experiment

Regime 1
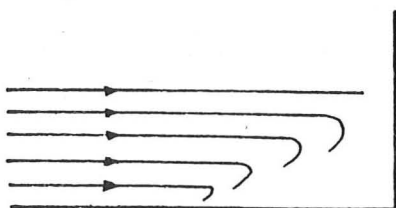
Regime 2
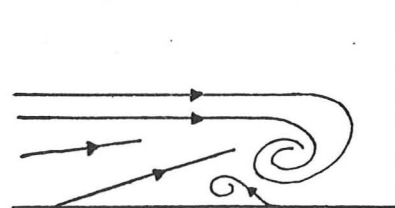
Regime 3
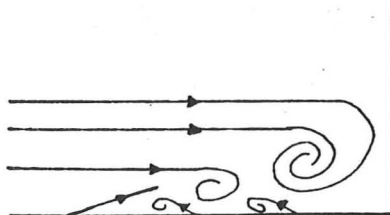
Regime 4
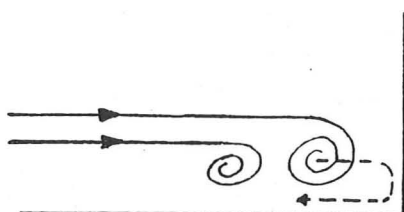
(a)
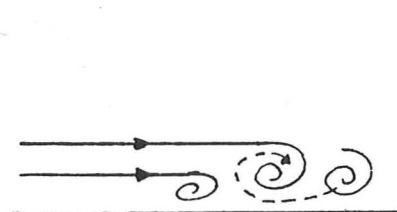
(b)

Regime 5
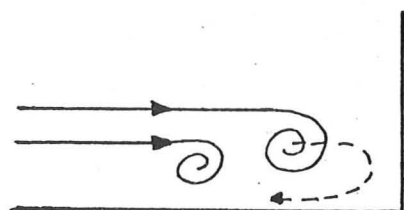
(a)
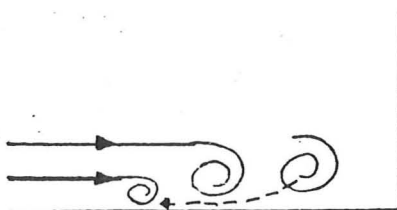
(b)

FIGURE 2.1.1 Schwind's Experiments
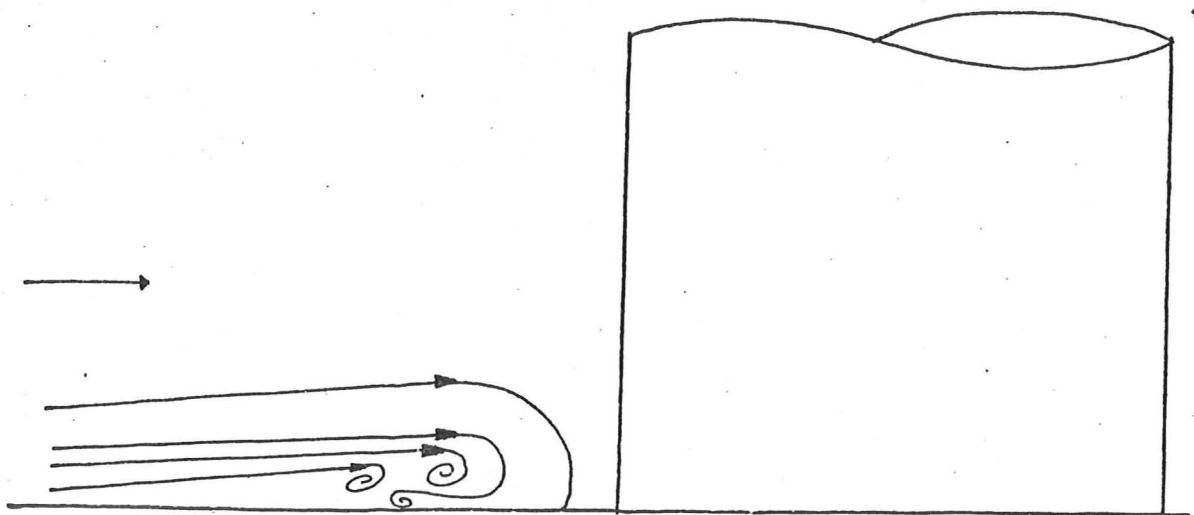
FIGURE 2.1.2 Peake and Galway's Experiments
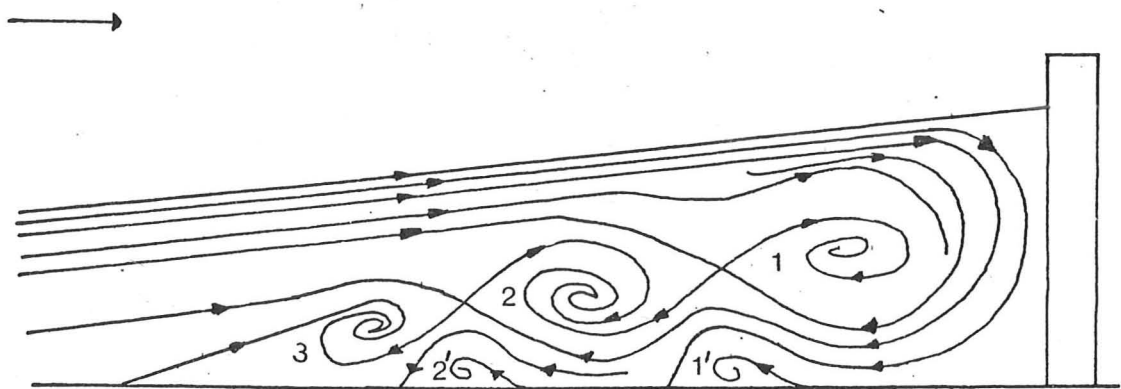
(a) Jet-maze model
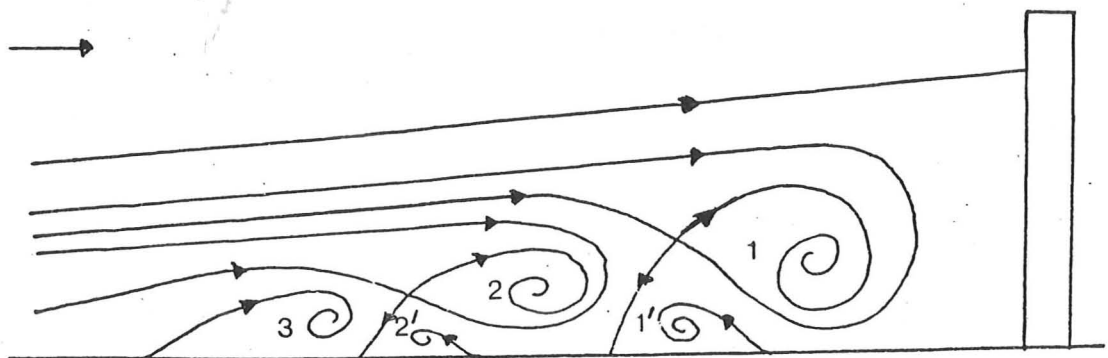
(b) Stairstep model

FIGURE 2.1.3 Norman's Experiments

FIGURE 2.1.4 Bossel and Hannold's
Experiments
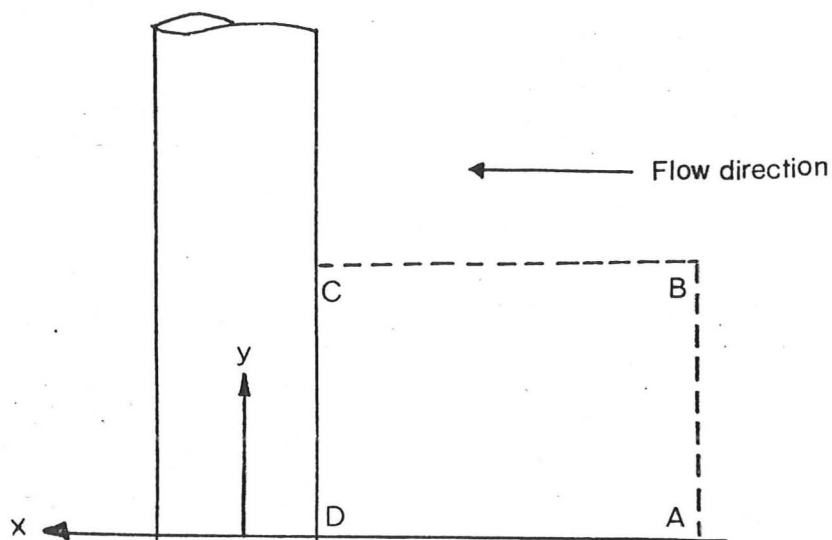
FIGURE 2.1.5 Roper's Control Volume

Vorticity concentrations downstream of hemisphere (flow out of page)
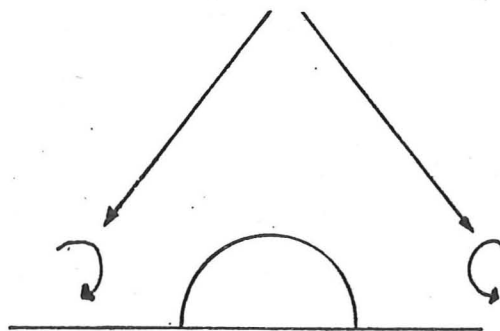
FIGURE 2.1.6 Hawthorne and Martin's
Experiment

Light Source — · · · Working Section

1m.

Honeycomb — Gauze

(a) Schematic Section

Cylinder on plate

perspex

A ← → A

56 cm

Smoke wing
(20 Tubes , I|D 2mm
O|D 3mm)

Smoke

(b) Working Section

30·5 cm

15·3 cm
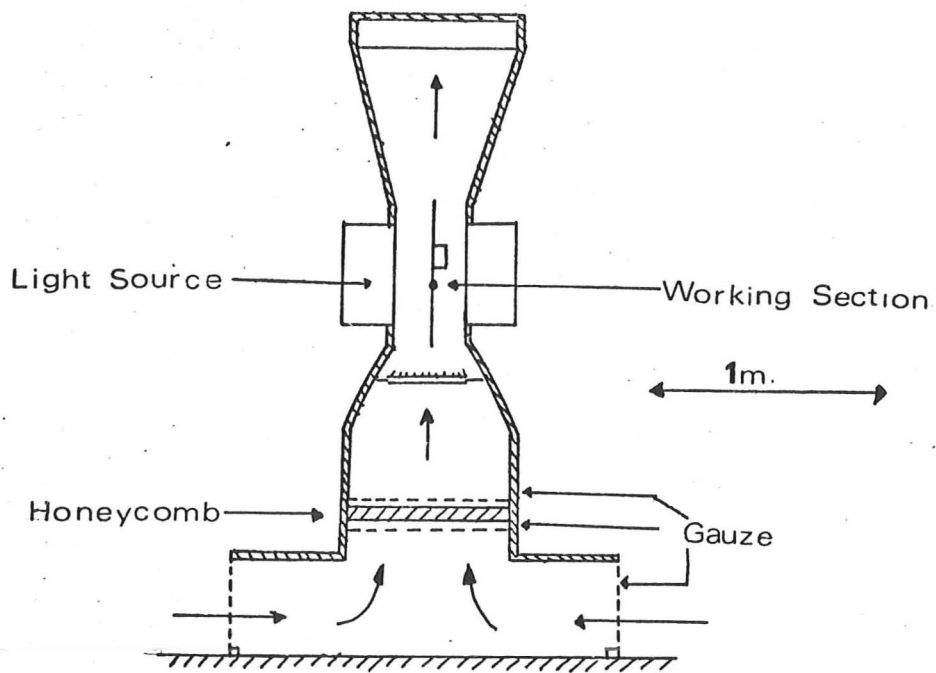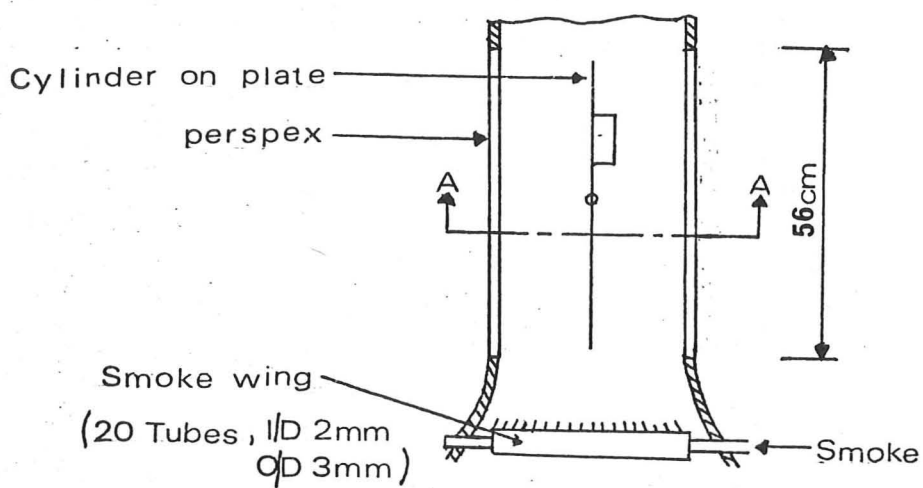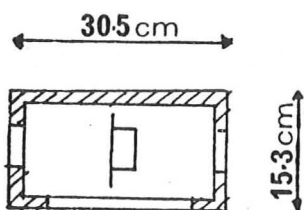
(c) Section A A

FIGURE 2.3.1 Smoke Tunnel

1 m

Pitot static tube

94 cm

71 cm

A   A

Extra gauges   Suction slot   Model

Contraction

(a) Sectional plan

Suction slot   46 cm   51 cm
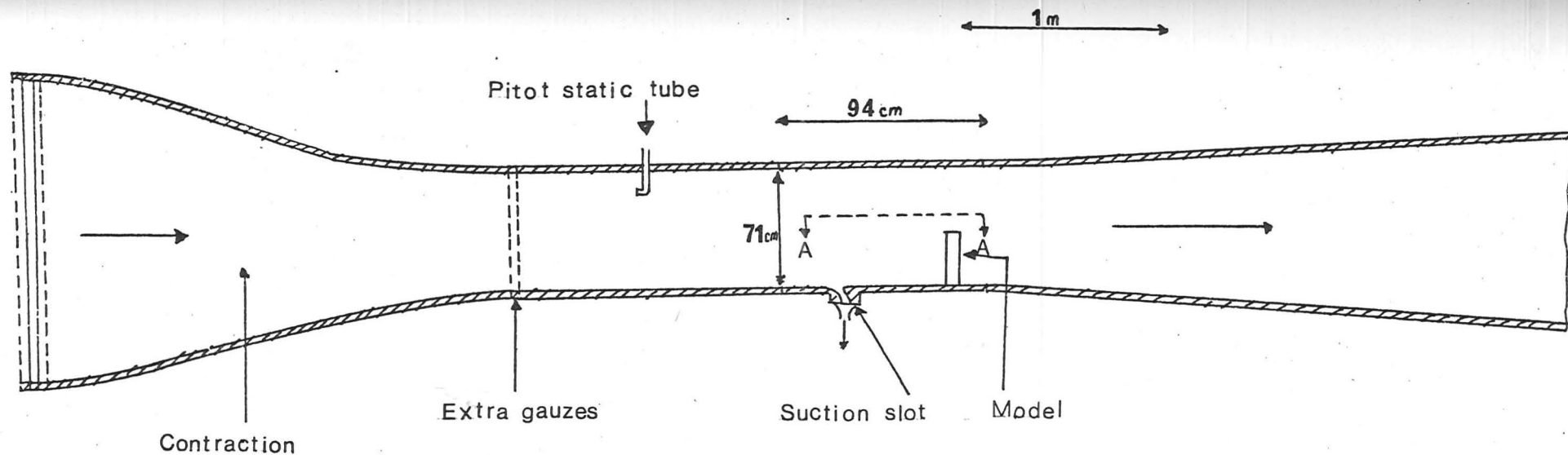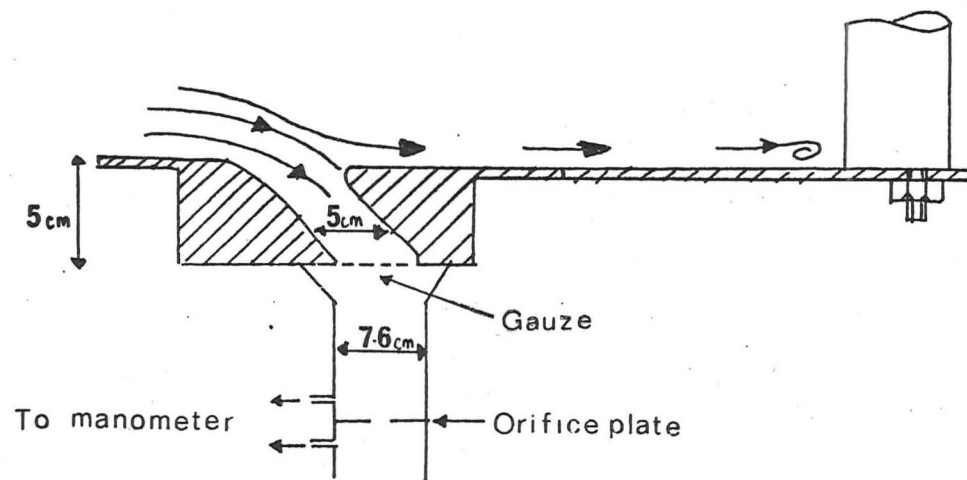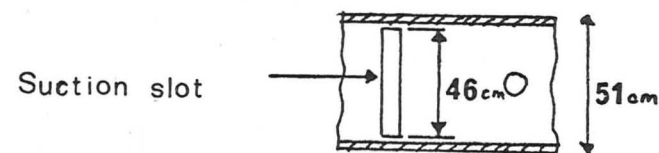
(c) Suction slot (section AA)

5 cm   5 cm   Gauze

7·6 cm

To manometer   Orifice plate

FIGURE 2.3.2   1B Wind Tunnel

(b) Suction slot

0.3 cm

0.15 cm

x

y

b

c

C
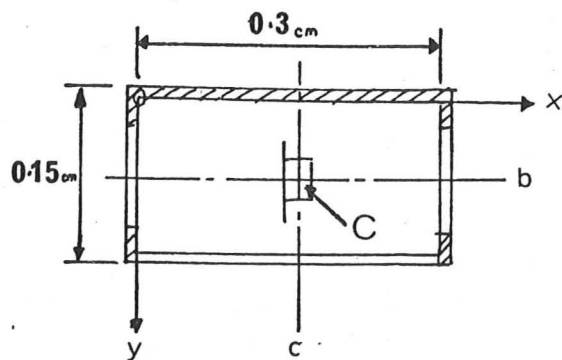
Tunnel cross section

u_c - Centre line velocity

(a) Coordinate system

u/u_c

1.0

0.7

0.1

x (m)

0.2

C
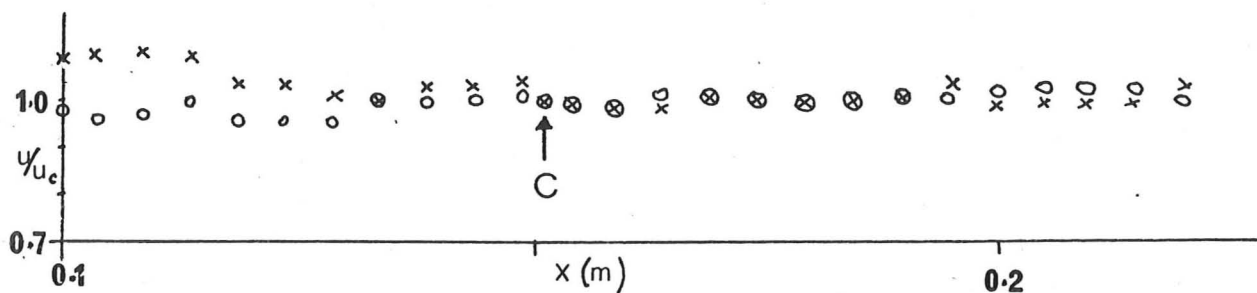
(b)

O $u_c = 0.59$ ms^{-1}

X $u_c = 0.35$ ms^{-1}

u/u_c

1.0

0.7

0

0.05

y (m)

0.1

C
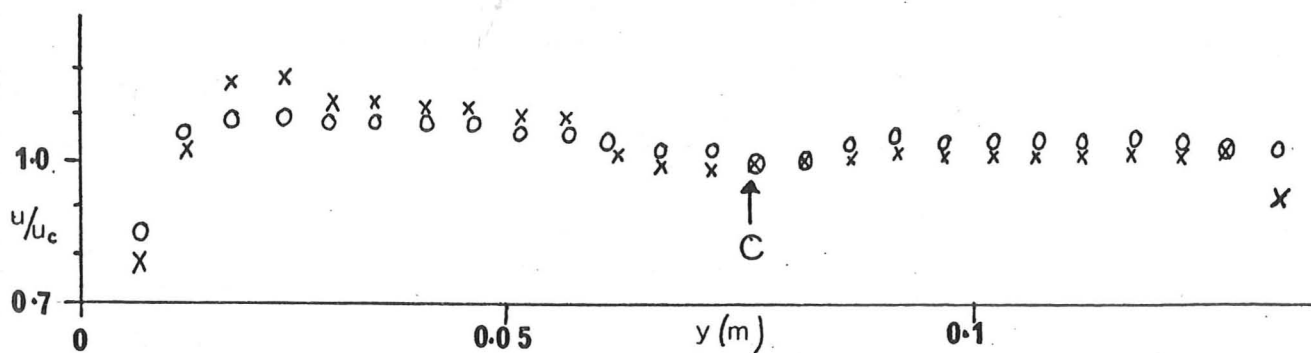
(c)

FIGURE 2.3.3 Velocity distributions in smoke tunnel
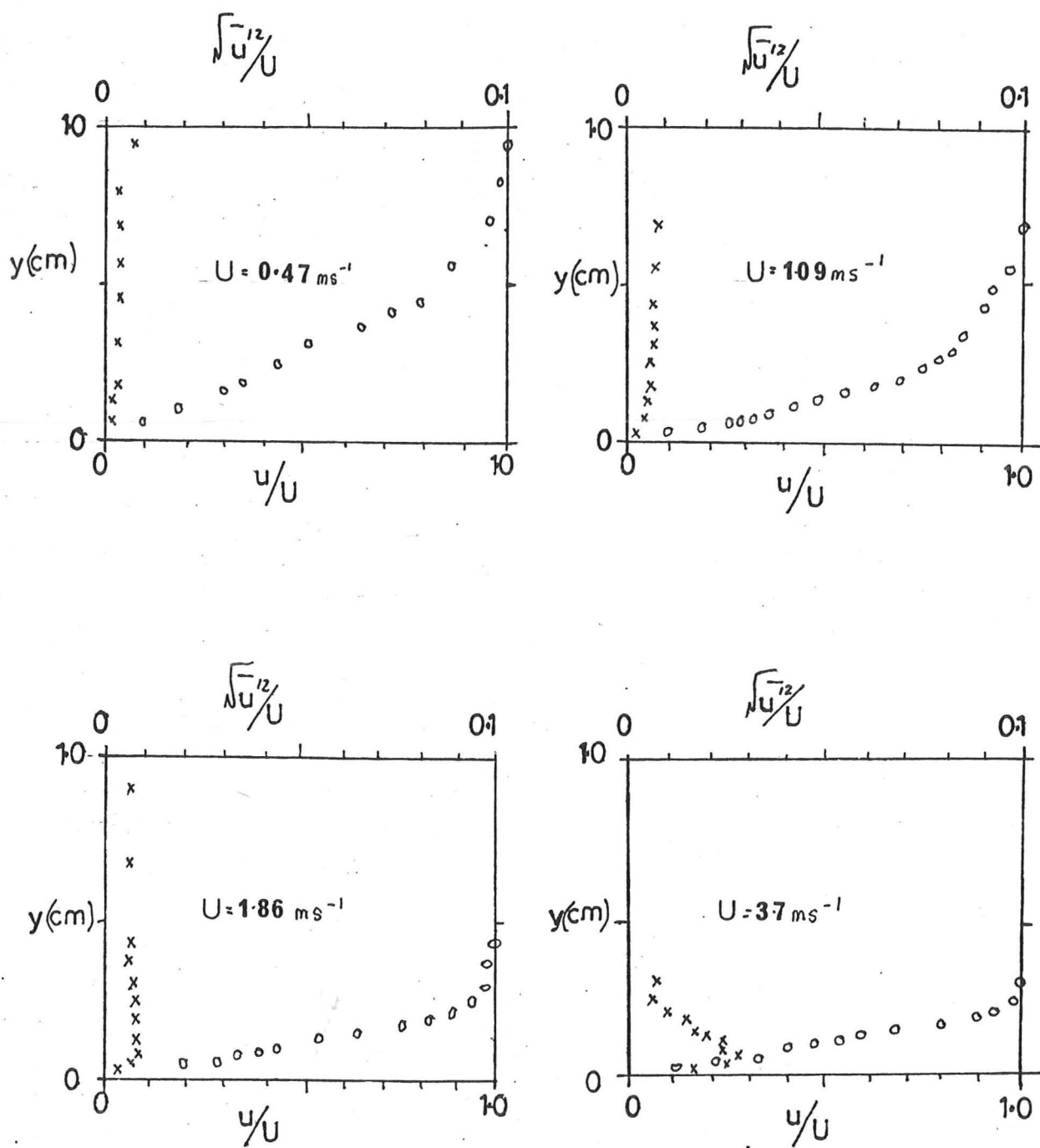
Suction slot position 1

FIGURE 23.4 Velocity and turbulence profiles
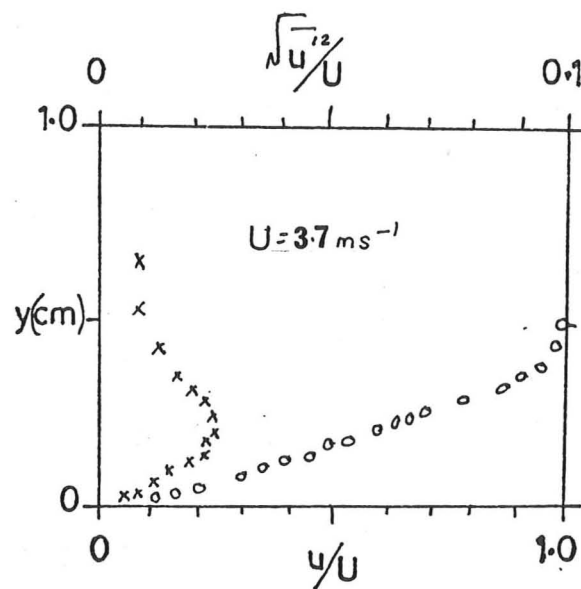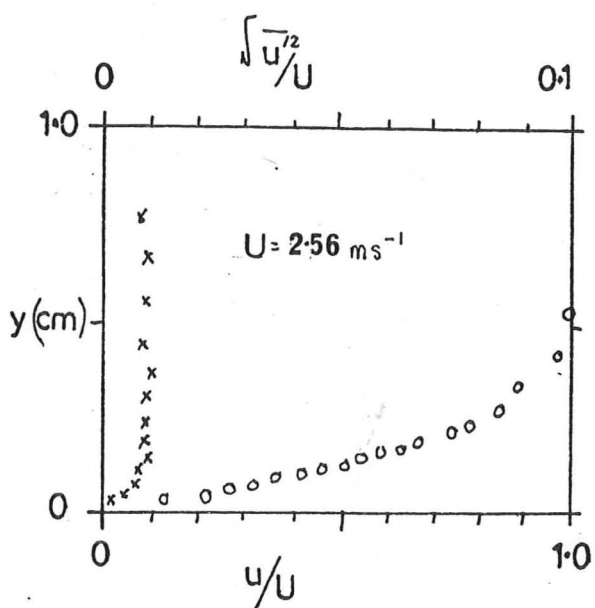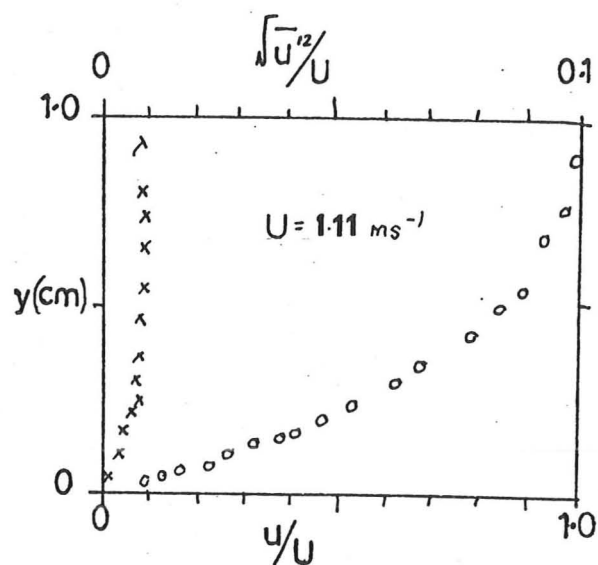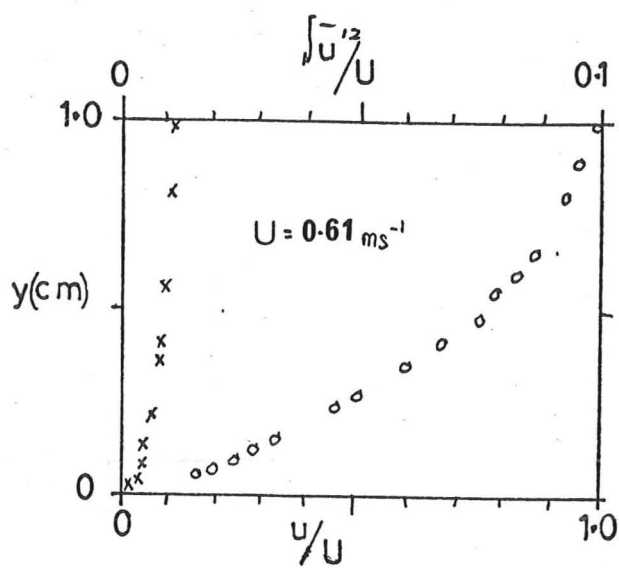
Suction slot position 2

FIGURE 2.3.4 (cont.)
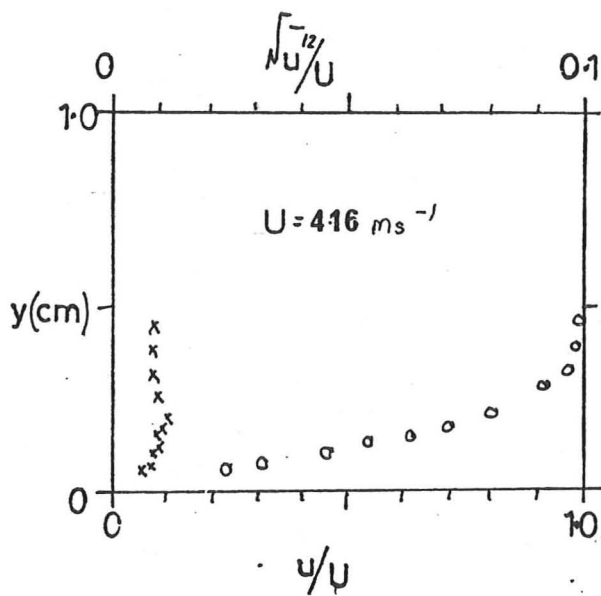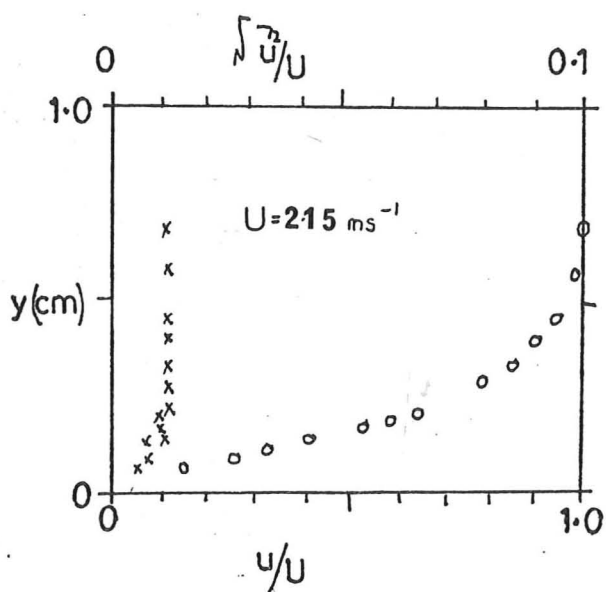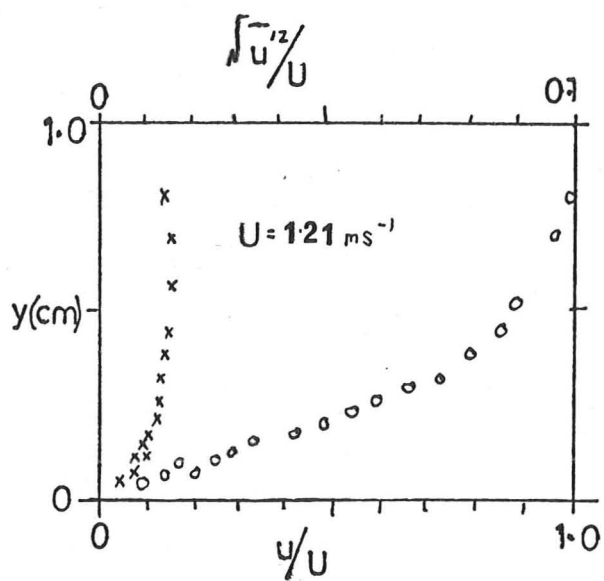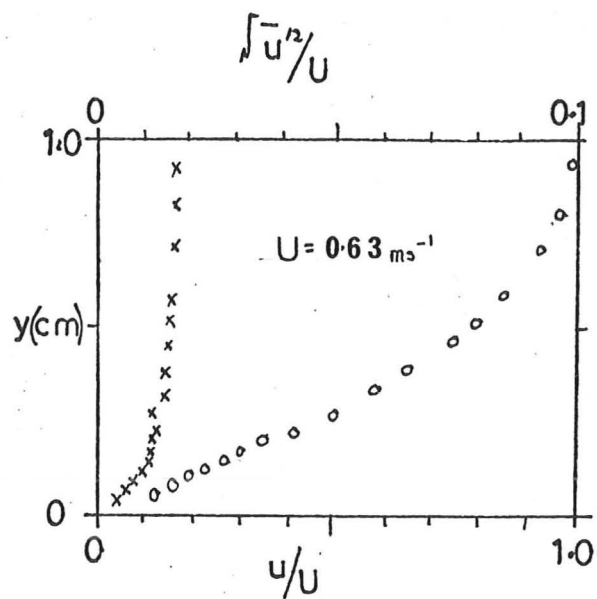
Suction slot position 3

FIGURE 2.3.4 (cont.)
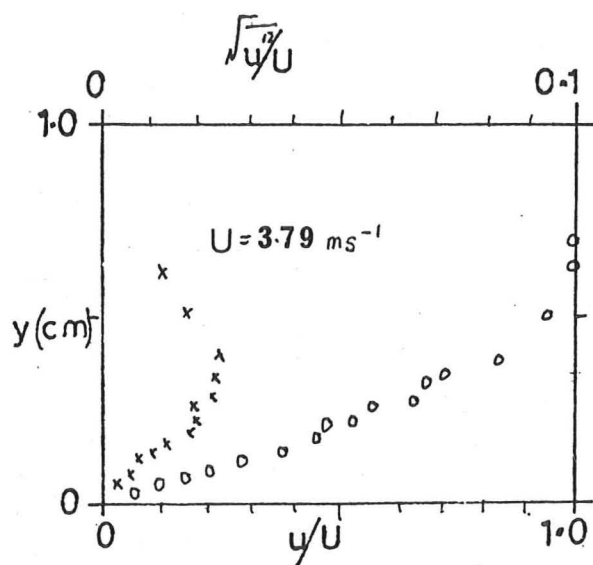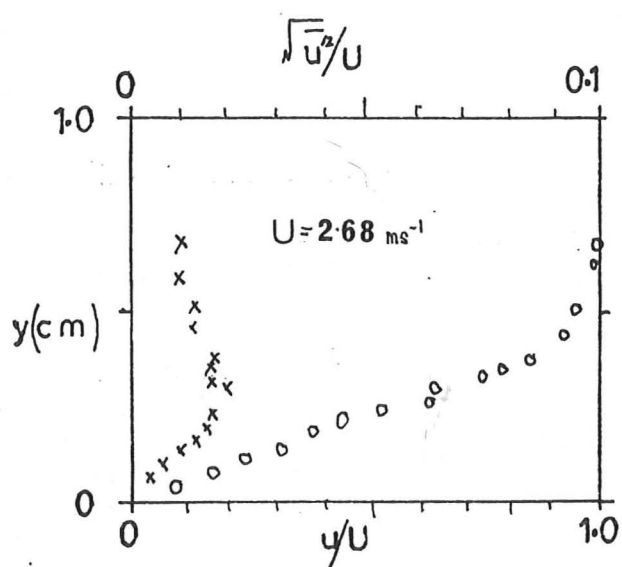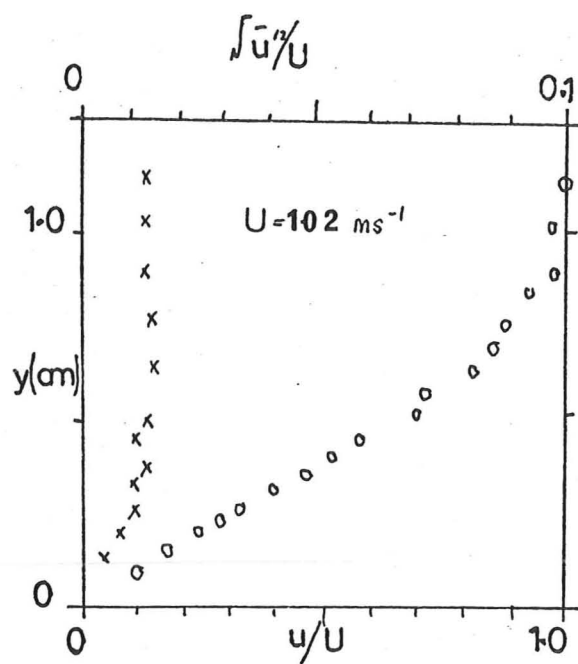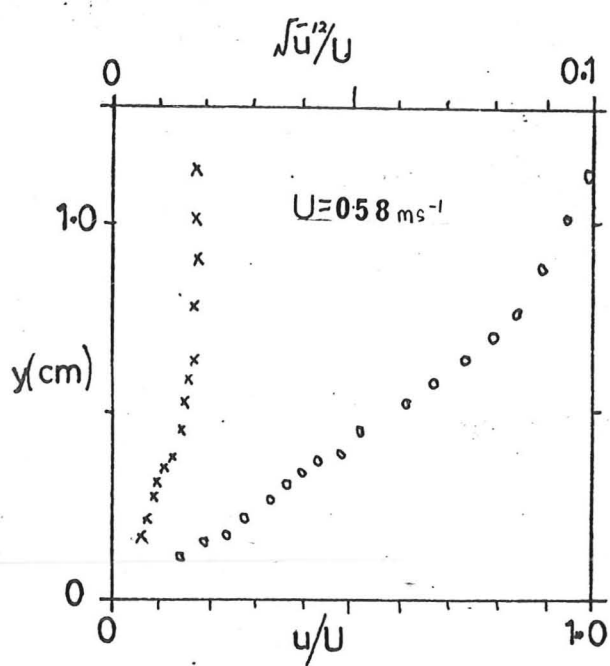
Suction slot position 4

FIGURE 2.3.4 (cont.)

Suction slot position	H ($\pm 9\%$)	x_c (cm)
X	1	2·56	28.0
O	2	2·69	35·6
+	3	2·61	43·2
Δ	4	2·79	50·8
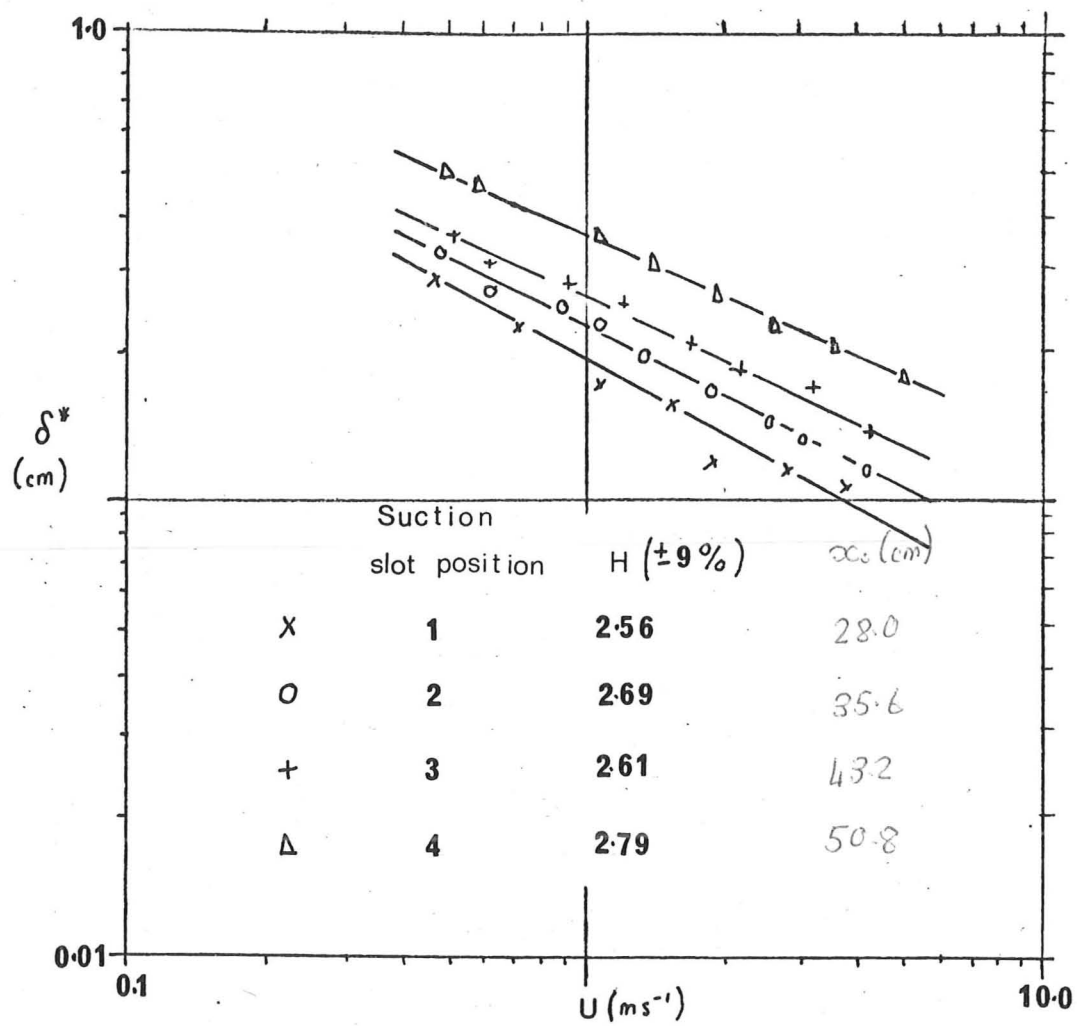
FIGURE 2.3.5 Boundary layer parameters
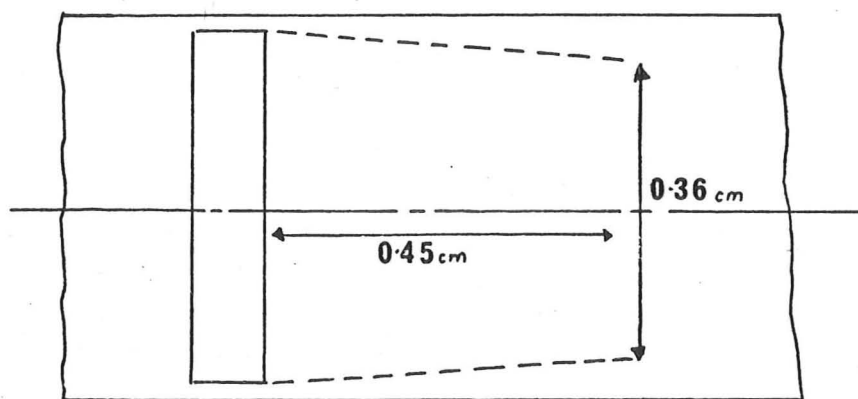
FIGURE 2.3.6 Laminar flow on wind tunnel wall
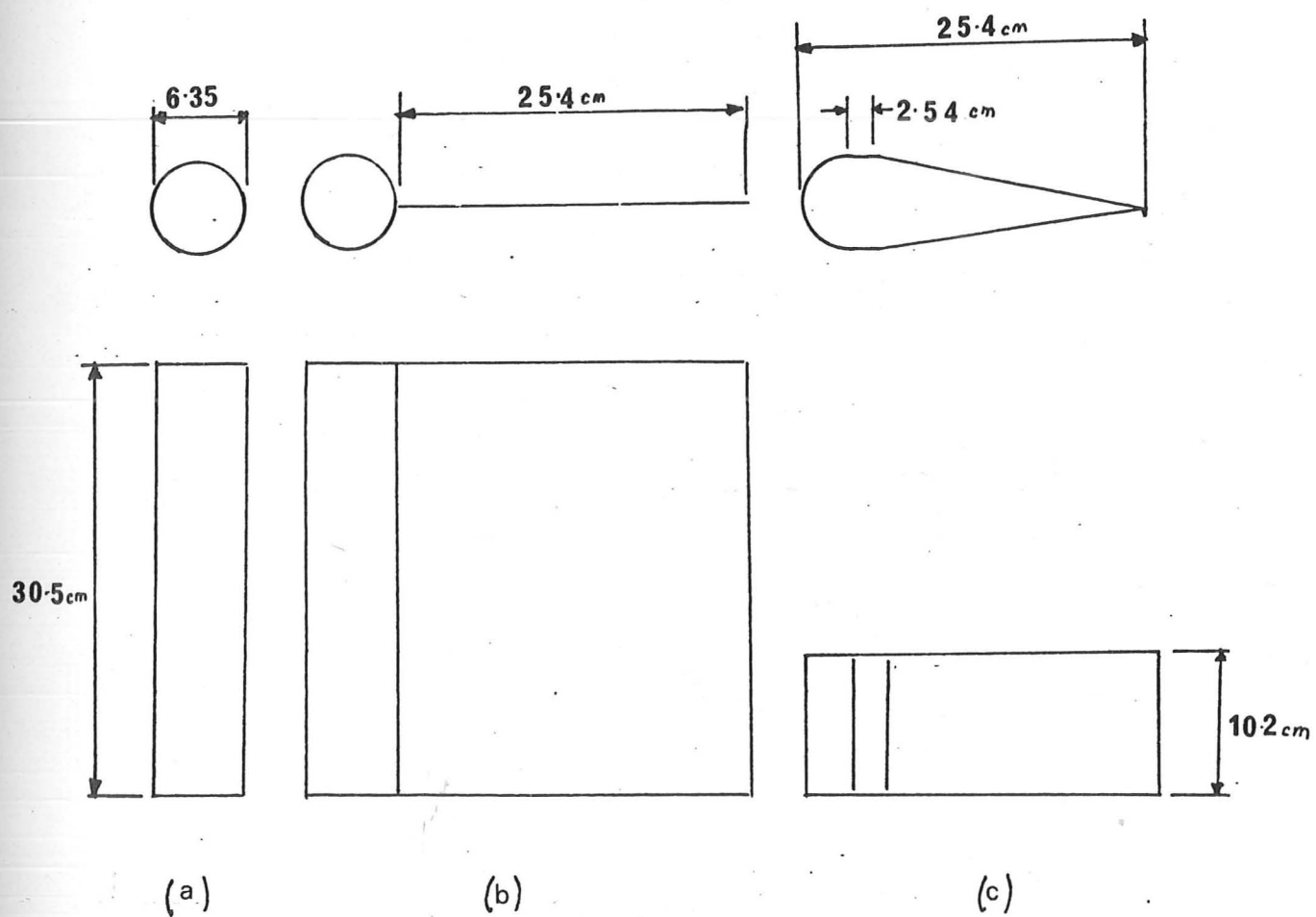
FIGURE 2.3.7   Model   dimensions

Pressure tapping
$(0.8 mm I/D)$

Slot in wall

2cm

Traverse gear

Micromanometer

Voltmeter

Voltmeter

Potentiometer

D C Supply

Chart Recorder
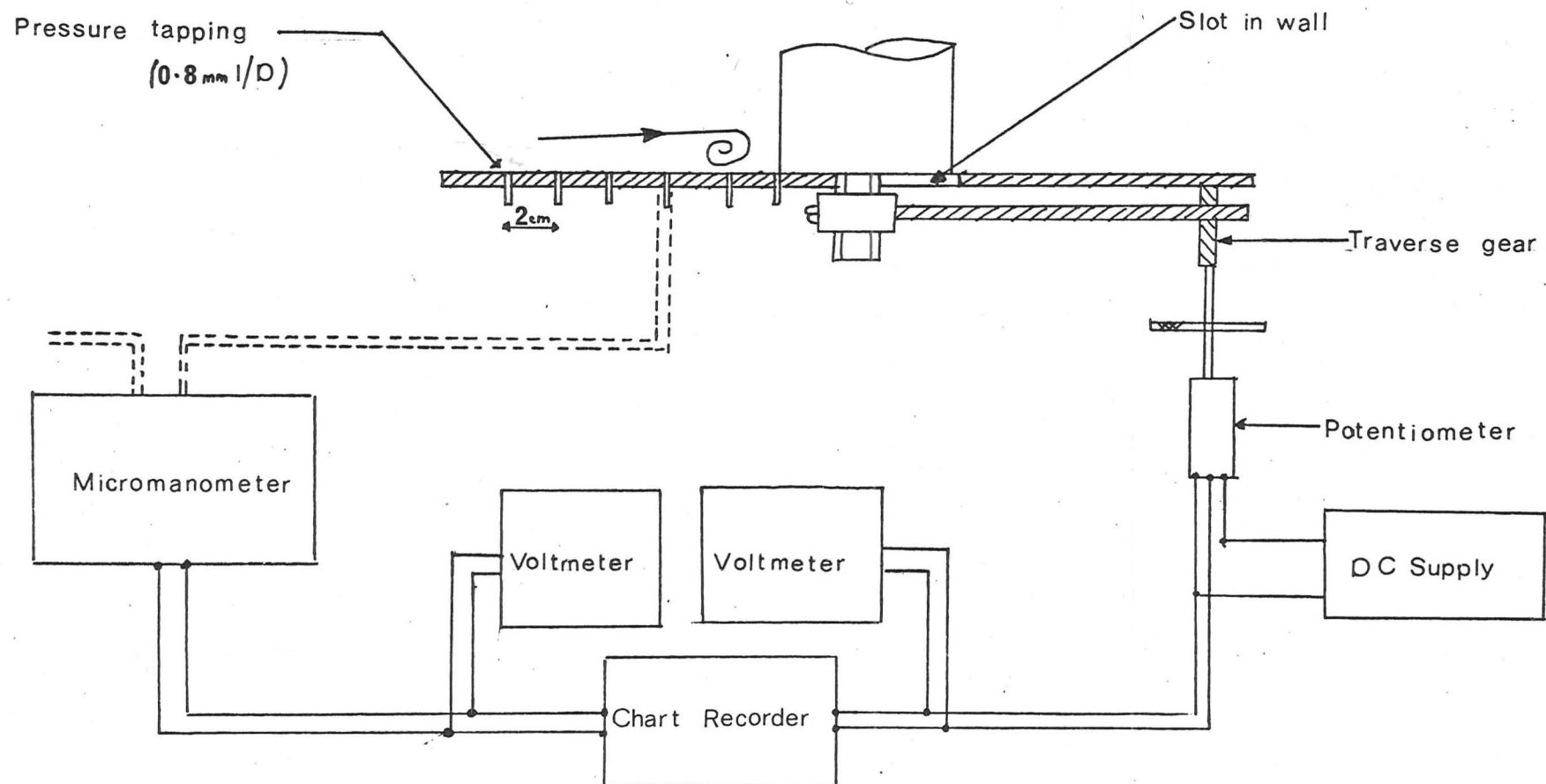
FIGURE 2.3.8 Pressure measuring apparatus
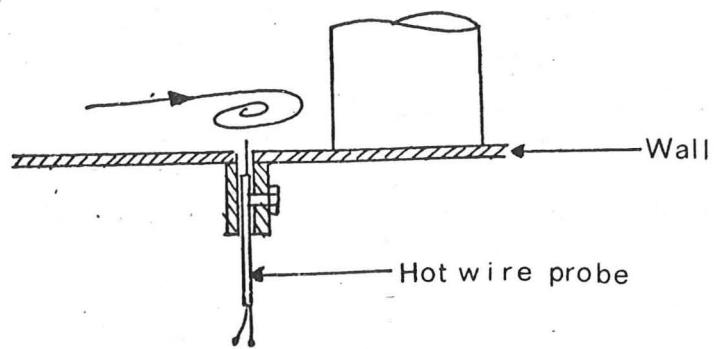
(a) Probe in wind tunnel wall
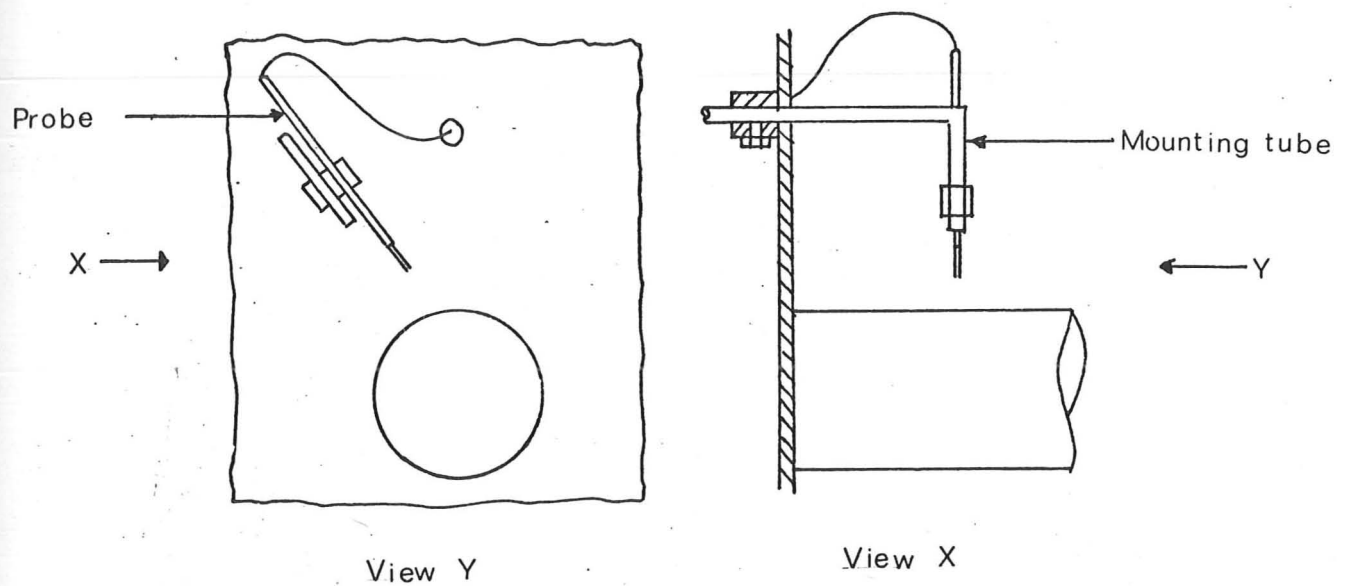
(b) Probe in model wake
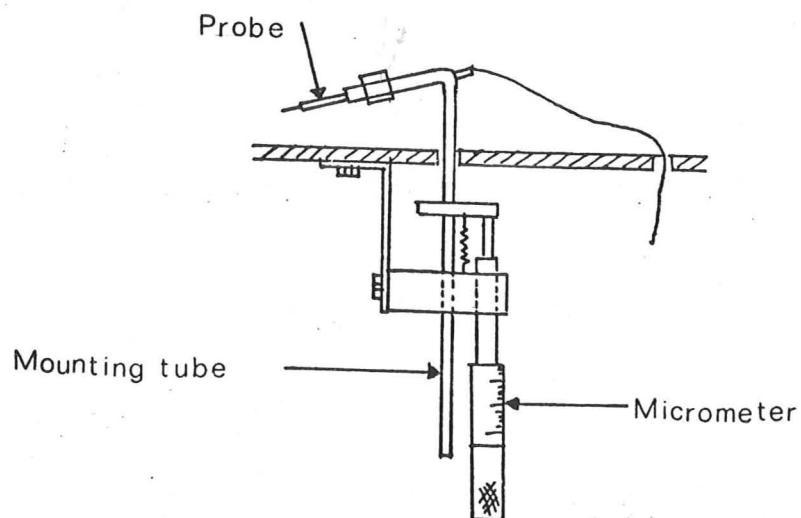
(c) Traverse gear

FIGURE 2.3.9 Hot wire probe mountings
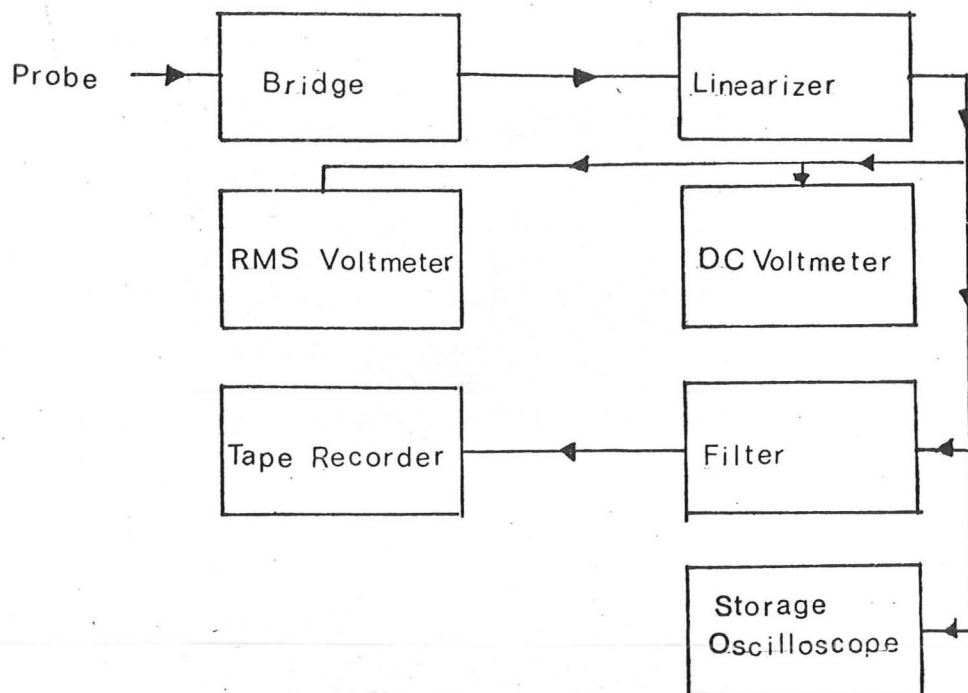
FIGURE 2.3.10 Hot wire apparatus
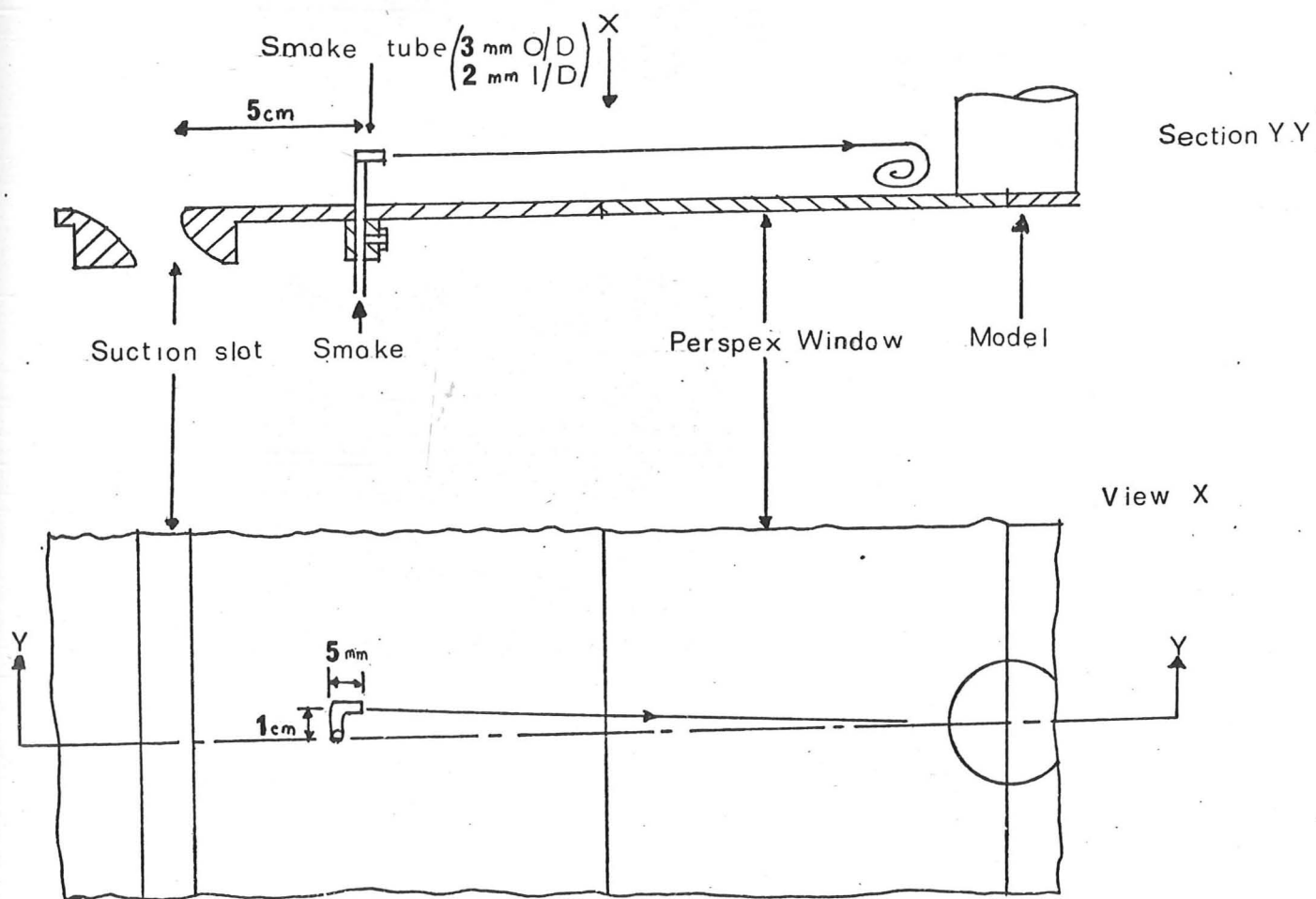
FIGURE 2.3.11 Position of smoke tube
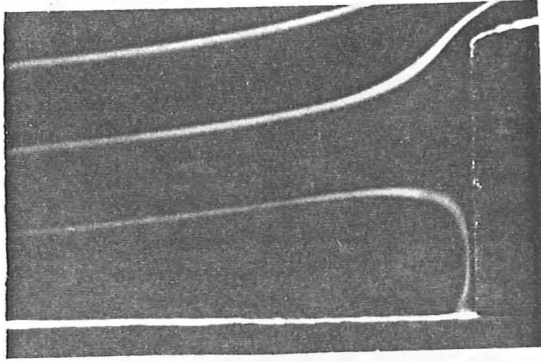
(a)
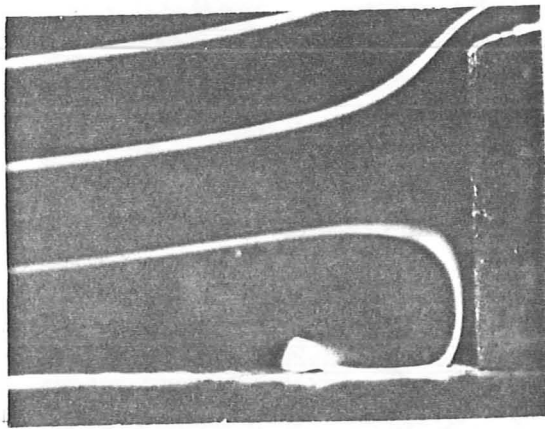
(b)
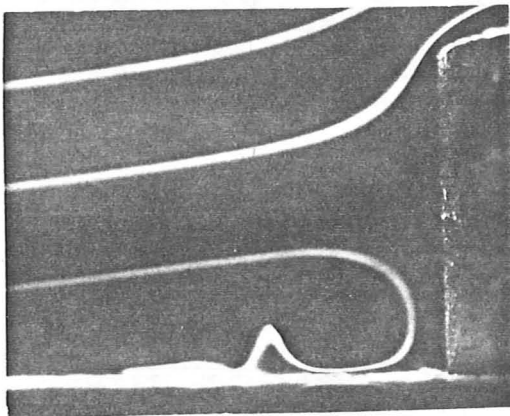
(c)

FIGURE 2.4.1 Smoke flow visualization

$(UD/\nu = 4370 , D/\delta^* = 21.3 , D/l = 2.0)$
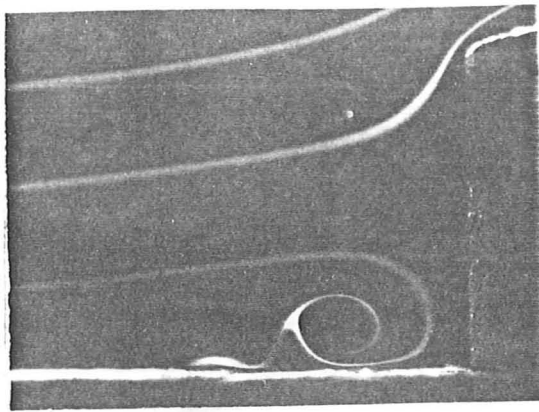
(d)
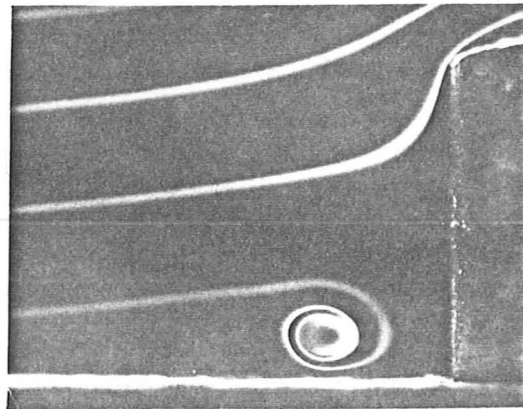
(e)

(f)

(g)

FIGURE 24.1 Continued

(a) Six vortices

(b) Four vortices

(c) Two vortices

FIGURE 2.4.2 Streamline patterns

(a) Six vortices

(b) Four vortices

(c) Two vortices
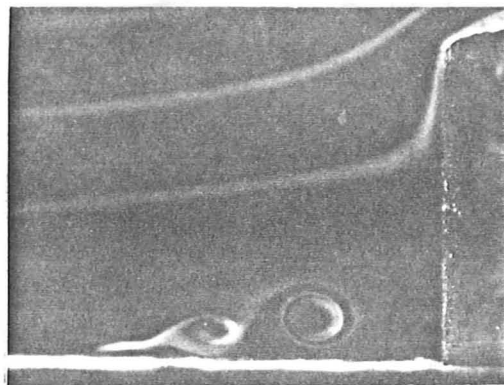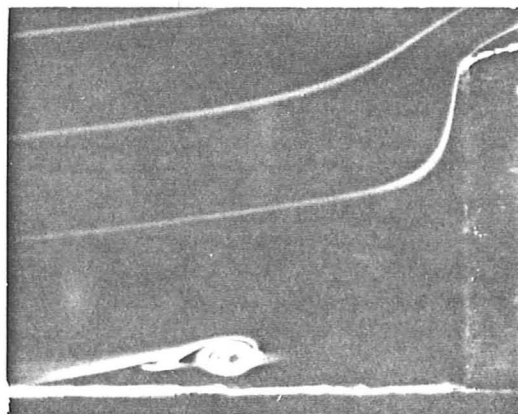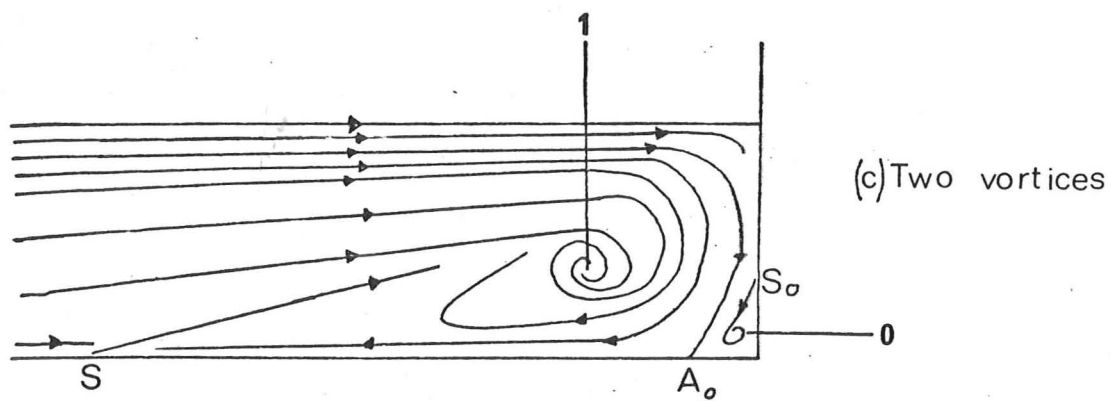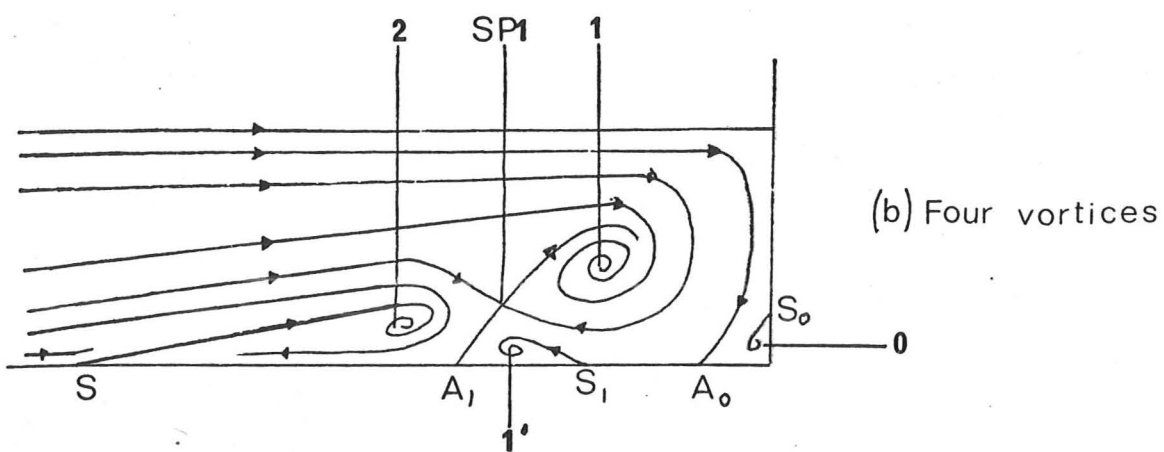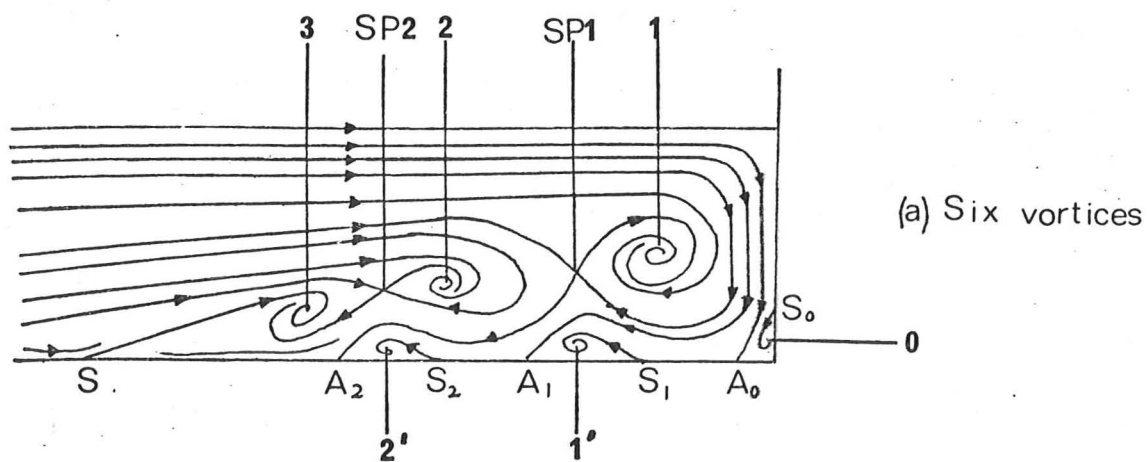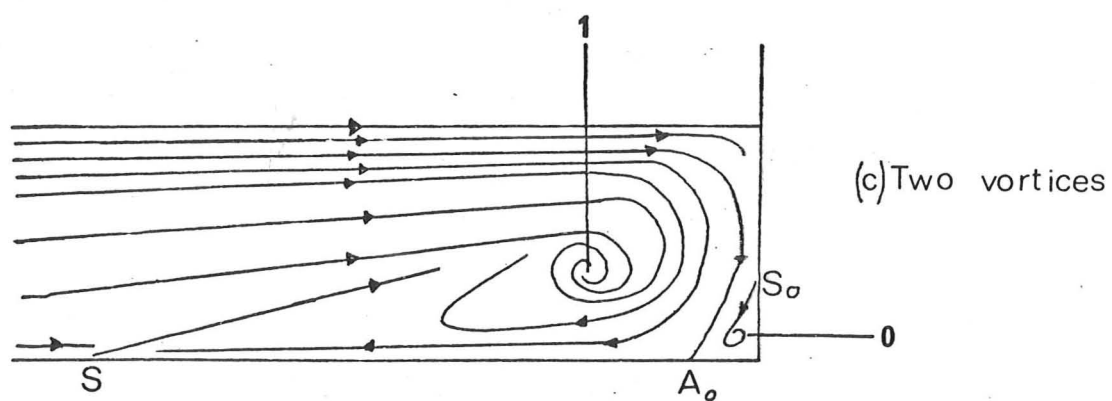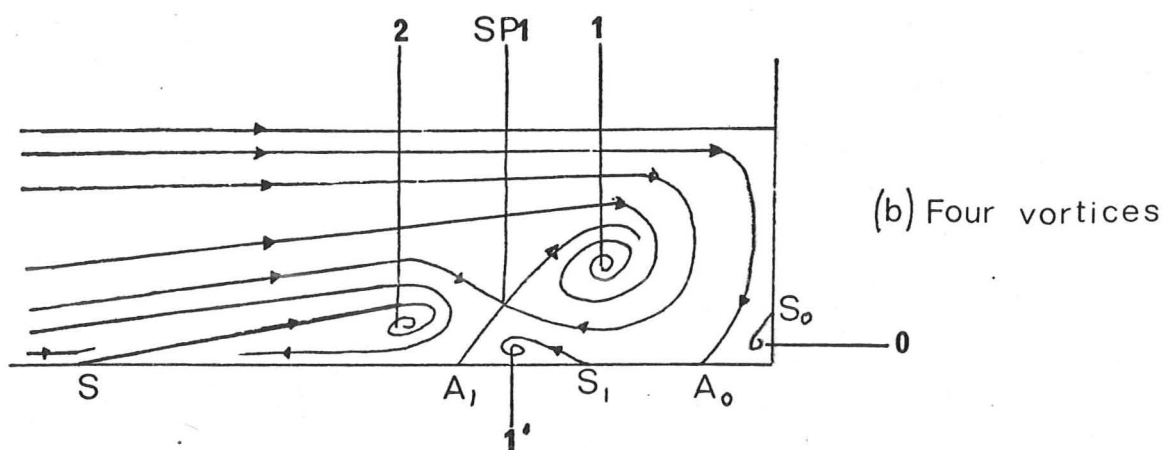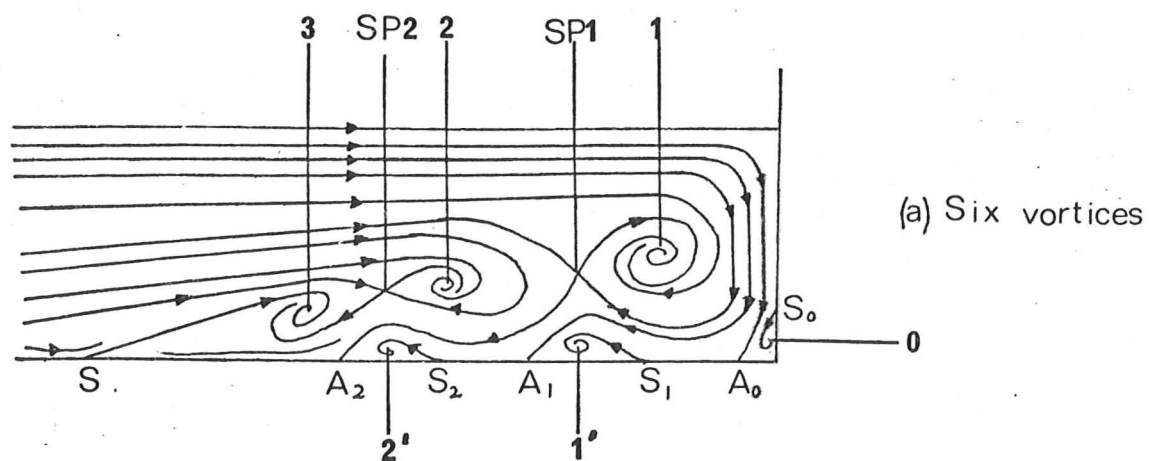
FIGURE 2.4.2 Streamline patterns
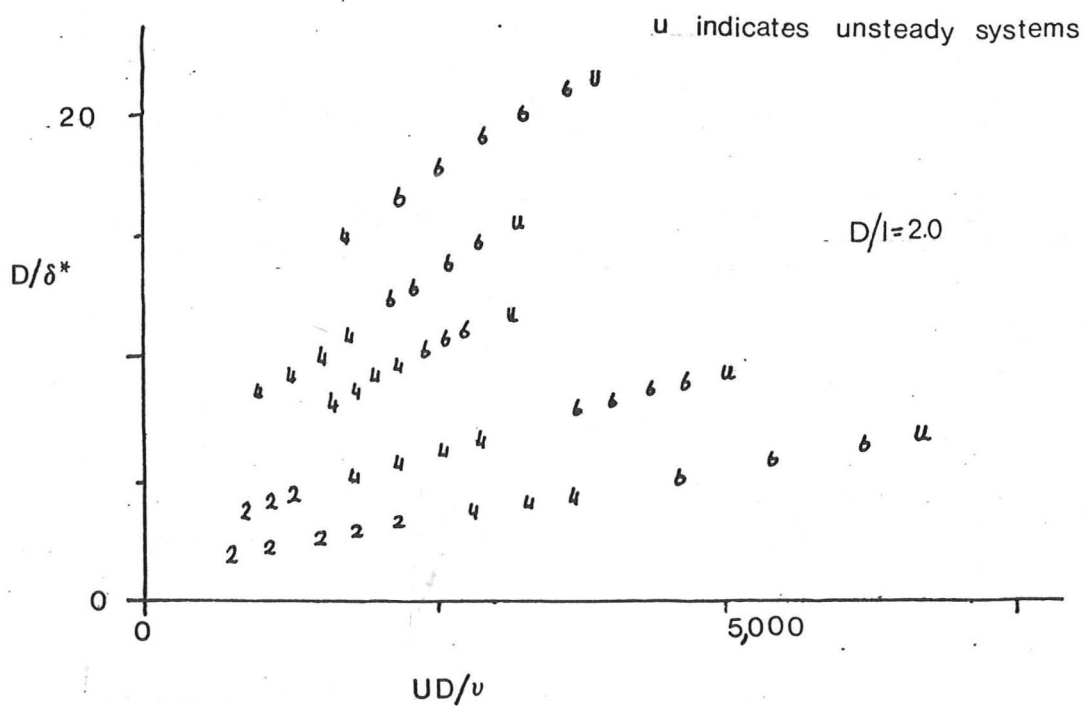
FIGURE 2.4.3 Variation in the number of vortices observed
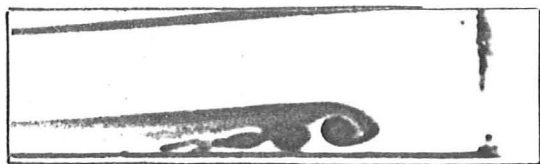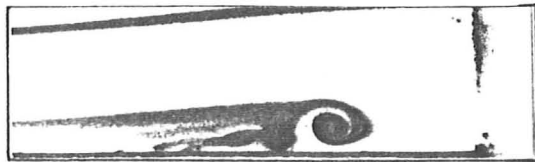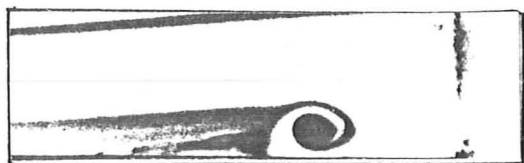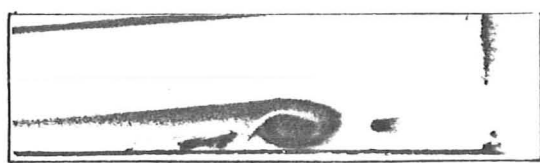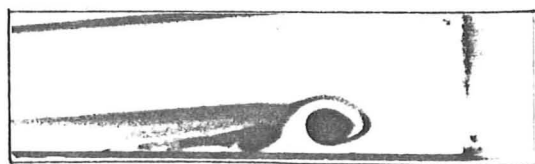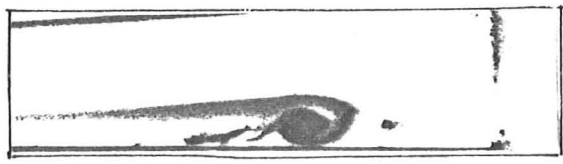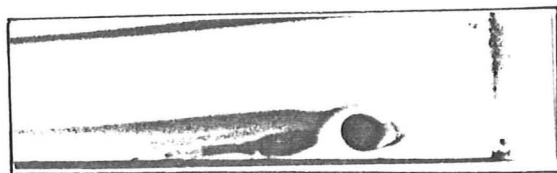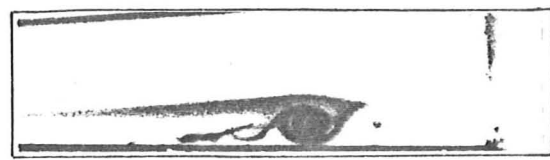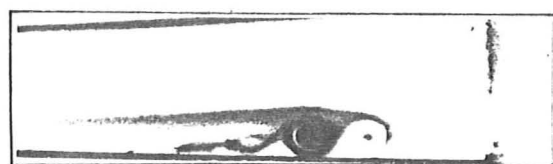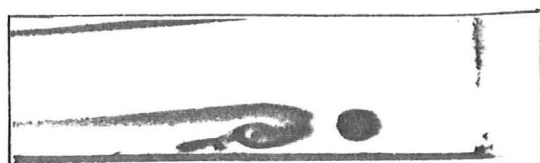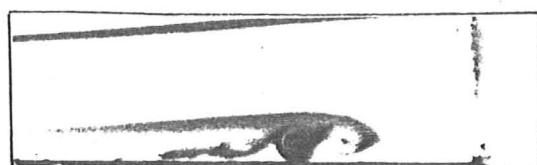
FIGURE 2.4.4 Oscillating Vortex System : $\left(UD/\nu = 5,200 ; D/\delta^* = 23.2 ; D/l = 2.0\right)$

Labels on figure: 3, 4-5-6, 7-8-9, 2, 1, 10, 14 — 13-12, 10—11, 12-13, 9, 7-8, 2-1—14, 6-5-3, 12— 1, 2, 7-6 — 5-4

vortex 3   vortex 2   vortex 1

y/D

0.05

0

-1.0   x/D   - 0.5
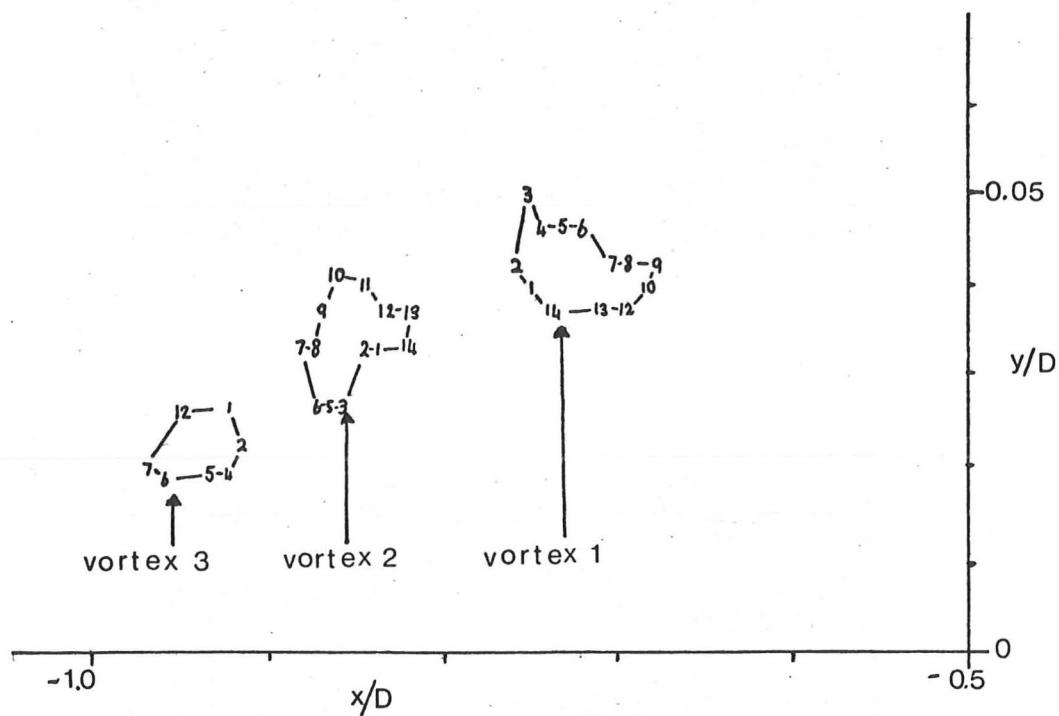
FIGURE 2.4.5 Variation of vortex position

(from figure 2.4.4)

(a) Image systems   (b) Influence of 1' on 2
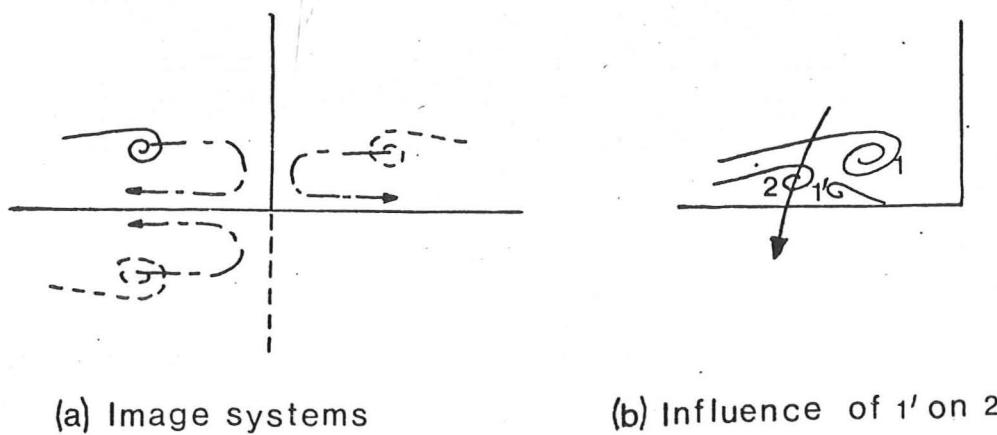
FIGURE 2.4.6 Potential vortex approximation
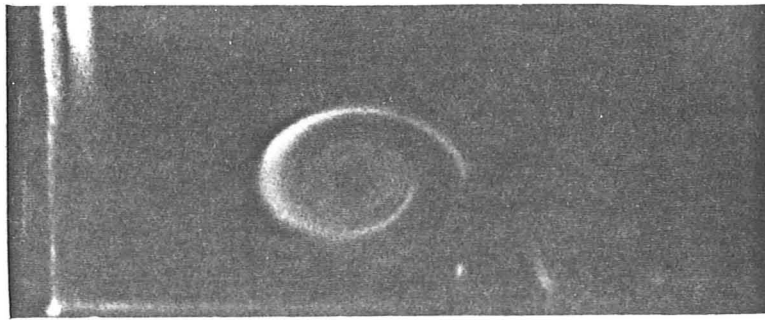
(a)
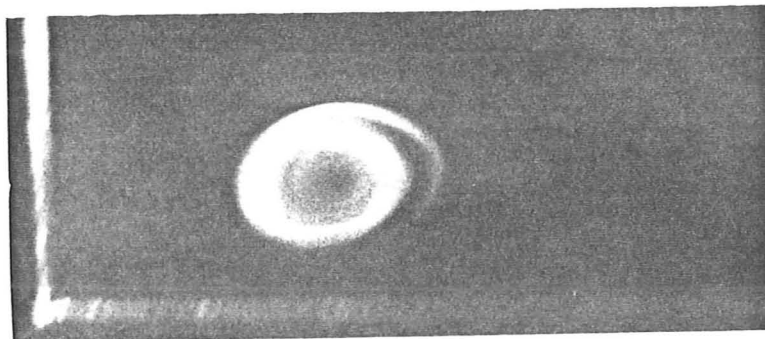
(b)
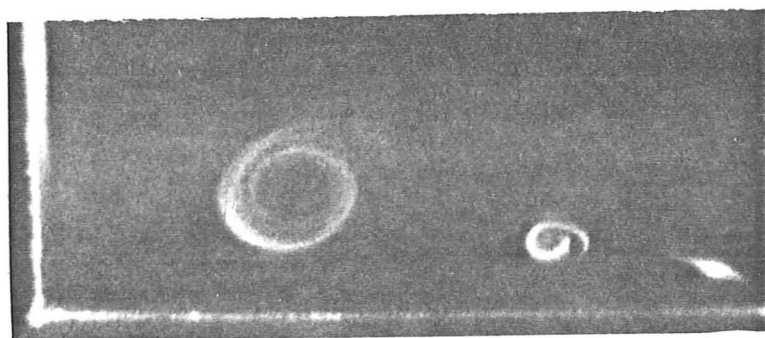
(c)

FIGURE 24.7 The horseshoe vortex away from the

plane of symmetry ($UD/\nu = 4370$, $D/\delta^* = 21.3$, $D/l = 2.0$)
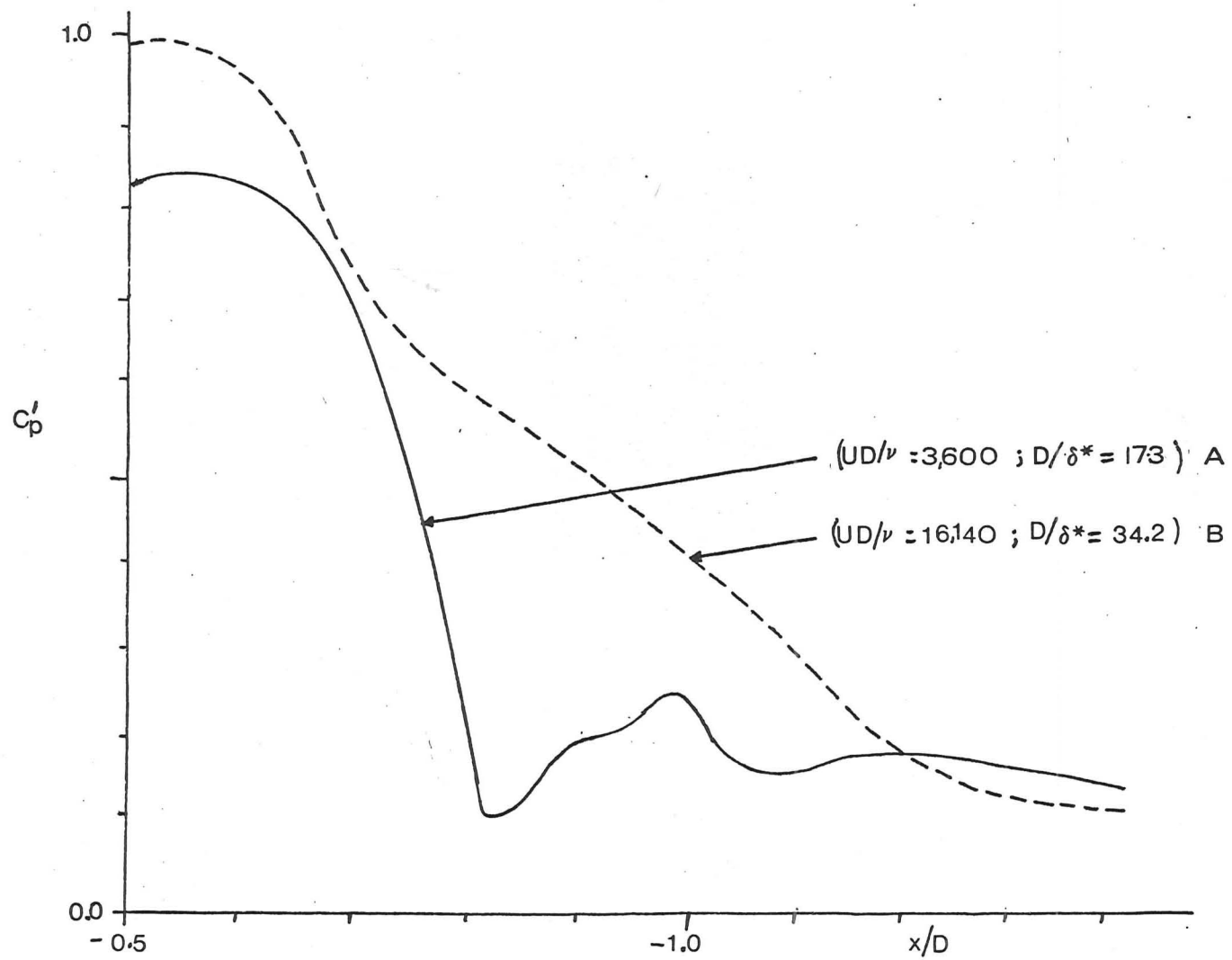
FIGURE 2.4.8 Pressure distributions upstream of cylinder (D/l=1.14)
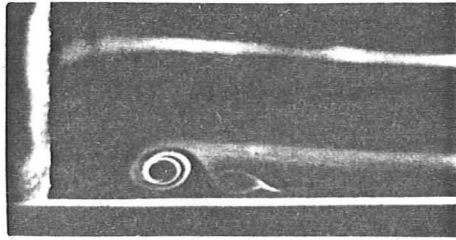
(a) no probe
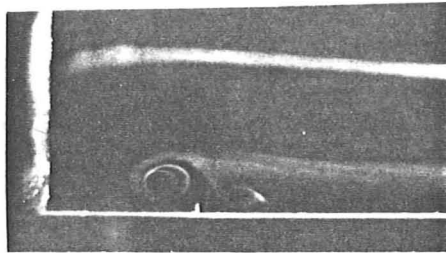
probe

(b) probe in position

FIGURE 2.4.9   Effect of hot wire probe on flow

$(UD/\nu = 4,370; \; D/\delta^* = 21.3; \; D/l = 2.0)$
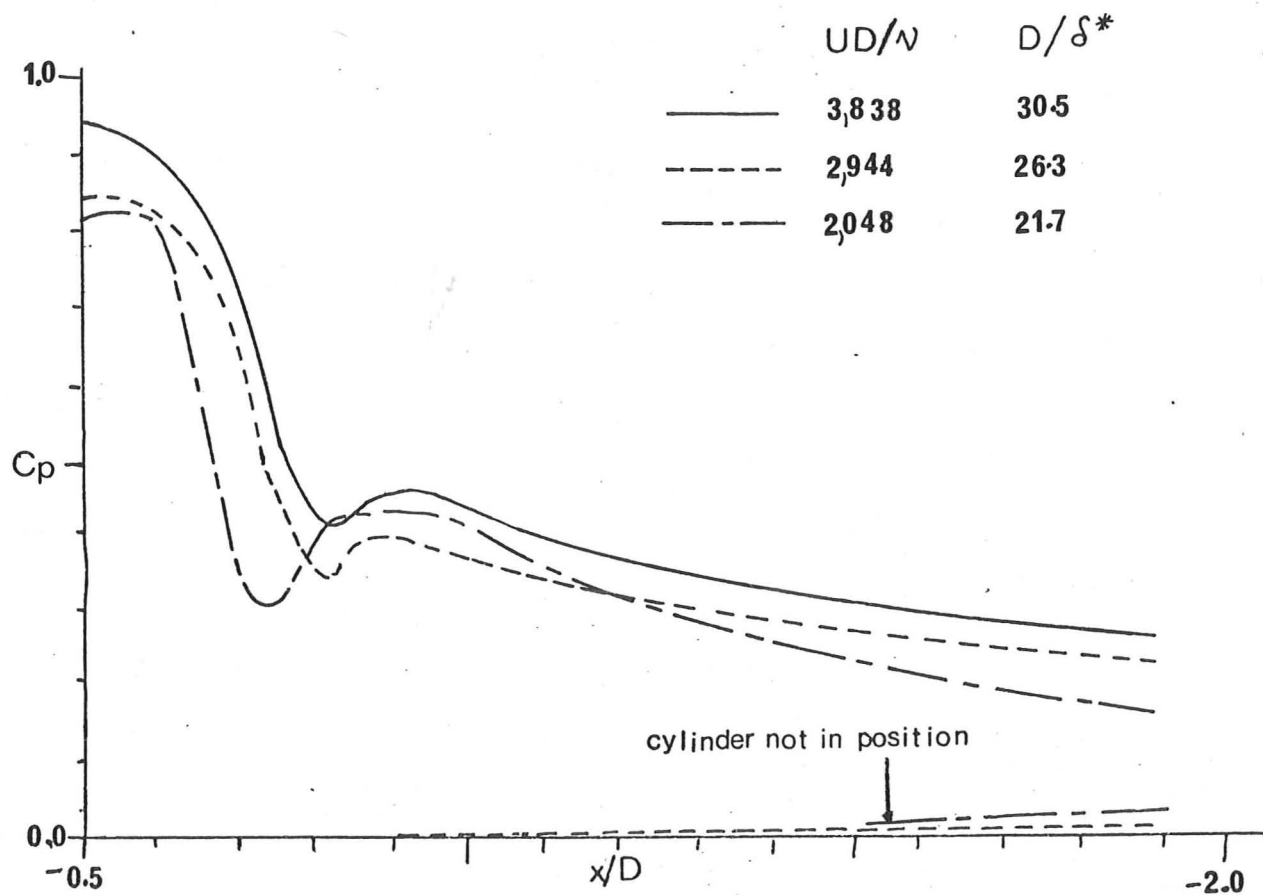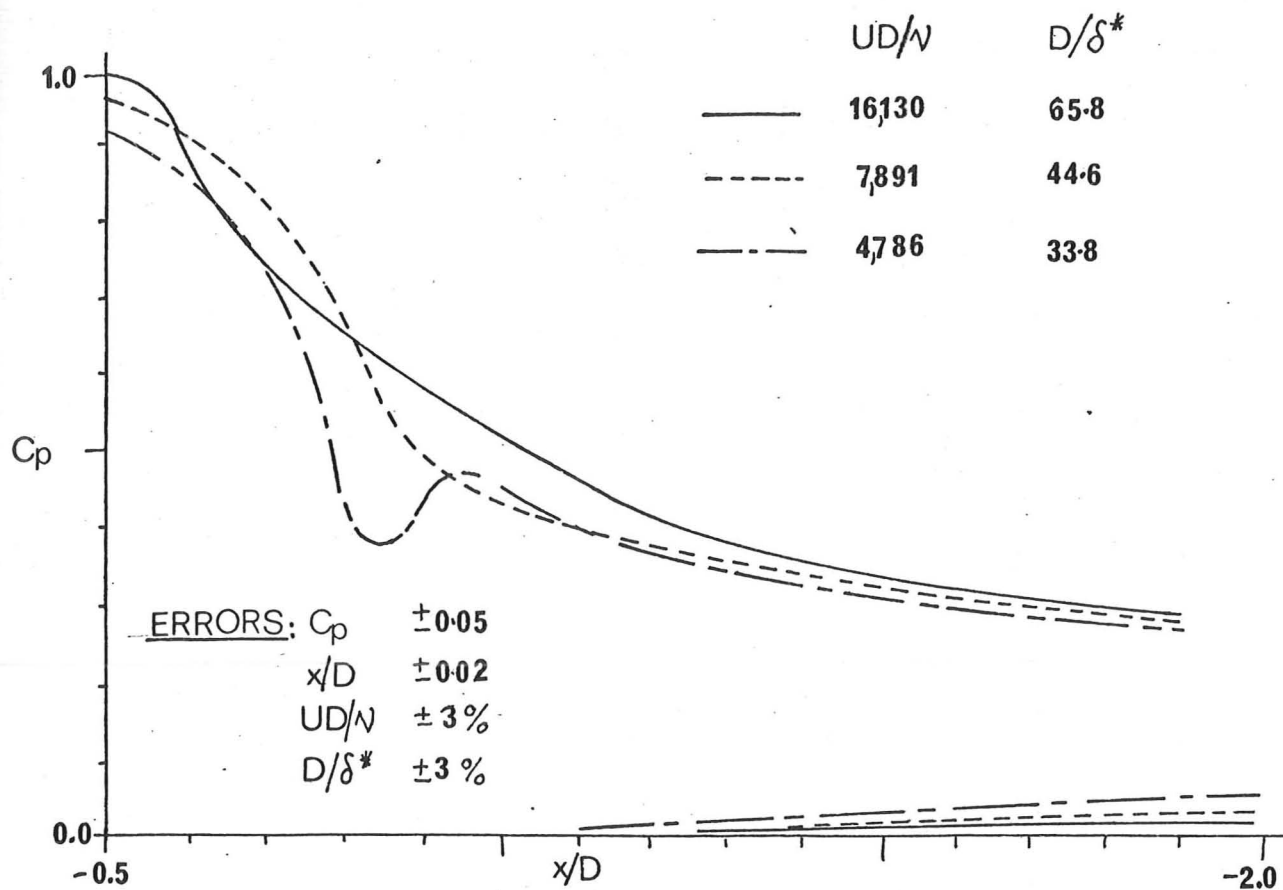
FIGURE 2.5.1 Pressure distributions upstream of cylinder (plane of symmetry)

UD/ν	D/δ*	Suction slot position
16,128	65·8	1
15,706	52·6	2
15,379	42·4	3

ERRORS: See figure 2.5.1

UD/ν	D/δ*	Suction slot position
3,838	30·5	1
3,713	25·0	2
3,719	21·7	3
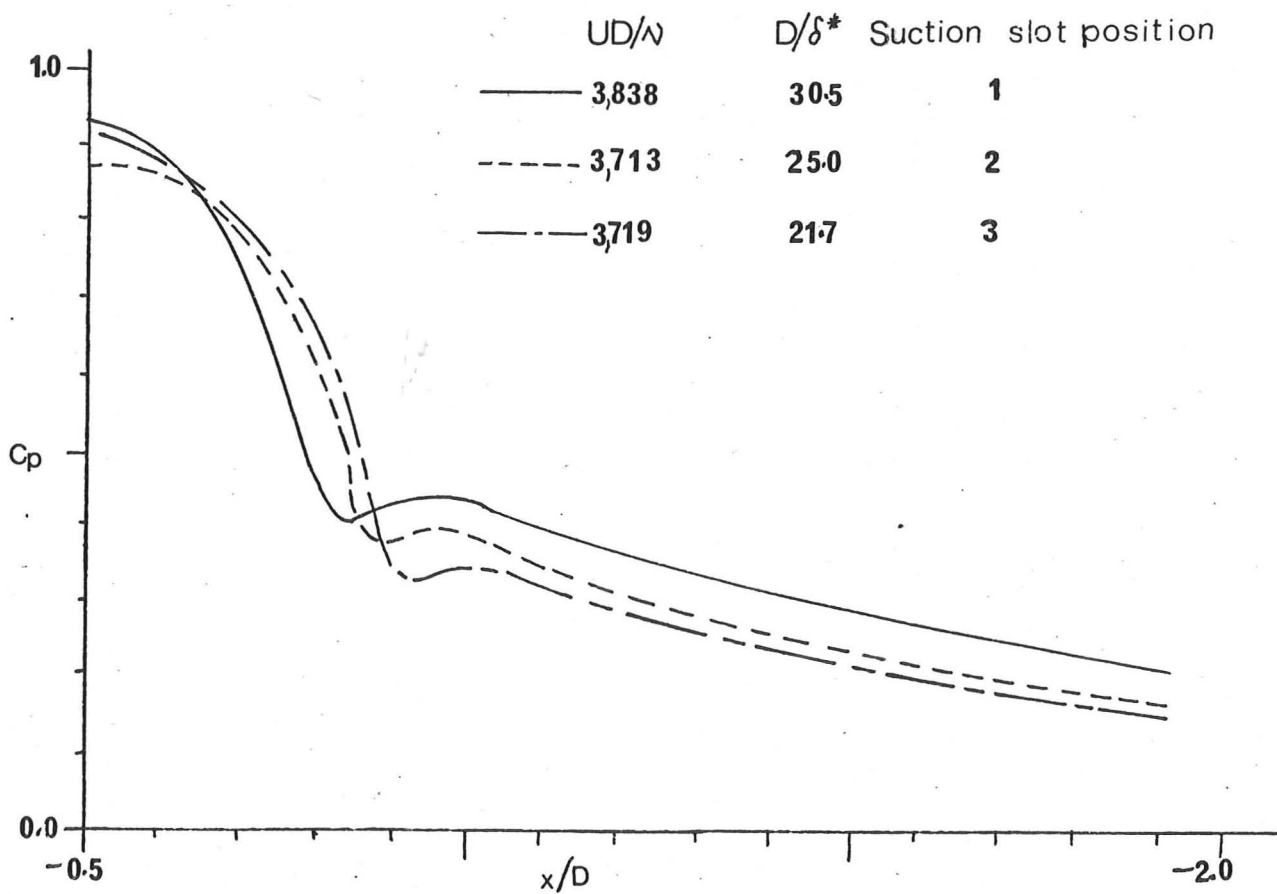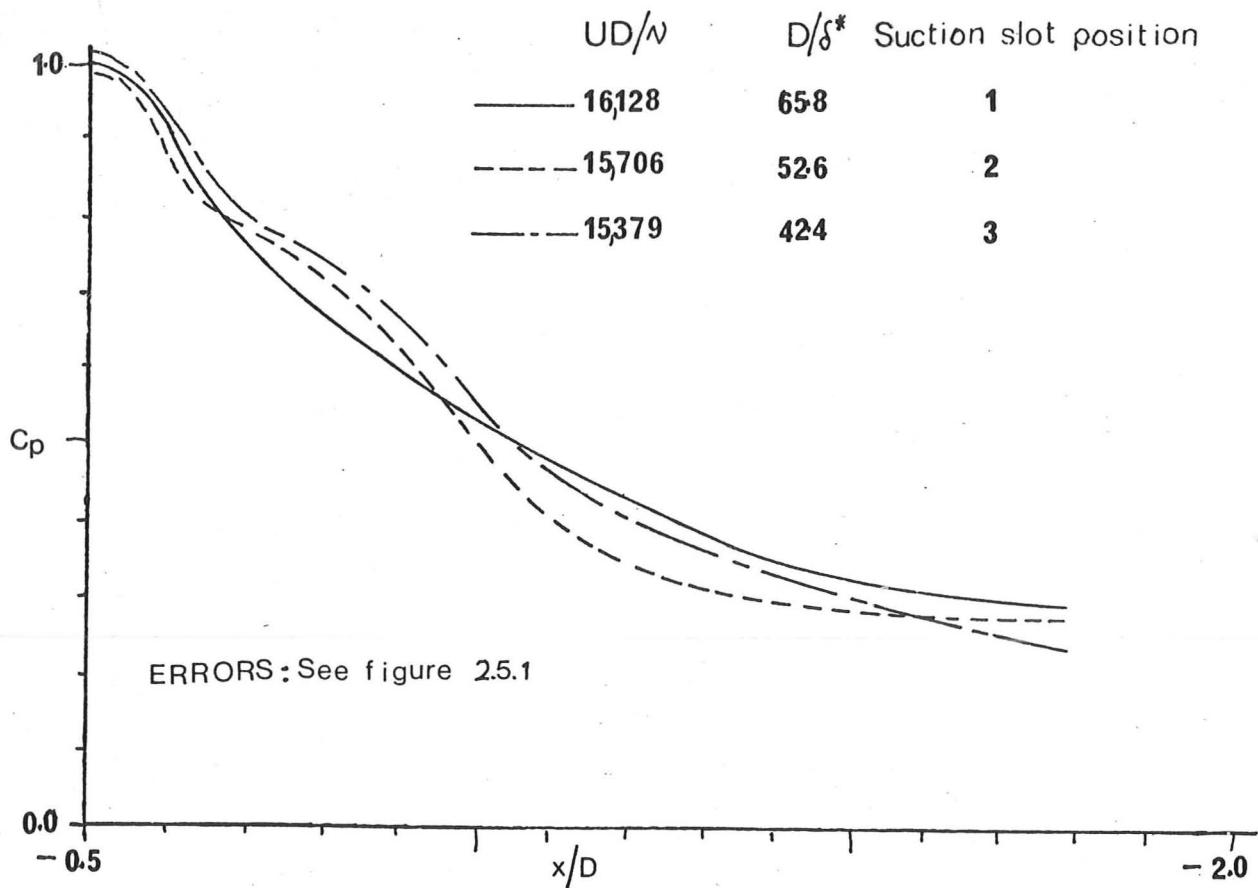
FIGURE 2.5.2 Pressure distributions upstream of cylinder (plane of symmetry)

at different suction slot positions
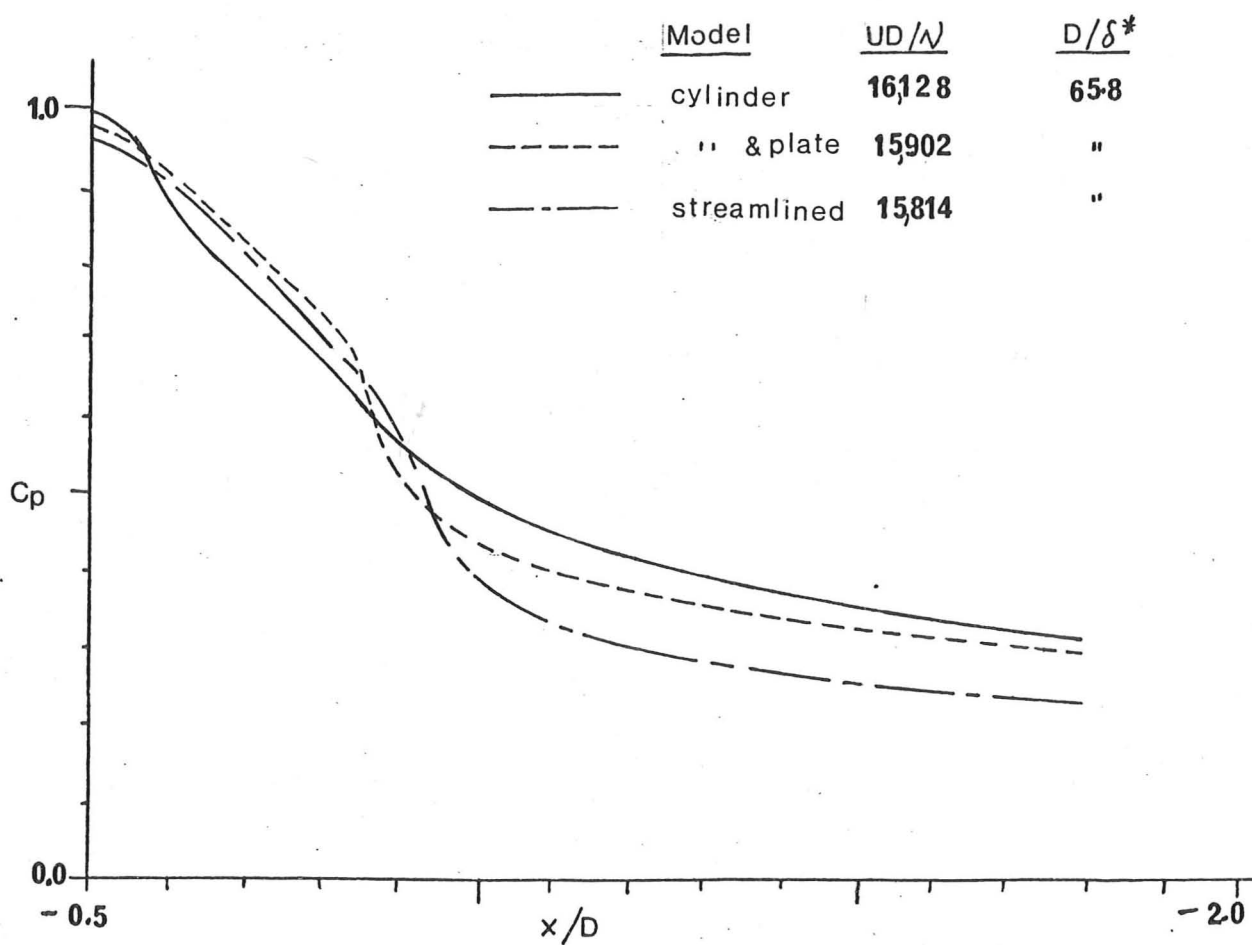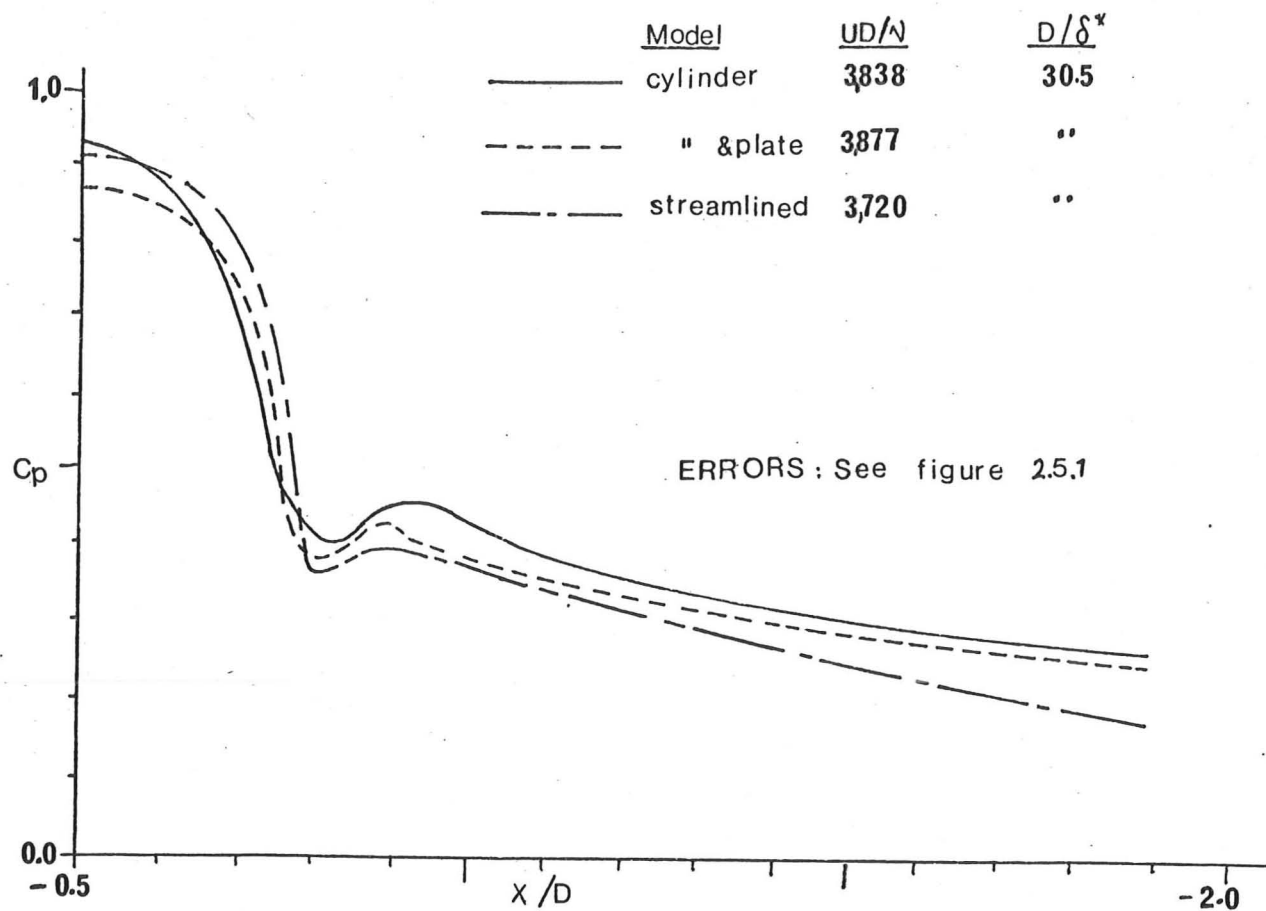
FIGURE 2.5.3 Pressure distributions on plane of symmetry upstream

of different models

Experiment: Suction slot position 1: $2{,}560 < UD/\nu < 4{,}140$

$x_s/D = 1{\cdot}18 \pm {\cdot}02$

Equation 2.6.17

"   2.6.20
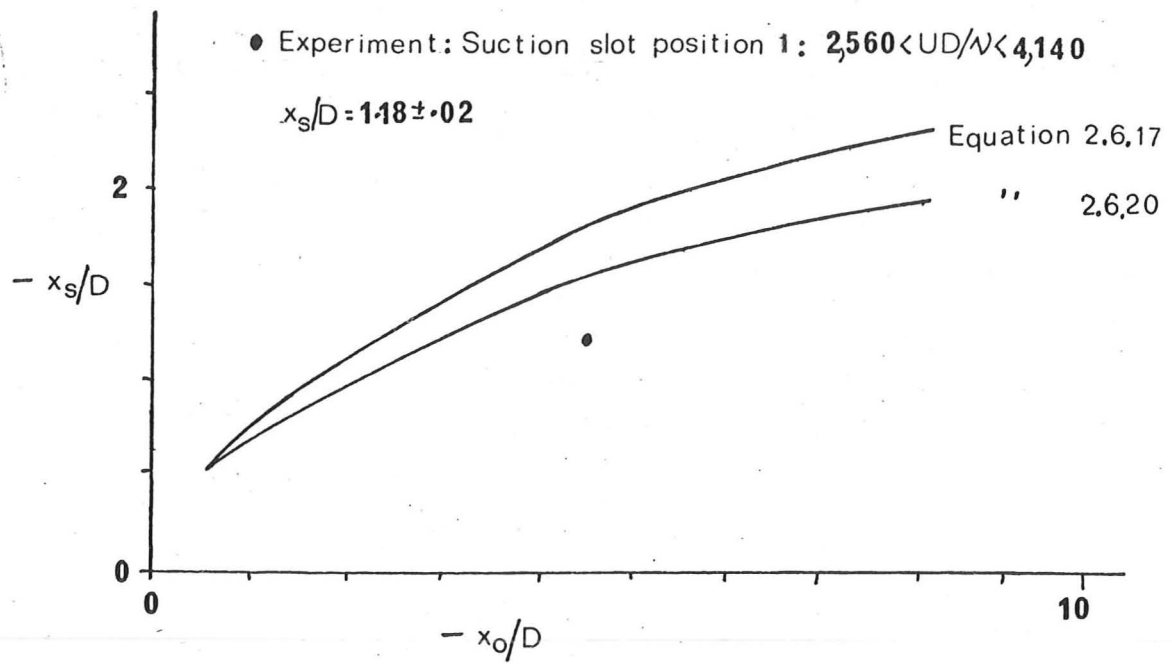
FIGURE 2.6.1 Separation position upstream of a cylinder

on a plate

Potential flow

$UD/\nu = 3{,}838$; $D/\delta^* = 30.5$

" $= 16{,}128$; " $= 65.8$
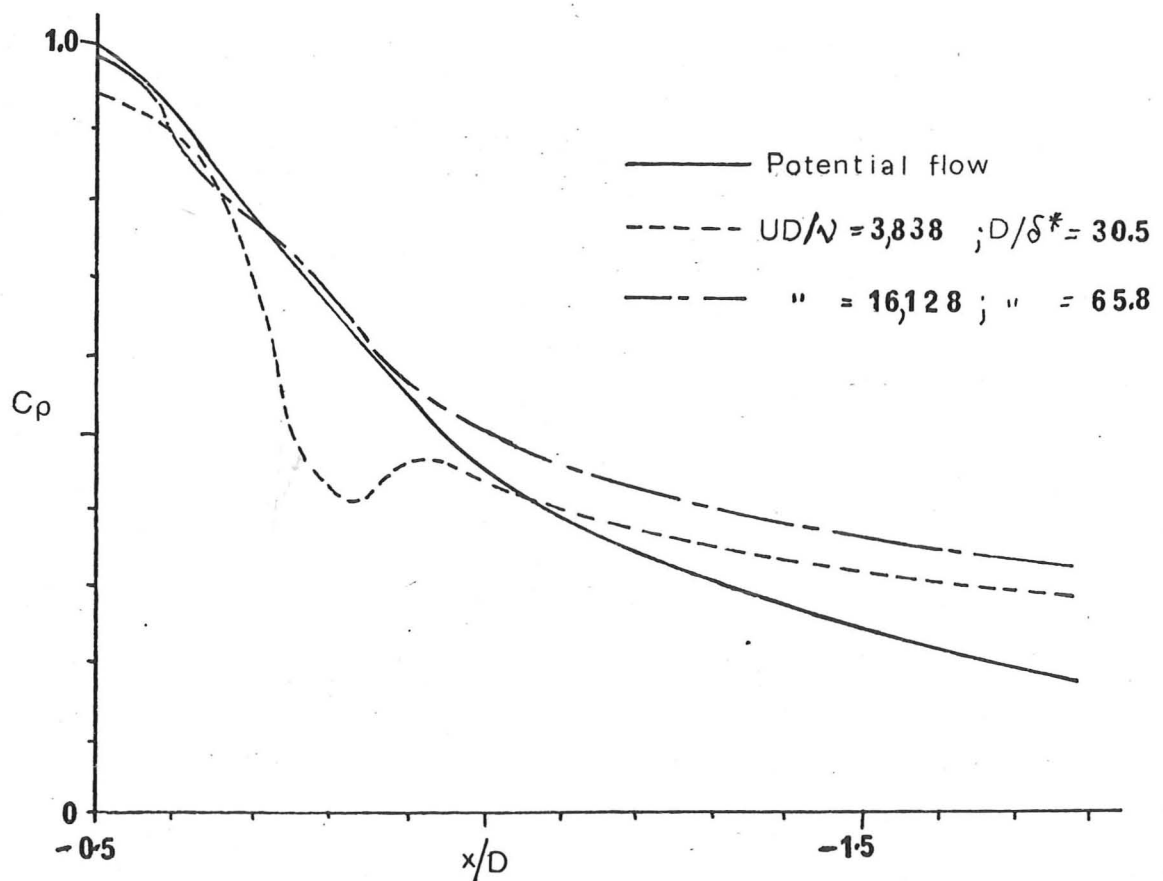
FIGURE 2.6.2: Theoretical and experimental pressure distributions
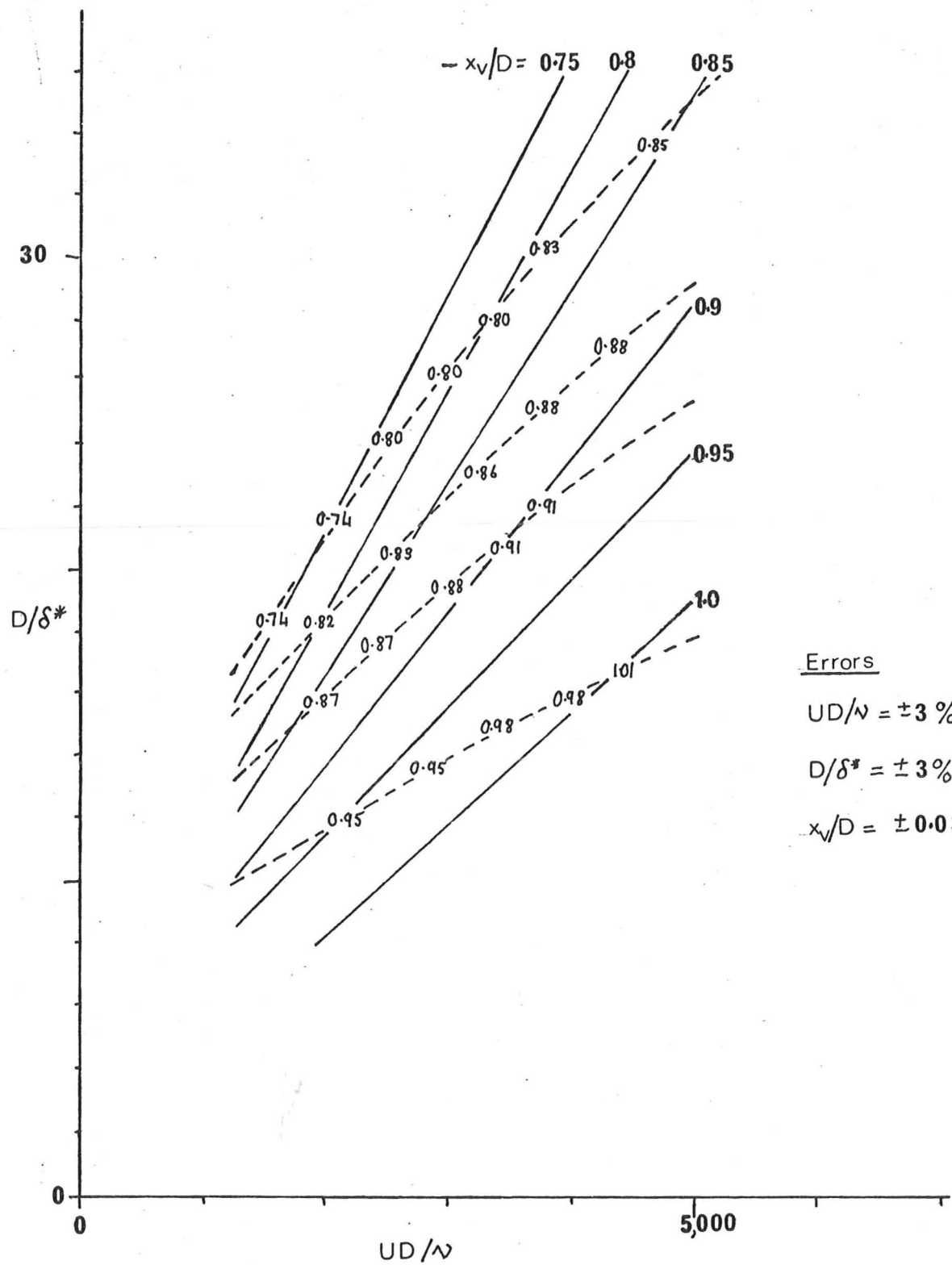
FIGURE 2.7.1 Distance of vortex 1 from cylinder centre

FIGURE 2.7.2 Distance of vortex 1 from centre of

cylinder with splitter plate
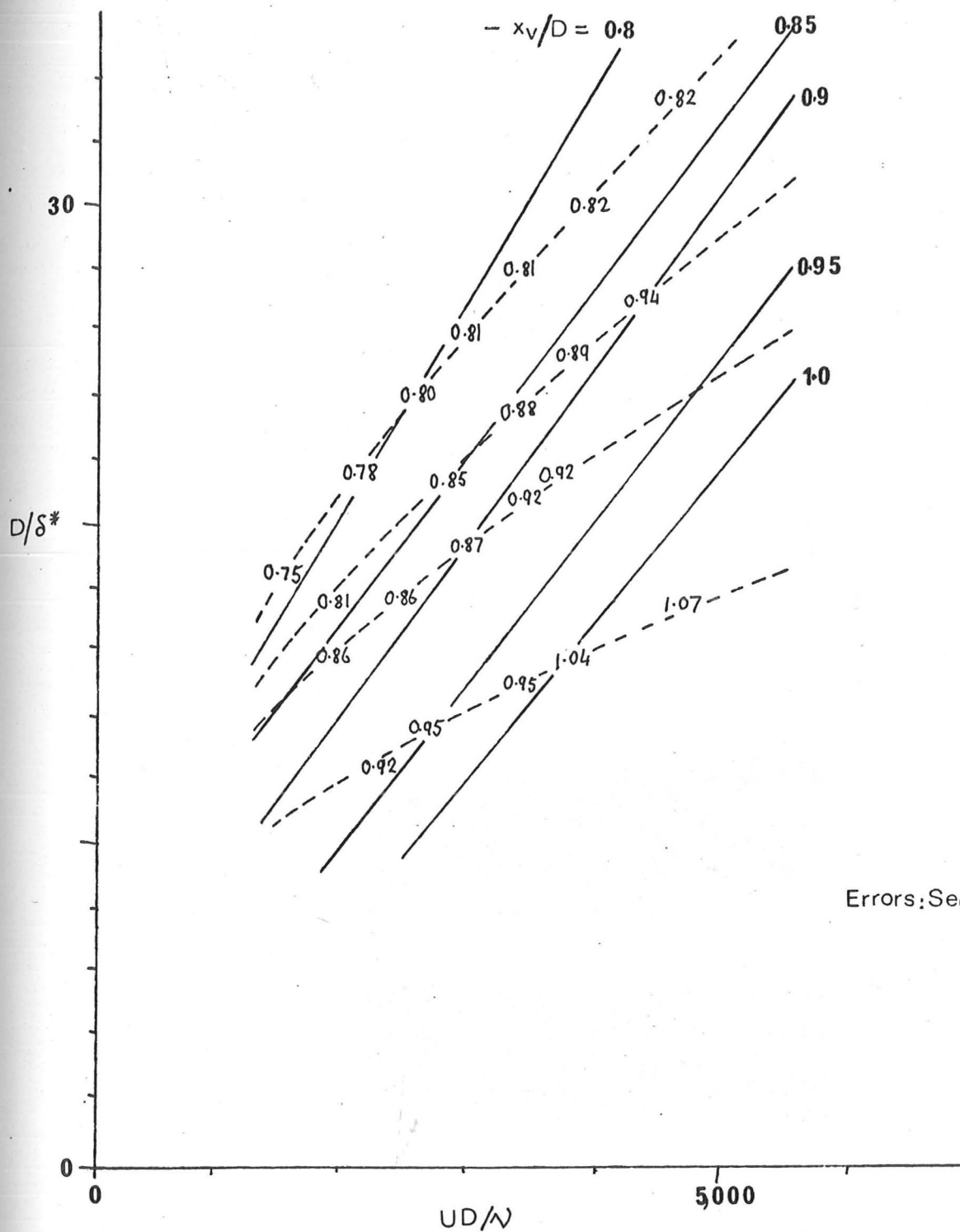
FIGURE 2.7.3 Distance of vortex I from centre of streamlined

model
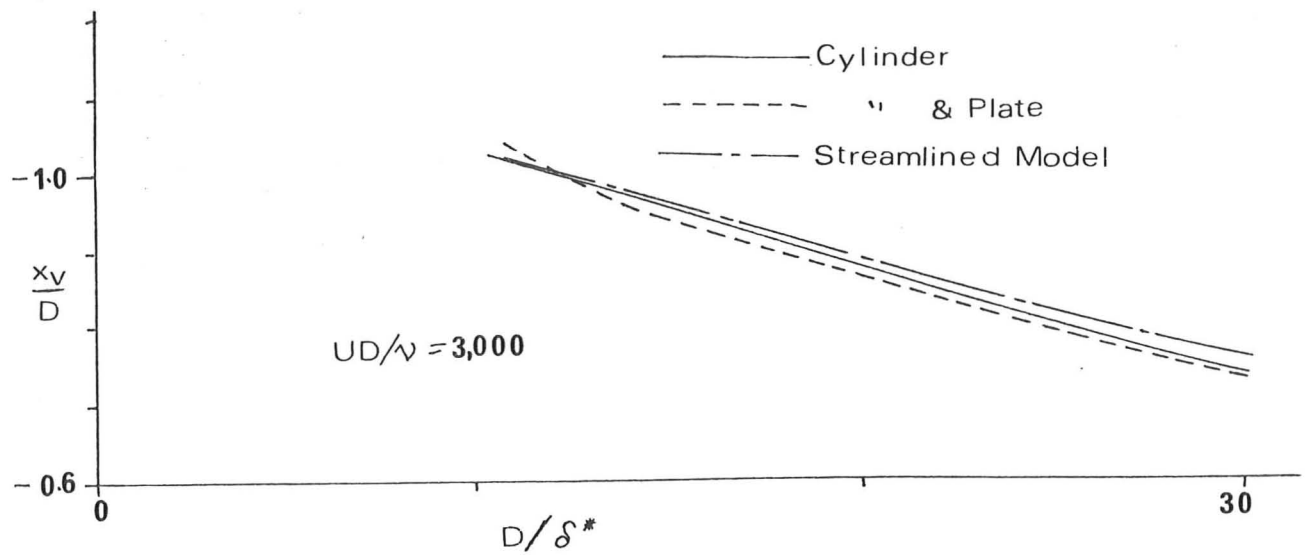
FIGURE 2.7.4 Variation of x_v/D with D/δ^*
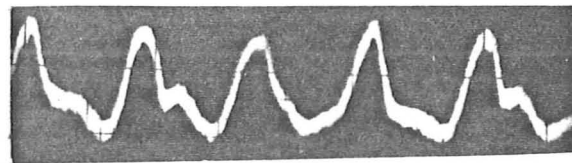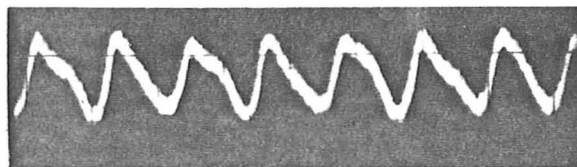
(a) Low frequency

(b) High frequency
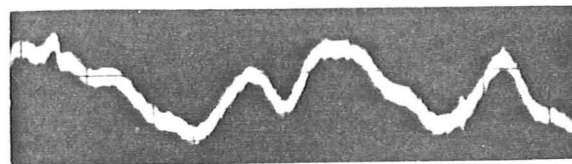
(c) Irregular trace

FIGURE 2.8.1 Observed hot wire output - probe within vortex system upstream of cylinder $\left(UD/\nu = 4{,}920 \quad D/\delta^* = 34\cdot8 \right)$

(a) Low frequency oscillation

St=0.26

$\left(UD/\mathcal{N} = 4,720 , D/\delta^* = 33.8 \right)$

Errors

$UD/\mathcal{N}$	$\pm 3\%$
D/δ^*	$\pm 3\%$
St	± 0.03
f	± 0.6 Hz
P	$\pm 10\%$

(b) High frequency oscillation

St=0.36

$\left(UD/\mathcal{N} = 4,780 , D/\delta^* = 34.2 \right)$
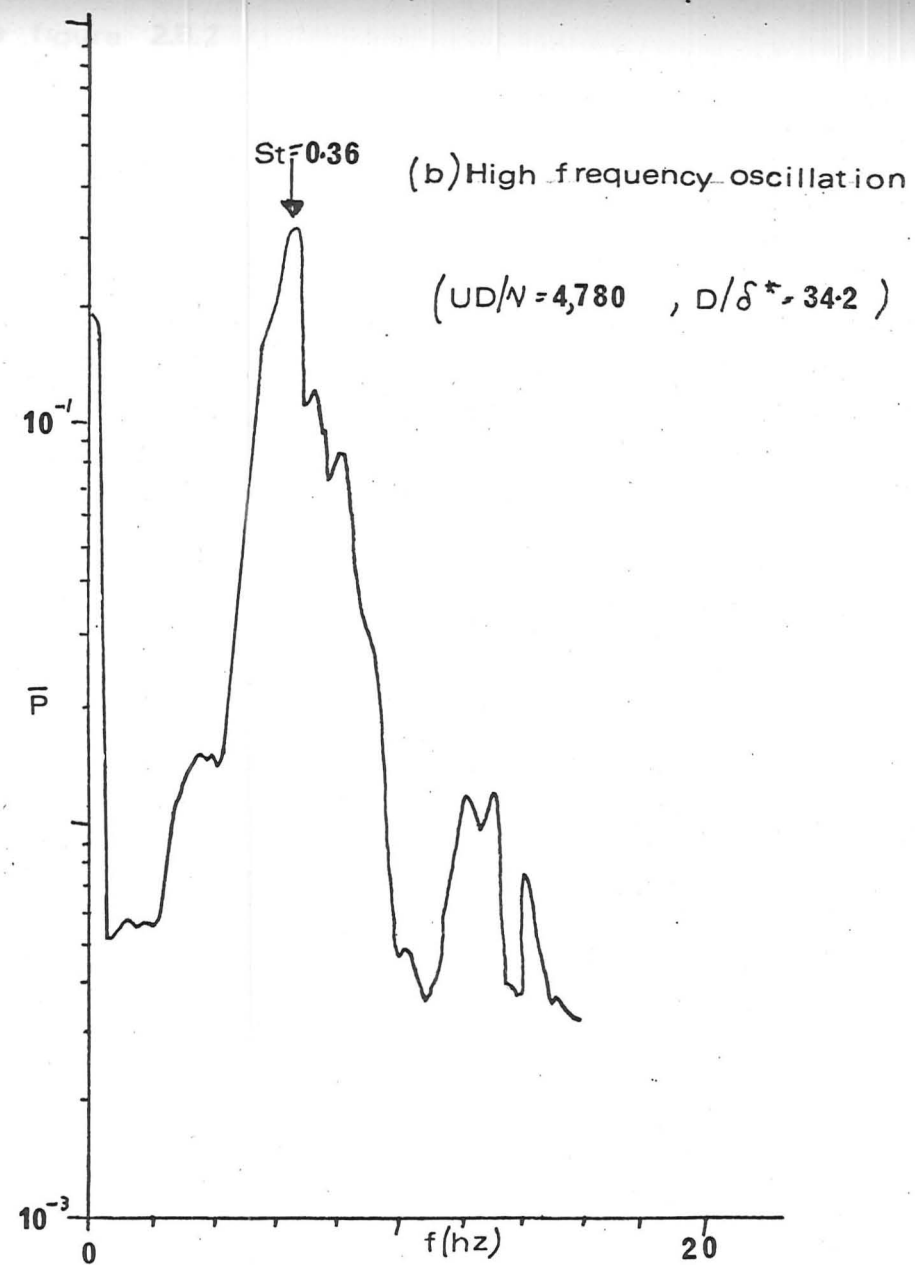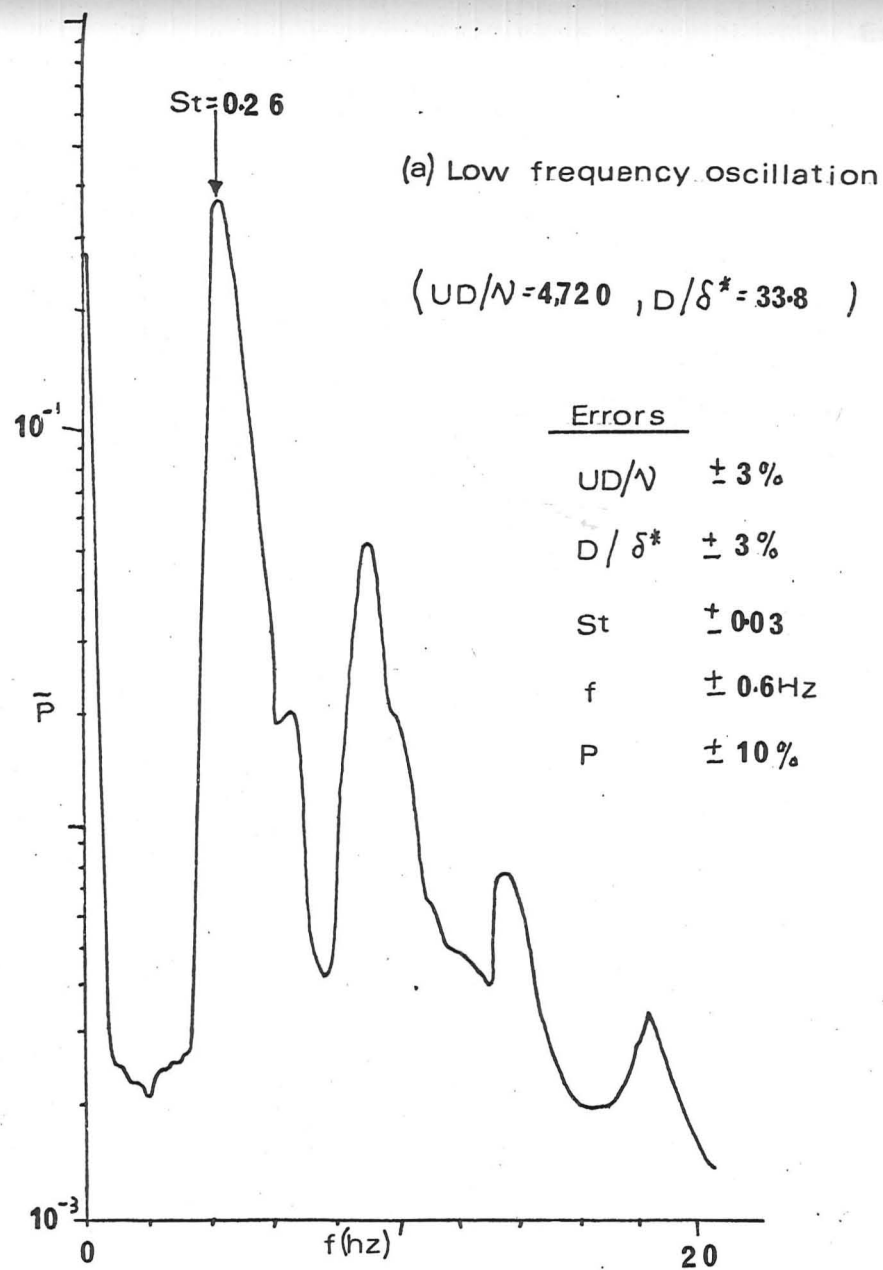
FIGURE 2.8.2 Horshoe vortex oscillation spectra $\left(x/D = -0.82, y/D = 0.063, z/D = 0 \right)$

St =041

St =028

$x/D = -0 82$, $y/D = 0063$, $z/D = 0$

10^{-1}

$\bar{P}$

$UD/\nu = 5,050$, $D/\delta^* = 34.8$

10^{-3}

0   f(hz)   20
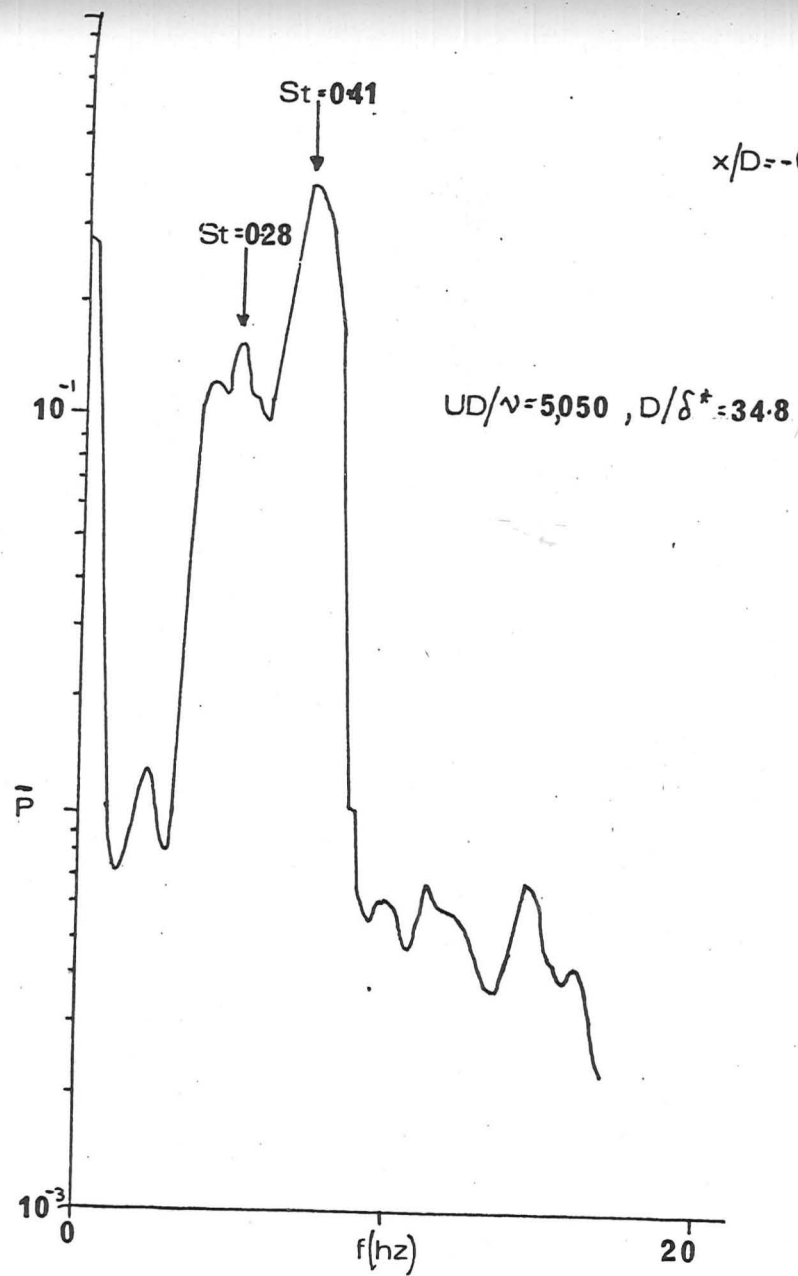
FIGURE 2.8 3 Horseshoe vortex oscillation

spectrum-both types of oscillation

10^{-1}

$\bar{P}$

$UD/\nu = 14,350$, $D/\delta^* = 62.5$

10^{-3}

0   f(hz)   20
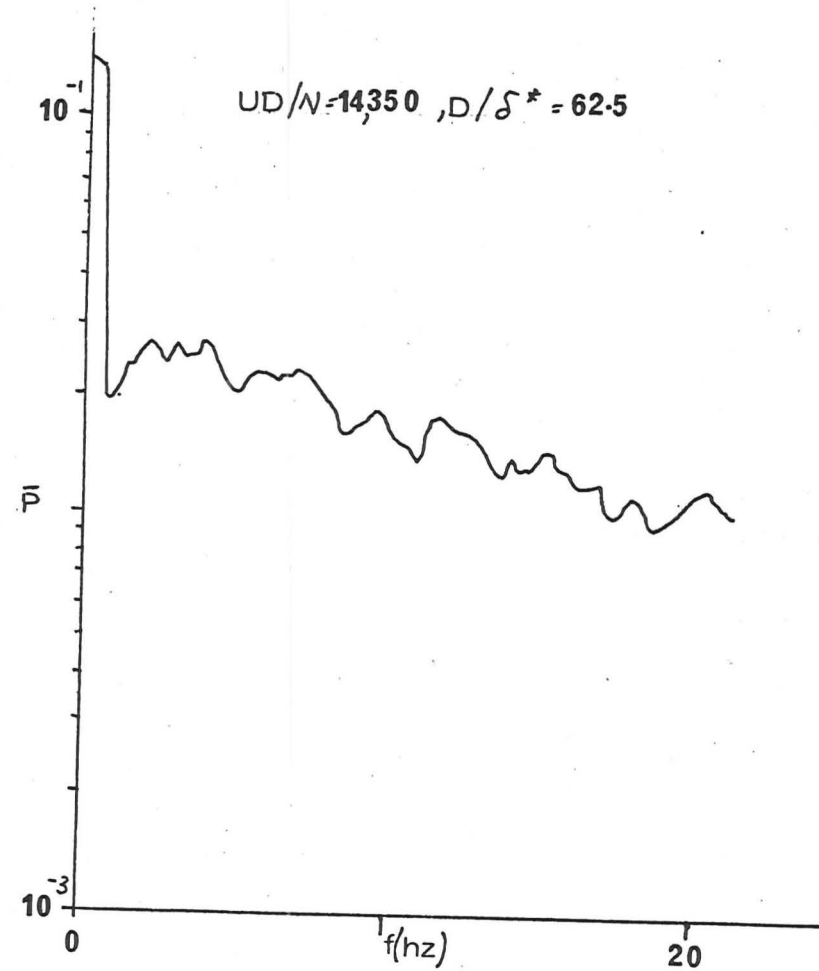
FIGURE 2.8.4 Horseshoe vortex oscillation

spectrum-no regular oscillations

+ indicates that only primary oscillations were visible

X   " .   " " secondary   "   "   "

Δ   "   "   no regular   "   "   ..

(a) Primary Oscillations

(b) Secondary oscillations

FIGURE 2.8.5   Variation of vortex oscillation frequencies

(a) $UD/\nu = 11,200$, $D/\delta^* = 43.8$

(b) $UD/\nu = 11,500$, $D/\delta^* = 44.8$

(c) $UD/\nu = 11,800$, $D/\delta^* = 44.8$

(a) Cylinder

(b) Cylinder with splitter plate

(c) Streamlined model
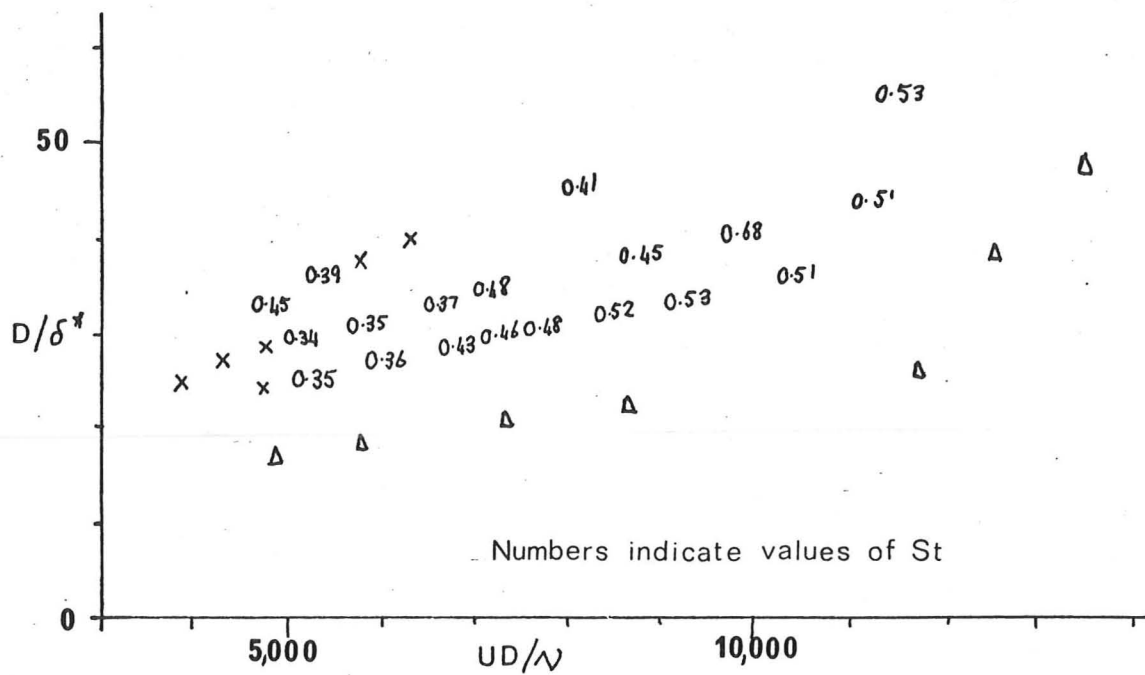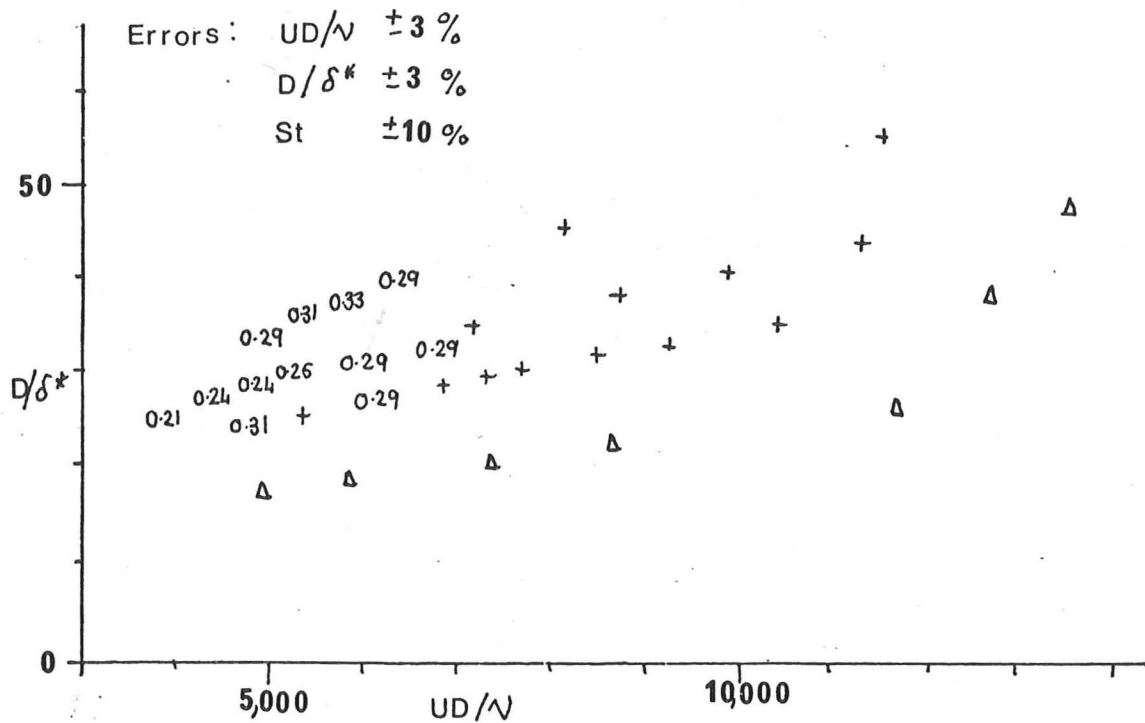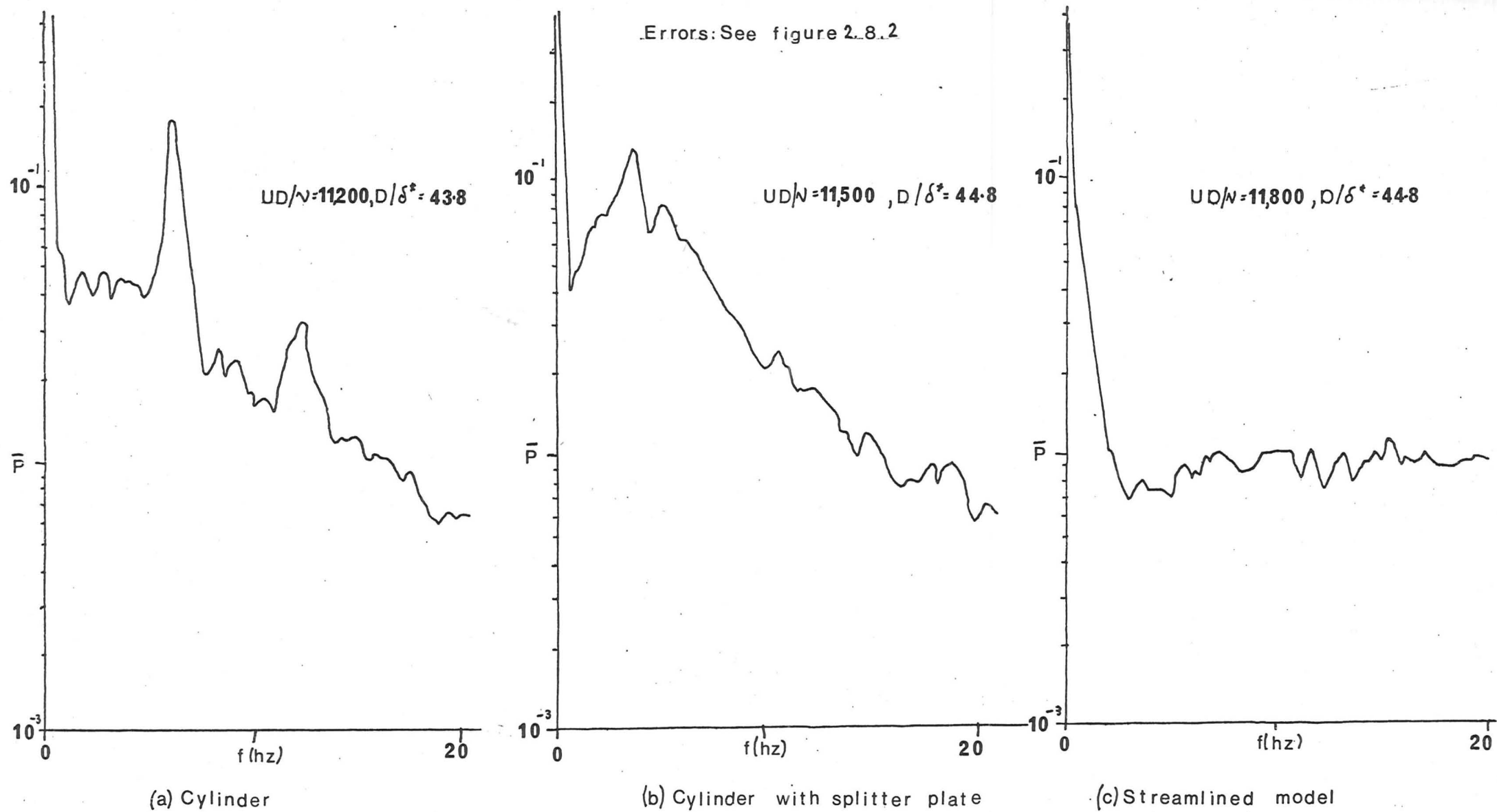
FIGURE 2.8.6   Wake   spectra ($x/D = 6.3$, $y/D = 1.42$, $z/D = 0.77$)
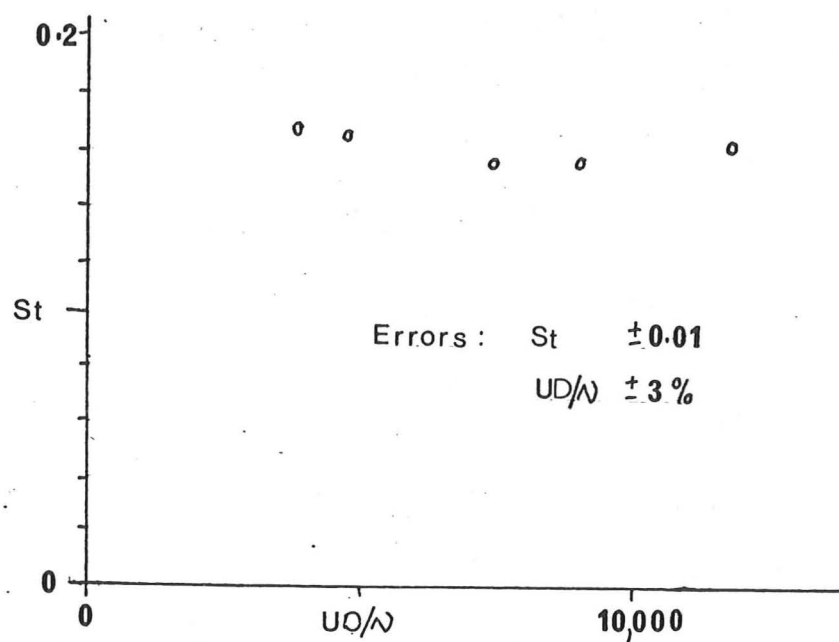
FIGURE 2.8.7 Vortex shedding from cylinder
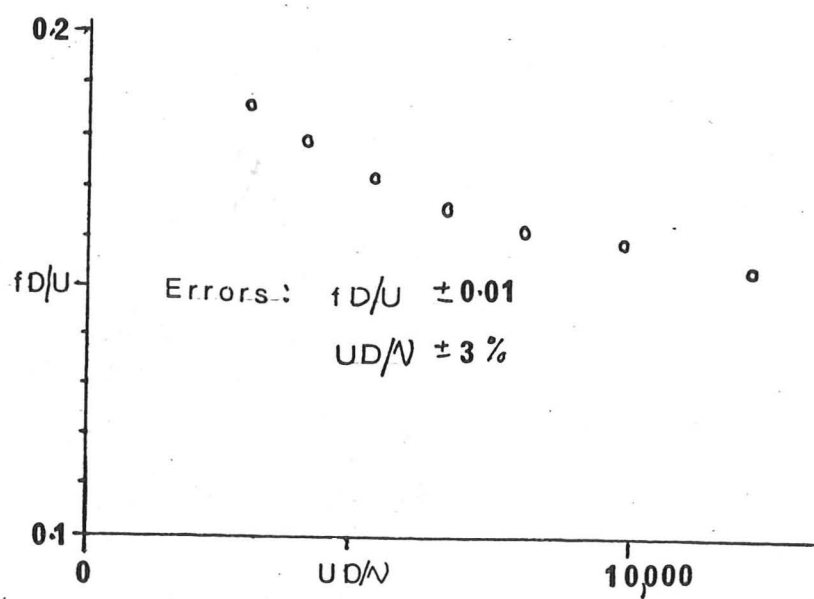
FIGURE 2.8.8 Variation in fan speed

Errors:See figure 2.8.2
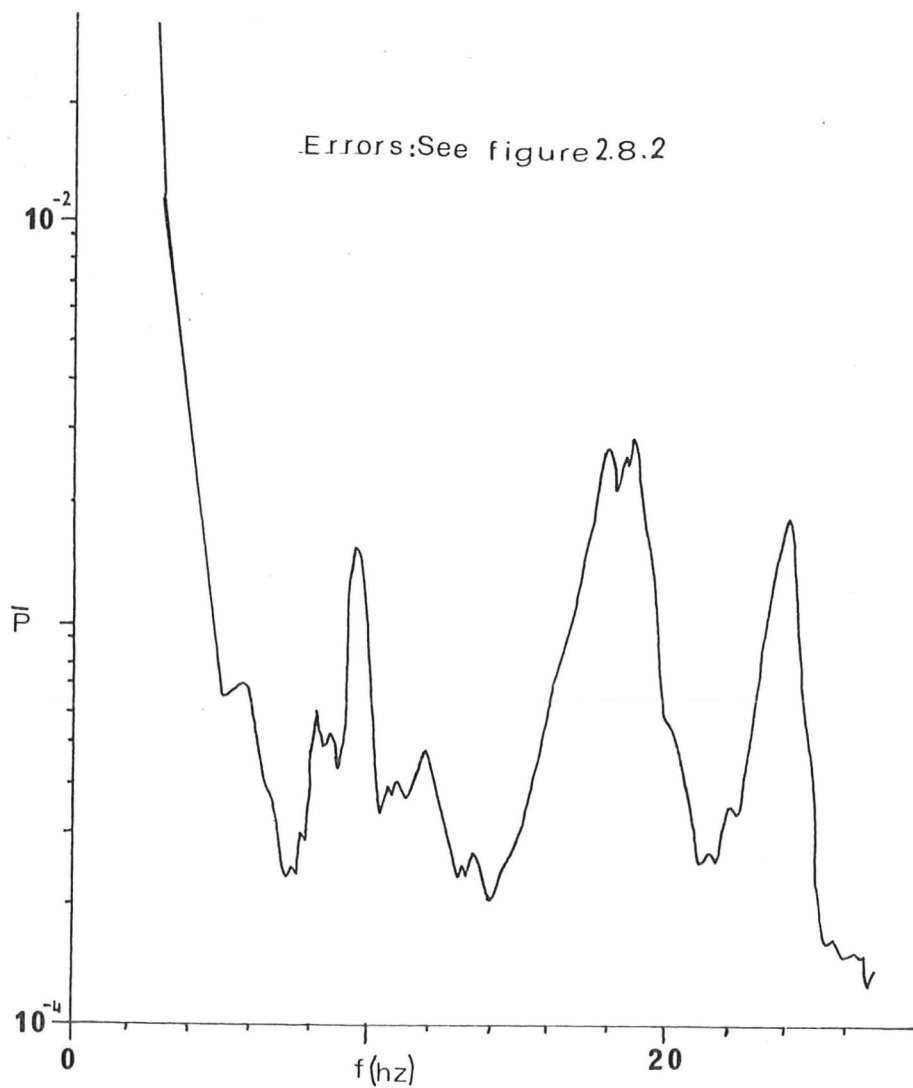
FIGURE 2.8.9. Boundary layer spectrum $\left(UD/\mathcal{N} = 4,750, D/\delta^* = 340, \right.$

$\left. y/D = 0.063 \right)$

$\leftarrow x/D = -2.08, y/D = 0.031, z/D = 0$

$\leftarrow x/D = -0.81,$ ''   ''

1 s
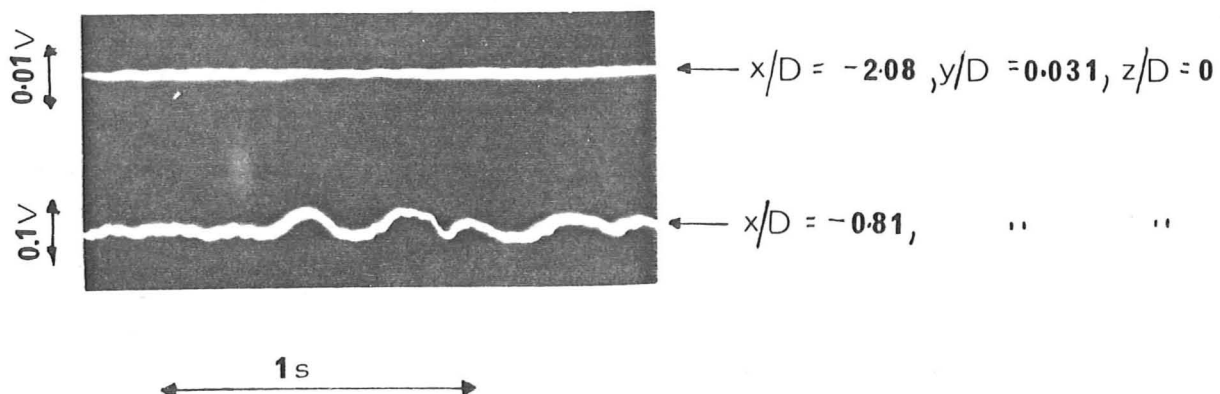
FIGURE 2.8.10 Start of vortex oscillations $\left(UD/\mathcal{N} = 5,330, D/\delta^* = 36.2 \right)$

Plan

View A A

FIGURE 2.9.1

FIGURE 2.9.2

Equation 2.9.25

Equation 2.9.26
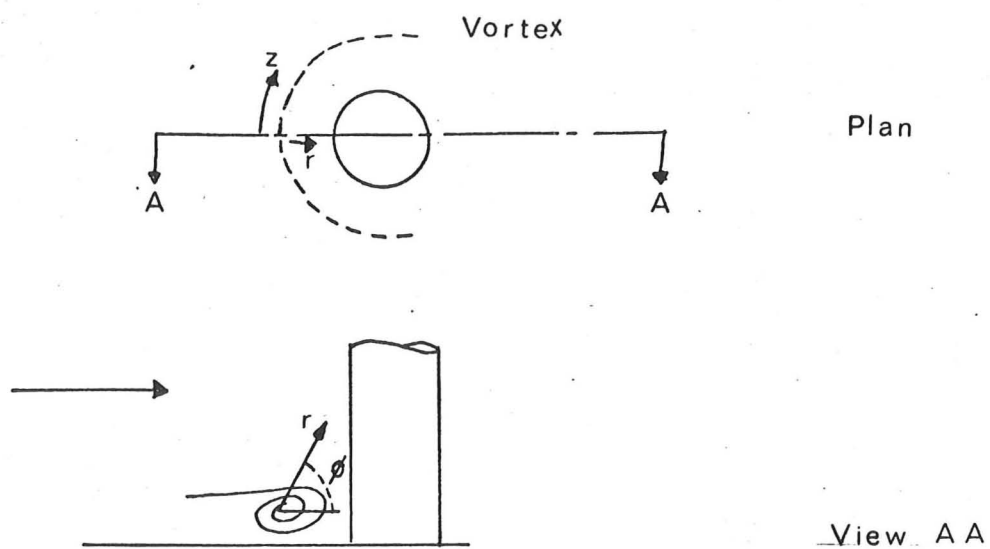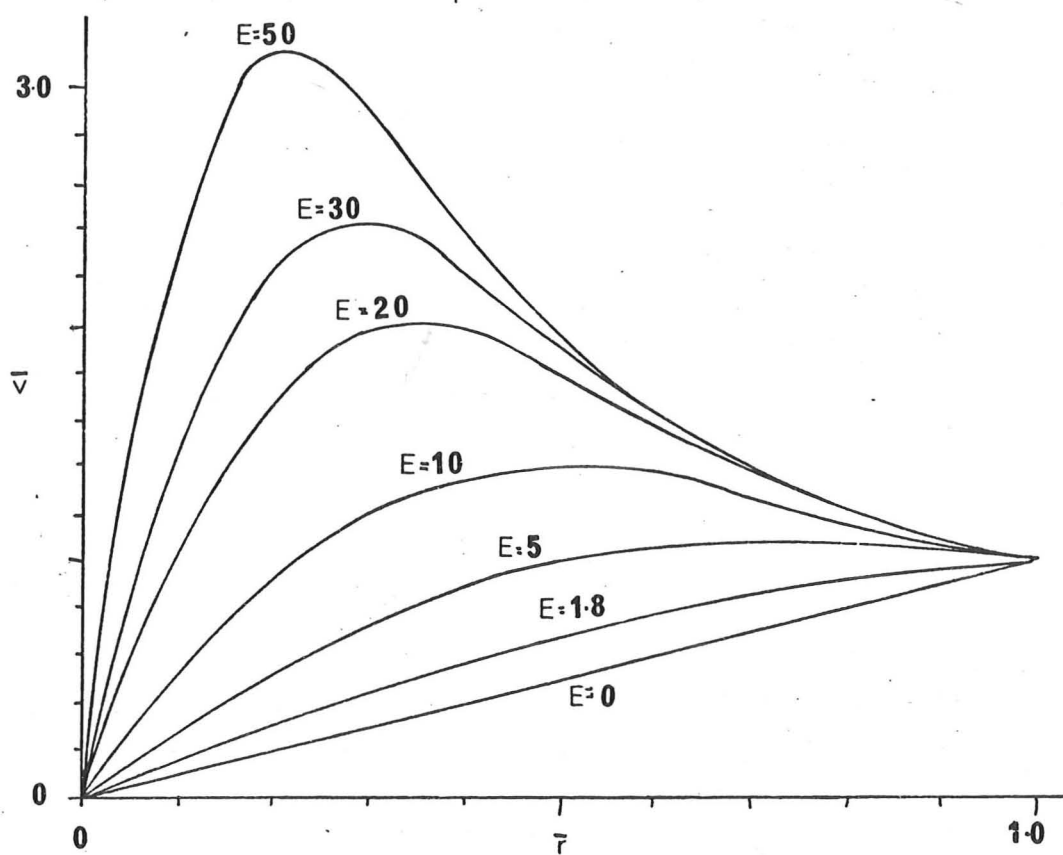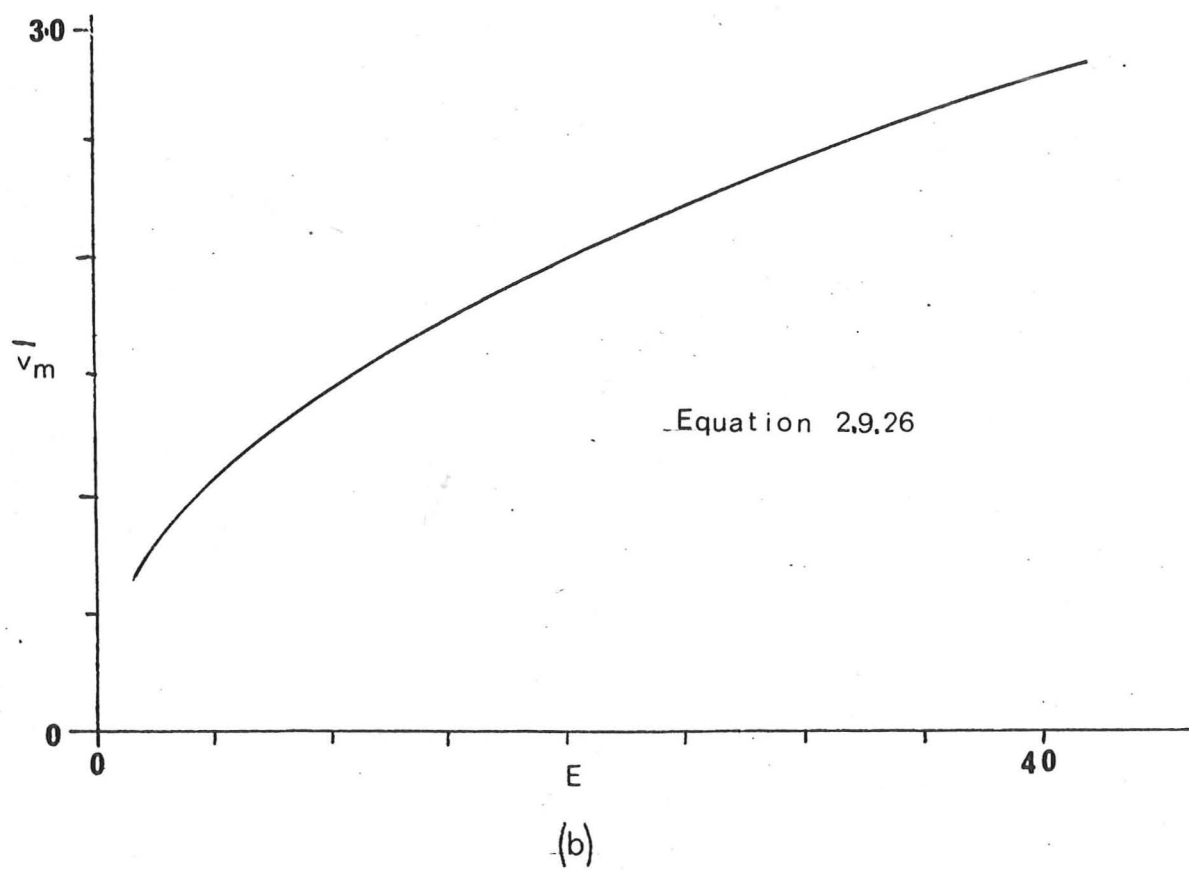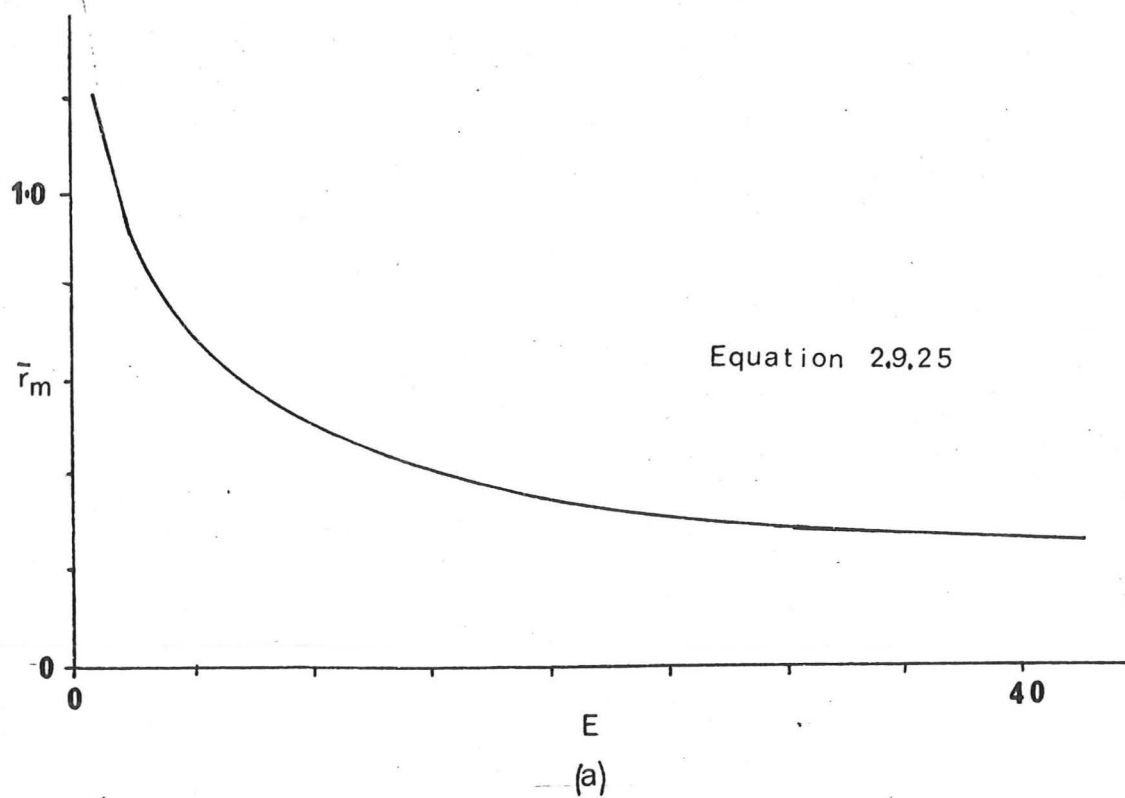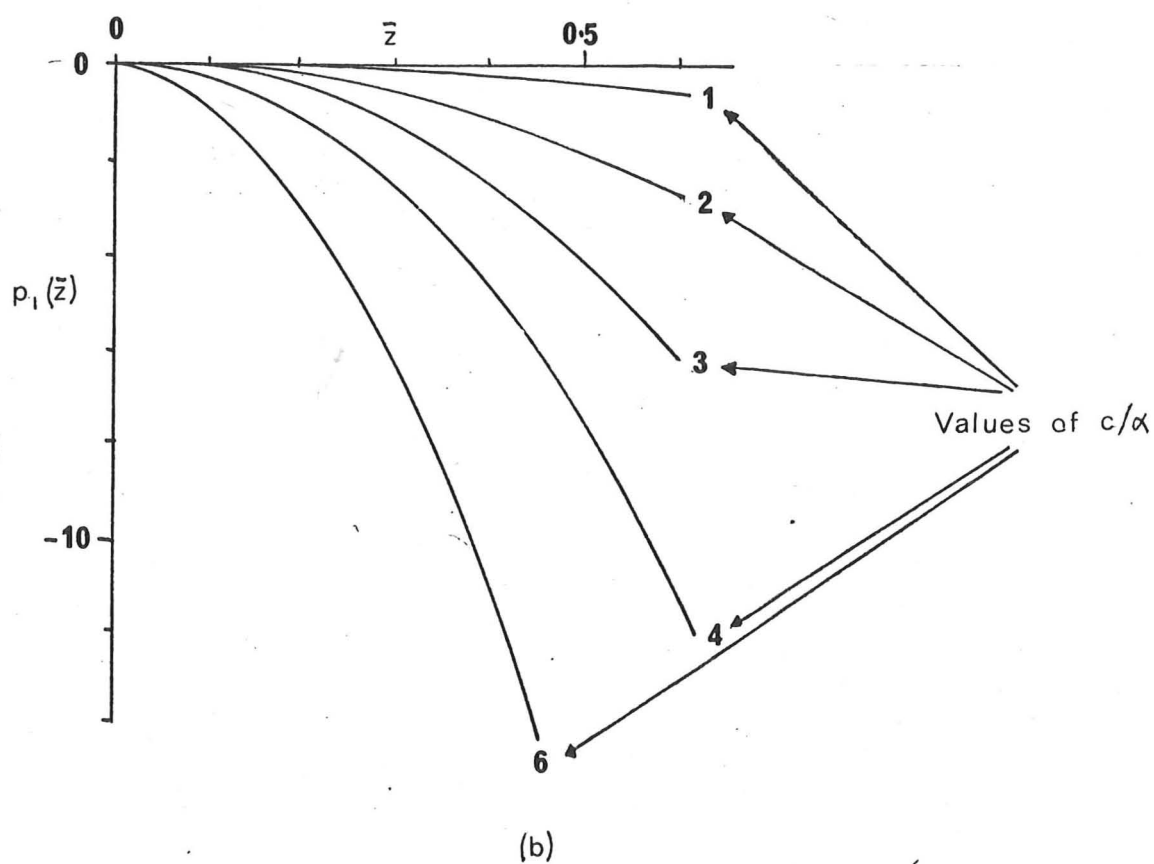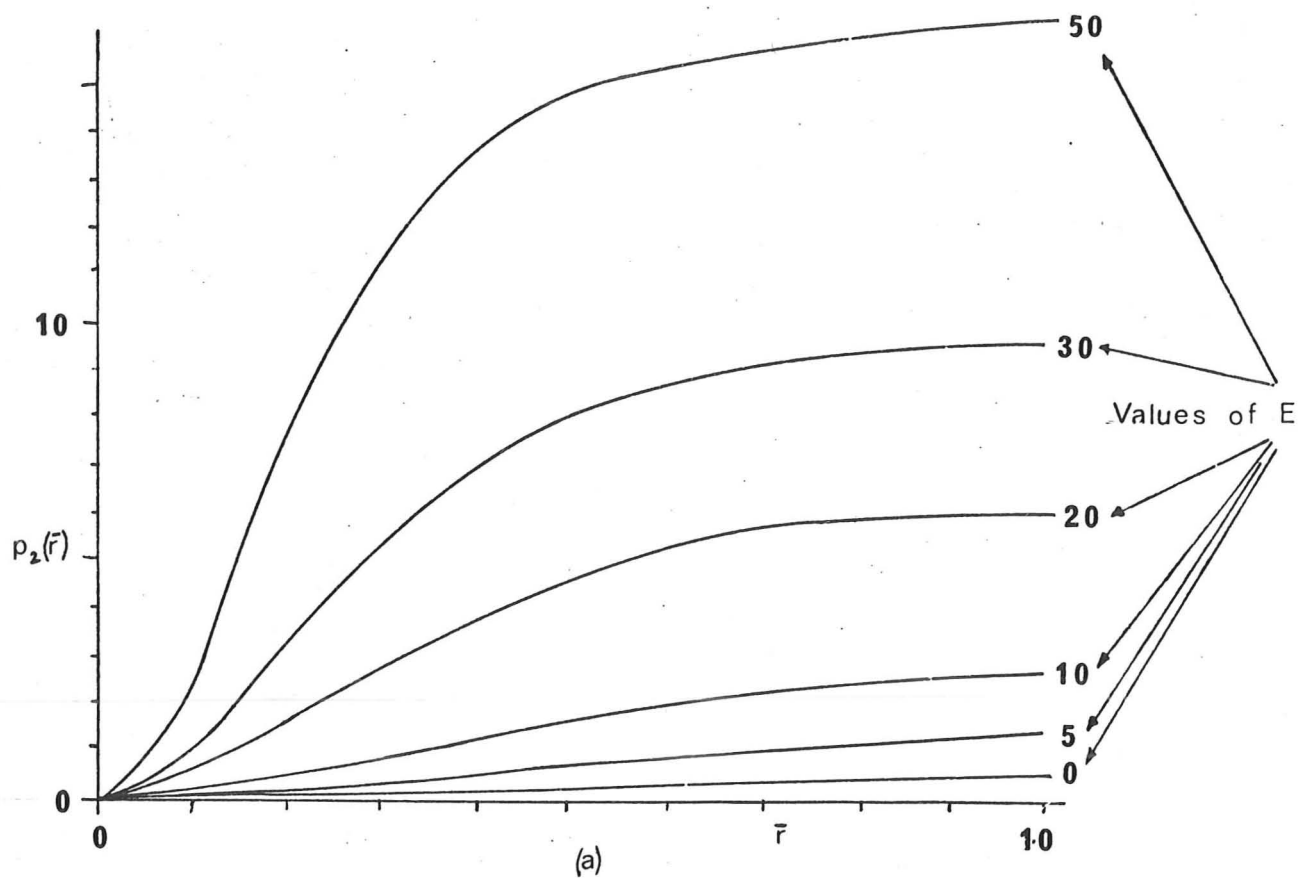
FIGURE 2.9.3

FIGURE 29.4

FIGURE 2.9.5 (after Vasanta Ram)

FIGURE 2.9.6

Influence
of images →
on flow

cylinder

"images"

51cm x 71cm tunnel·

cylinder

"images"
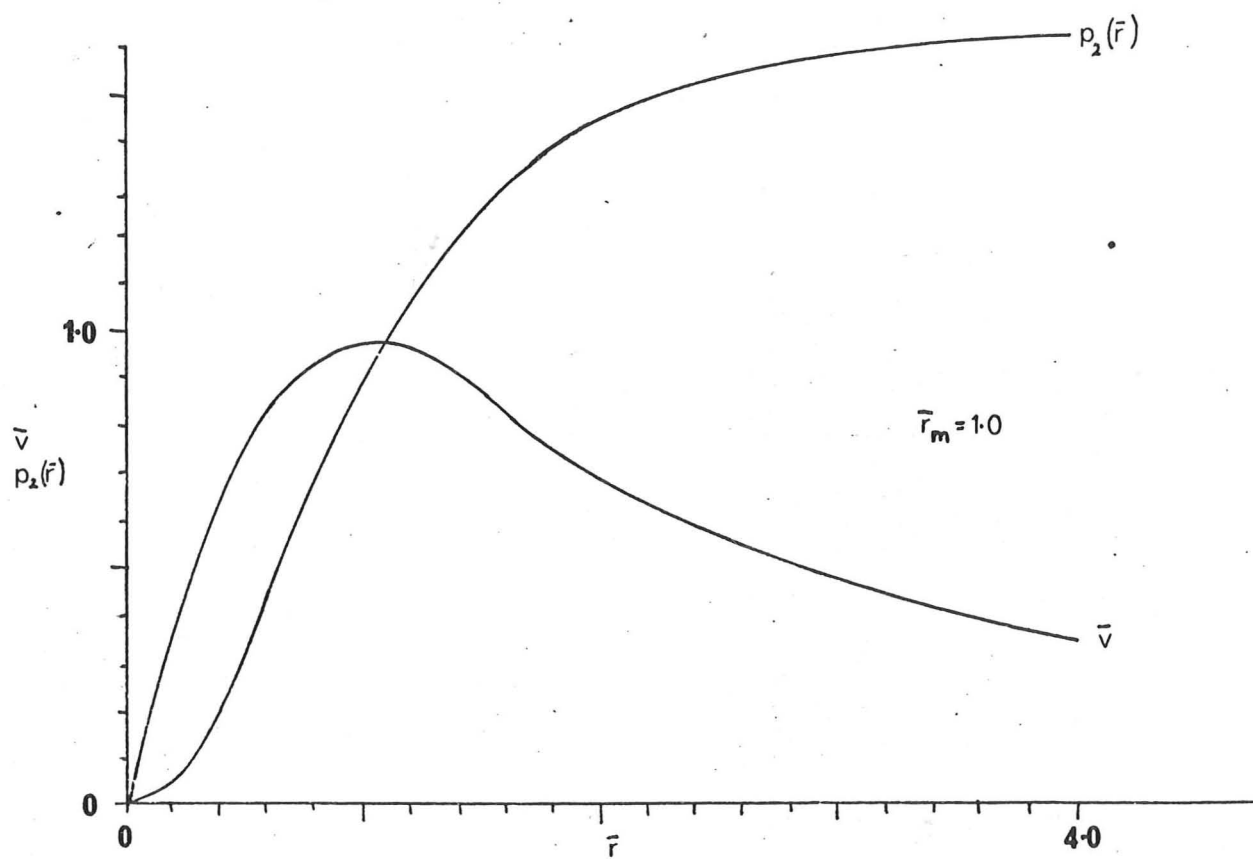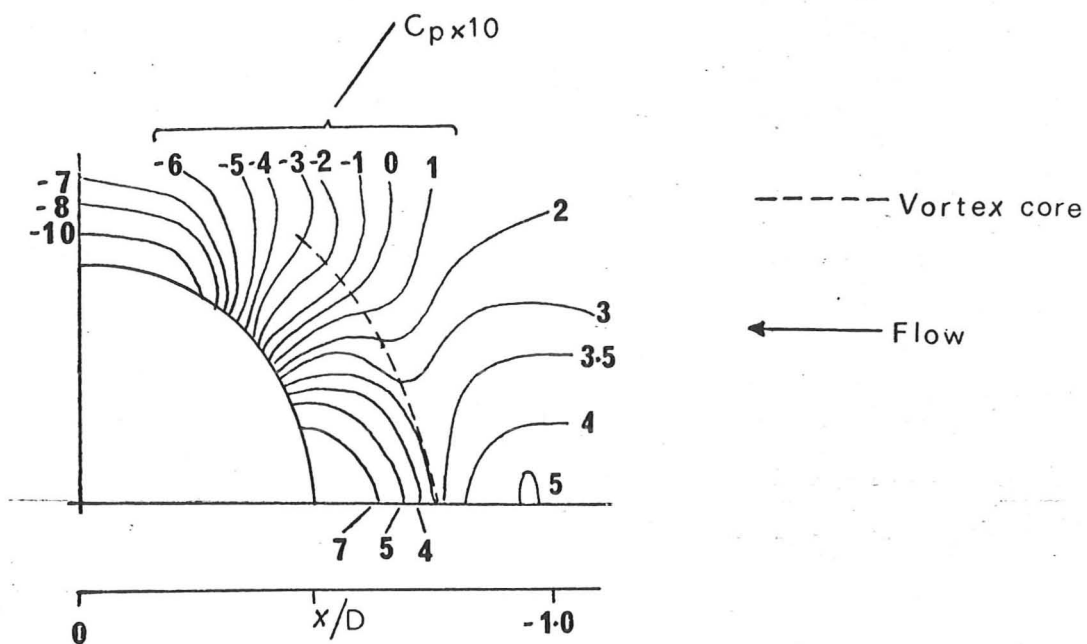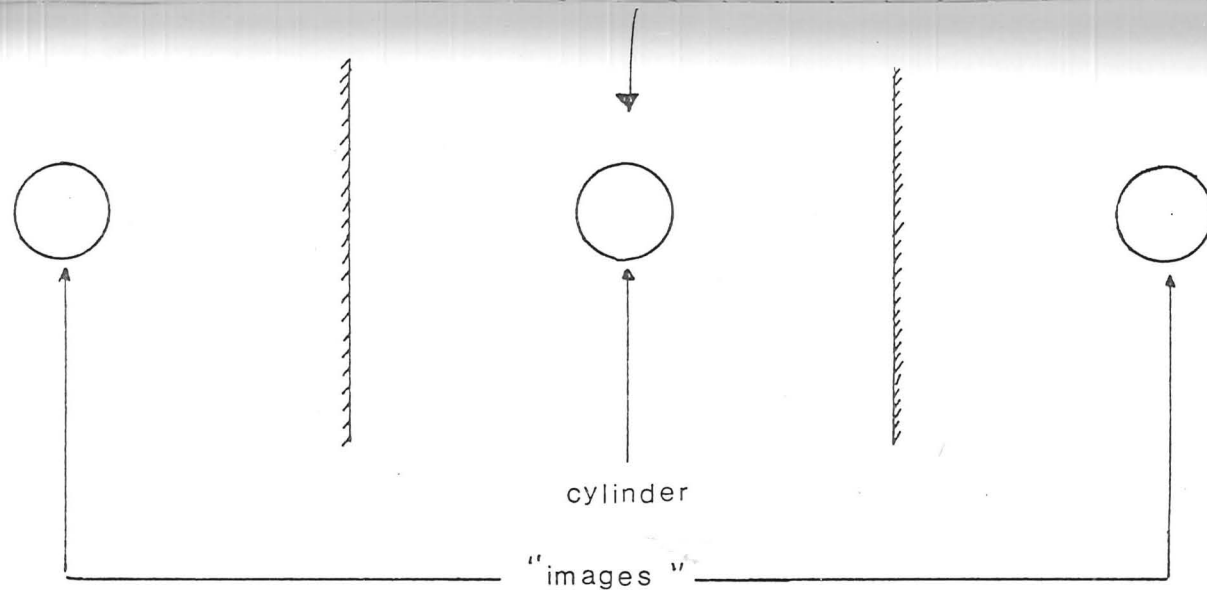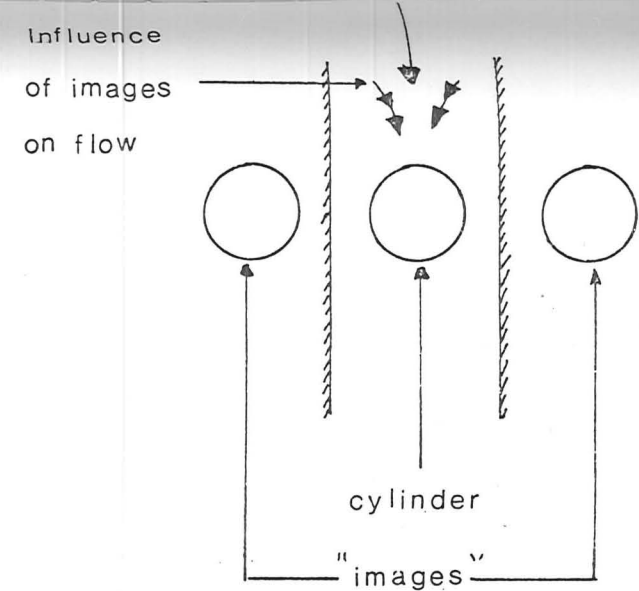
Smoke tunnel

(a) Effect of varying tunnel width
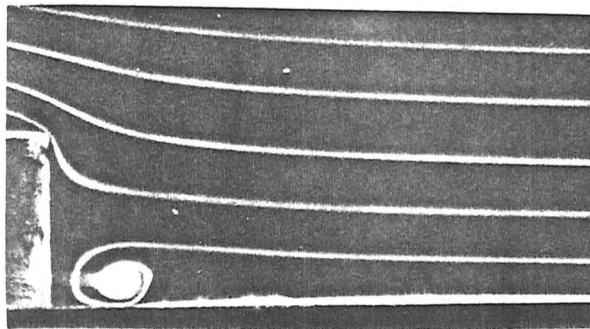
$D/l = 2.0$
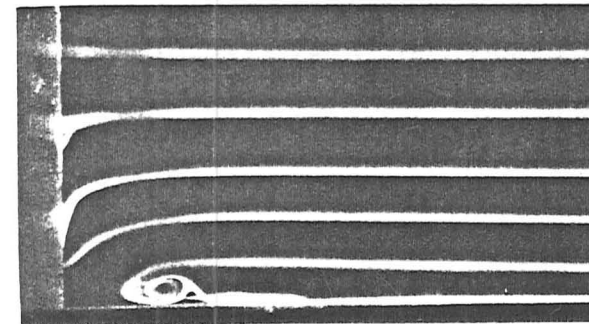
$D/l = 0.6$

(b) Effect of varying cylinder height $\left(UD/\nu = 3{,}100, \ D/\delta^* = 16.1 \right)$

FIGURE 2.10.1 Variation in flow patterns
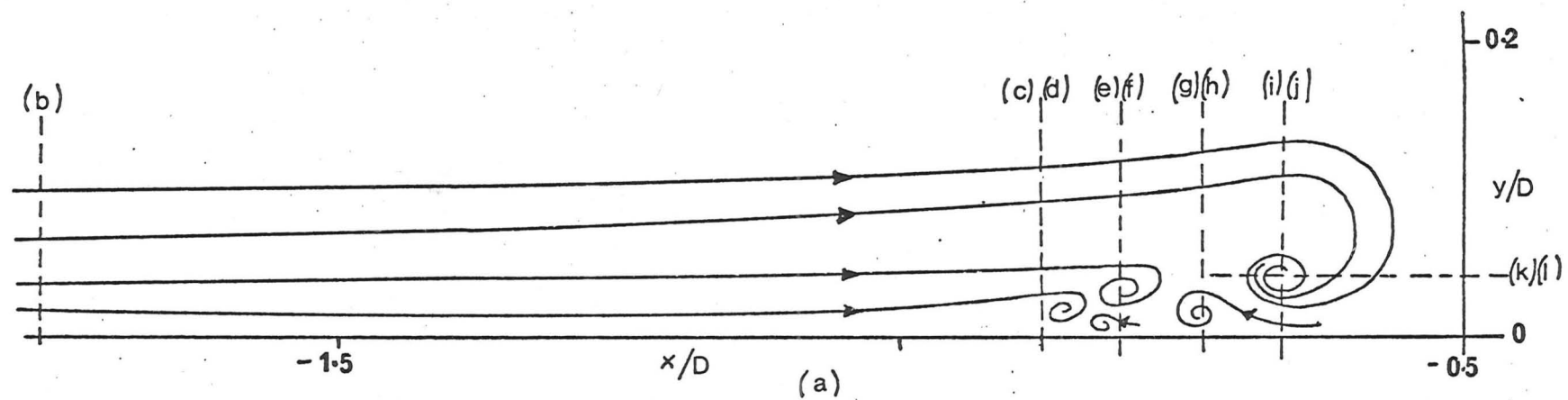
FIGURE 2.10.2. Velocity profiles ... $\left(UD/\nu = 2610, D/\delta^* = 14.8\right)$

Errors

x/D	± 2%
y/D	± 2%
u/U	± 0.05
v/U	± 0.02

Upstream of separation

X/D = -1.75

Vortex 1'
" 2'
" 1
" 3
" 2

(b)

Downstream of

separation

X/D = -0.87

(c)

(d)

Vortex 2

X/D = -0.79

(e)

(f)

FIGURE 2.10.2 (continued)

Vortex 1'

x/D = -0.73

(g)

(h)

Vortex 1

x/D = -0.66

(i)

(j)

Vortex 1

y/D = 0.06
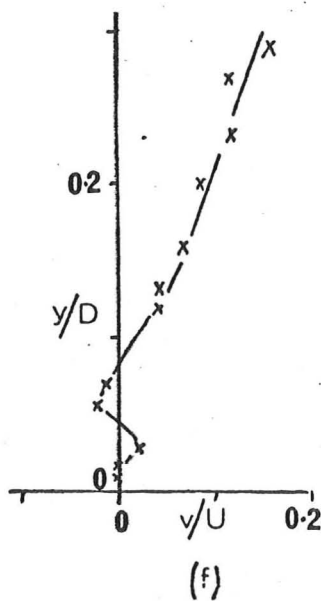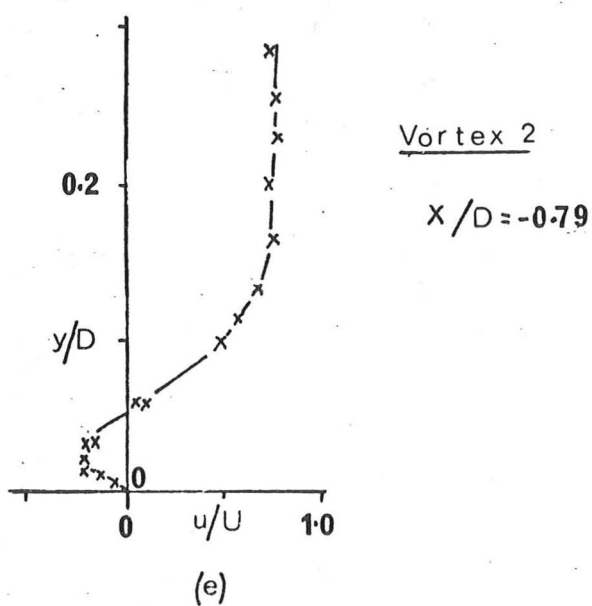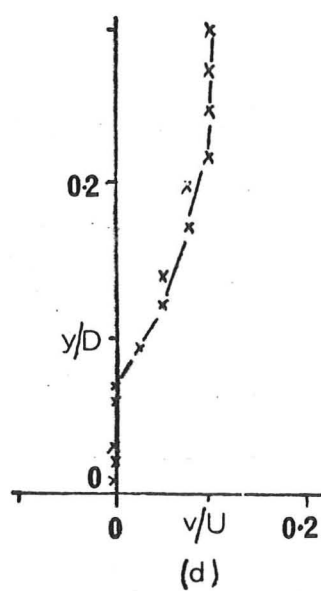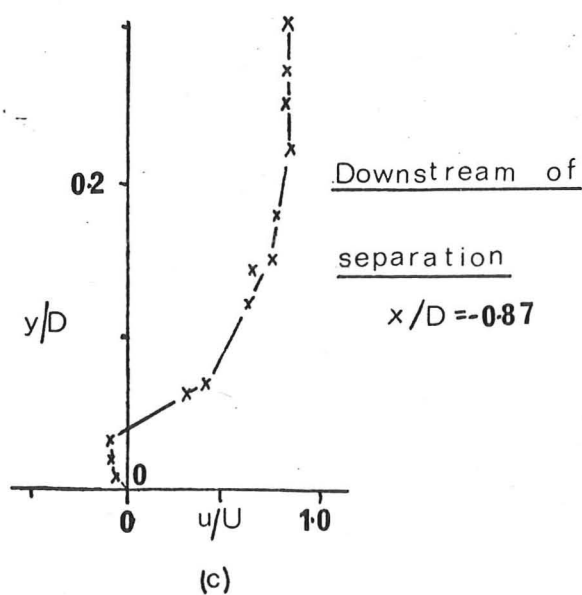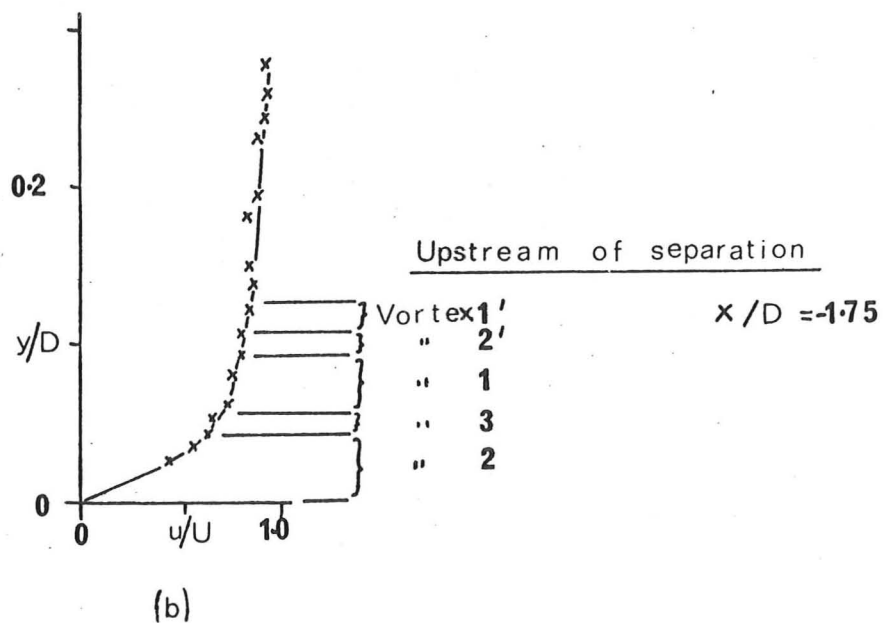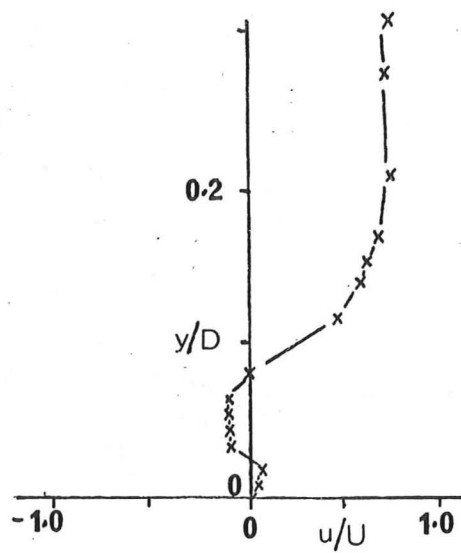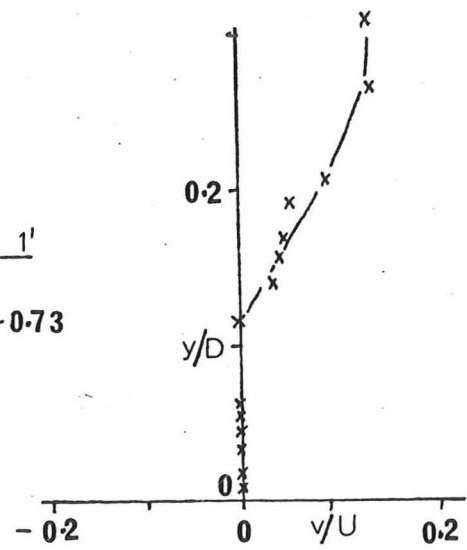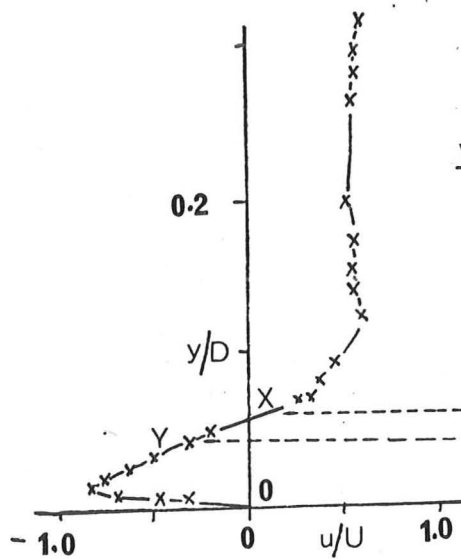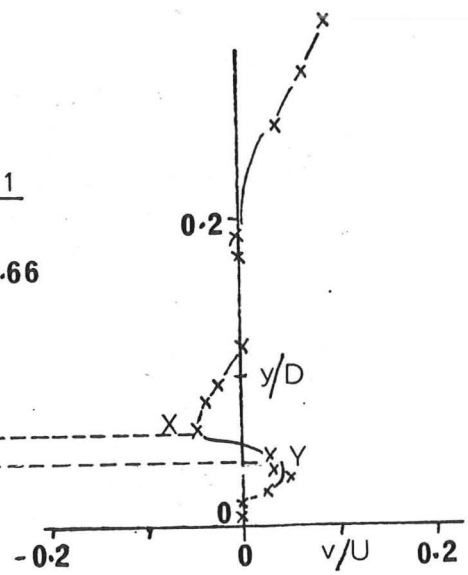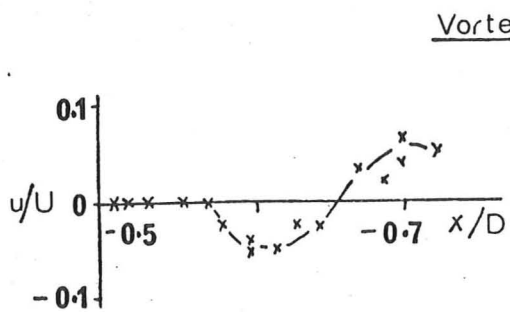
(k)
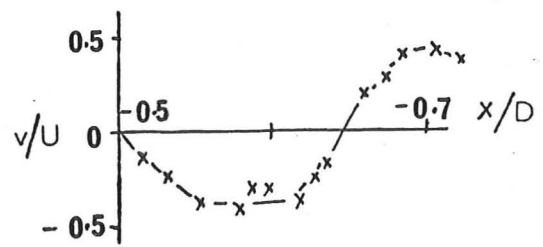
(l)

FIGURE 2J0.2 (continued)
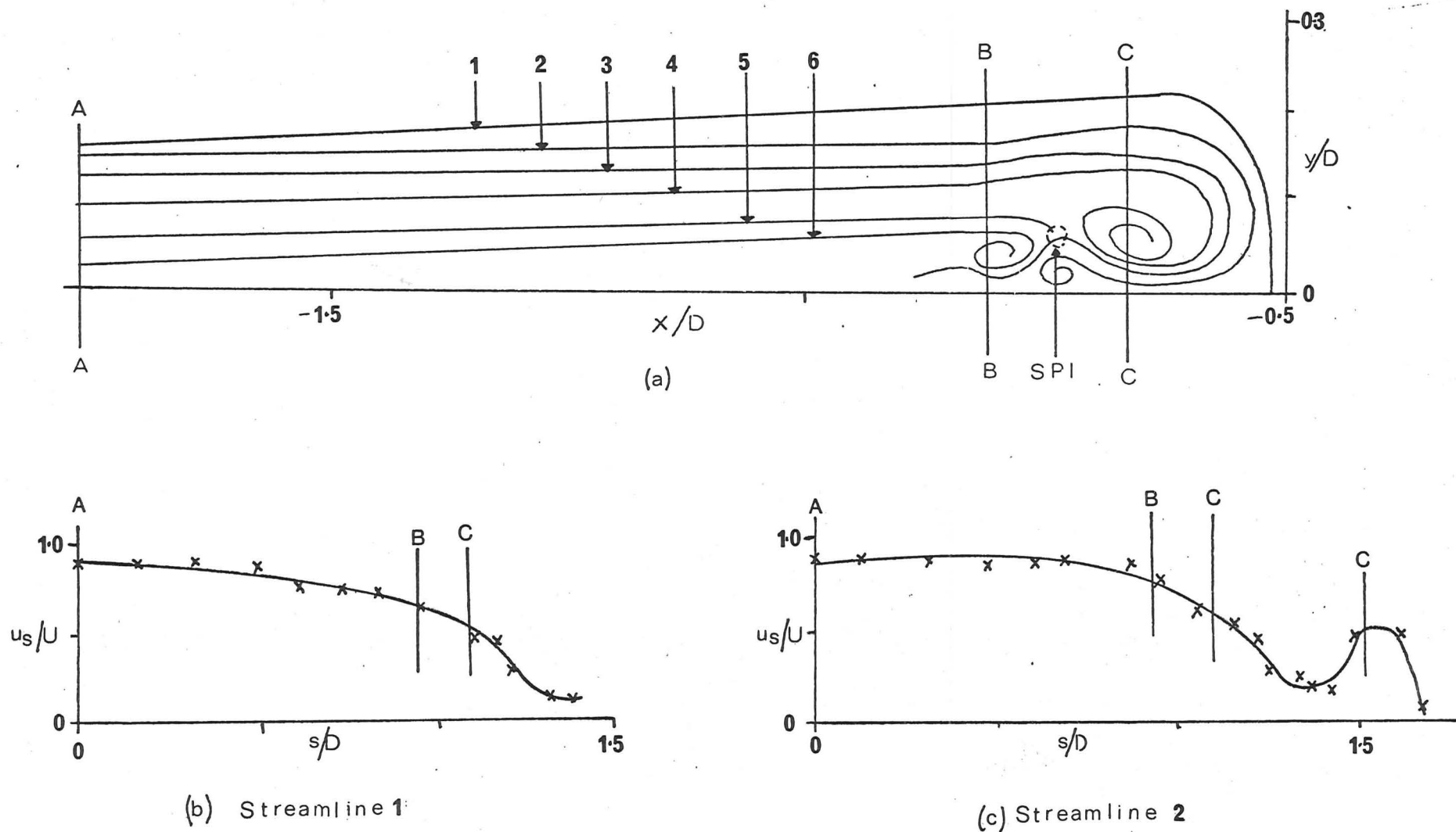
FIGURE 2.10.3 Velocity variation along streamlines ($UD/\nu = 2{,}610$, $D/\delta^* = 14.8$)
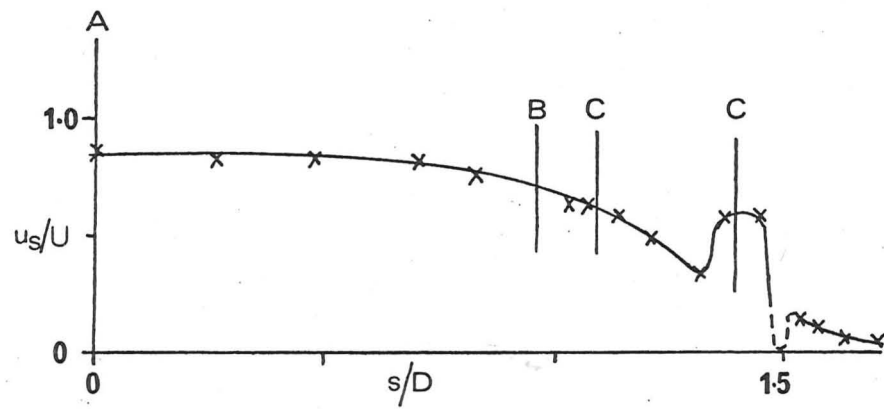
(d) Streamline 3
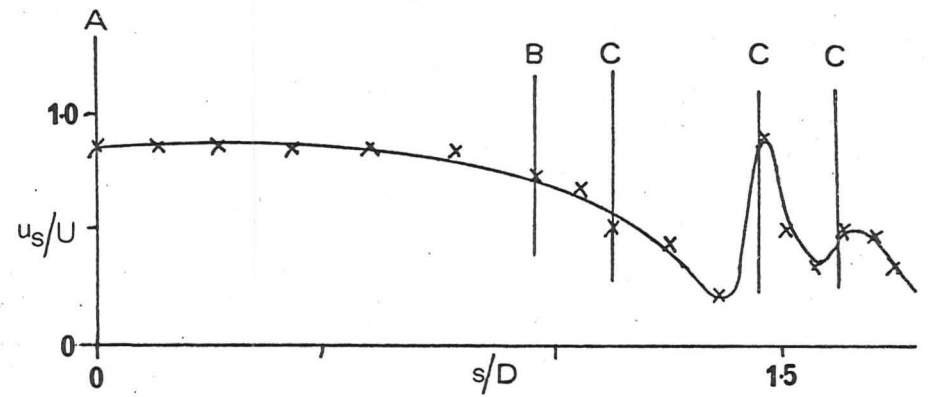
(e) Streamline 4
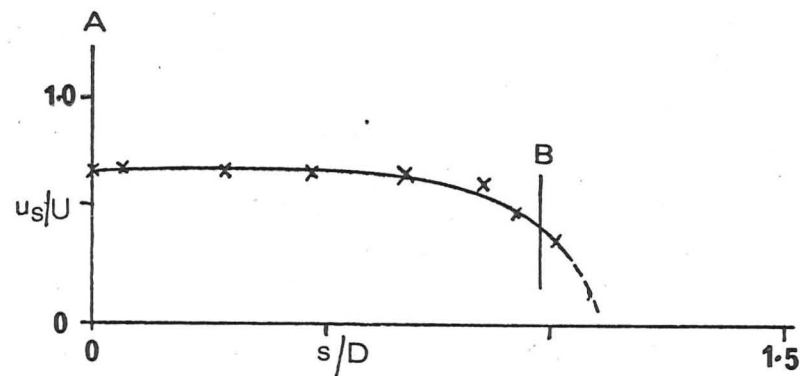
(f) Streamline 5
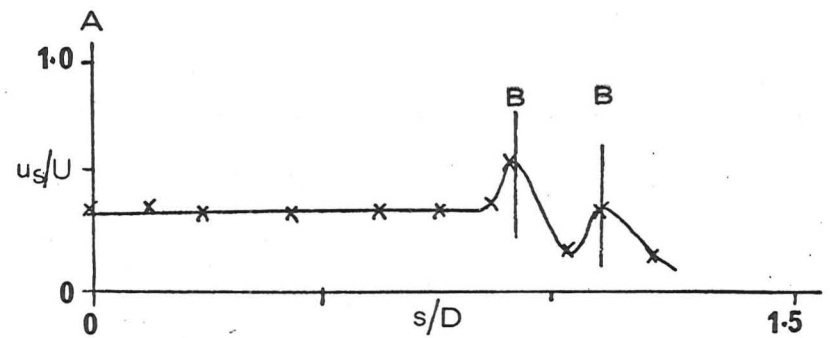
(g) Streamline 6

FIGURE 2.10.3 (continued)

	UD/ν	D/δ*	x/D
x	2610	14·8	−0·66
+	3100	16·1	−0·67
Δ	3600	17·3	−0·68
∇	4240	18·8	−0·69
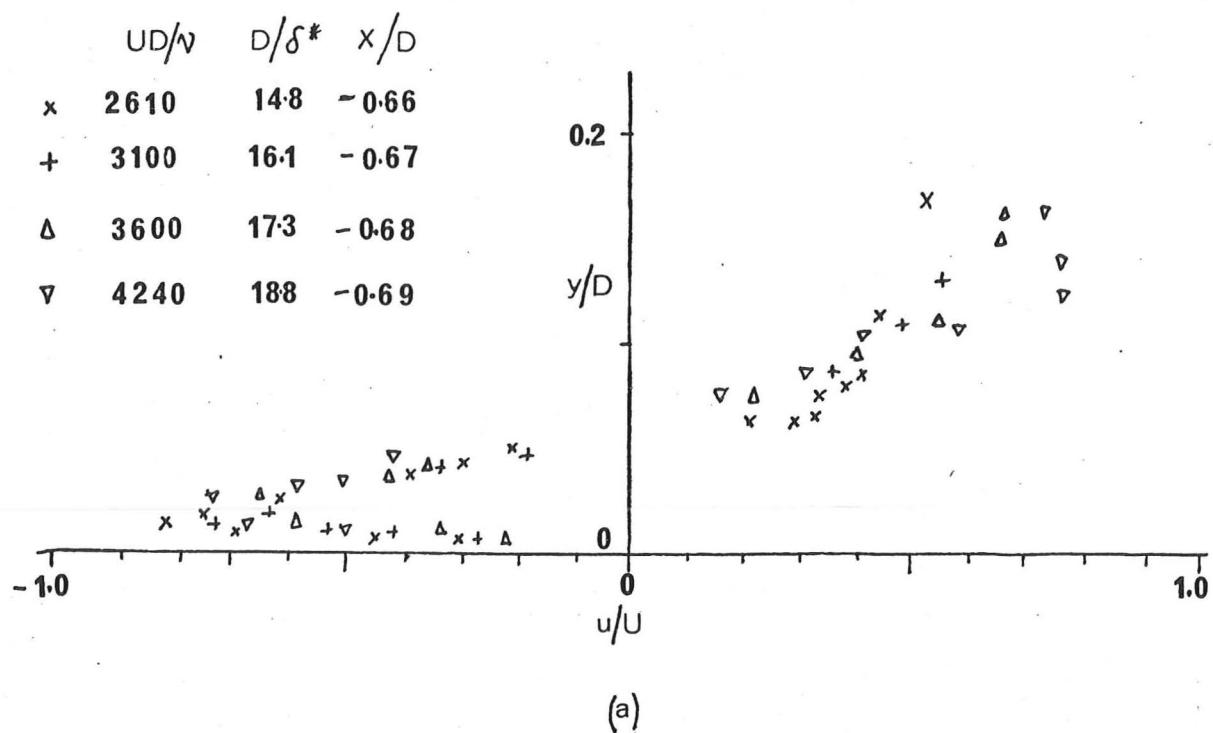
Errors: See figure 2.10.2

(a)

(b)
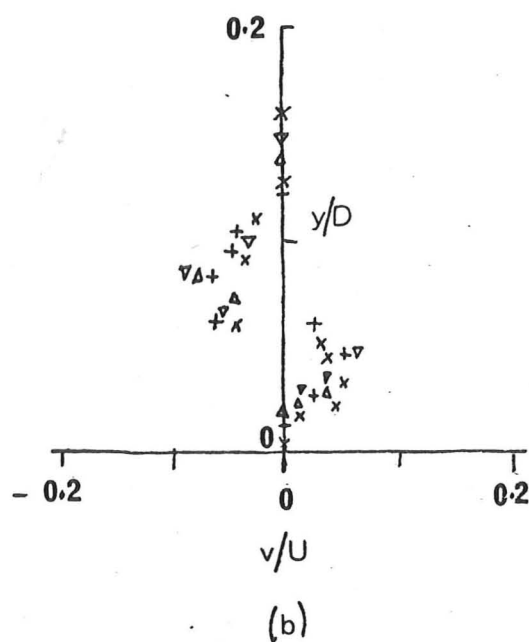
FIGURE 2.10.4   Velocity profiles through vortex 1 (several speeds)

$$C_f = \frac{\mu \left(\partial u / \partial y\right)_{y=0}}{\frac{1}{2} \rho U^2}$$
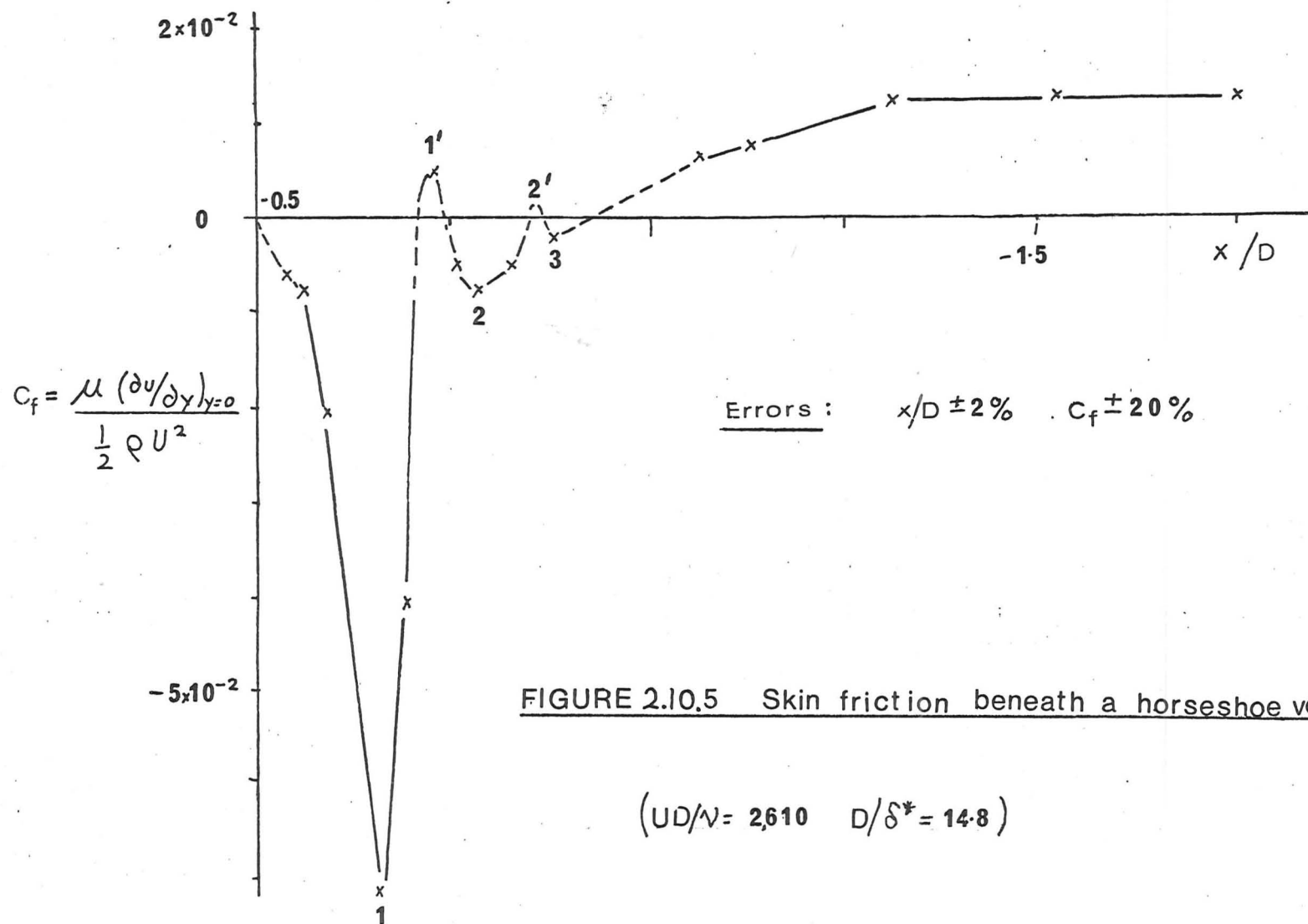
Errors : $x/D \pm 2\%$. $C_f \pm 20\%$

FIGURE 2.10.5   Skin friction beneath a horseshoe vortex system

$\left(UD/\nu = 2{,}610 \quad D/\delta^* = 14{\cdot}8\right)$

Vorticity concentration   Stretched vortex tubes
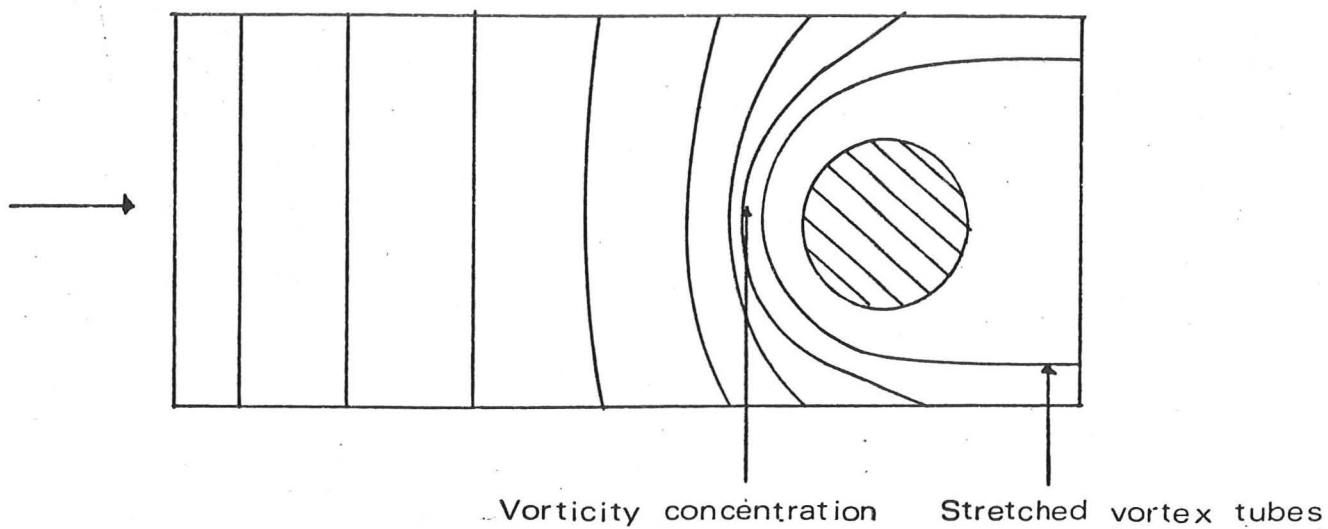
FIGURE 2.II.I Vortex tubes around a cylinder on a plate

(a)

(b)

C_p (c)

x

(d)

direction of diffusion of +ve vorticity
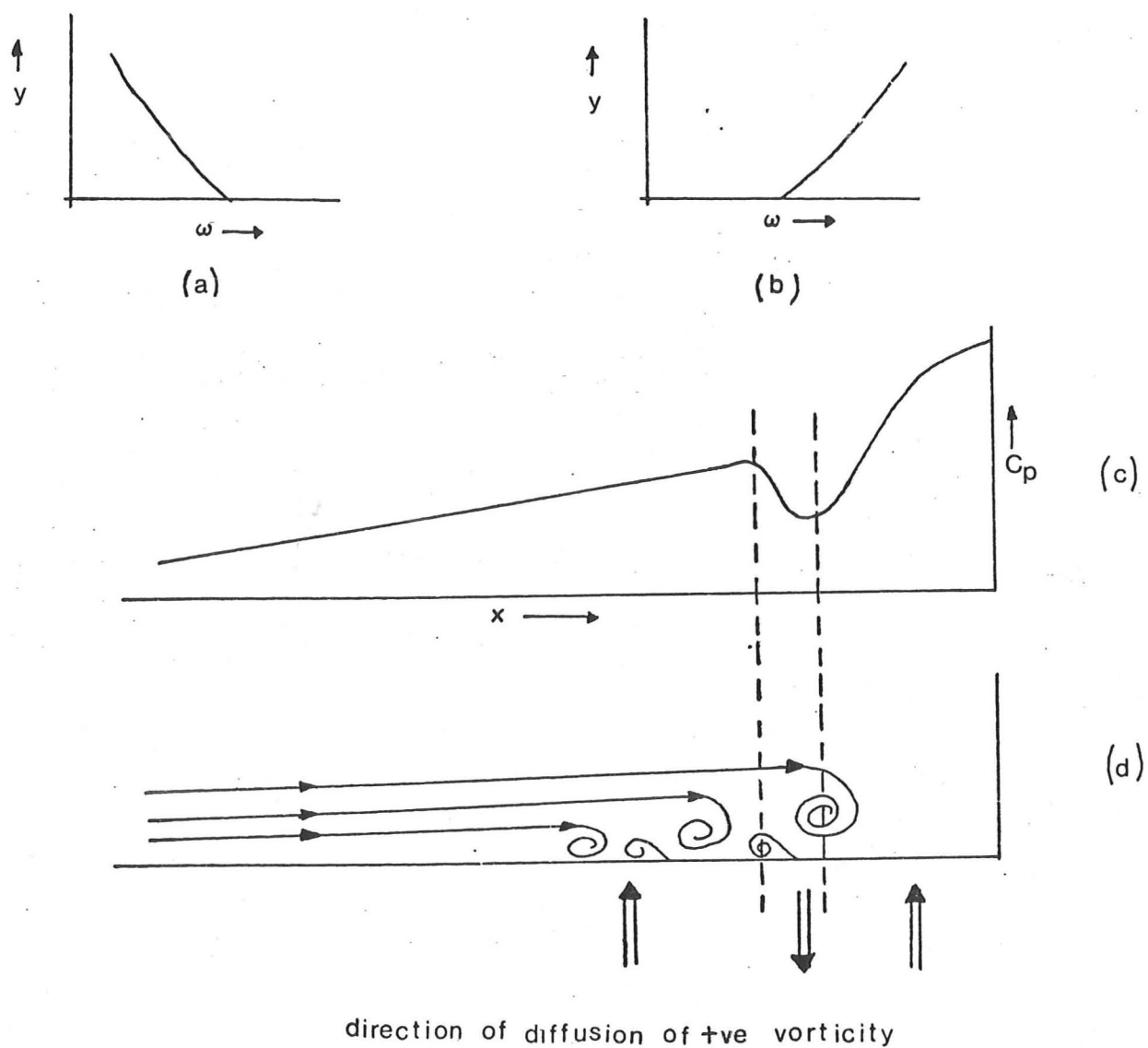
FIGURE 2.11.2 Vorticity diffusion

(a) x/D = -1.75

(b) x/D = -0.87

Errors

x/D ±2%

y/D ±2%

ωD/U ±10%
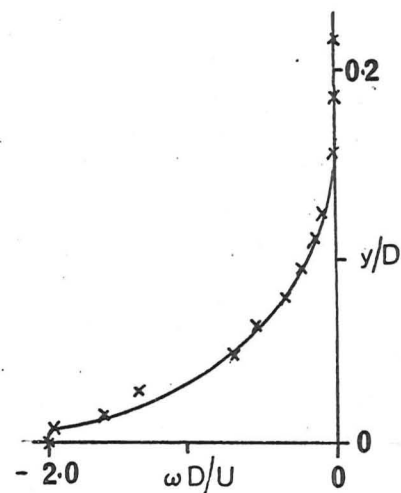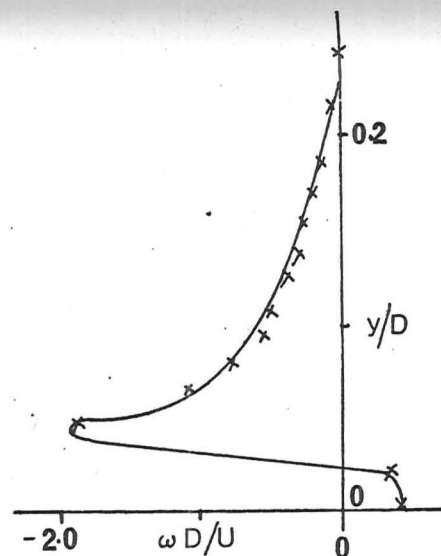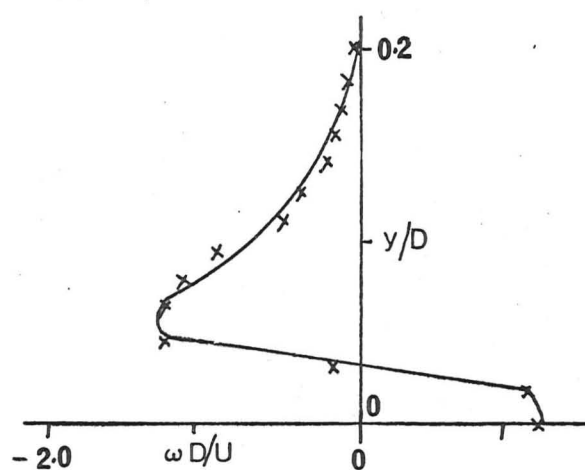
(c) x/D = -0.79
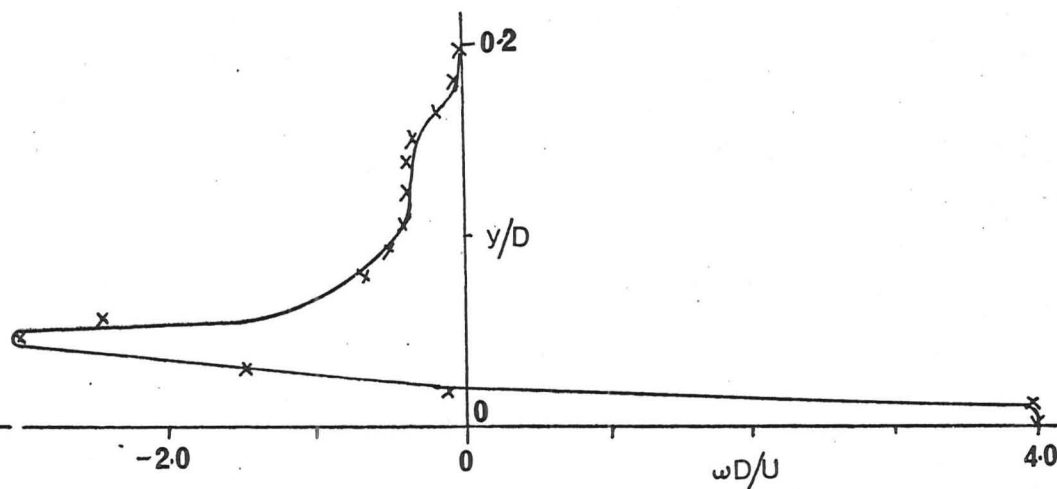
(d) x/D = -0.66

FIGURE 2.11.3 Vorticity profiles (UD/ν = 2610, D/δ^* = 14.8)

FIGURE 2.11.4 Flow visualisation with plate removed in separated

flow region : $UD/\nu = 2{,}580$, $D/\delta^* = 16{\cdot}3$, $D/l = 2{\cdot}0$
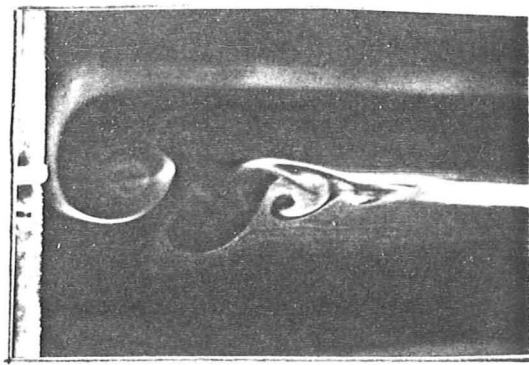
(d)
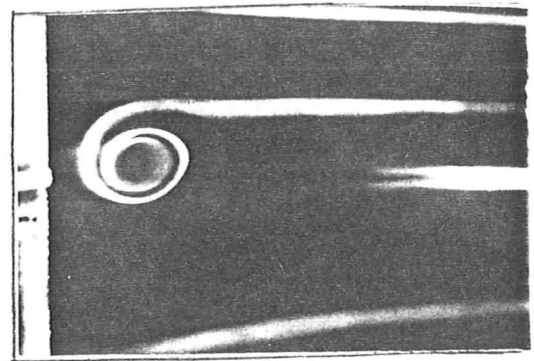
(e)
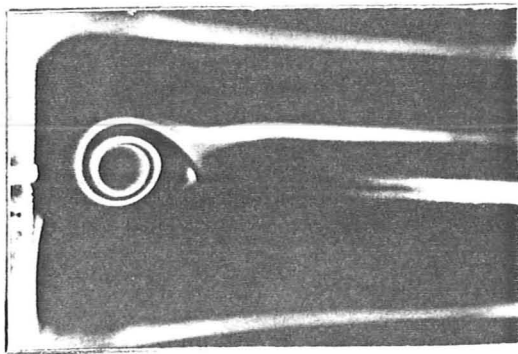
(f)
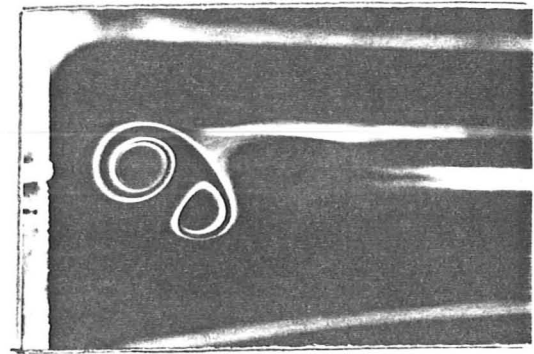
(g)

FIGURE 2.11.4 continued

FIGURE 2.11.5 Streamline pattern

Key:

x Vasanta Ram $UD/\nu = 4\cdot1\times10^5$
$D/\delta^* = 33\cdot3$
$H = 1\cdot56$

o Belik $UD/\nu = 8\cdot4\times10^4$
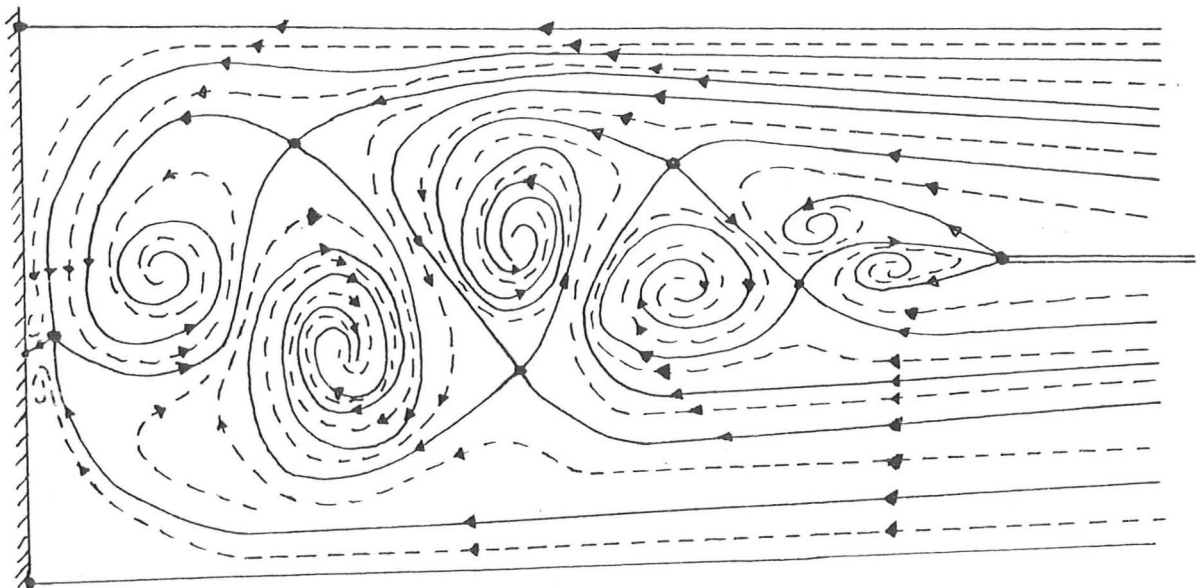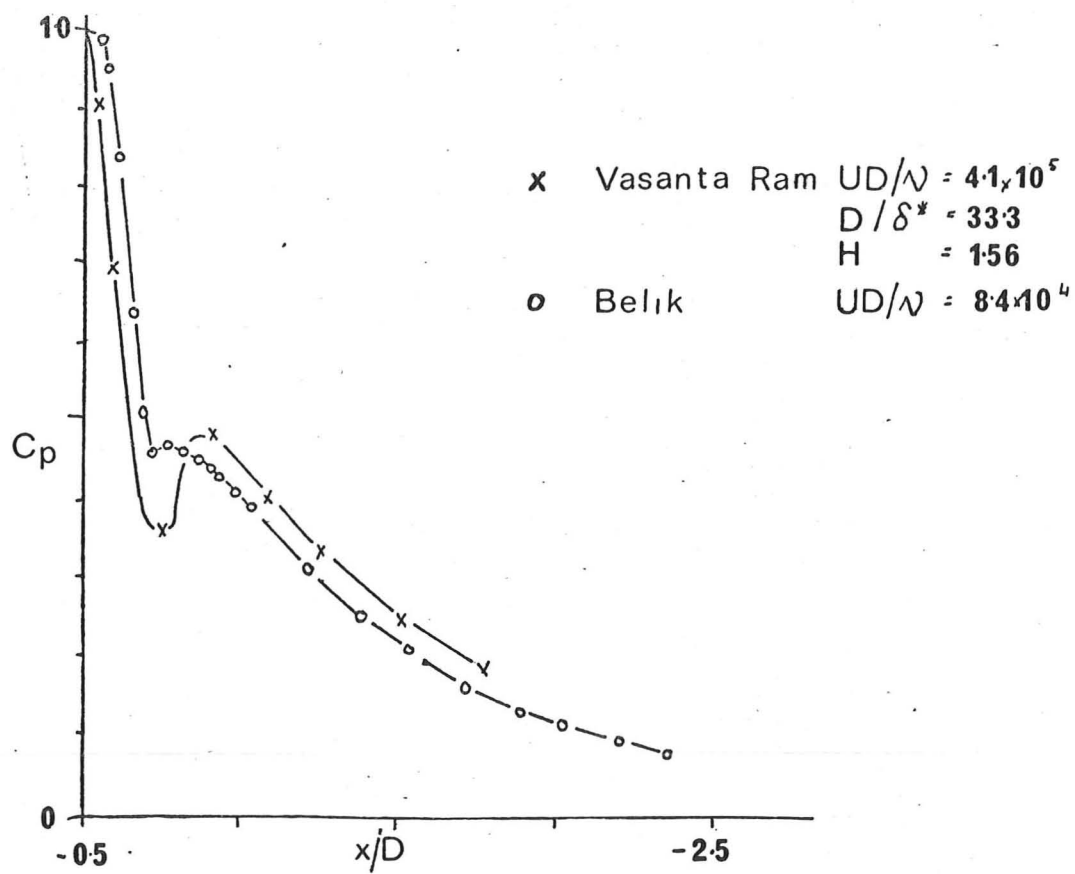
FIGURE 3.1.1 Pressure distributions

(a)

(b)

(c)

(d)
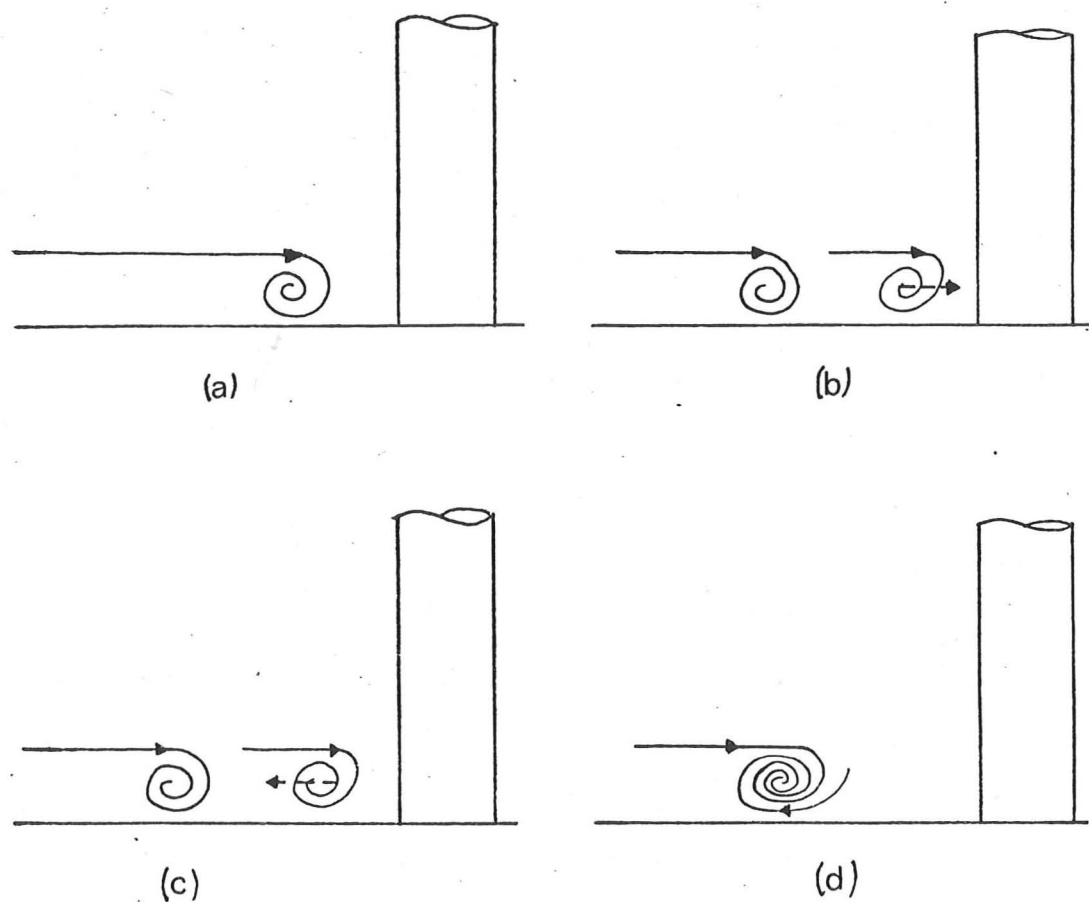
FIGURE 3.1.2 Vortex oscillations observed by Roper
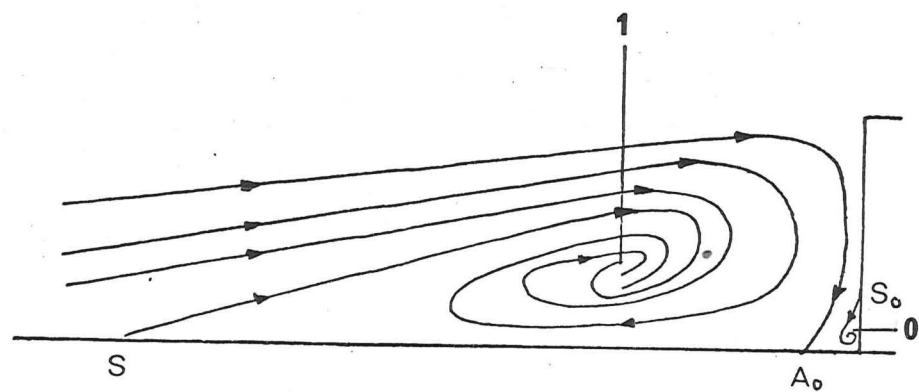
(a) Two vortex system
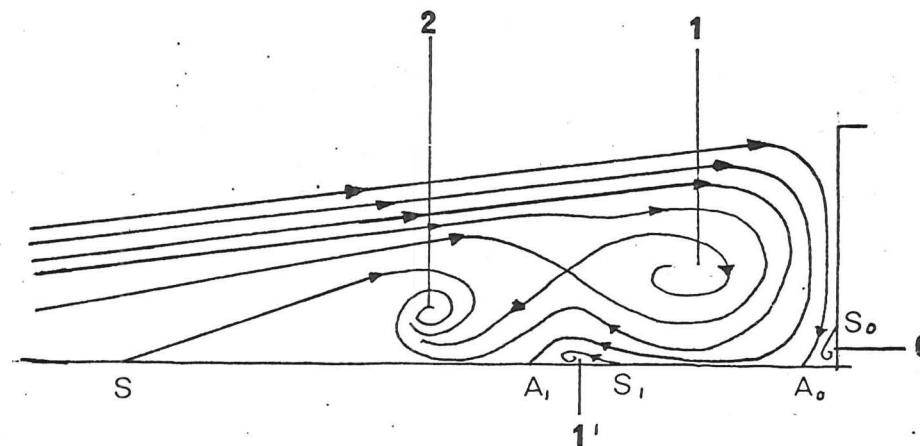
(b) Four inner vortex system
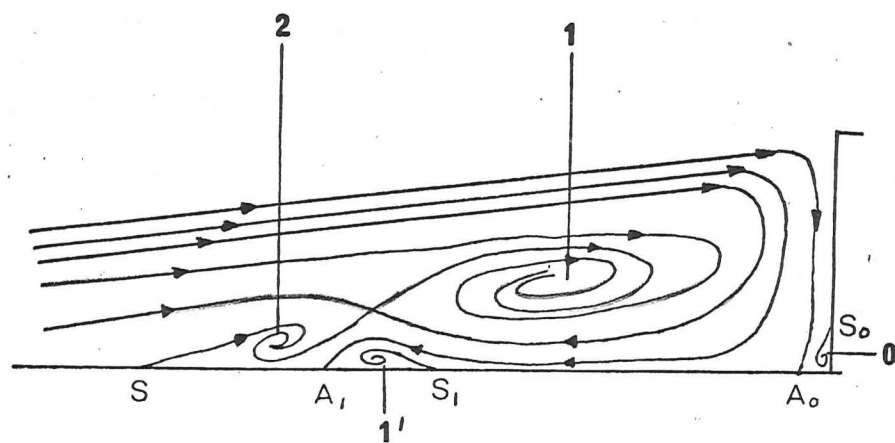
(c) Four outer vortex system
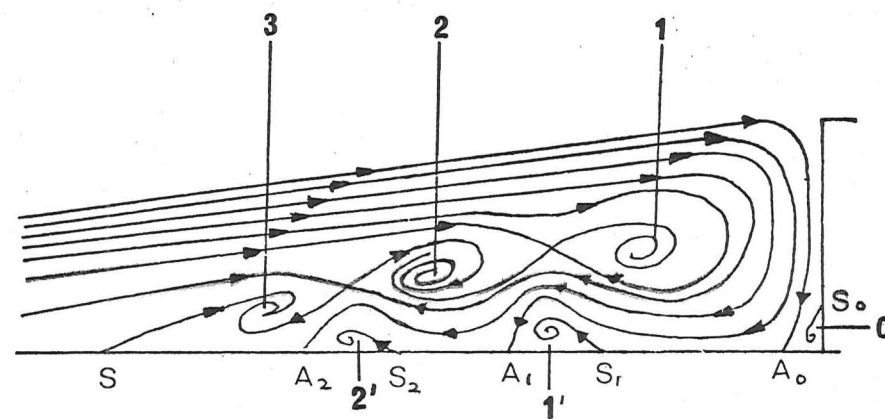
(d) Six vortex system

FIGURE 3.1.3 Vortex systems observed by Sedney and Kitchens

$\Delta^2/_4 > J > O$ (Nodes)

(a) $\Delta > 0$

(b) $\Delta < 0$

(c) $\Delta < 0$

(d) $\Delta > 0$

$J < 0$ (Saddle points)

(e) $\Delta < 0$

(f) $\Delta > 0$

(g) $\Delta = 0$

$J > \Delta^2/_4$ (Nodes or foci)
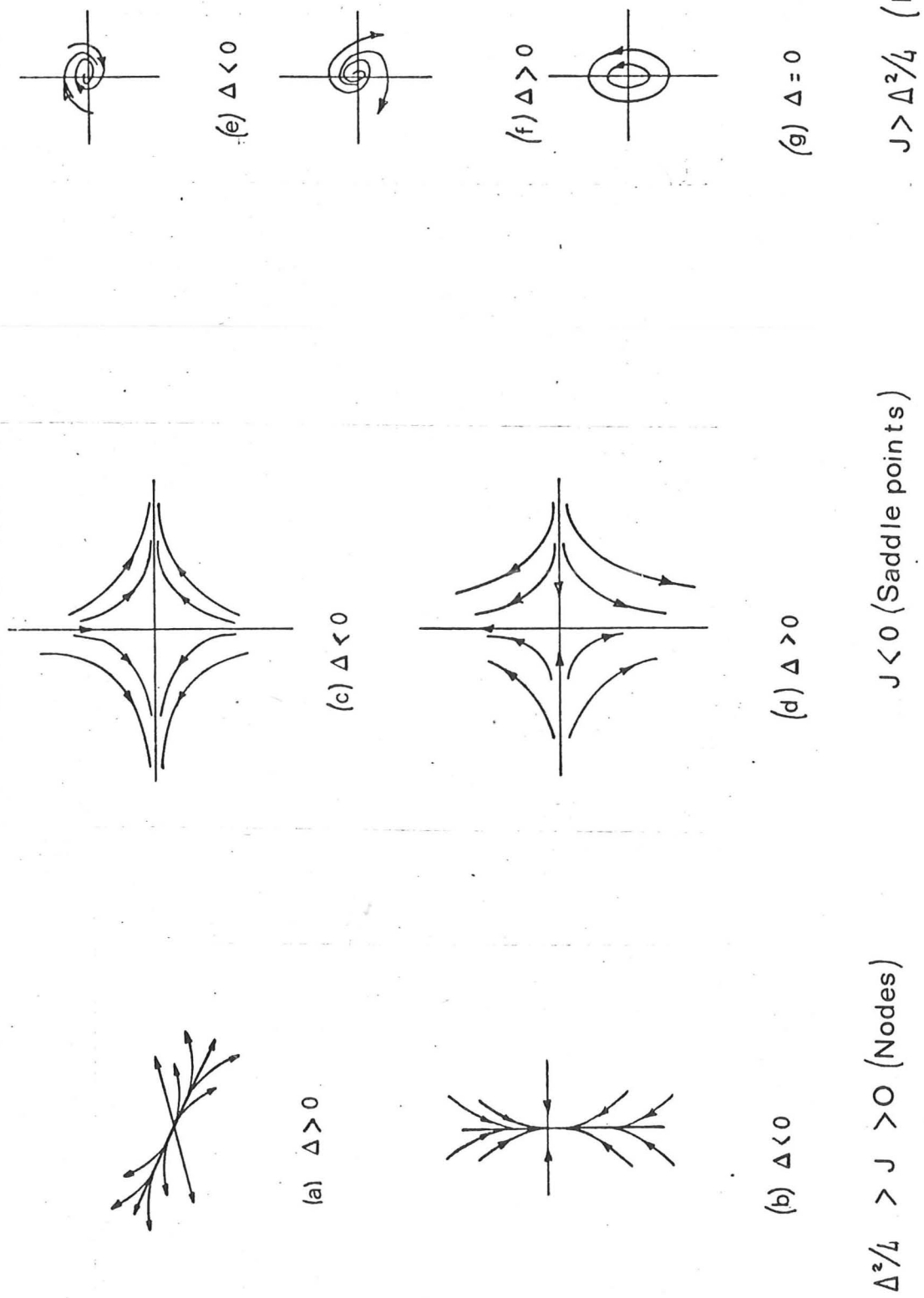
FIGURE 31.4 Singular points (after Hunt et. al.)
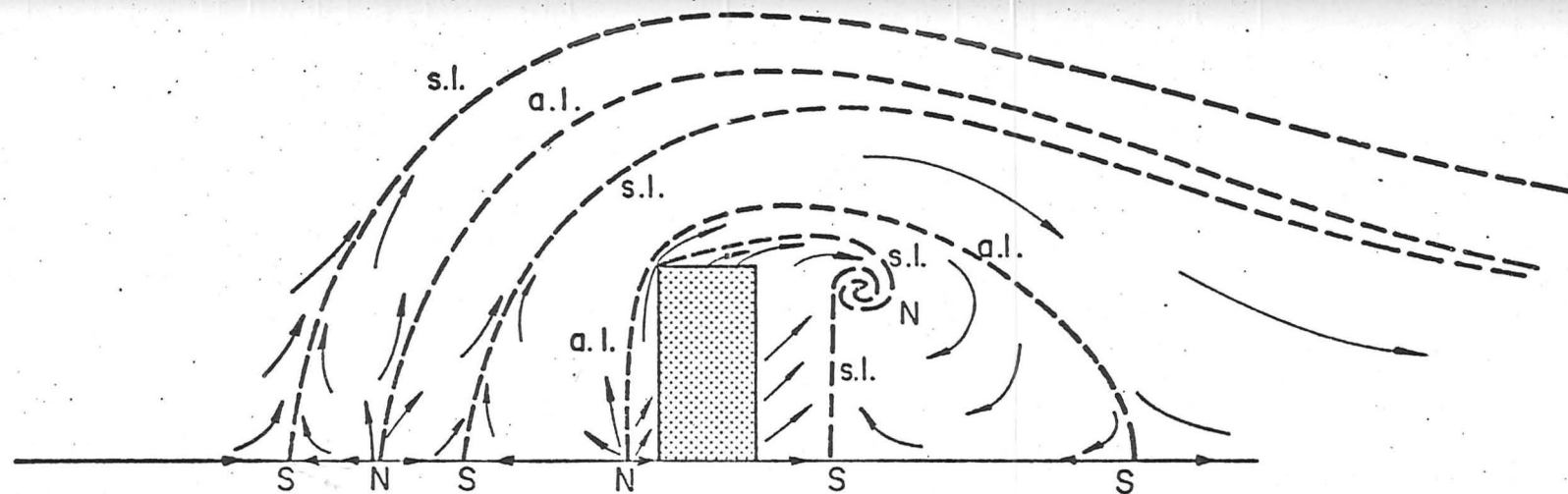
(a) Plan View of Shear Stress Lines

(b) Sides and Top – Shear Stress Lines
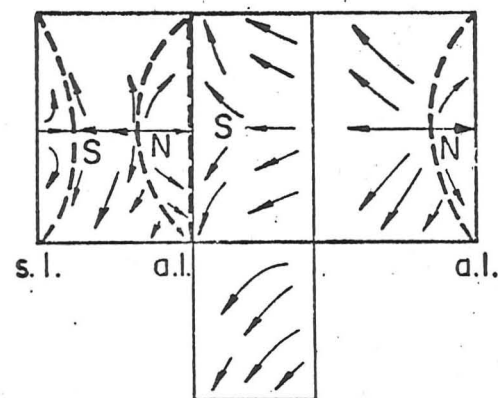
—————▶	Shear Stress Lines
− − − − −	Shear Stress Lines Through Singular Points
s.l.	Separation Lines
a.l.	Attachment Lines
N	Surface Node
S	Surface Saddle

FIGURE 3.1.5 Flow around a cuboid on a plane (after Hunt et. al.)

N – Node of Streamline Pattern

S, S' – Saddles of Streamline Pattern
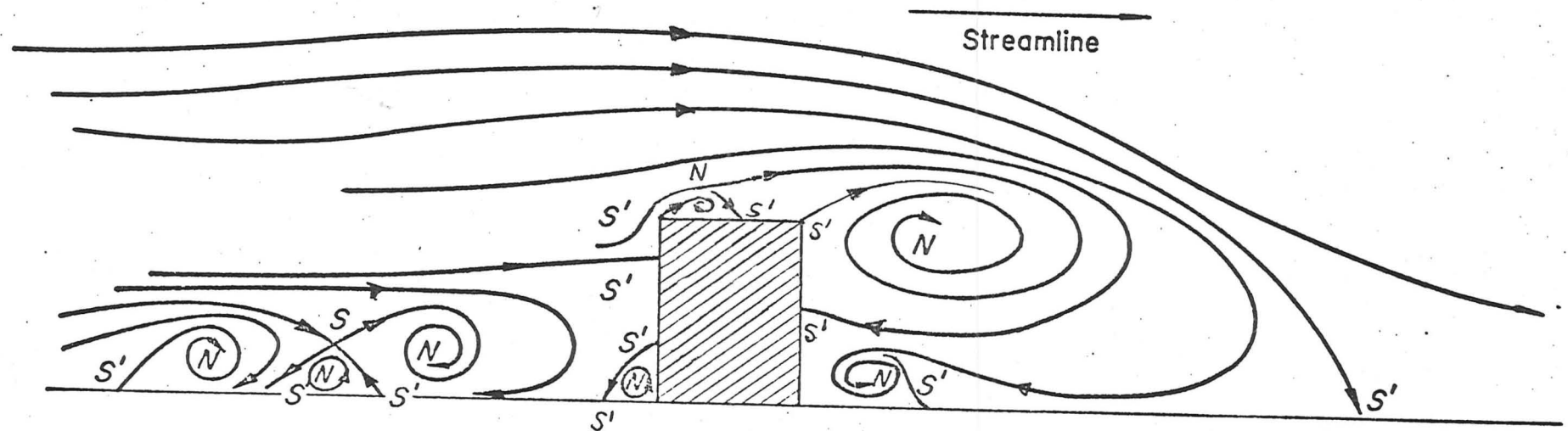
Streamline

(c) Streamlines on ₵ of Block

FIGURE 3.1.5 (continued)

Tunnel wall

A   A   View B

42 cm

61 cm

20 Pressure tappings

96 cm

B

Cylinder

Section A A

Trip (1mm Diam)

15cm

To manometer
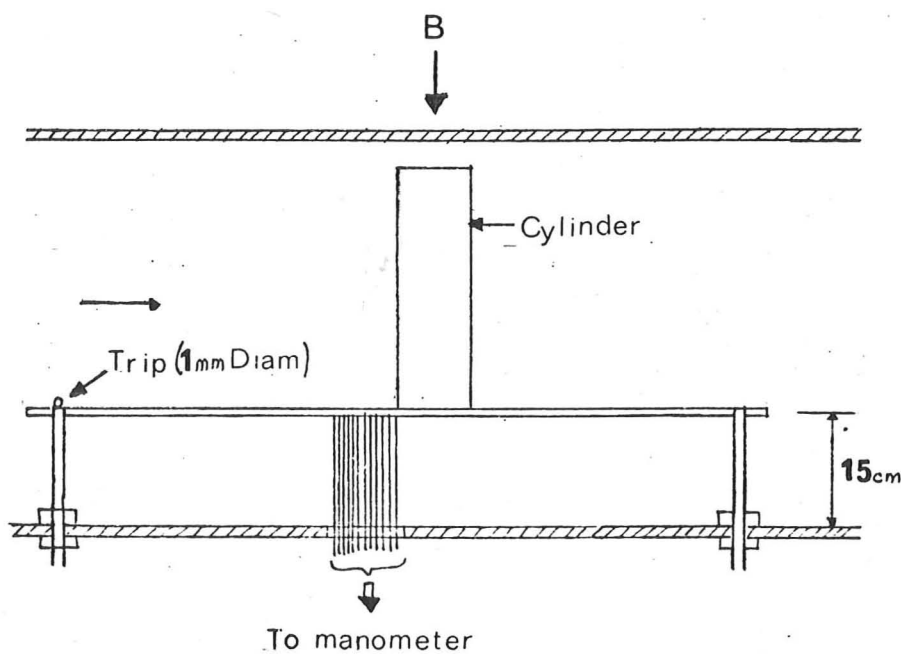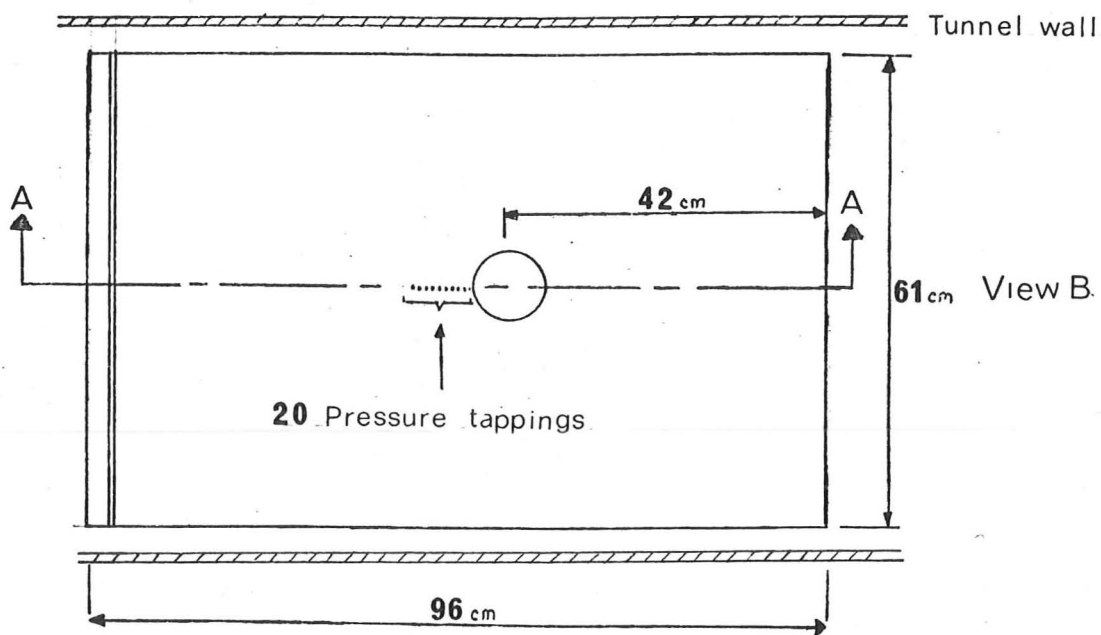
FIGURE 3.21 False floor in wind tunnel
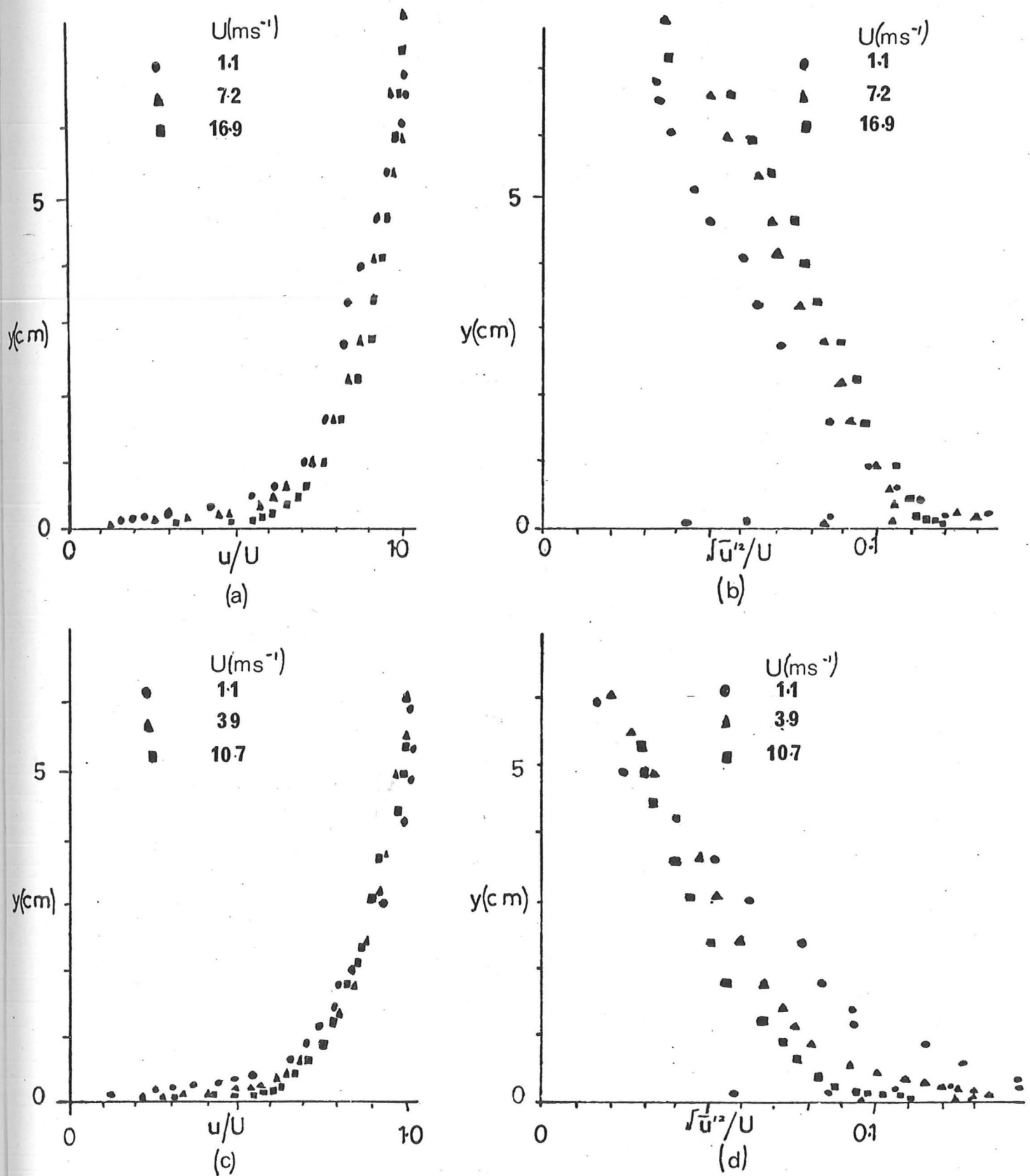
FIGURE 3.2.2 Velocity and turbulence profiles
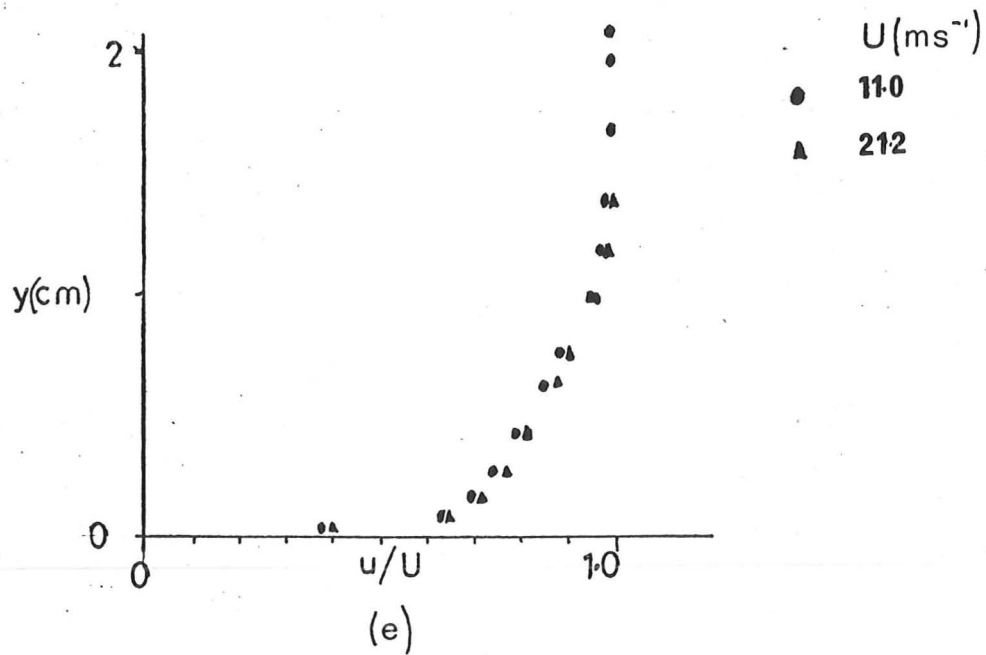
FIGURE 3.2.2 (cont)
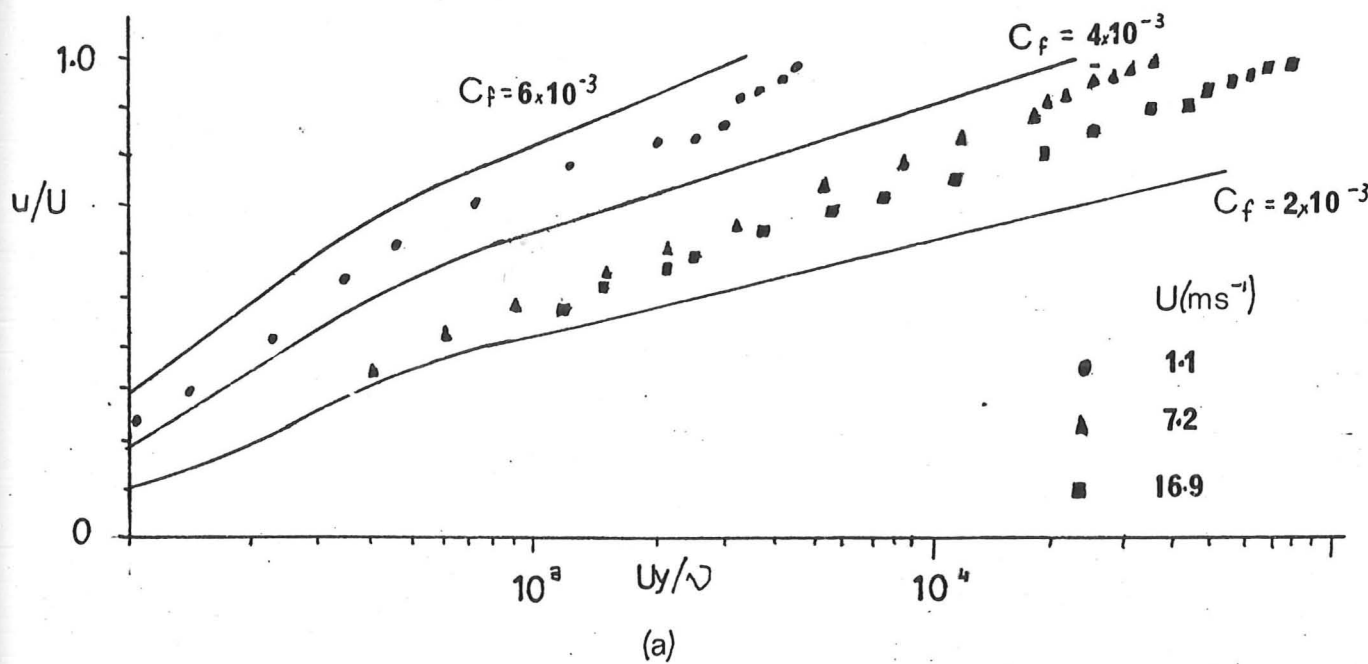
FIGURE 3.2.3   Clauser diagrams

(b)

(c)
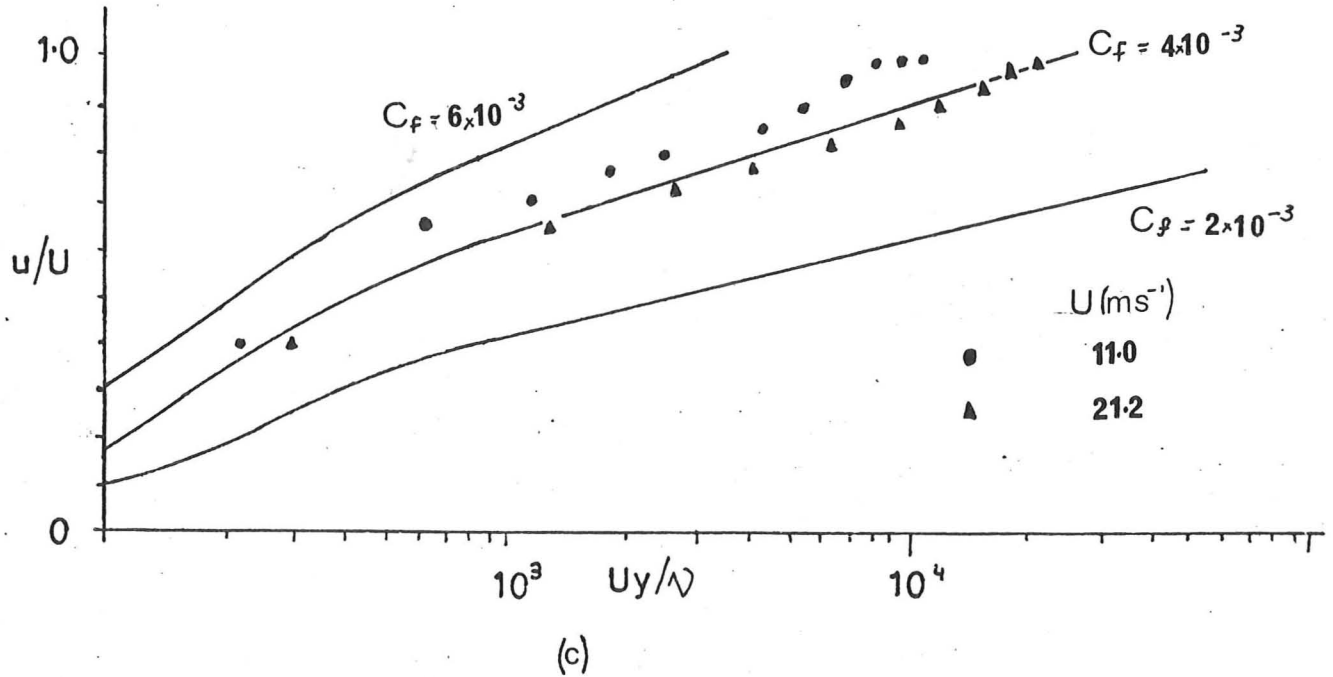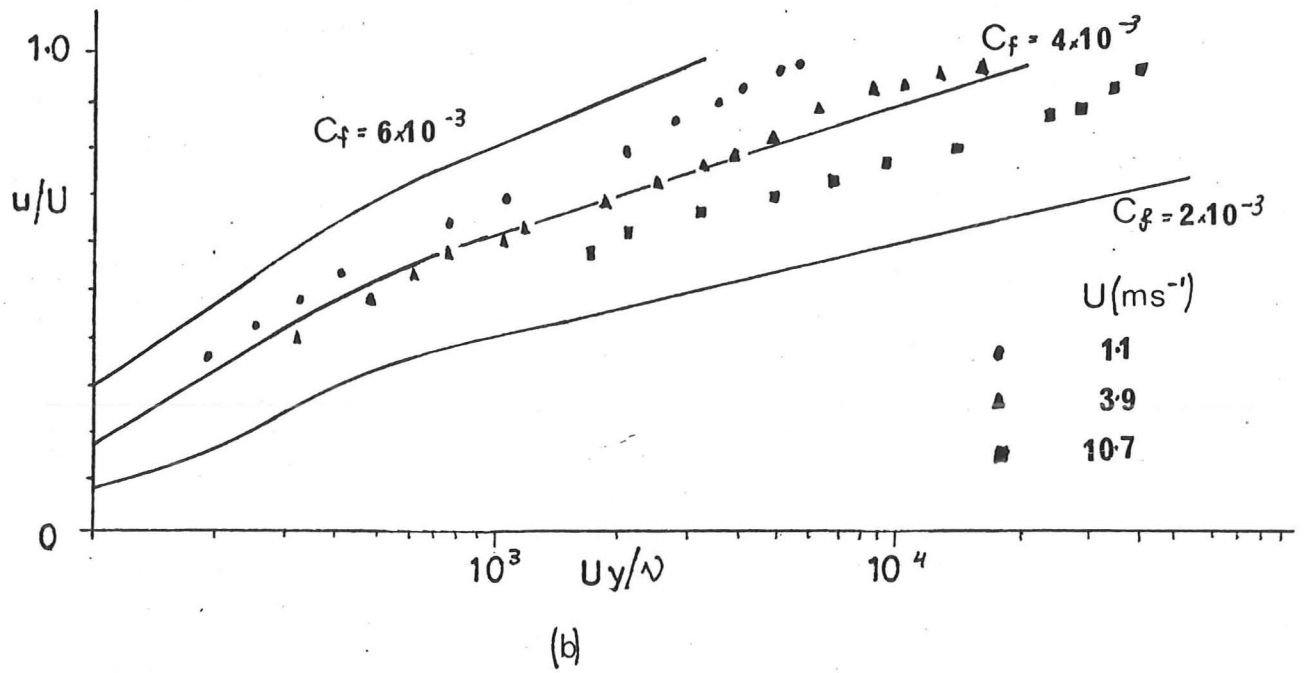
FIGURE 3.2.3 (cont.)
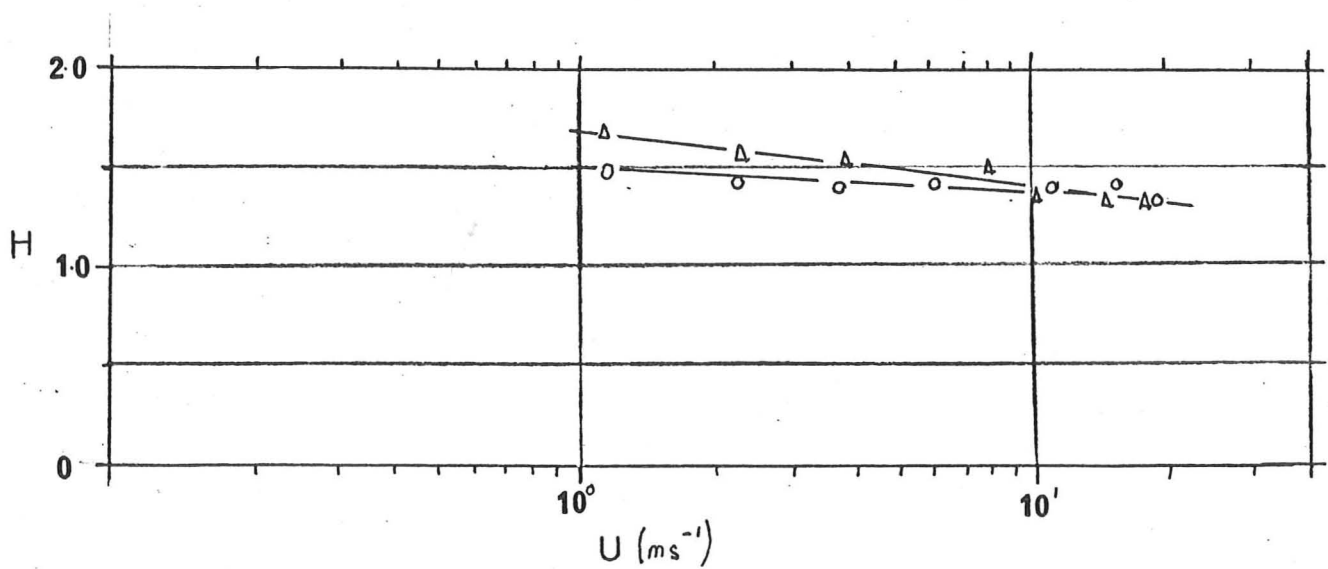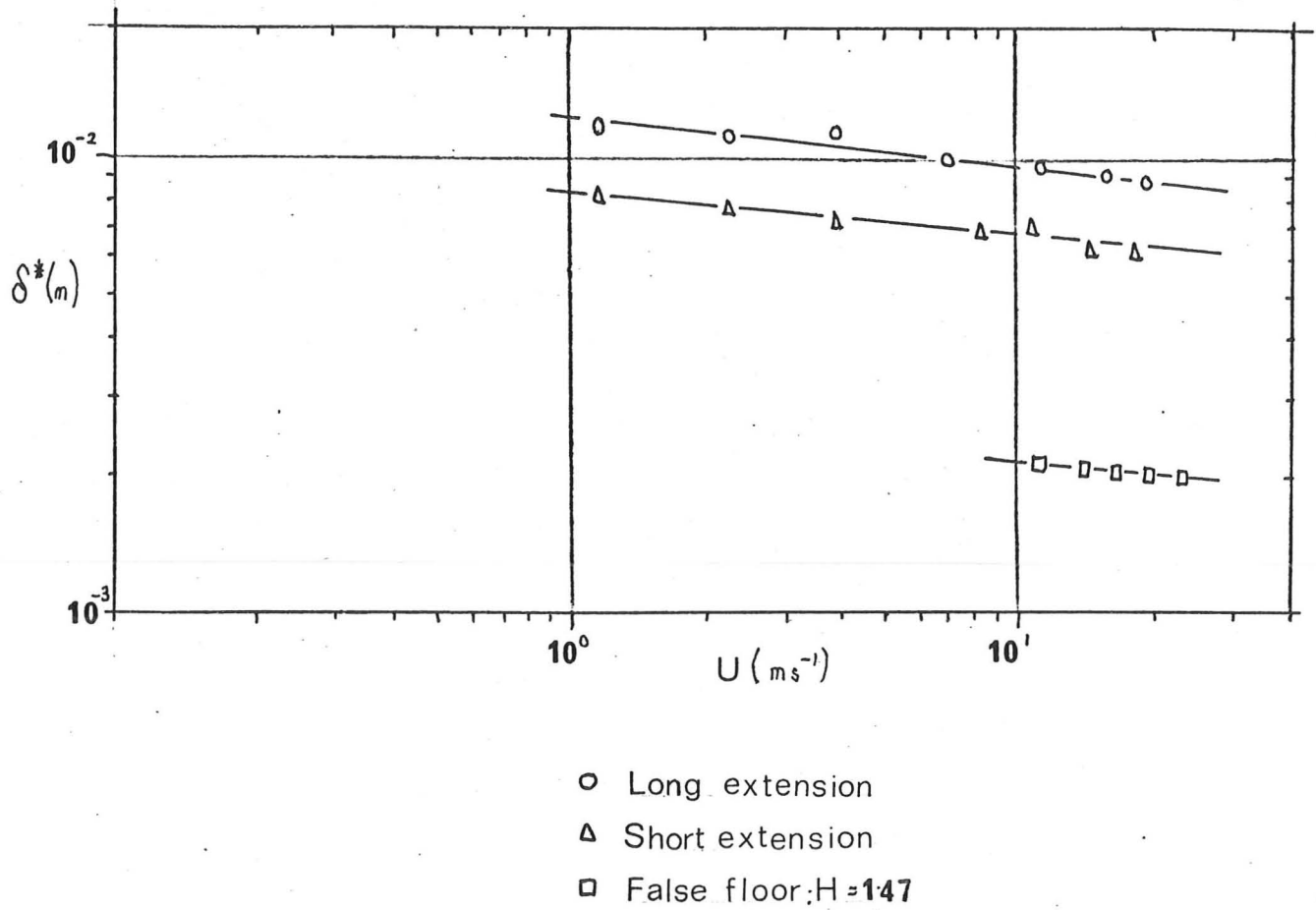
FIGURE 3.2.4 Variation of H and δ^* with wind speed
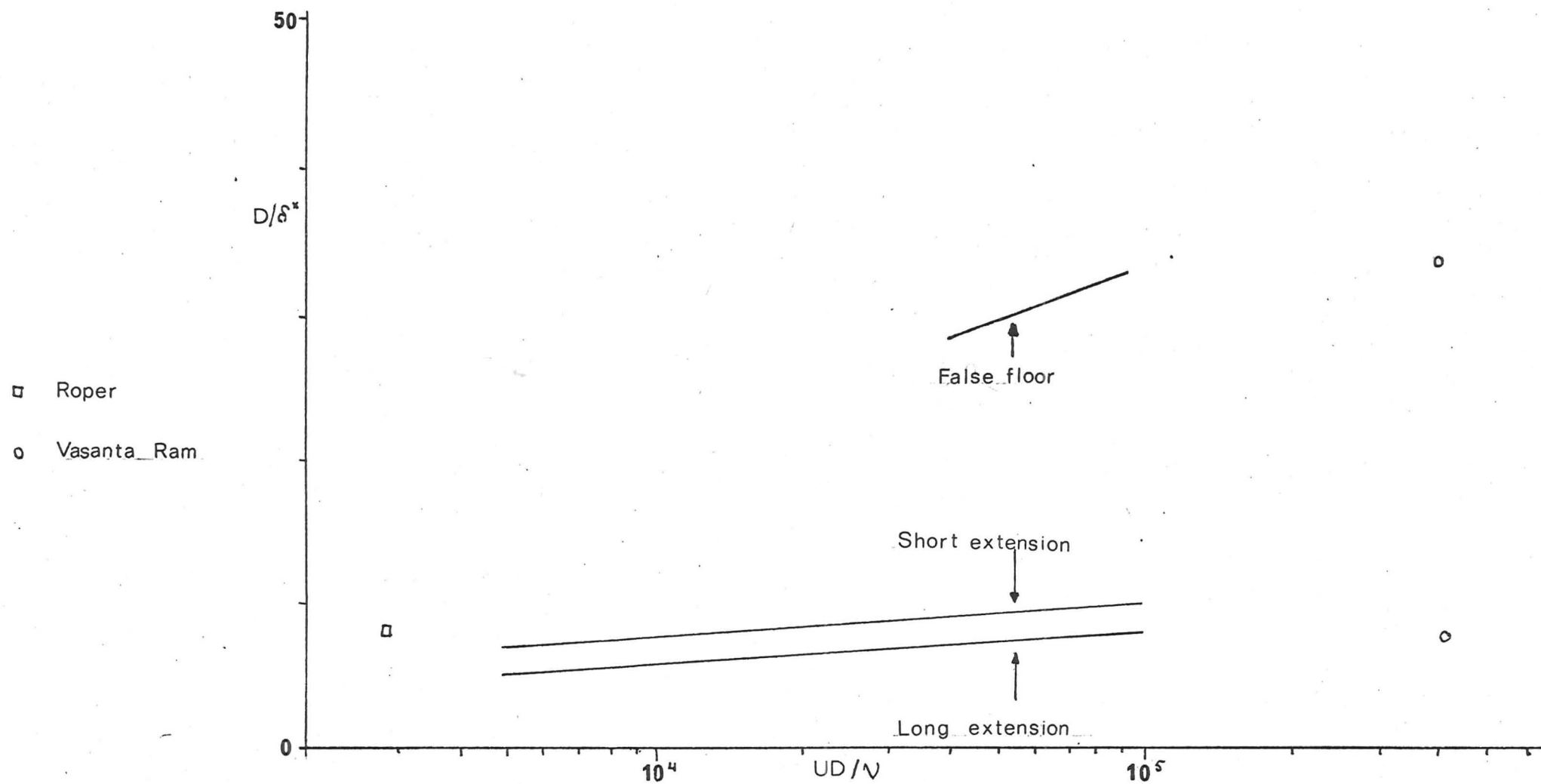
FIGURE 3.2.5 Experimental conditions

Wattastar lamp

Cooling air

Lens

Slit

Lens

Illuminated region

Cylinder

View YY

View XX
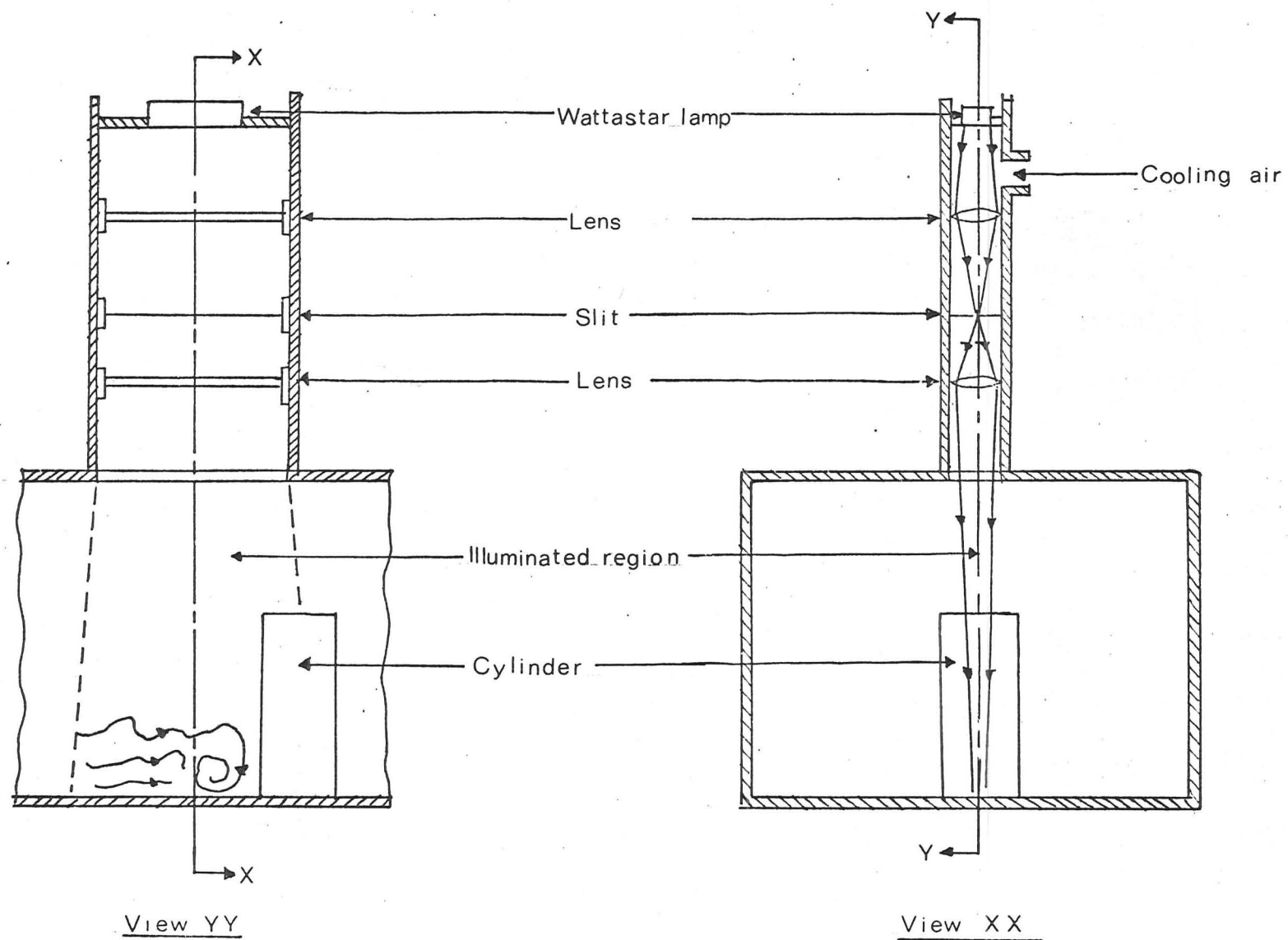
FIGURE 3.2.6 Smoke Illumination system

(a)

———— —— Separation

— — — — —Attachment

S

S_1

A_0

(b)
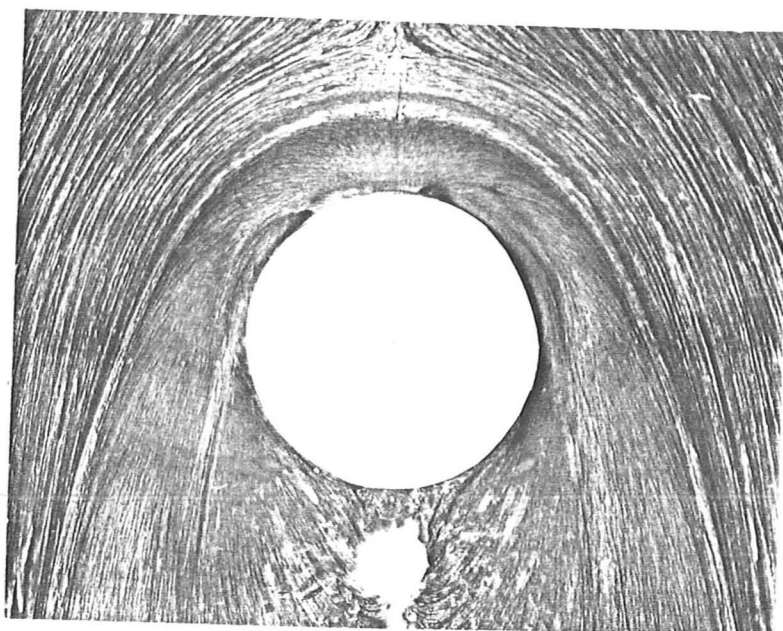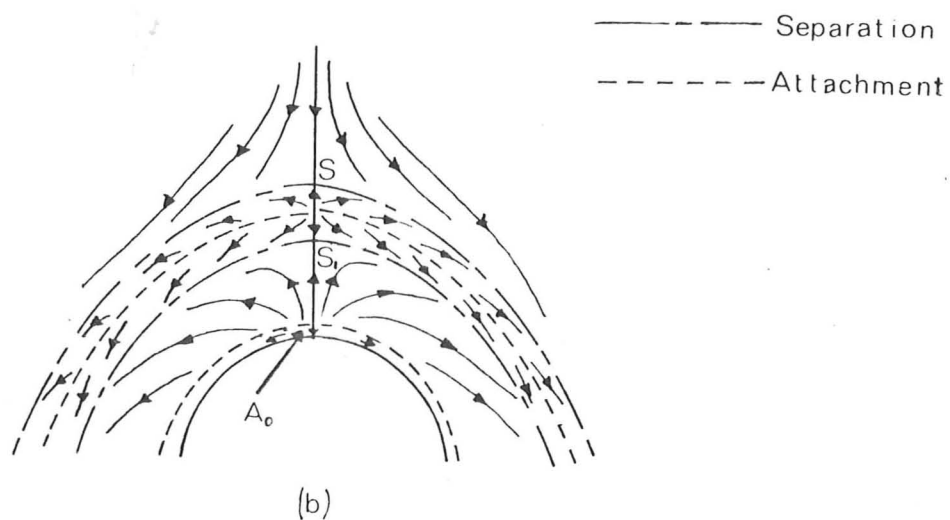
FIGURE 3.3.1 Oil flow visualization: $UD/\nu = 1.1 \times 10^5, D/\delta^* = 11.3, H = 1.37$
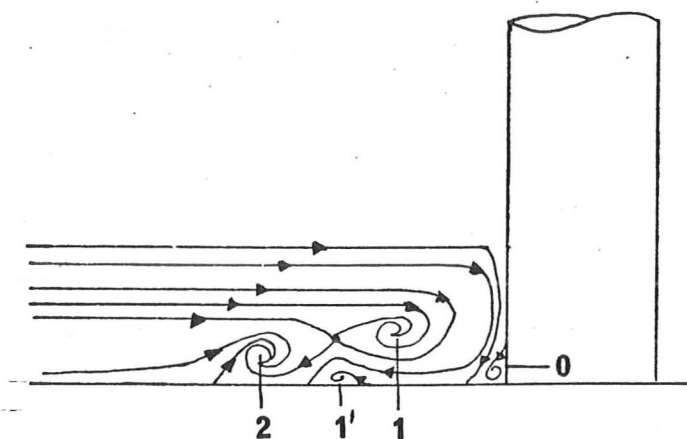
FIGURE 3.3.2   Inferred flow pattern on plane of symmetry
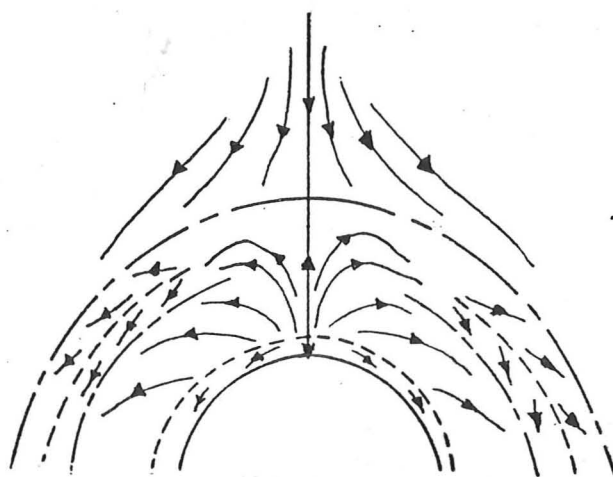
FIGURE 3.3.3.'Split' separation line flow pattern

Plans

Elevations

S_0
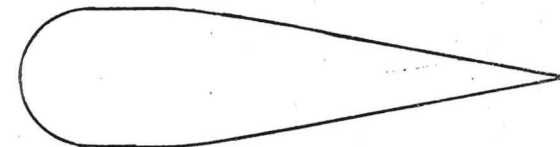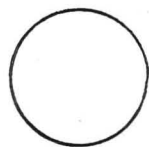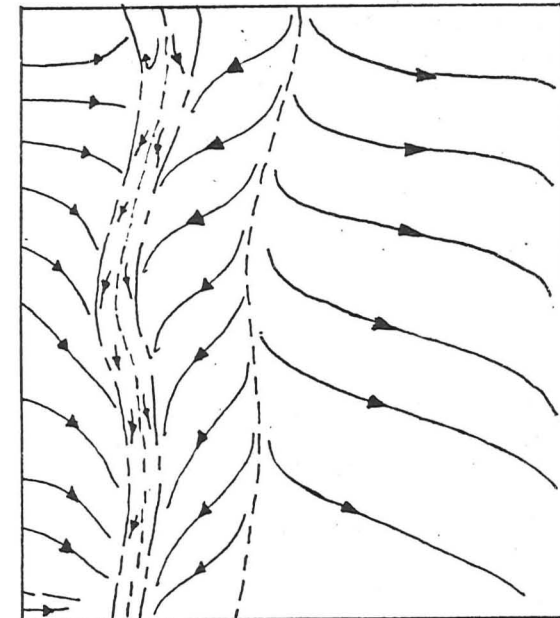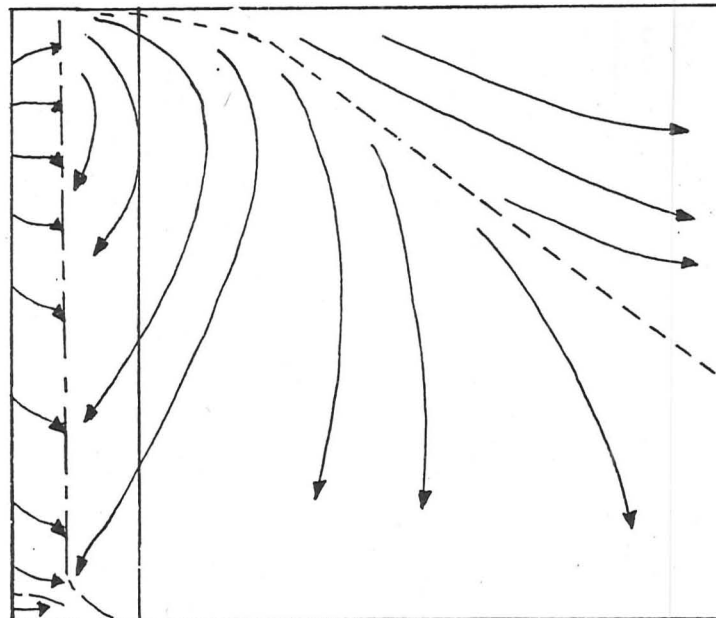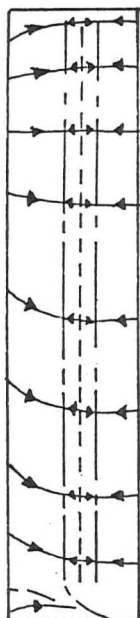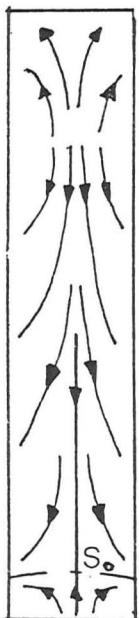
(a) Front of models (b) Cylinder   (c) Cylinder with splitter plate   (d) Streamlined model

————— — — Separation

— — — — — — Attachment

FIGURE 3.3.4 : Flow patterns on surface of models, $UD/\nu = 59,100$; $D/\delta^* = 9.6$; $H = 1.4$

(a)

5 cm

Flow

vortex

(b)

B

A

5 cm

40°
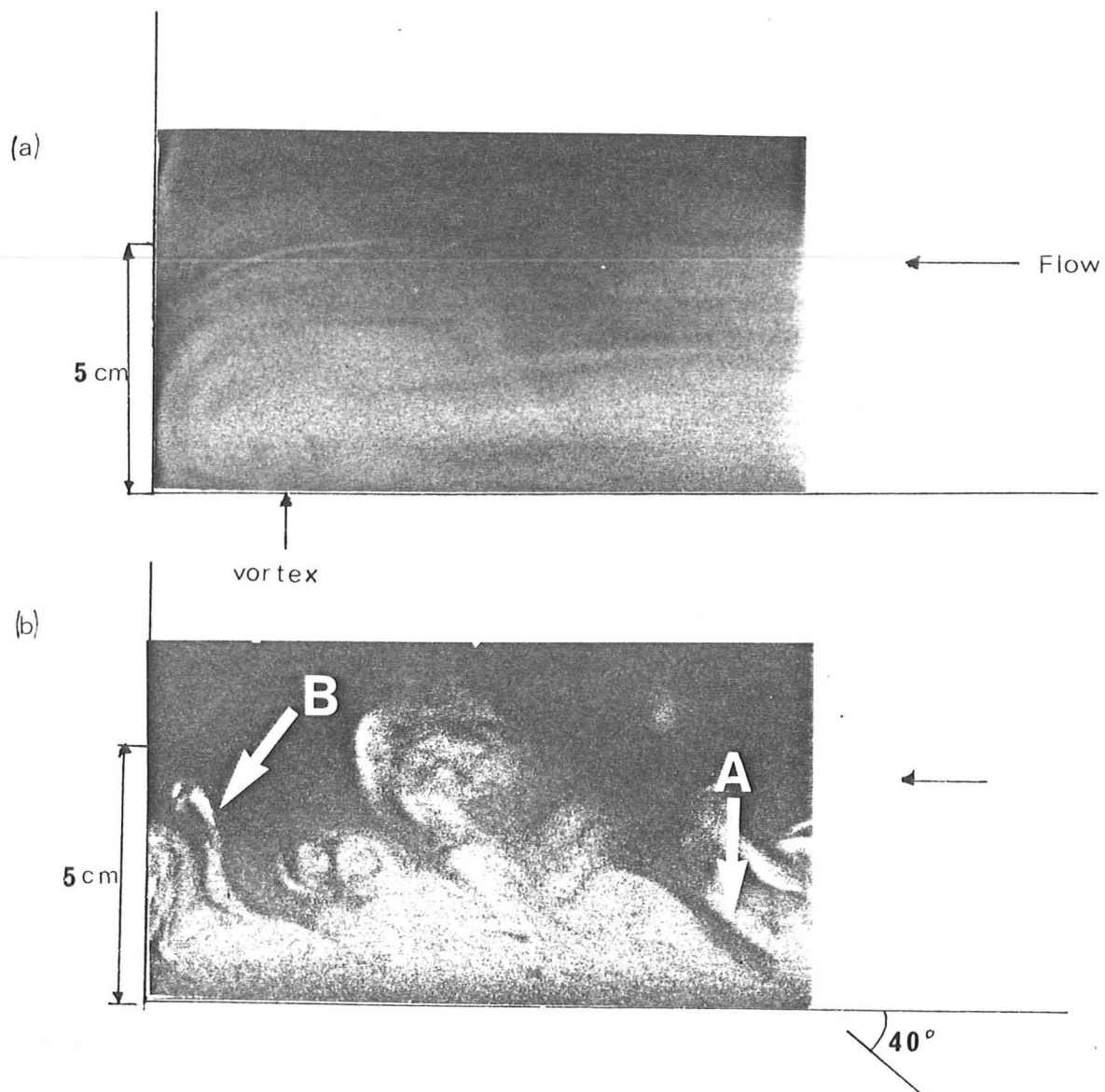
FIGURE 3.3.5: Smoke flow visualisation $UD/\nu = 7.65 \times 10^3$
$D/\delta^* = 7.7$
$H = 1.75$
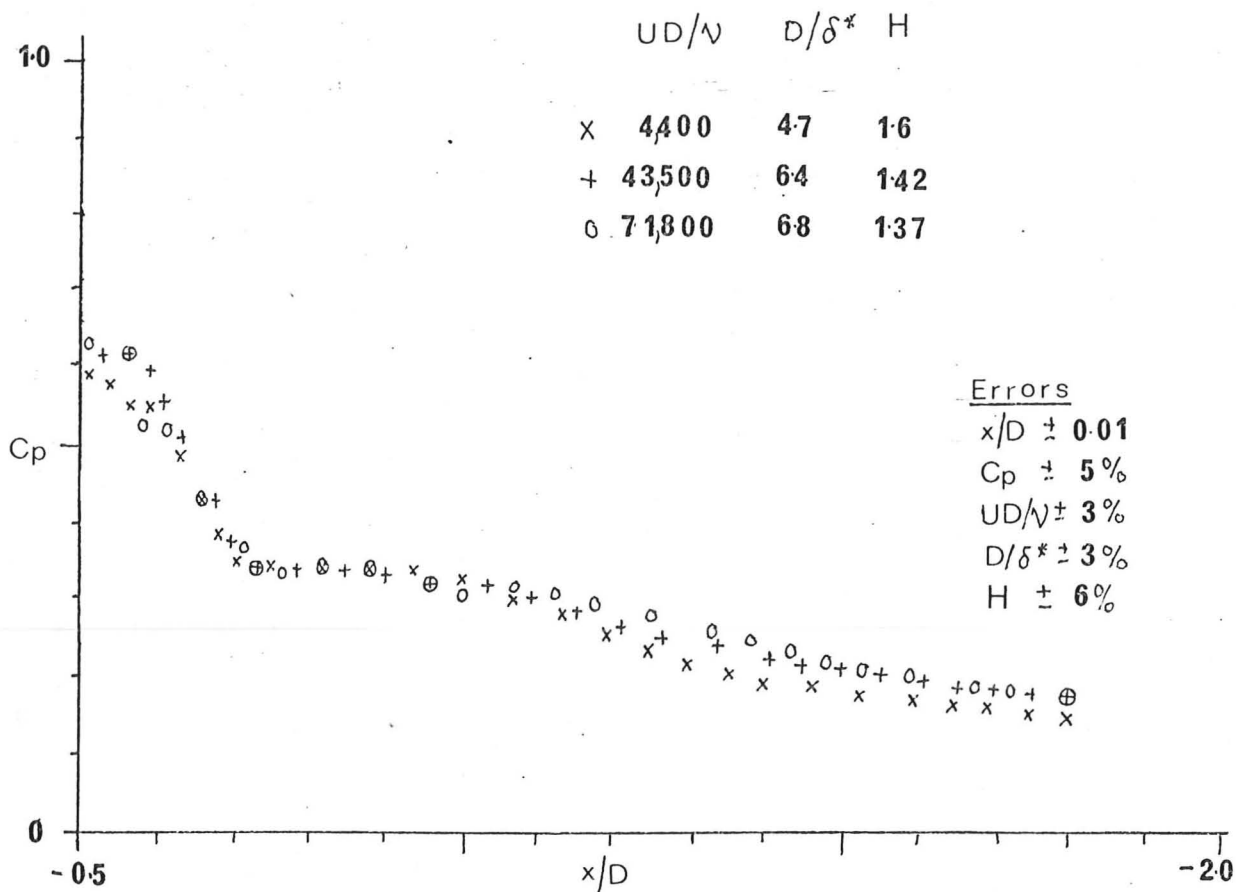
FIGURE 3.4.1   Pressure distributions upstream of cylinder (long extension)
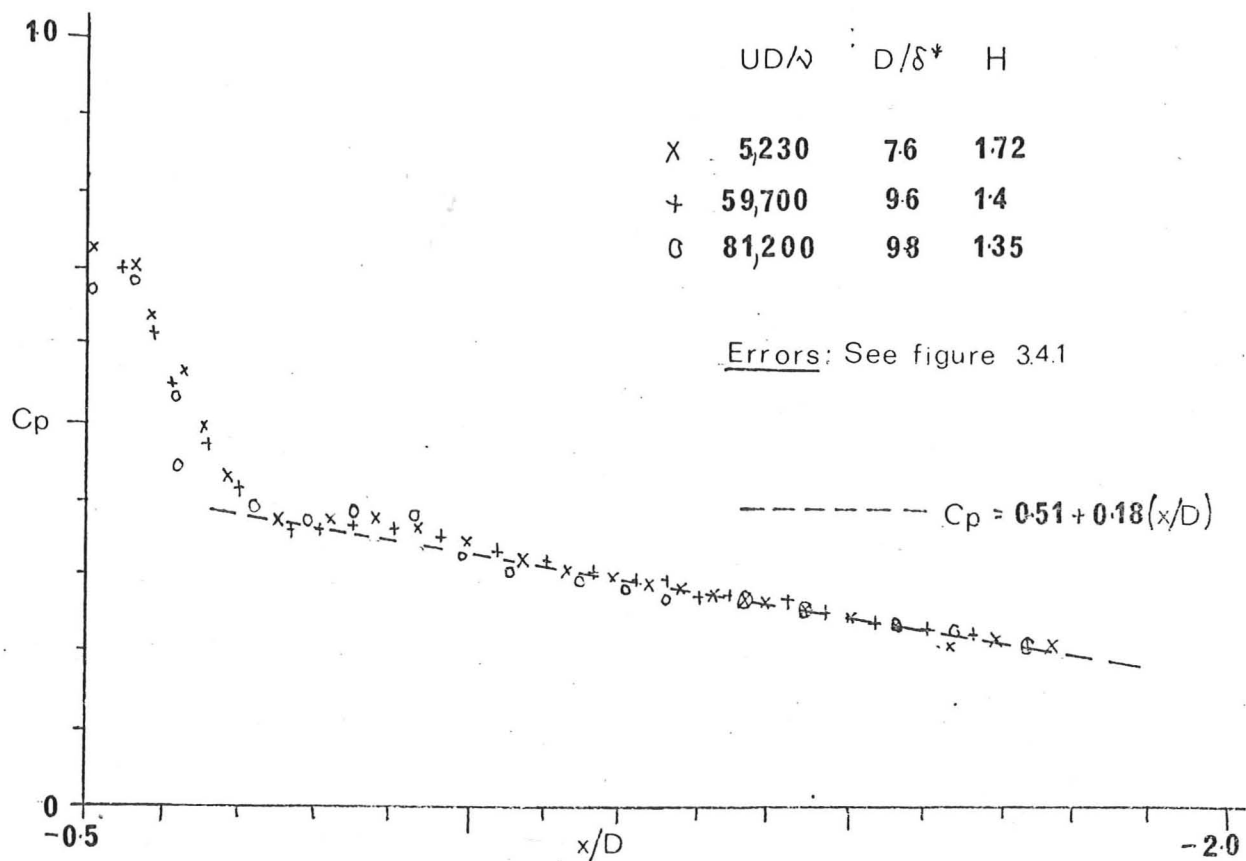
FIGURE 3.4.2 Pressure distribution upstream of cylinder (short extension)

The graph shows pressure distribution data with axes C_p (vertical, 0 to 1·0) and x/D (horizontal, -0·5 to -2·0).

Legend:

	UD/ν	D/δ^*	H
□	44,800	29·4	1·47
o	68,900	30·9	1·47
x	94,700	32·1	1·47

Errors: See figure 3.4.1
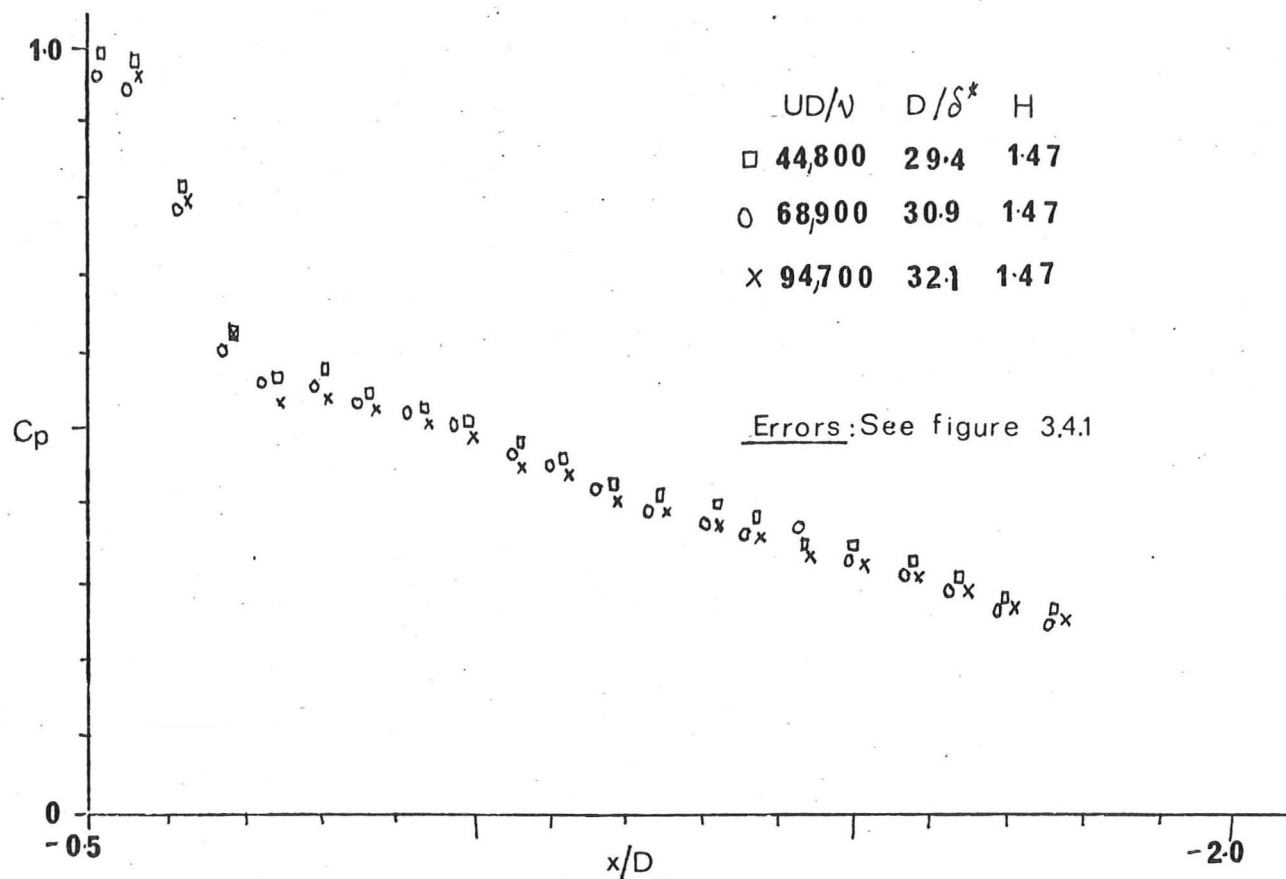
FIGURE 3.4.3 Pressure distributions upstream of cylinder (false floor)

The graph shows pressure distribution data with axes C_p (vertical, 0 to 1·0) and x/D (horizontal, -0·5 to -2·0).

Legend:

		UD/ν	D/δ^*	H
□	Cylinder	4,120	7·4	1·75
o	" with plate	4,120	7·4	1·75
x	Streamlined model	4,080	7·4	1·75

Errors: See figure 3.4.1
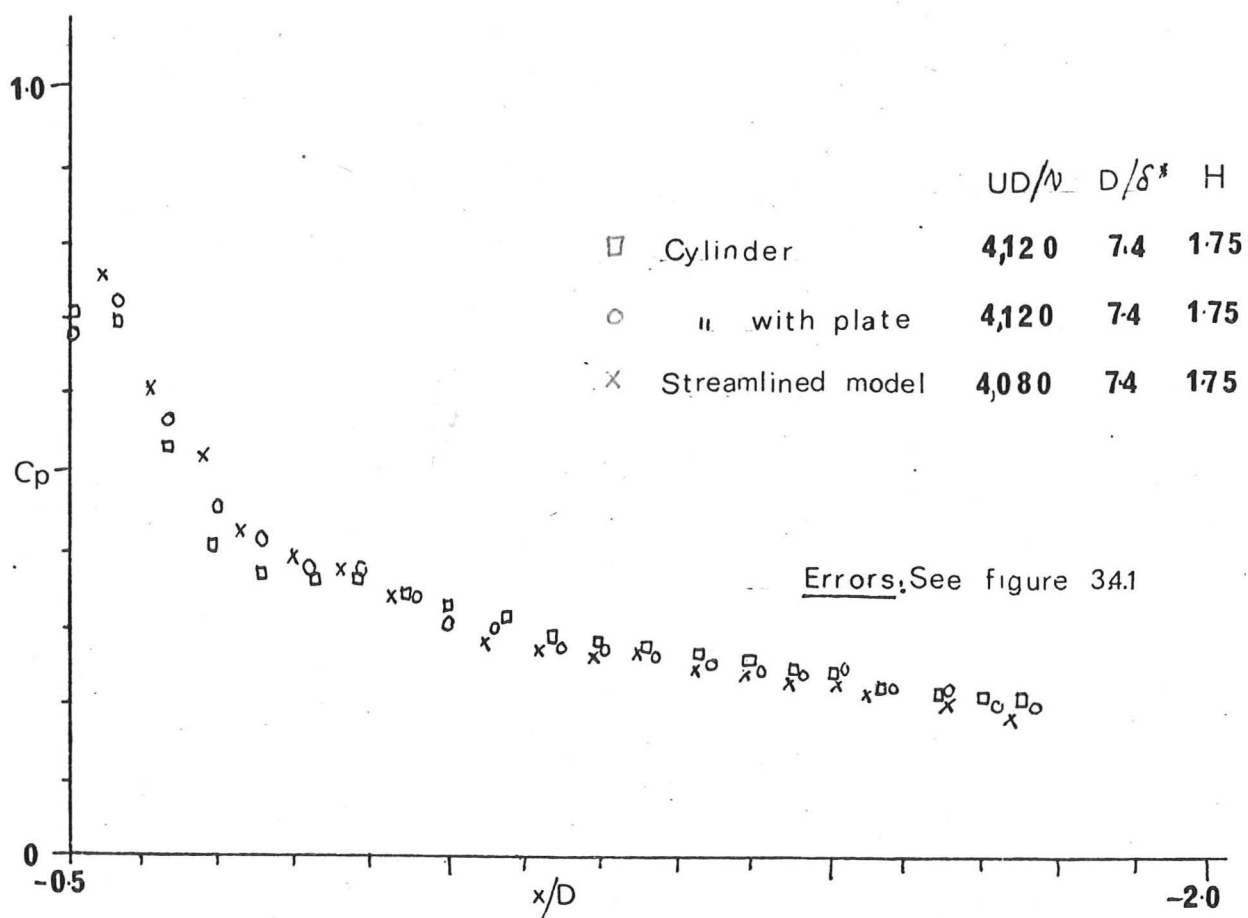
FIGURE 3.4.4 Pressure distributions upstream of different models

(short extension)

FIGURE 3.5.1
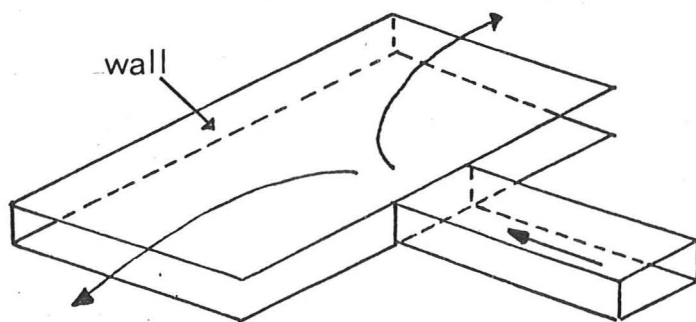
Johnston's experiment
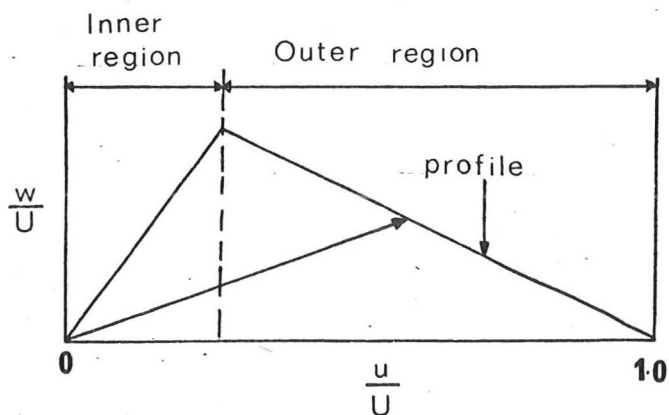
FIGURE 3.5.2

Triangular profile
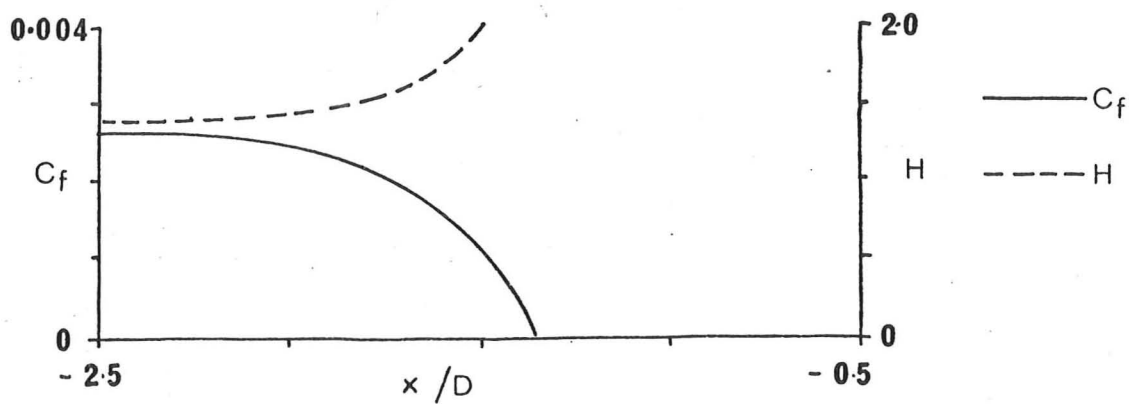
FIGURE 3.5.3 Typical result using Johnston's model
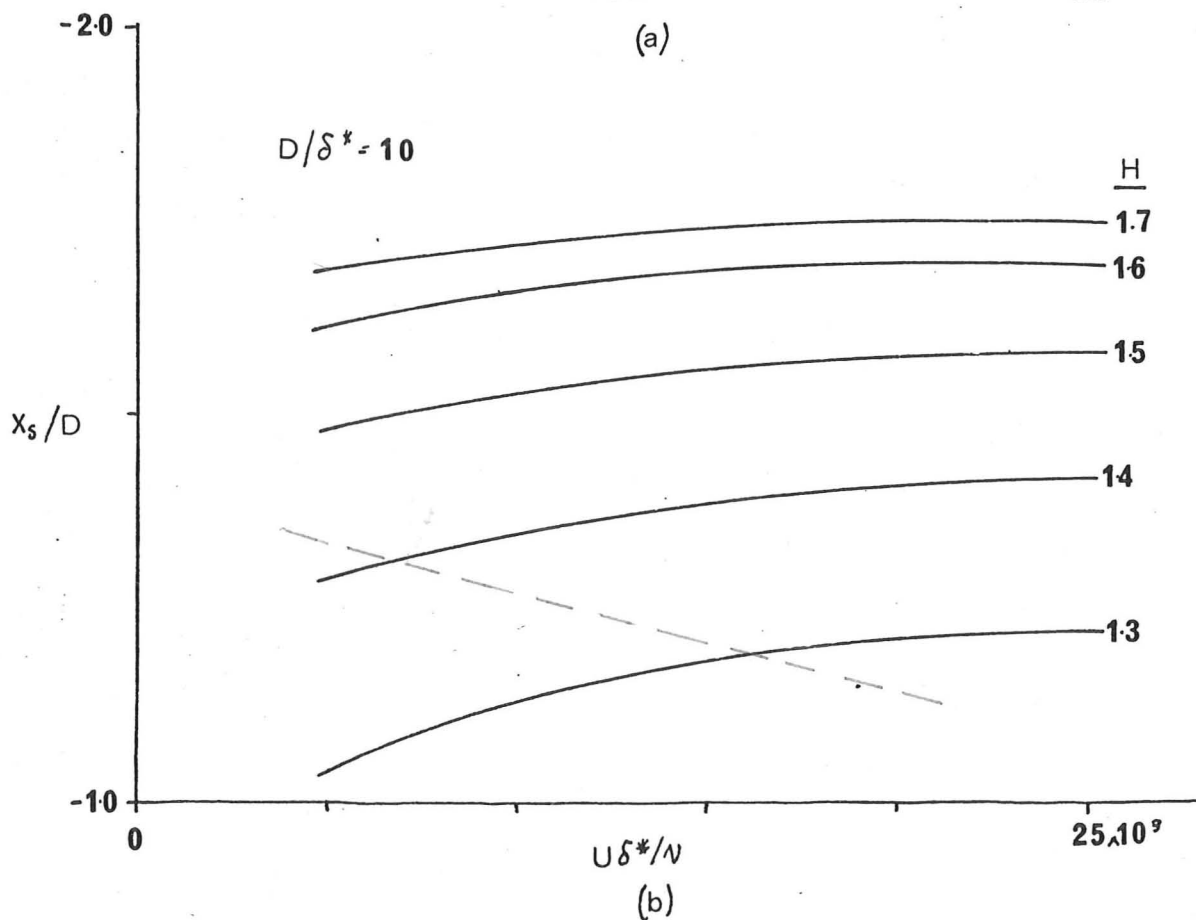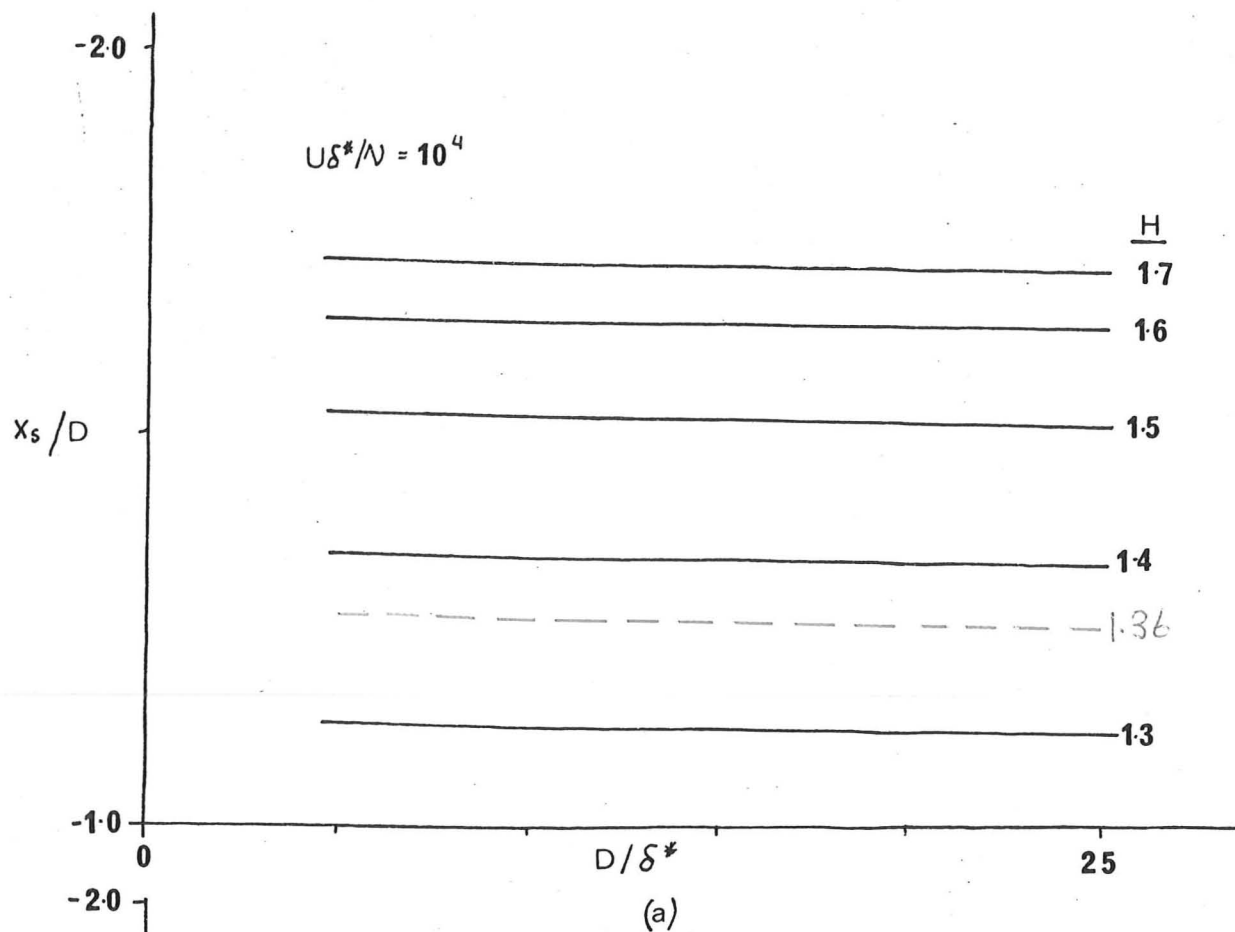
$$\left(U\delta^*/_{\mathcal{N}} = 10^4, D/\delta^* = 10\cdot0, H = 1\cdot4 \right)$$

FIGURE 3.5.4 Variation of x_s/D with $U\delta^*/\mathcal{N}, D/\delta^*$ and H
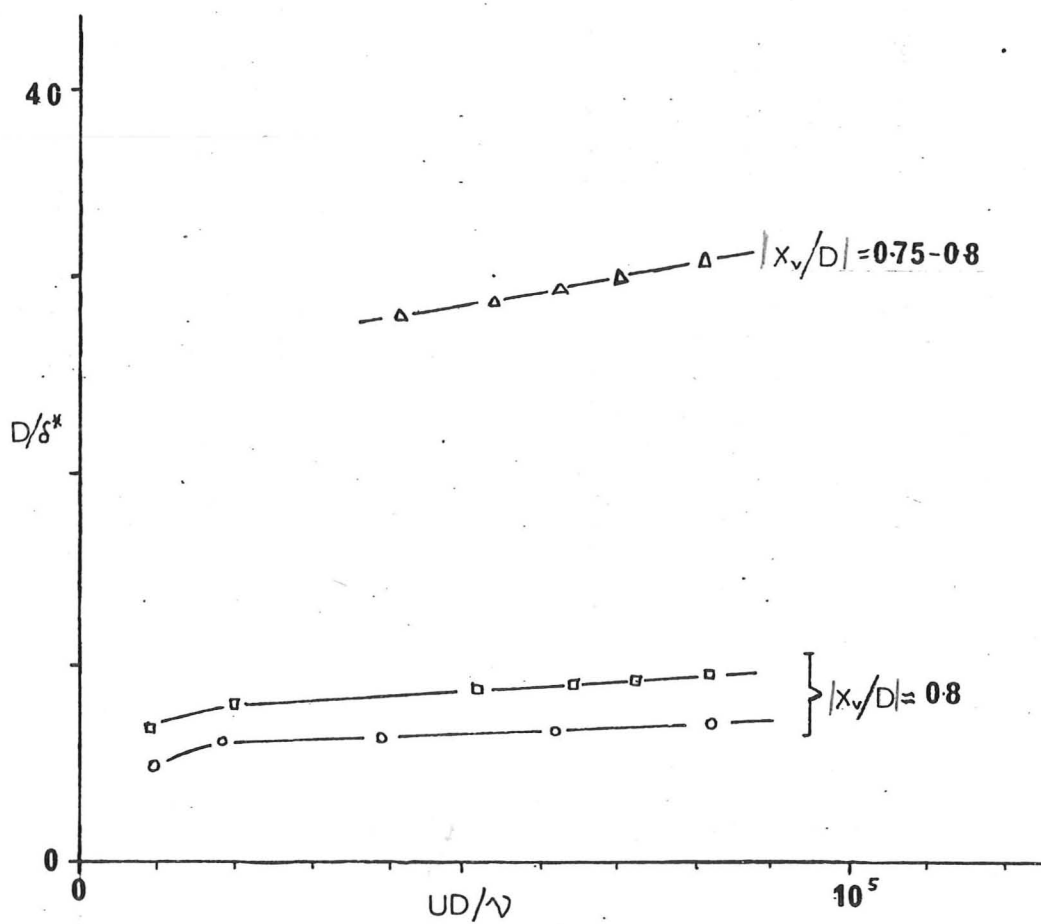
FIGURE 3.6.1 Variation of vortex position

Errors: $U\delta^*/\nu = \pm 6\%$, $X_s/D = \pm 0.04$
$D/\delta^* = \pm 3\%$, $X_{s'}/D = \pm 0.02$
$H = \pm 6\%$.

$H = 1.47$

Numbers indicate values of $|x_s/D|$
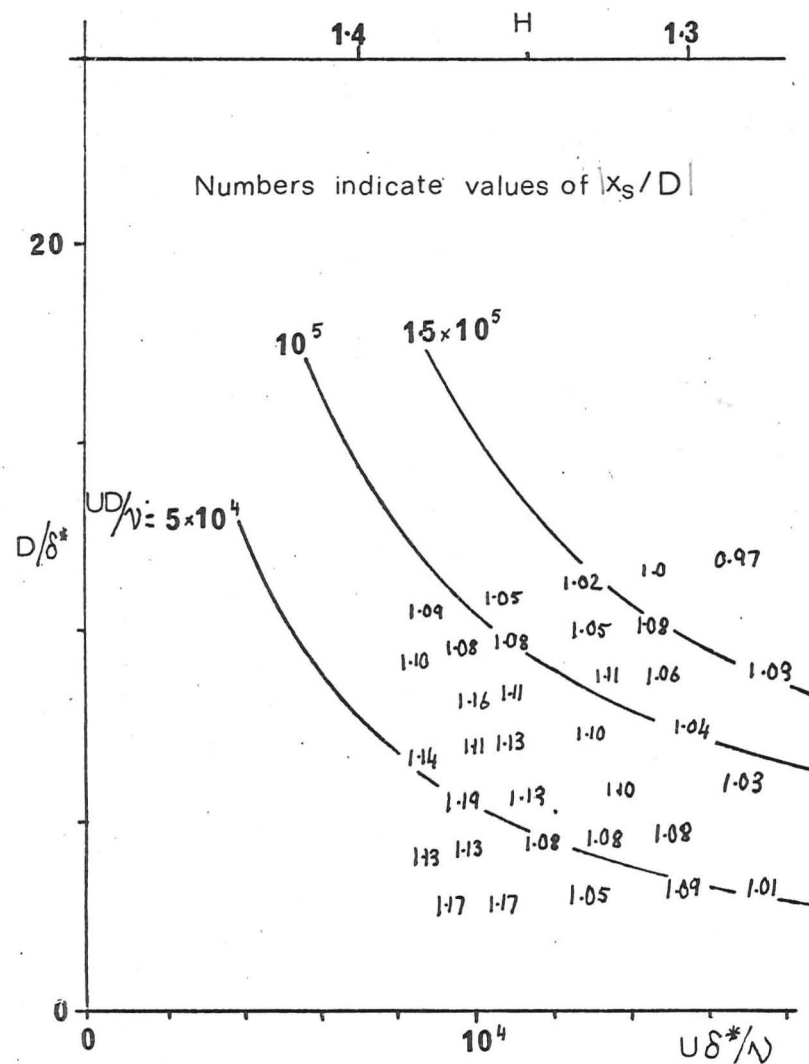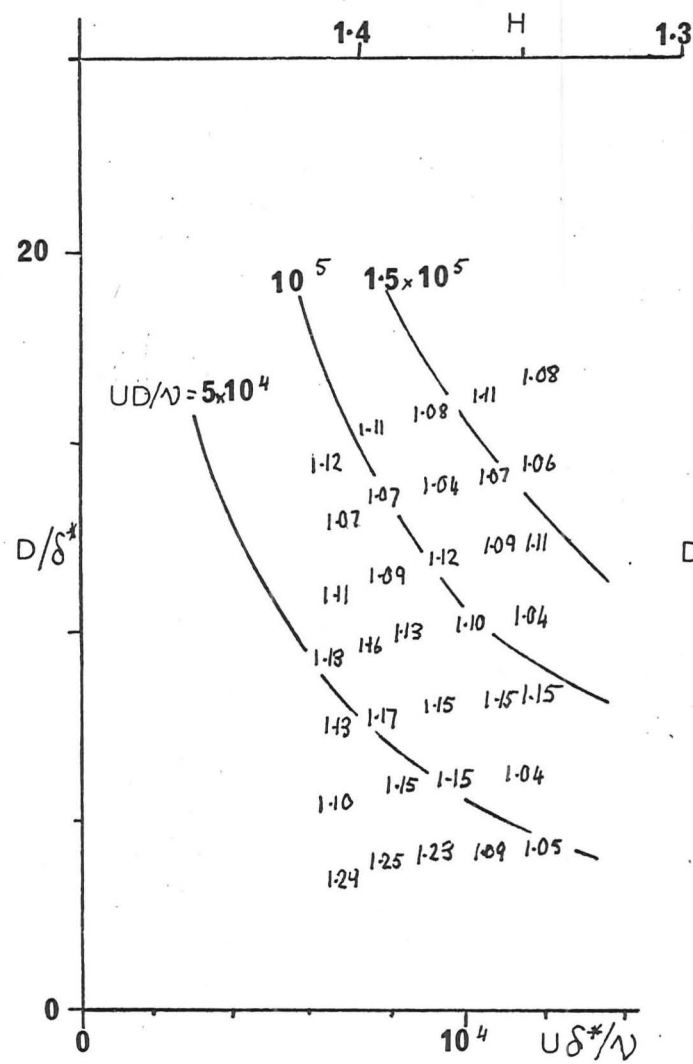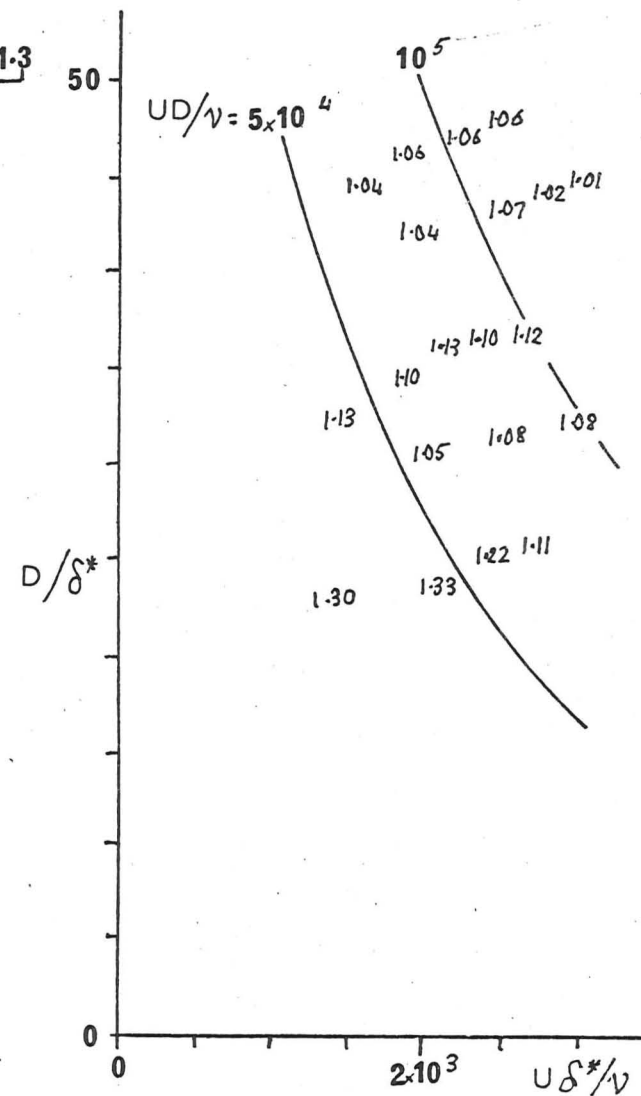
FIGURE 3.6.2 Variation of x_s/D
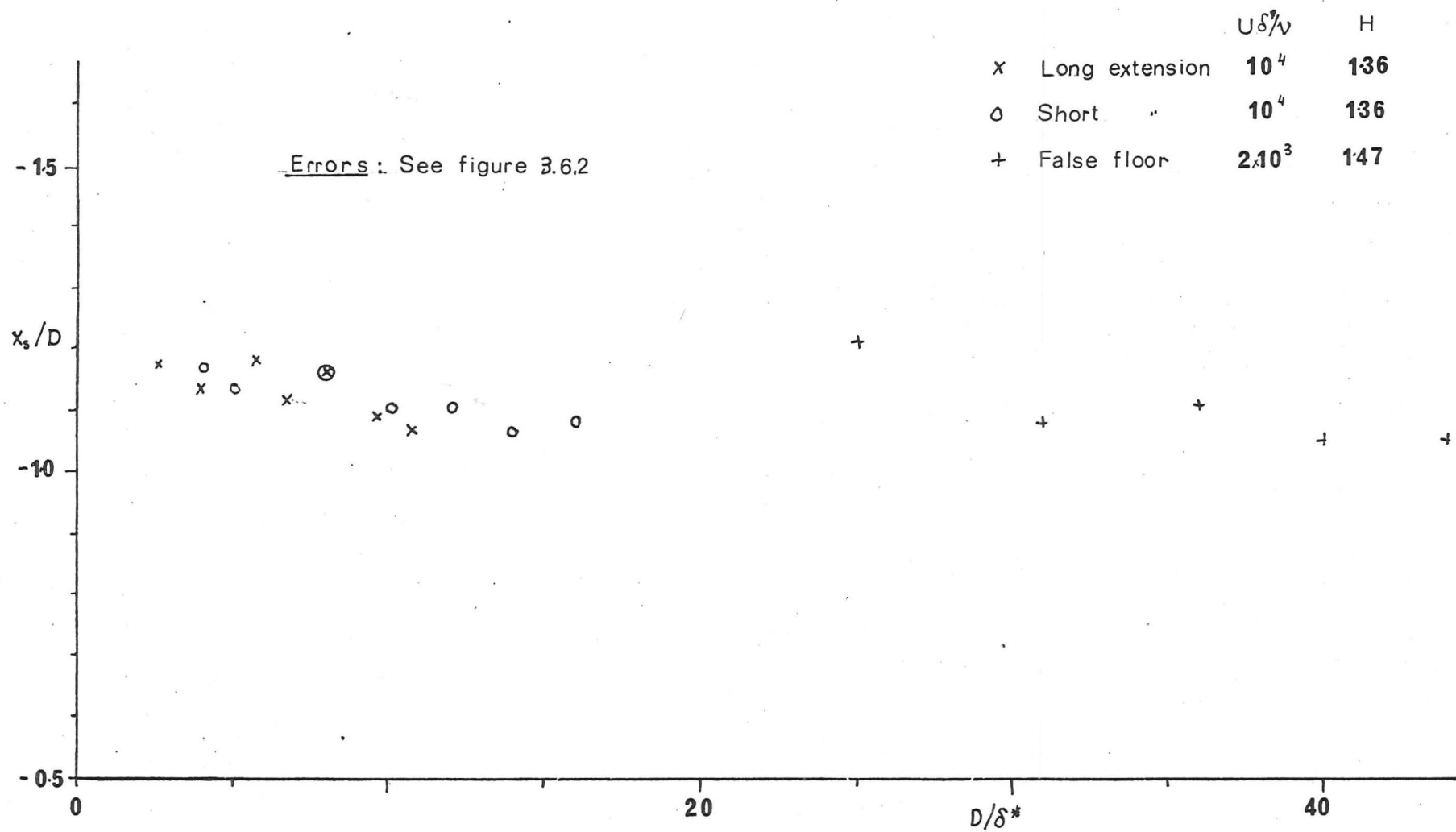
FIGURE 3.6.3: Variation of x_s/D with D/δ^*

Errors: See Figure 3.6.2
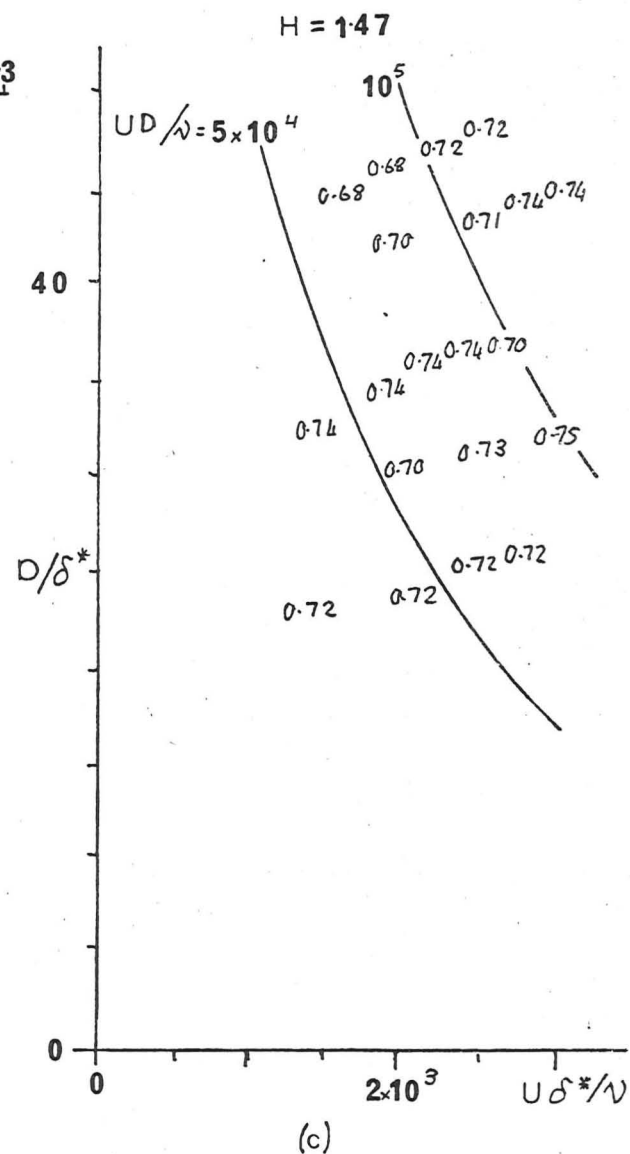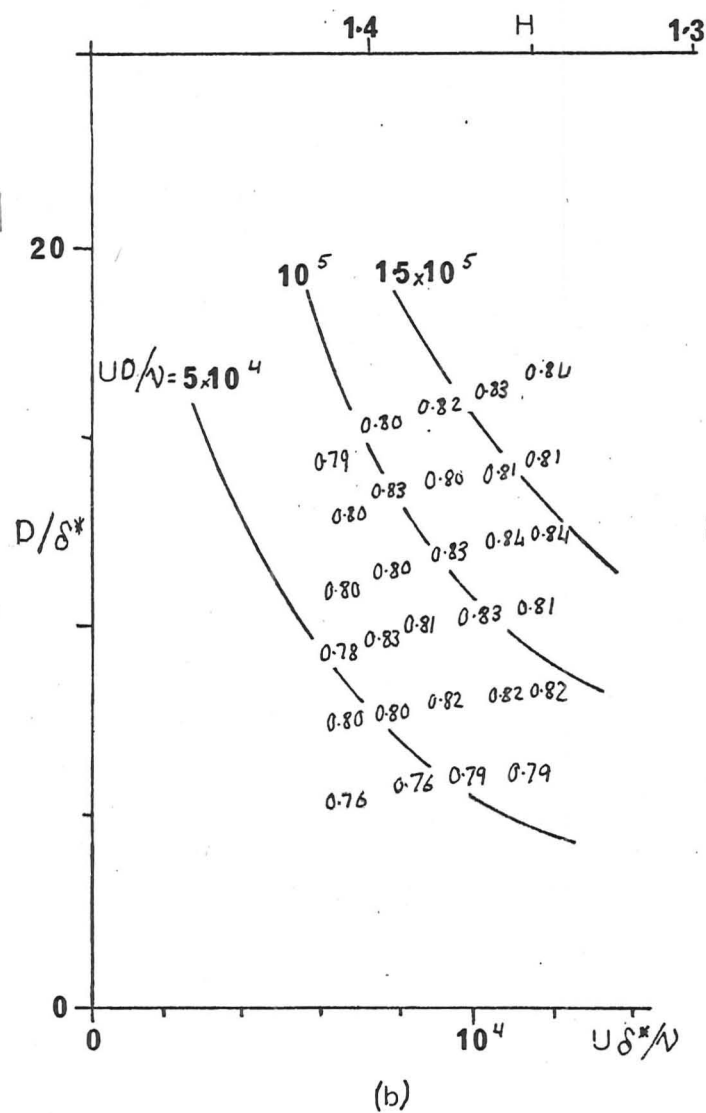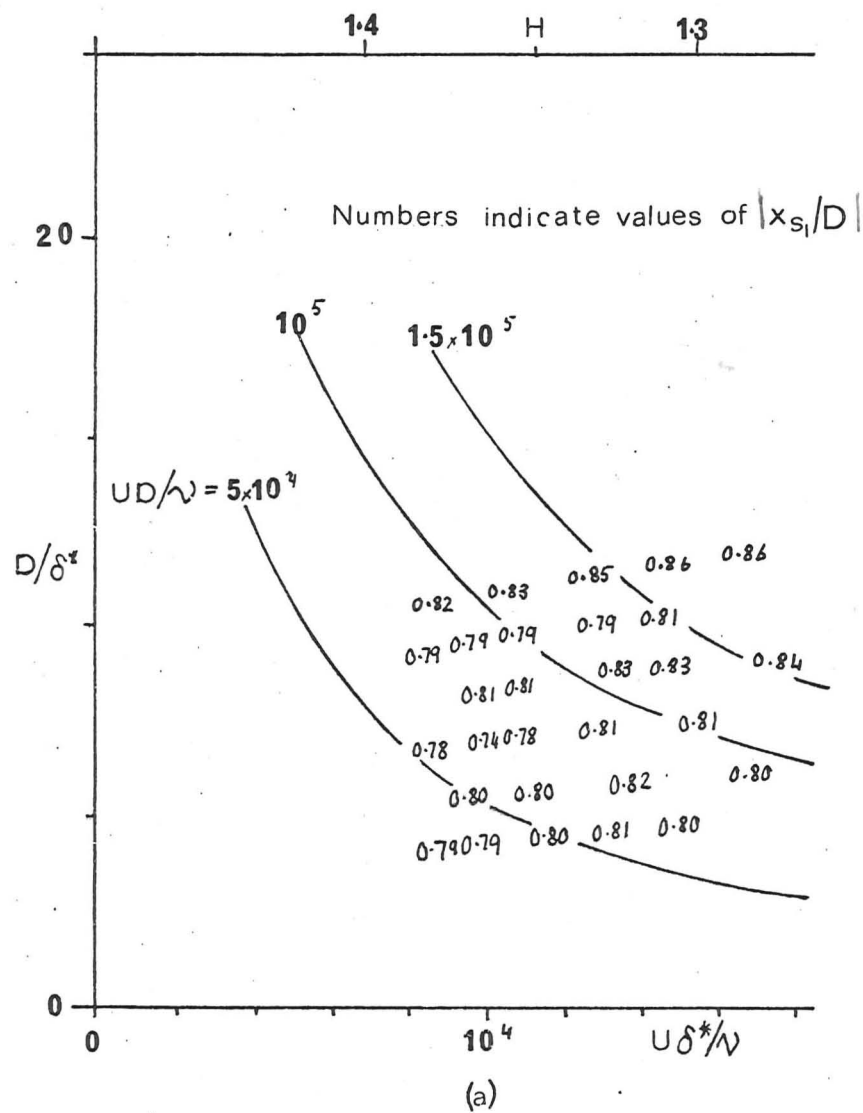
FIGURE 3.6.4 Variation of x_{s_1}/D
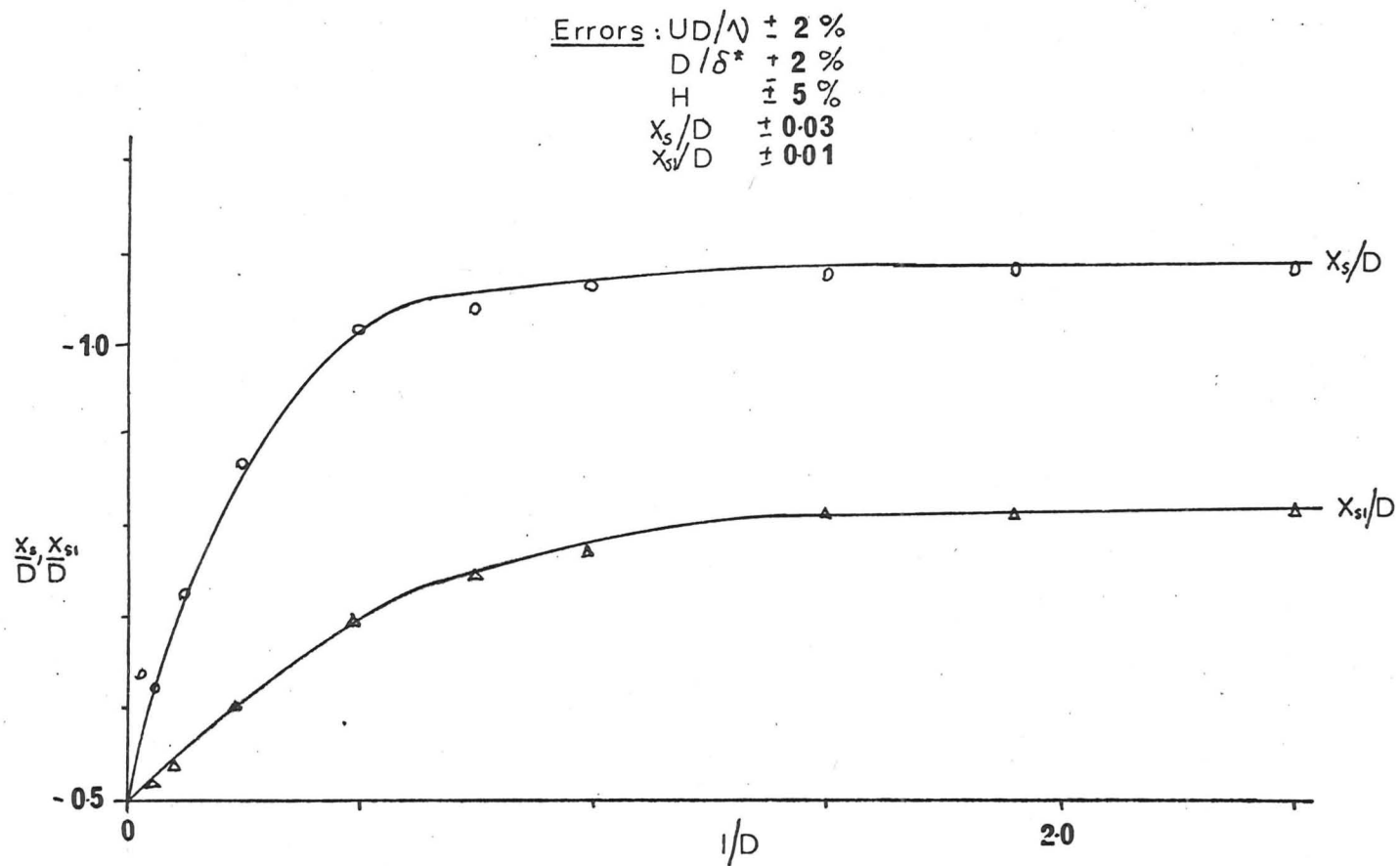
FIGURE 3.6.5 Variation of X_s/D and X_{s_1}/D with l/D : $UD/\nu = 1.43 \times 10^5$
$D/\delta^* = 15.1$
$H \;\; = 1.37$
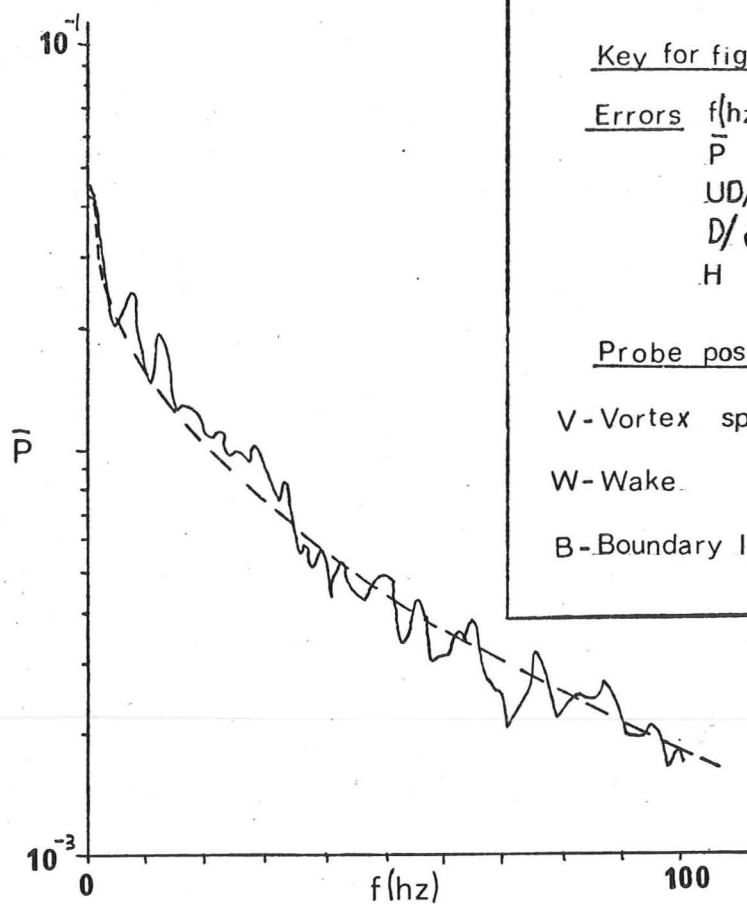
Probe position	x/D	y/D	z/D
V - Vortex spectrum	-0.81	0.06	0
W - Wake "	4.7	1.8	0.95
B - Boundary layer "	0	0.06	0

FIGURE 3.7.1 Horseshoe vortex spectrum (cylinder) ($UD/\nu = 62,800$, $D/\delta^* = 9.6$, H = 1.39)

	UD/ν	D/δ^*	H
V ———			
B - - - -	57,200	6.6	1.39
V —·—·—			
B —— ——	9,100	5.1	1.45
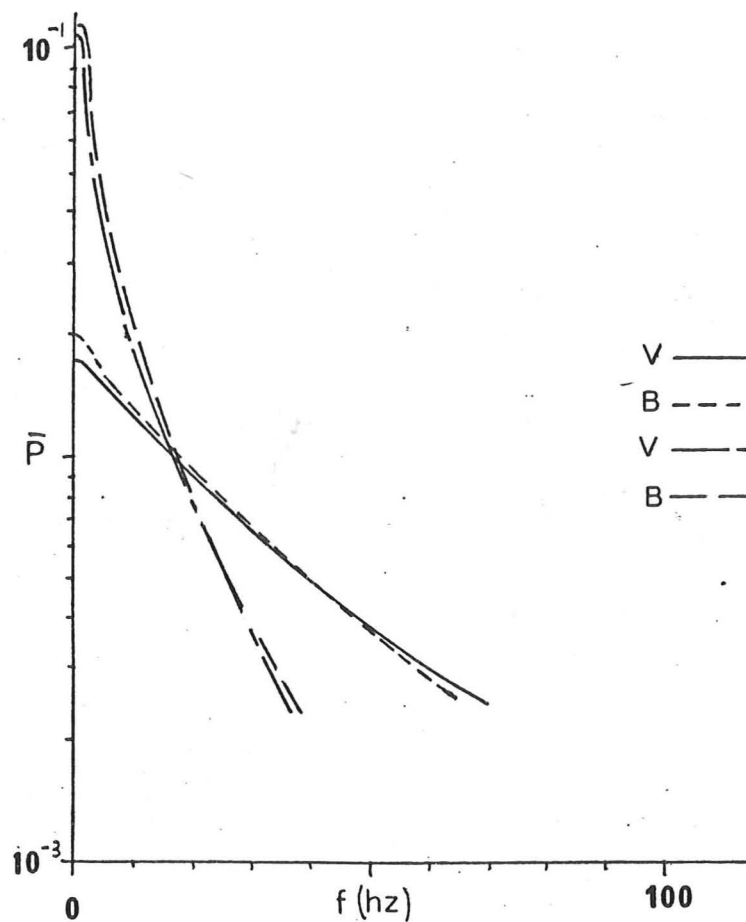
(a) Long extension

FIGURE 3.7.2 Horseshoe vortex spectra (cylinder)
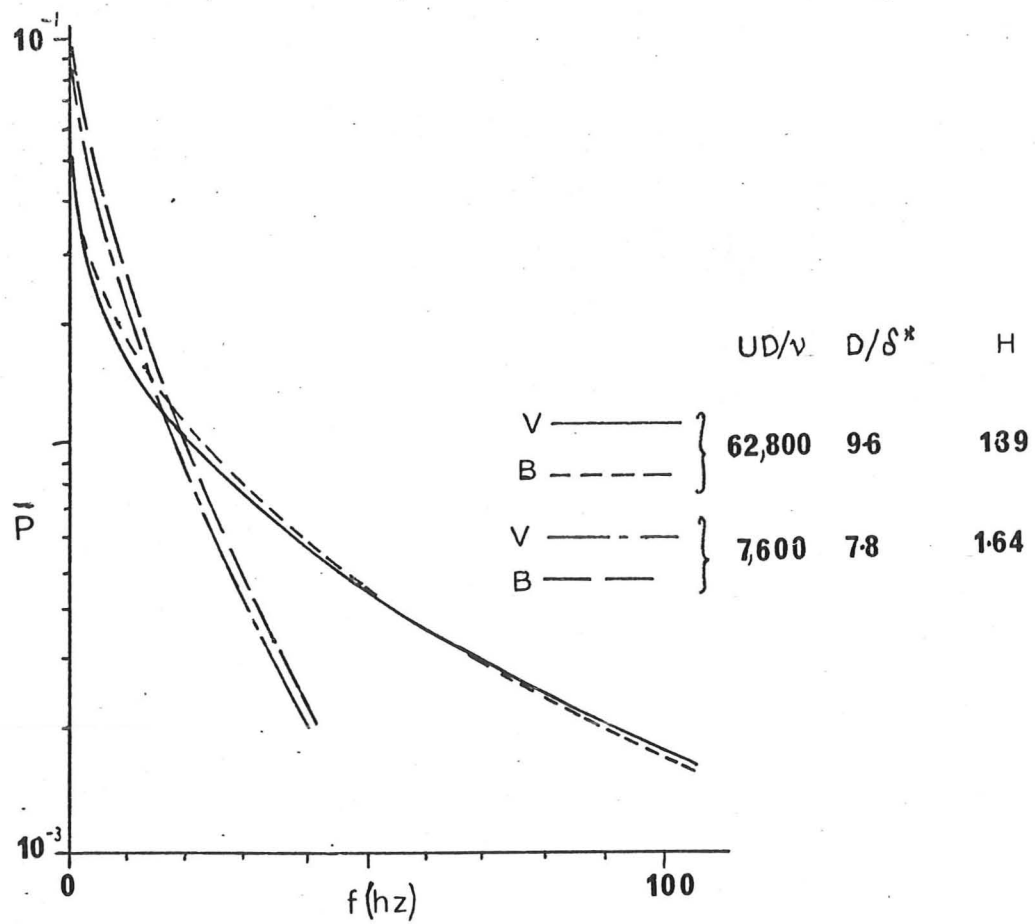
(b) Short extension

(c) False floor

FIGURE 3.7.2 (cont)

	UD/ν	D/δ^*	H
——————	57,200	6·6	1·39
– – – – –	62,800	9·6	1·39
— ·· — ·· —	63,640	30·5	1·47

FIGURE 3.7.3 Effect of D/δ^* on vortex spectra

		UD/ν	D/δ^*	H
——————	Cylinder	62,800	9·6	1·39
– – – – –	" and plate	63,000	9·6	1·39
— · — · —	Streamlined	61,000	9·6	1·39
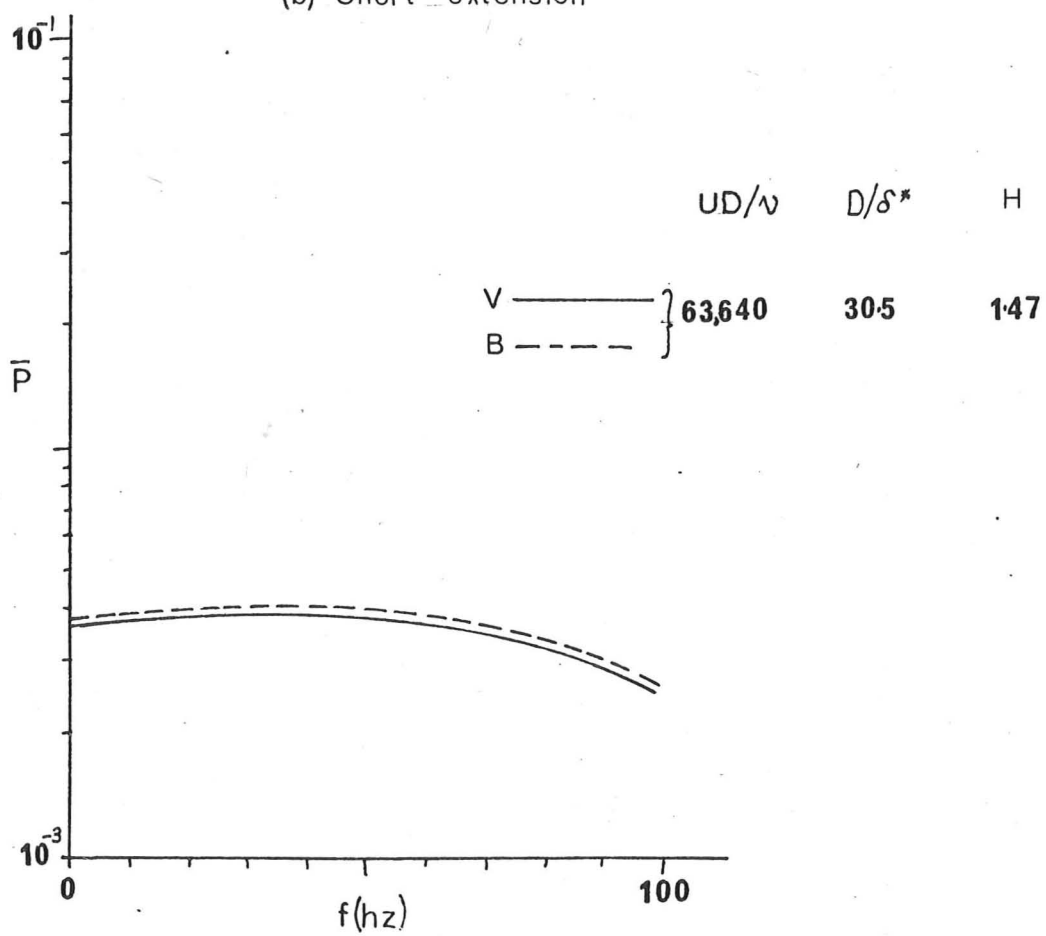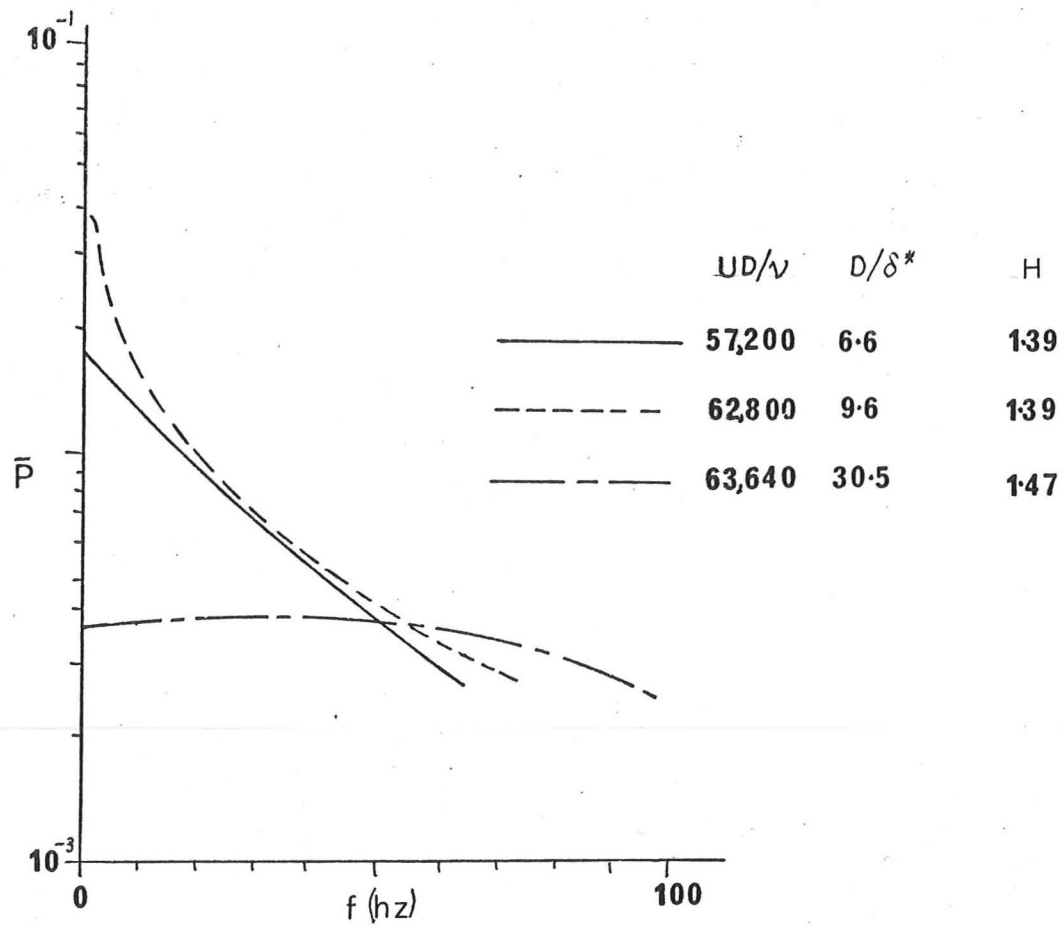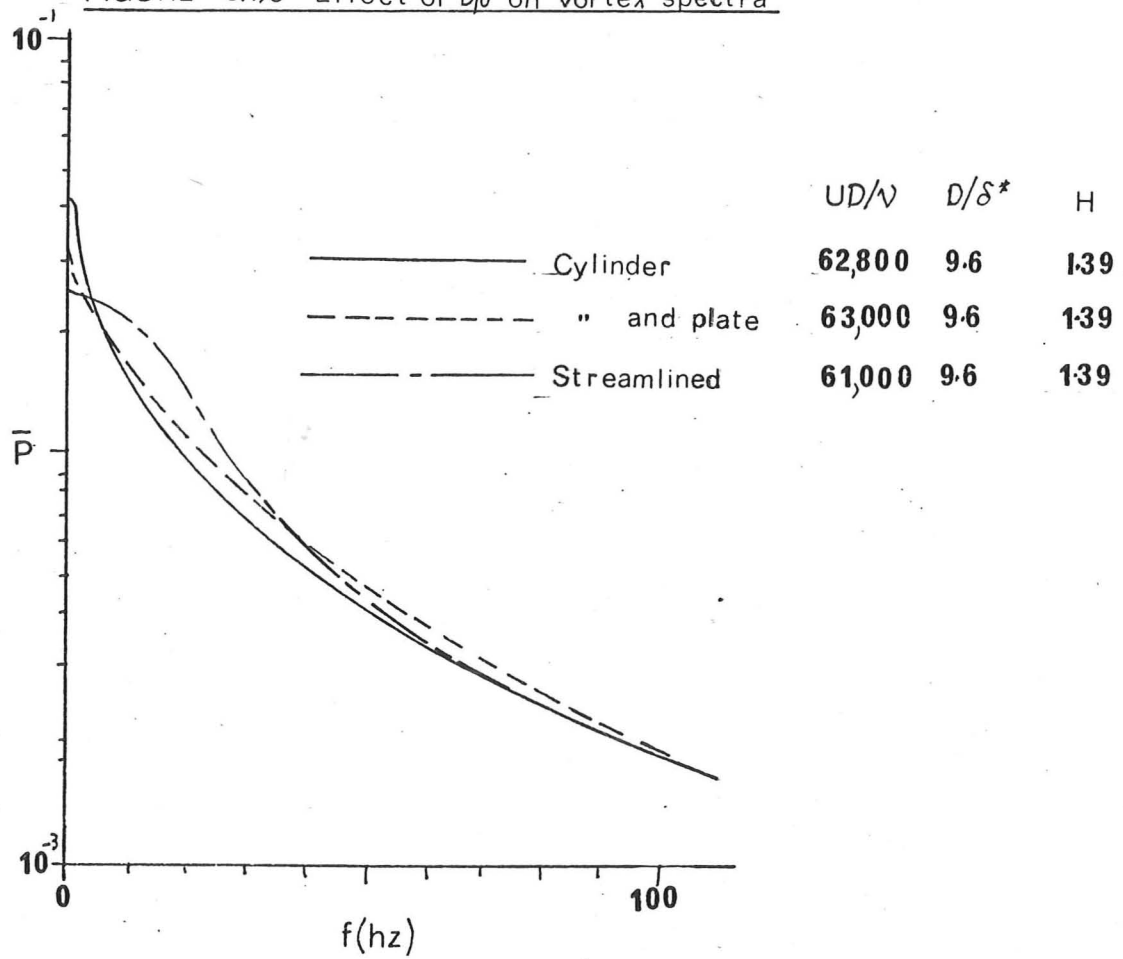
FIGURE 3.7.4 Effect of model shape on vortex spectra

	$U D/\nu$	D/δ^*	H
(a) cylinder	64,200	9·6	1·39
(b) streamlined	61,600	9·6	1·39
(c) cylinder with plate	61,800	9·6	1·39
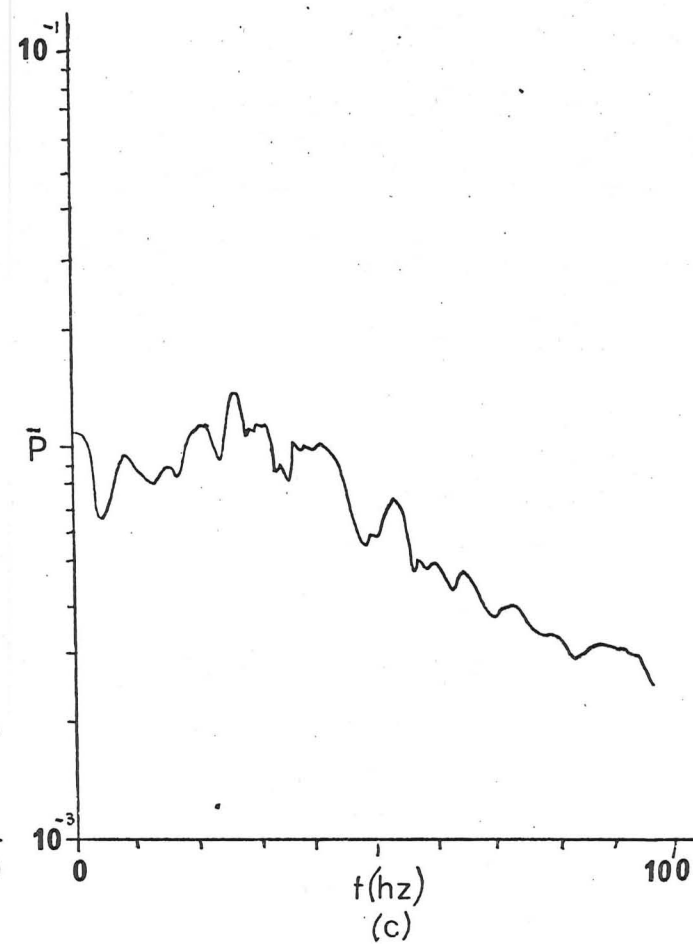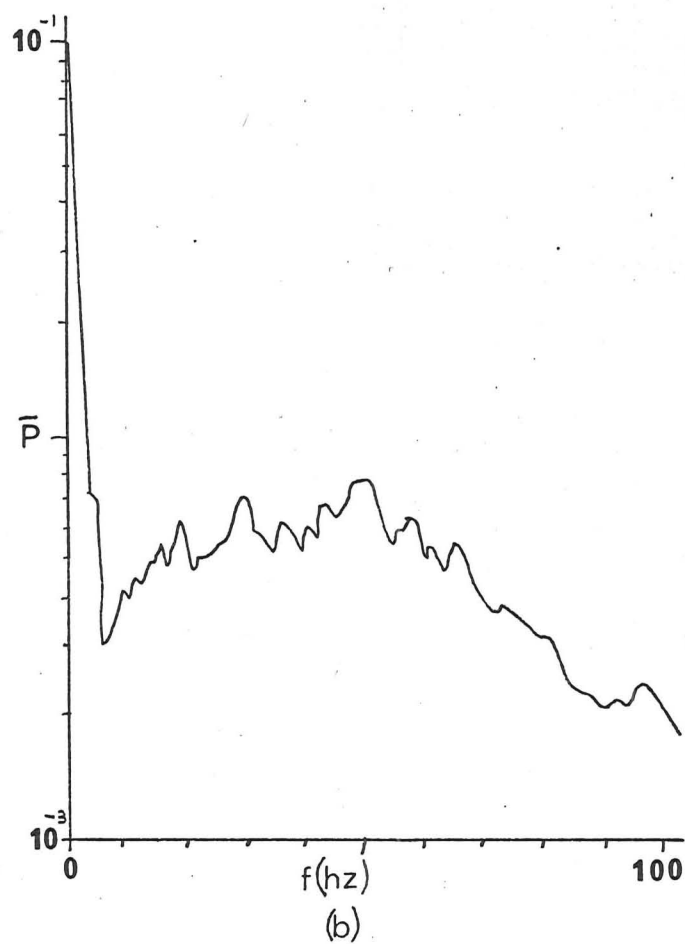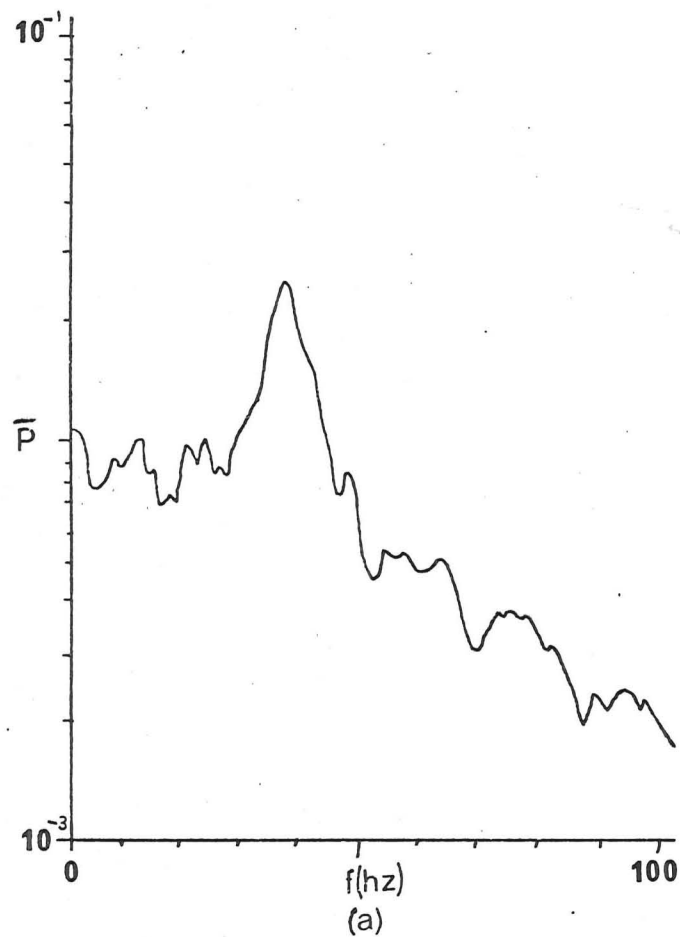
FIGURE 3.7.5 Wake spectra

Ripple pattern in wake

Deposited sediment

(a)

Scour hole

Flow
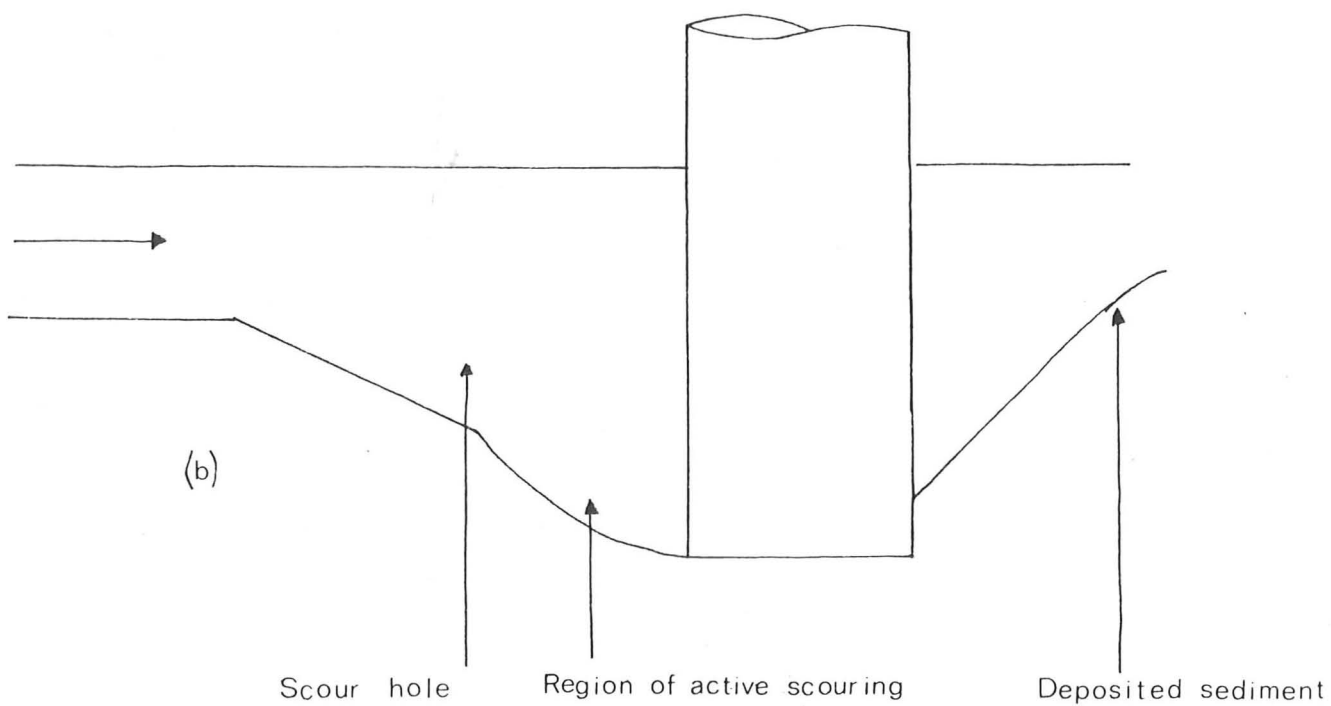
(b)

Scour hole   Region of active scouring   Deposited sediment

FIGURE 4.31 Scour holes observed by Melville
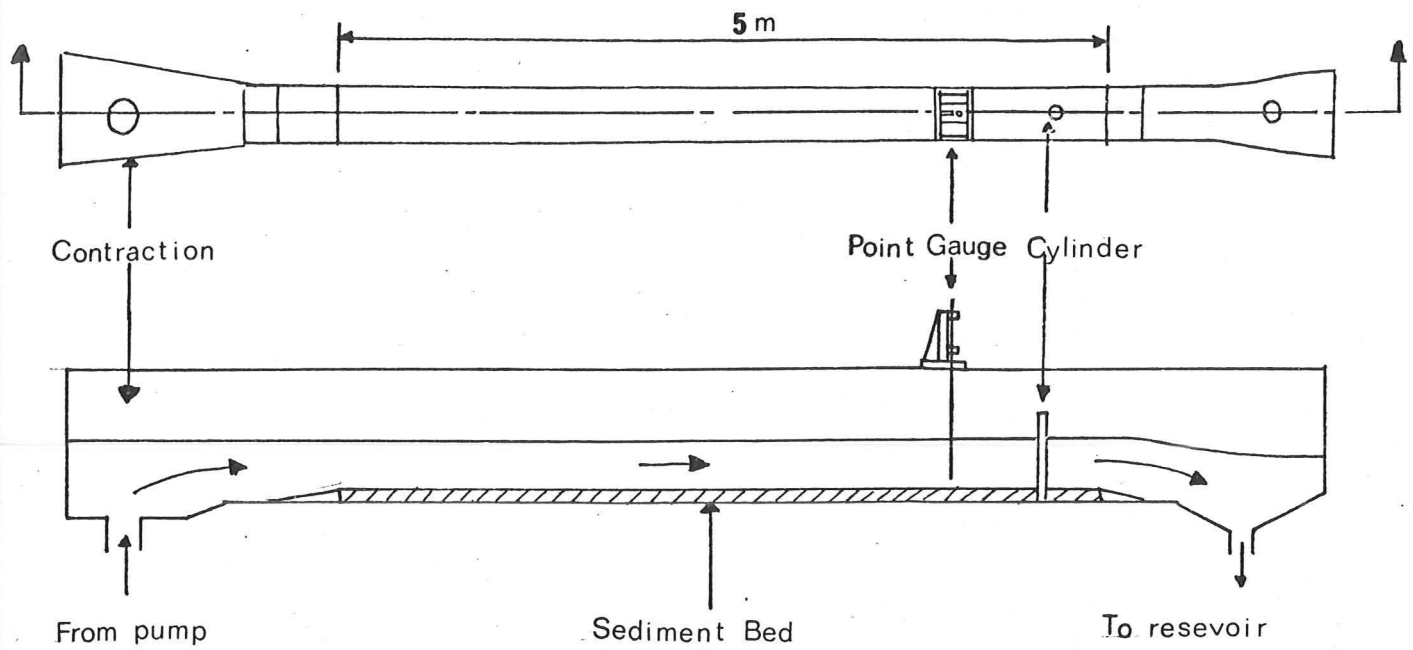
FIGURE 4.4.1   Sediment transport flume
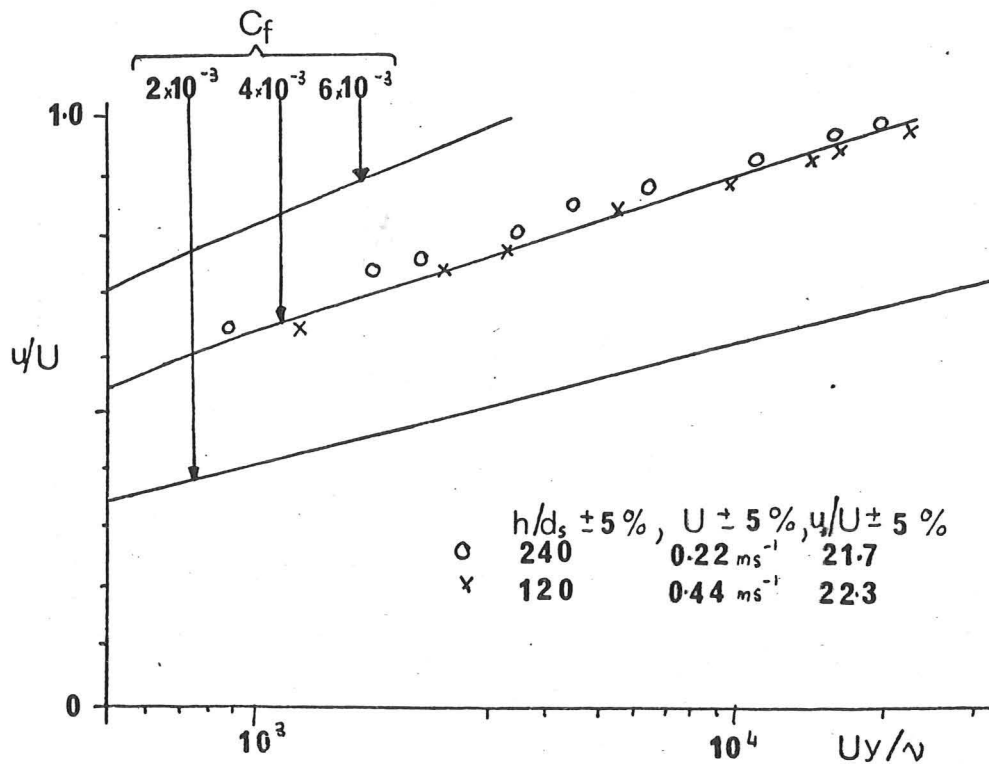
FIGURE 4.4.2 Velocity profiles at cylinder position
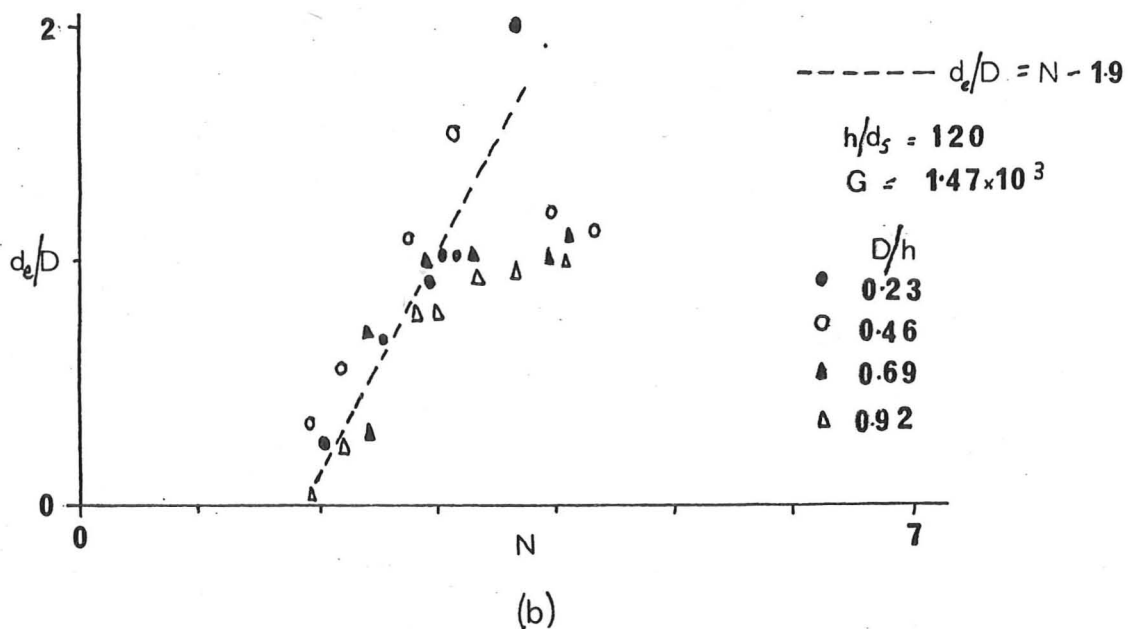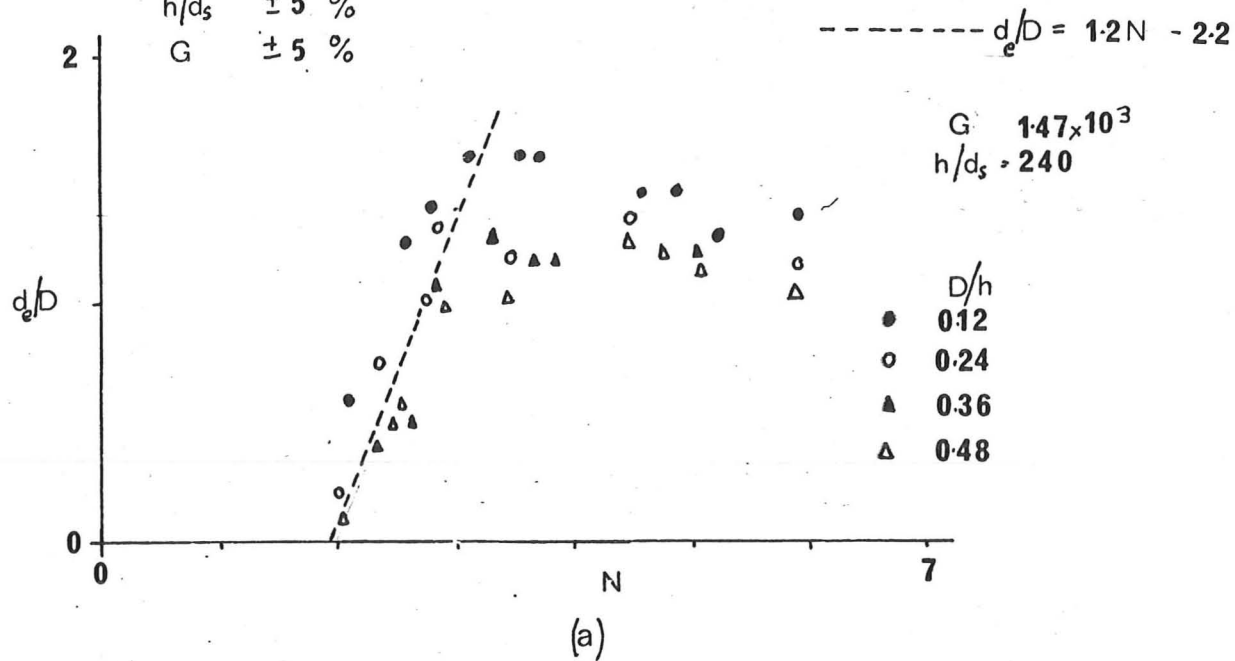
FIGURE 4.5.1 Equilibrium scour depth

$$d_e/D = (D/h)^{-0.18}$$

$h/d_s = 240$

$G = 1.47 \times 10^3$

$N > 3.5$

(c)

FIGURE 4.5.1 continued

$h/d_s = 240$

$G = 1.47 \times 10^3$

$D/h = 0.48$

	N
CWS	σ 2.4
	Δ 2.5
	□ 2.85
SWCSM	● 3.4
	▲ 4.7
	■ 5.1

(a)

CWS   Clear water scour

SWCSM   Scour with continuous sediment motion
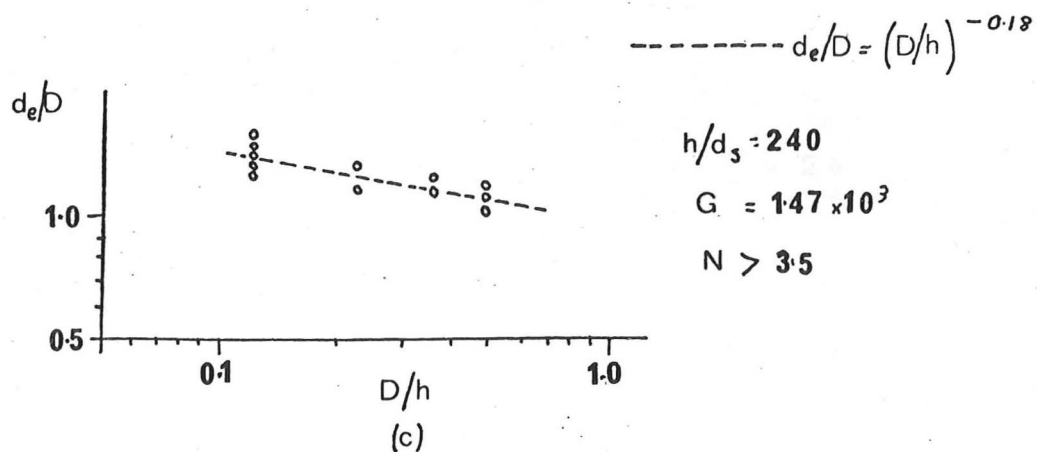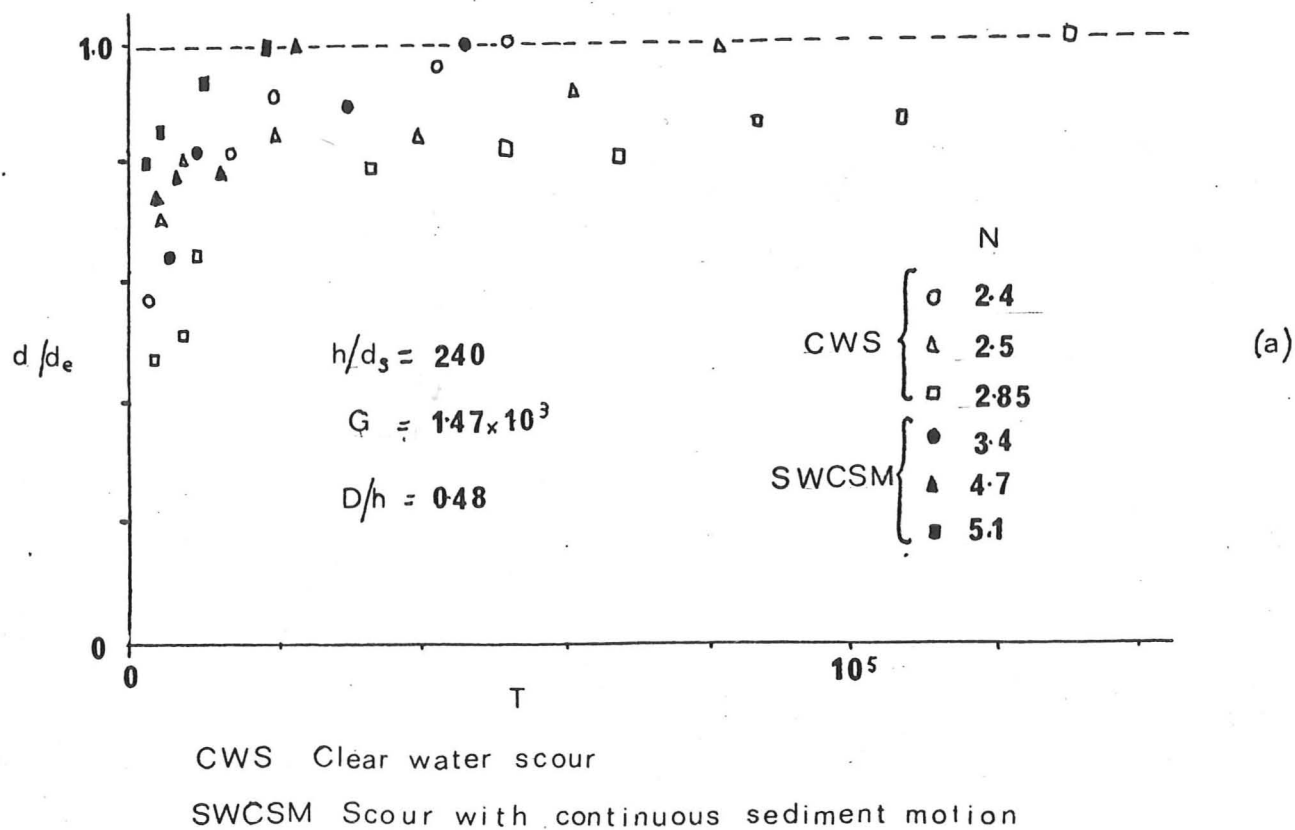
FIGURE 4.5.2 Time development of scour

(b)

$h/d_s = 240$

$G = 1.47 \times 10^3$

$D/h = 0.36$

CWS $\begin{cases} \circ & 2.6 \\ \triangle & 2.8 \\ \square & 3.3 \end{cases}$

SWCSM $\begin{cases} \bullet & 3.8 \\ \blacktriangle & 4.4 \\ \blacksquare & 5.0 \end{cases}$

N

(c)

$h/d_s = 240$

$G = 1.47 \times 10^3$

$D/h = 0.24$

CWS $\begin{cases} \circ & 2.0 \\ \triangle & 2.4 \\ \square & 2.6 \\ \triangledown & 2.8 \end{cases}$

SWCSM $\begin{cases} \bullet & 3.4 \\ \blacktriangle & 4.5 \end{cases}$

N
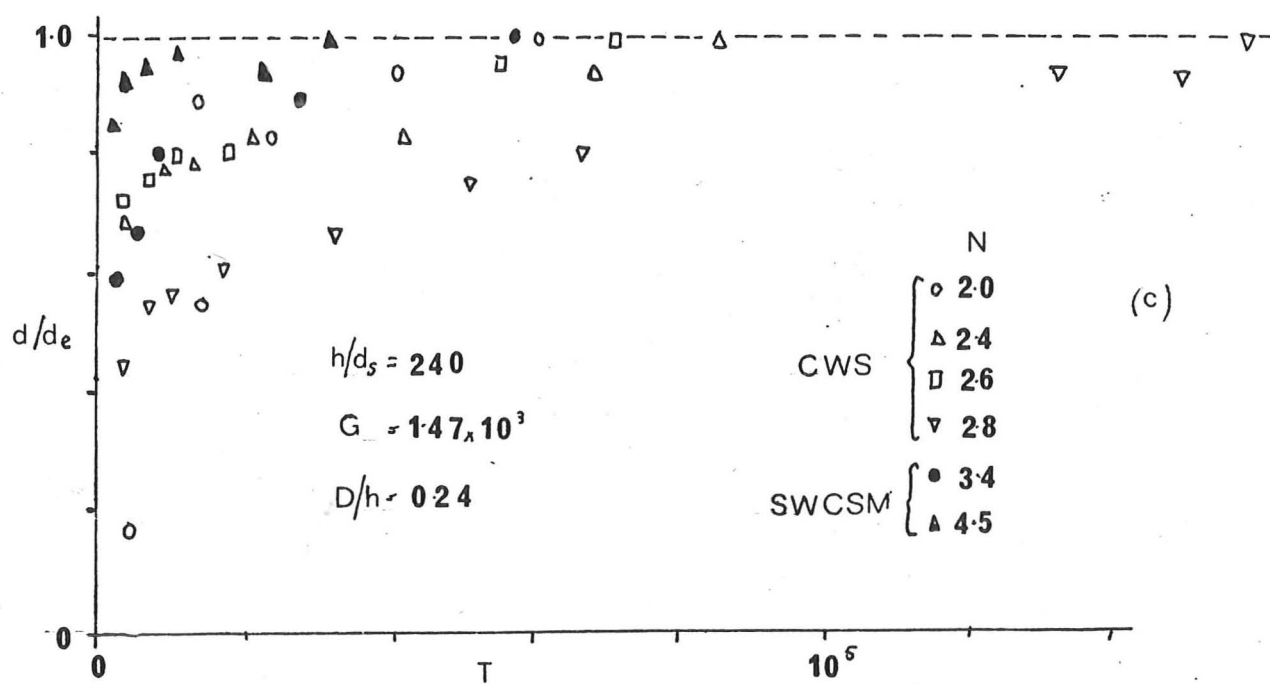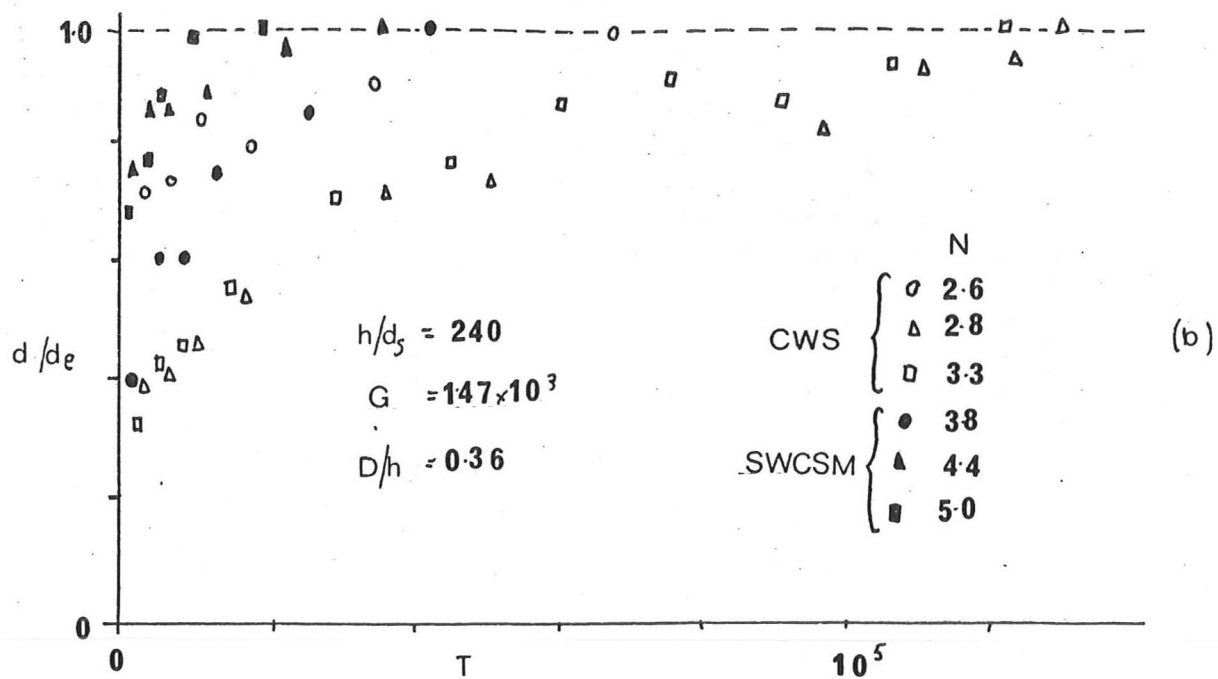
Errors

d/d_e	$\pm 20\%$		D/h	$\pm 5\%$
T	$\pm 6\%$		h/d_s	$\pm 5\%$
N	$\pm 4\%$		G	$\pm 5\%$

FIGURE 4.5.2 continued

(a) Before scour   (b) After scour
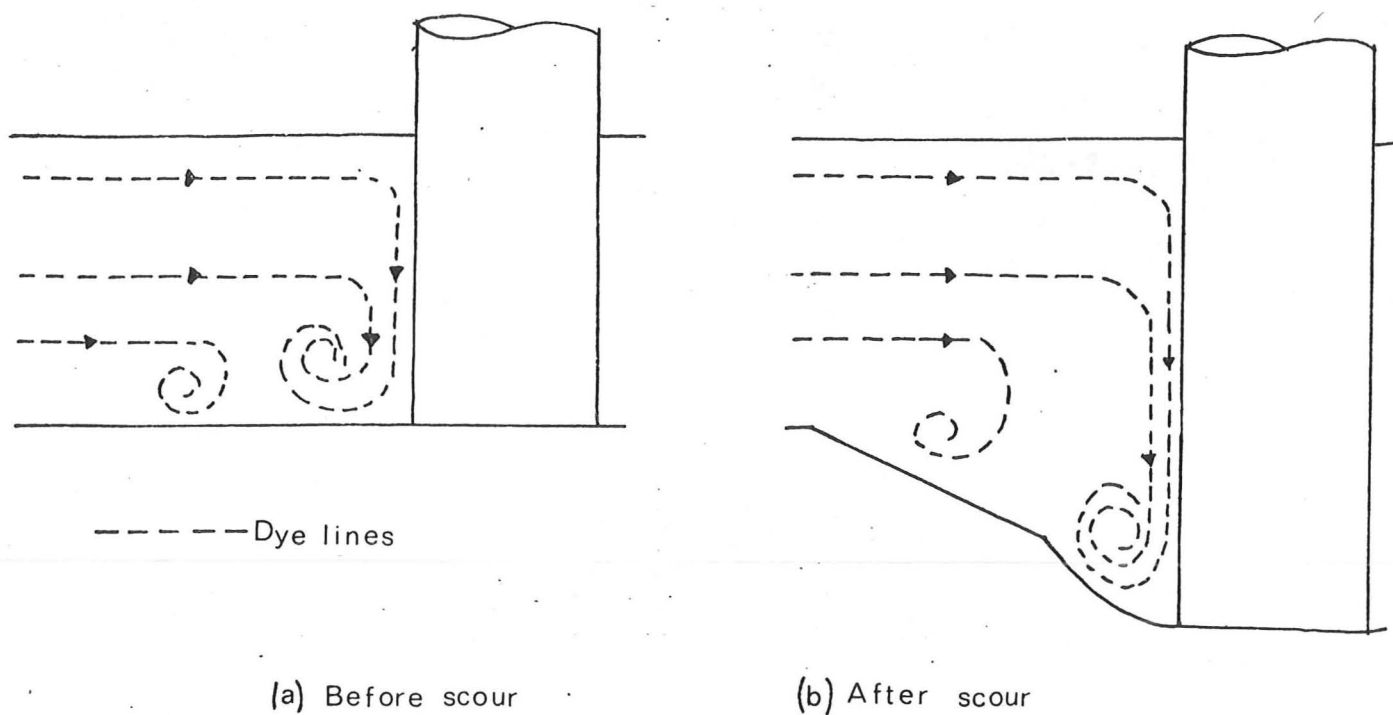
FIGURE 4.5.3 Dye flow visualization

(a)
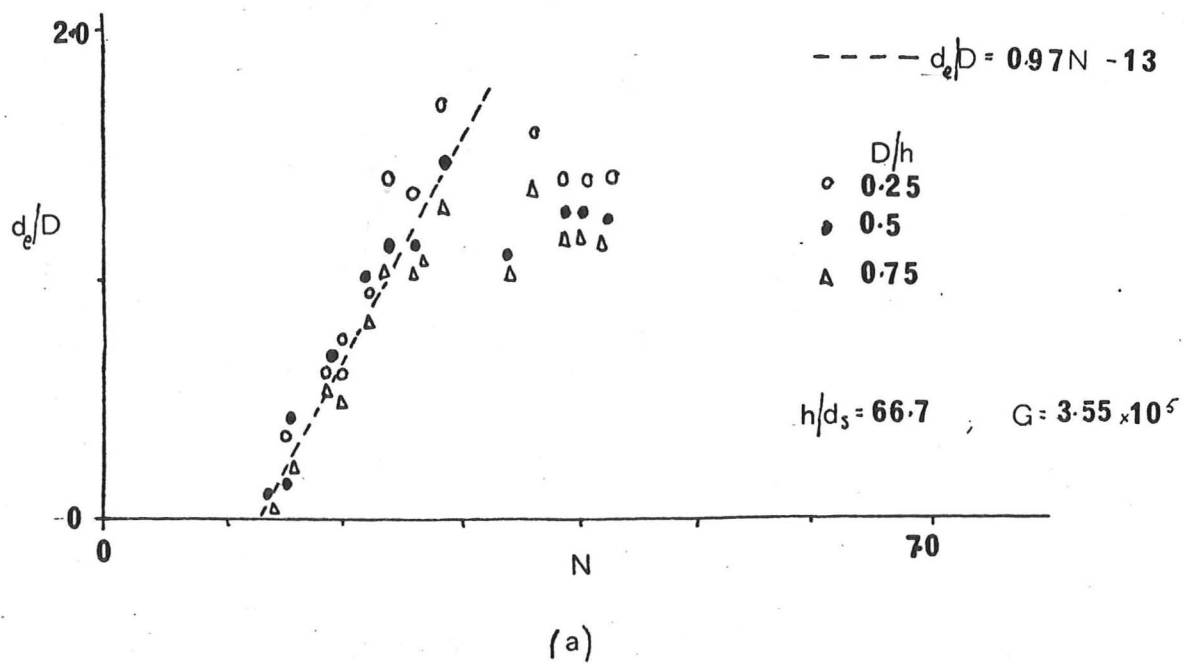
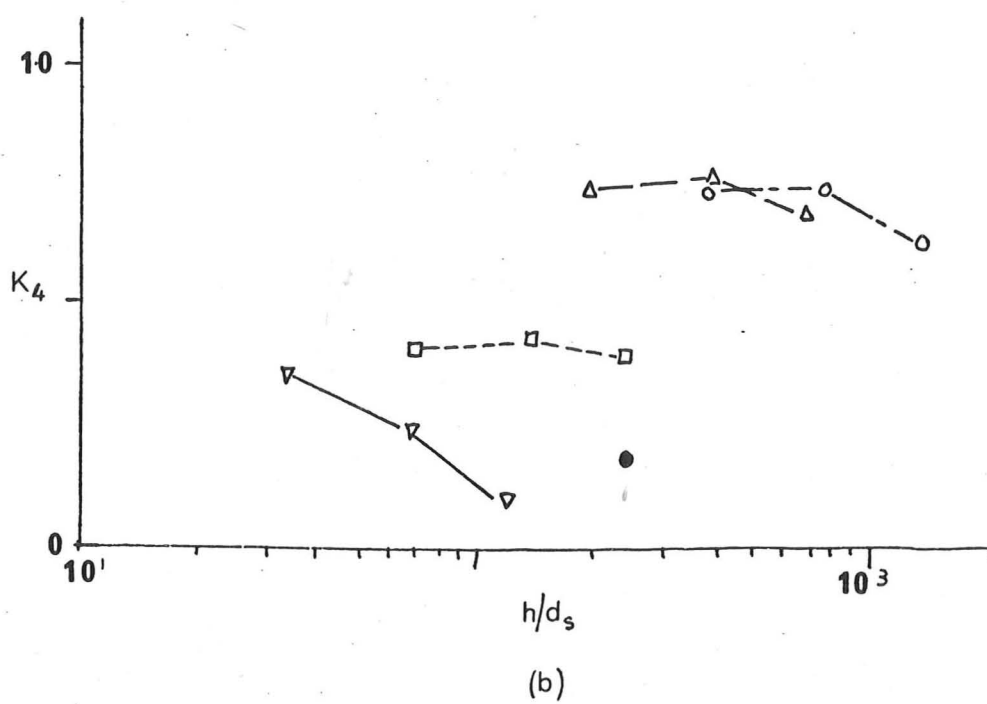FIGURE 4.6.1 Results of Chabert and Engeldinger

(b)

(c)
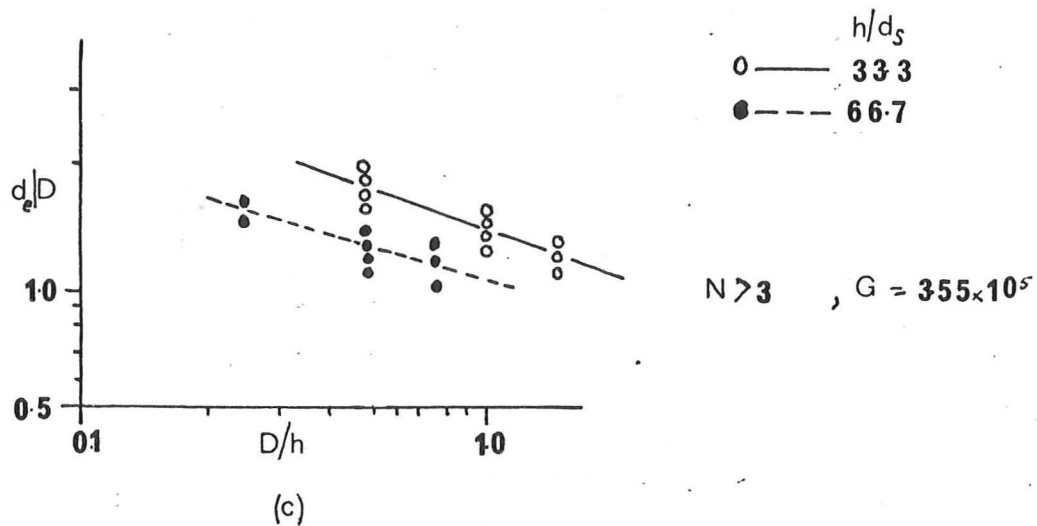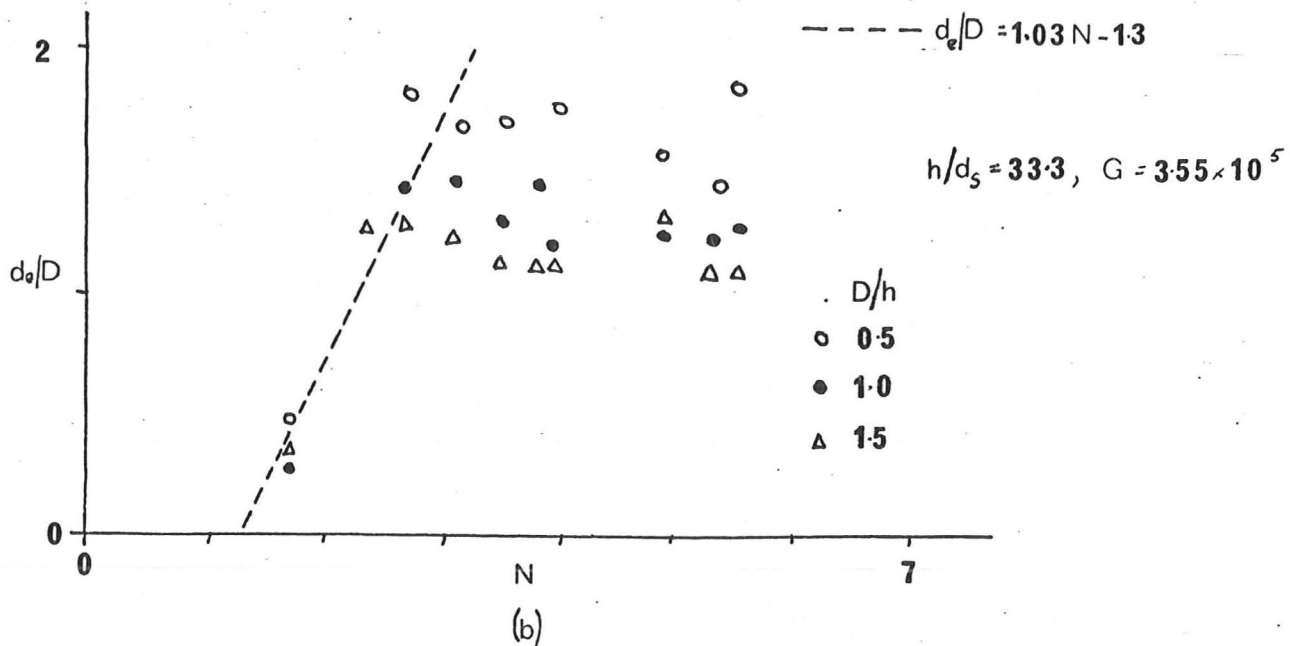
FIGURE 4.6.1 continued

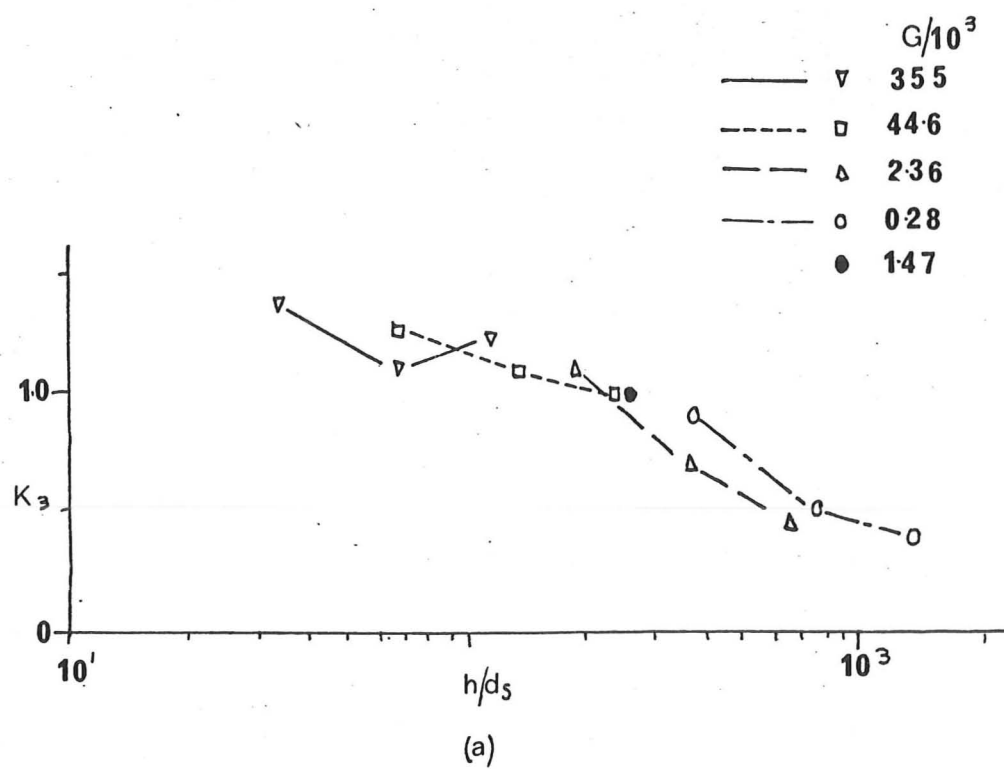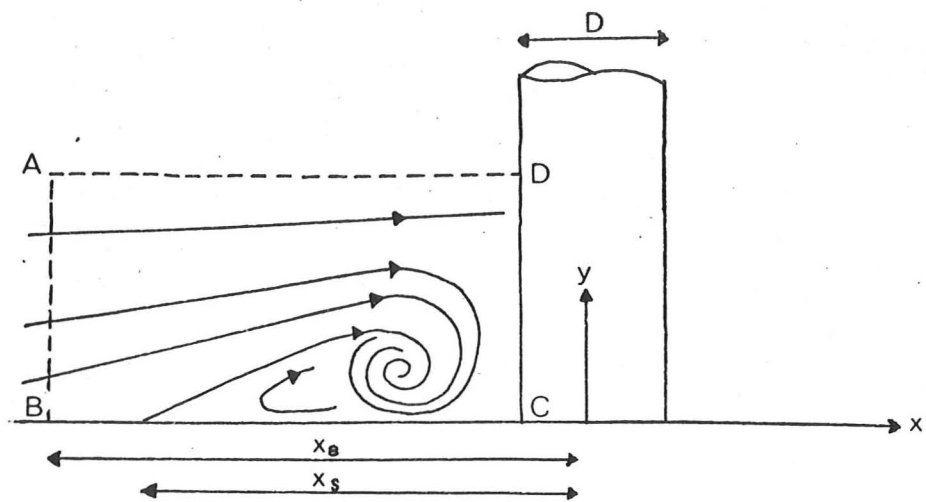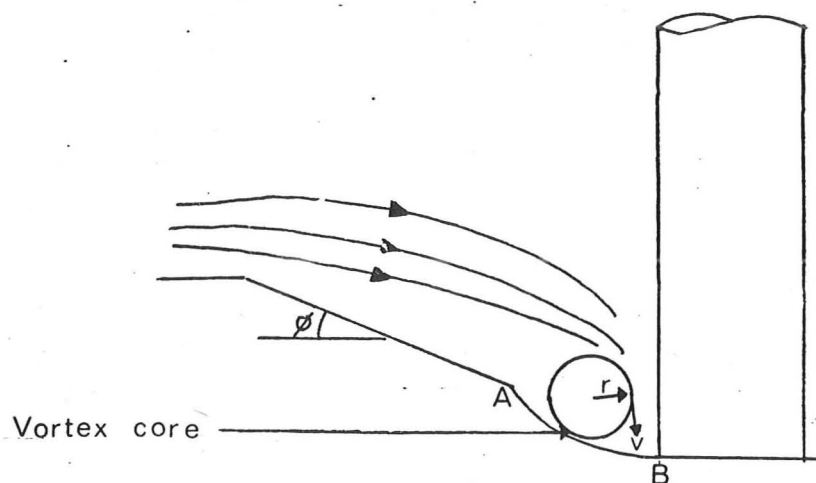FIGURE 4.6.2 Variation of K_3 and K_4

FIGURE 4.7.1

Vortex core

FIGURE 4.7.2

FIGURE 4.7.3